UNSTEADY HYDRODYNAMIC FORCES ON SPHEROIDAL BODIES

BY

RAJAI SAMIH ALASSAR

A Dissertation Presented to the

FACULTY OF THE COLLEGE OF GRADUATE STUDIES

KING FAHD UNIVERSITY OF PETROLEUM & MINERALS

DHAHRAN, SAUDI ARABIA

In Partial Fulfillment of the
Requirements for the Degree of

DOCTOR OF PHILOSOPHY

In

CIVIL ENGINEERING

DECEMBER, 1996

KING FAHD UNIVERSITY OF PETROLEUM & MINERALS

Dhahran 31261, SAUDI ARABIA

COLLEGE OF GRADUATE STUDIES

This dissertation, written by **RAJAI SAMIH ALASSAR** under the direction of his Dissertation Advisor and approved by his Dissertation Committee, has been presented to and accepted by the Dean of the College of Graduate Studies, in partial fulfillment for the degree of **DOCTOR OF PHILOSOPHY IN CIVIL ENGINEERING.**

Dissertation Committee

Dr. Rashid Allayla
(Chairman)

Dr. Hassan Badr
(Co-Chairman)

Dr. Ala Al-Rabeh
(Member)

Dr. Husain Al-Gahtani
(Member)

Dr. Achi Ishaq
(Member)

Dr. Mohammad Al-Suwayian
(Member)

Dr. Sahl Abdul Jauwad
(Department Chairman)

Dr. Abdallah Al-Shehri
(Dean, College of Graduate Studies)

Date : 15-2-97

When I was six, she had a hard time convincing me to go to school on my first day. She had four other children to raise up while her husband was away for nine years. She was incredibly patient and made unlimited sacrifices. I am fortunate to be engaged to a woman who is as patient as the one who raised me.

I dedicate this dissertation

TO

MY MOTHER & J.R.

ACKNOWLEDGMENT

I have been most fortunate to have Dr. Rashid Allayla and Dr. Hassan Badr as my dissertation committee chairmen. Through their support and guidance, this work has been possible. I extend my thanks and appreciation to my committee members: Dr. Ala Al-Rabeh, Dr. Husain Al-Gahtani, Dr. Achi Ishaq, and Dr. Mohammad Al-Suwaiyan. Through the course of this work, I had several fruitful conversations with Dr. J.D. Walker, Lehigh University, Pennsylvania; and Dr. I. H. Tarman, KFUPM and hereby express my appreciation. Special thanks are extended to Dr. Hasan Al-Ahmadi , Mr. Mohammad Al-Hafez, and Mr. Mohammad Al-Daous whose help can not be forgotten. I would like also to thank my family and all my friends especially Dr. Khalaf Al-Ofi, Mr. Adnan Blaibel, Dr. Nabil Abuzaid, Mr. Badie Eqnaibi, and Mr. Ibrahim Abdallah Al-Omar for their support and encouragement. Acknowledgment is also due to King Fahd University of Petroleum and Minerals for support of this research.

CONTENTS

LIST OF TABLES v

LIST OF FIGURES vi

ABSTRACT (Arabic) xi

ABSTRACT (English) xii

1. INTRODUCTION 1

1.1 Present Status of the Problem 3

1.1.1 Spheres 3

1.1.2 Spheroids 4

1.2 Objectives 4

2. LITERATURE REVIEW 5

2.1 Spheres 5

2.1.1 Steady, Uniform, and Rotating Flows 5

2.1.2 Oscillating and Accelerating Flows 7

2.2 Oblate and Prolate Spheroids 9

3. PROBLEM STATEMENT AND THE GOVERNING EQUATIONS 11

3.1 Preliminaries 11

3.2 Navier-Stokes Equations in the Stream Function and Vorticity Form 12

3.3 The Spheroidal Bodies under Consideration 14

3.3.1 The Sphere 14

3.3.2 The Oblate and Prolate Spheroids 16

4. POTENTIAL FLOW OVER OBLATE AND PROLATE SPHEROIDS 19

4.1 Potential Flow over Oblate Spheroids 19

4.2 Potential Flow over Prolate Spheroids 24

4.3 Observations and Comments 26

5. VISCOUS FLOW OVER SPHERES 31

5.1 Basic Equations and Method of Solution 32

5.2 The Numerical Method 35

5.3 Oscillating Flow 41

5.4 Fluctuating Flow 76

6. VISCOUS FLOW OVER OBLATE SPHEROIDS 102
6.1 Steady Flow 102
6.1.1 Formulation of the Problem and the Method of Solution 102
6.1.2 Results and Discussions 106
6.2 Unsteady Flow 121
6.2.1 Formulation of the Problem and the Method of Solution 121
6.2.2 The Impulsively Started Flow 123
6.2.3 Oscillating Flow 140
7. VISCOUS FLOW OVER PROLATE SPHEROIDS 166
7.1 Governing Equations and Method of Solution 166
7.2 Results and Discussions 168
8. CONCLUSIONS AND RECOMMENDATIONS 187
APPENDIX 191
BIBLIOGRAPHY 192
VITA 196

LIST OF TABLES

5.1 Phase angles at which drag components change sign 47

5.2 Flow characteristics for the range of parameters 97

6.1 Parameters of calculations 108

6.2 Vorticity modes on the surface of the oblate spheroid 110

6.3 Comparison of C_D with equations (6.23) and (6.24) 115

6.4 Comparison of C_D for the sphere 124

6.5 Phase angles at which drag components change sign 147

LIST OF FIGURES

3.1 The spherical coordinate system 15

3.2 The oblate spheroidal coordinate system 17

3.3 The prolate spheroidal coordinate system 18

4.1 Inviscid surface pressure distribution for the spheroids 28

4.2 The inviscid drag coefficient of the oblate spheroid 29

4.3 The inviscid drag coefficient of the prolate spheroid 30

5.1 The computational algorithm 39

5.2 Drag over an oscillation cycle, Re=16.7, S=0.625 42

5.3 The time variation of the drag coefficient for the case $S=\pi/4$ at different Reynolds numbers 44

5.4 The time variation of the pressure component of drag coefficient for the case $S=\pi/4$ at different Reynolds numbers 45

5.5 The time variation of the friction component of drag coefficient for the case $S=\pi/4$ at different Reynolds numbers 46

5.6 The time variation of the total, pressure, and friction drag for the case Re=50, (a)$S=\pi/4$, (b)$S=\pi/2$, (c)$S=\pi$, (d)$S=2\pi$ 51

5.7 The time variation of the pressure coefficient during one quarter of a complete oscillation for the case $S=\pi/4$ 53

5.8 The time variation of the surface vorticity distribution during one-half of a complete oscillation for the case Re=50, $S=\pi/4$ 54

5.9 The time variation of the surface vorticity distribution during one-half of a complete oscillation for the case Re=200, $S=\pi/4$ 55

5.10 Instantaneous streamlines for the case Re=200, $S=\pi/4$ 59

5.11 Instantaneous vorticity distribution for the case Re=200, $S=\pi/4$ 62

5.12 The time variation of the separation angle (a)$S=\pi$, (b)$S=\pi/2$, (c)$S=\pi/4$ 65

5.13 The time variation of the separation angle (a)Re=50, (b)Re=100, (c)Re=200 68

5.14 The time variation of the wake length (a)Re=50, (b)Re=100, (c)Re=200 ... 72

5.15 The time variation of the wake length for the case $S=\pi/4$ 73

5.16 Time-averaged patterns over the fourth cycle for the case Re=200, $S=\pi/4$, (a)stream function, (b)vorticity 74

5.17 The time development of averaged stream function for the case Re=50, $S=\pi/4$, (a)second cycle, (b)fourth cycle, (c) sixth cycle 75

5.18 The time variation of C_D for the case of $S=\pi/4$, $\gamma=0.5$ 77

5.19 The time variation of C_{DF} for the case of $S=\pi/4$, $\gamma=0.5$ 78

5.20 The time variation of C_{DP} for the case of $S=\pi/4$, $\gamma=0.5$ 79

5.21 The time variation of C_D for the case of Re=40, $\gamma=0.5$ 80

5.22 The time variation of C_D for the case of $S=\pi/4$, Re=100 81

5.23 The time variation of surface vorticity for the case Re=40, $S=\pi/4$, $\gamma=0.5$ 82

5.24 The time variation of P^* for the case Re=40, $S=\pi/4$, $\gamma=0.5$ 83

5.25 The time variation of surface vorticity for the case Re=100, $S=\pi/4$, $\gamma=0.1$ 85

5.26 The time variation of surface vorticity for the case Re=100, $S=\pi/4$, $\gamma=0.5$ 86

5.27 Time development of streamline patterns for the case Re=40, $S=\pi/4$, $\gamma=0.5$ 89

5.28 Time development of equi-vorticity patterns for the case Re=40, $S=\pi/4$, $\gamma=0.5$ 92

5.29 The time variation of the wake length for the case of $S=\pi/4$, $\gamma=0.5$ 94

5.30 The time variation of the wake length for the case of Re=10, $\gamma=0.5$ 95

5.31 The time variation of the wake length for the case of Re=100, $S=\pi/4$ 96

5.32 The time variation of the separation angle for the case of $S=\pi/4$, $\gamma=0.5$ 99

5.33 The time variation of the separation angle for the case of Re=10, $\gamma=0.5$ 100

5.34 The time variation of the separation angle for the case of Re=100, $S=\pi/4$ 101

6.1 Surface vorticity distribution for the case Re=0.1, $\xi_0=0.25$, at different N values 107

6.2 The drag components for the case ξ_o=1.0, at different Reynolds numbers 111

6.3 Surface pressure distribution for the case ξ_o=1.0, at different Reynolds numbers 112

6.4 Surface vorticity distribution for the case ξ_o=1.0, at different Reynolds numbers 114

6.5a Comparison of the present drag with the formula of Payne and Bell (1960) 116

6.5b Comparison of the present drag with the formula of Breach (1961) 117

6.6 Surface pressure distribution for the case Re=1.0 at different ξ_o values 118

6.7 Surface vorticity distribution for the case Re=1.0 at different ξ_o values 119

6.8 Streamlines and vorticity for the case ξ_o=0.25, (a)Re=0.1, (b)Re=1.0 120

6.9 Surface vorticity distributions for the cases of Re_s=20 and 40 125

6.10 Time development of surface vorticity distribution for the case of A_r=0.6 and Re=20 127

6.11 Time development of surface pressure distribution for the case of A_r=0.6 and Re=20 128

6.12a Surface vorticity distributions for the case of A_r=0.6, at different Reynolds numbers 129

6.12b Surface vorticity distributions for the case of A_r=0.76, at different Reynolds numbers 130

6.13 Surface pressure distributions for the case of A_r=0.6, A_r=0.76 at different Reynolds numbers 131

6.14 The time variation of the separation angle for the cases of A_r=0.6, A_r=0.76 at different Reynolds numbers 132

6.15a The time variation of the friction drag coefficient for the cases of A_r=0.6, A_r=0.76 at different Reynolds numbers 133

6.15b The time variation of the total drag coefficient for the cases of A_r=0.6, A_r=0.76 at different Reynolds numbers 134

6.16 Streamlines and equi-vorticity lines for the case of Re=100, A_r=0.6 138

6.17 The variation of the wake length with time for the cases of A_r=0.6, A_r=0.76 at different Reynolds numbers 139

6.18 The time variation of the drag coefficient for the cases Re=0.5, and 5.0,

at S=π / 4 142

6.19 $(C_D - C_{DLM}) / \max[C_{DLM}]$ versus Φ for the case Re=5 143

6.20 The time variation of the drag coefficient for the case S=π / 4, at different Reynolds numbers 144

6.21 The time variation of the friction component of drag for the case S=π / 4, at different Reynolds numbers 145

6.22 The time variation of the pressure component of drag for the case S=π / 4, at different Reynolds numbers 146

6.23 The time variation of the drag coefficient for the case Re=40, at different Strouhal numbers 148

6.24 The relative difference between the drag coefficient for the case Re=40, and the potential flow drag at different Strouhal numbers 149

6.25 The time variation of the pressure coefficient during one half of a complete oscillation for the case Re=100, S=π / 4 150

6.26 The time variation of the surface vorticity during one half of a complete oscillation for the case Re=100, S=π / 4 152

6.27 Comparison of the surface vorticity at phase angle =π / 4 for the case S=3π / 4 153

6.28 Comparison of the surface vorticity at phase angles 0, 3π / 4 for the case Re=20 at different S values 154

6.29 Streamlines and vorticity development with time for the case Re=100, S=π / 4 158

6.30 Time Development of the separation angle for the case S=π / 4 160

6.31 Time Development of the separation angle for the case Re=40 161

6.32 Time Development of the wake length for the case S=π / 4 162

6.33 Time Development of the wake length for the case Re=40 163

6.34 Time averaged patterns over the fifth cycle for the case Re=5, S=π / 4 165

7.1 Comparison of the drag coefficient with the analytical drag of Lai and Mockros (1972) 170

7.2 The difference between the drag of the present study and that of Lai and Mockros (1972) at different Reynolds numbers 171

7.3 The time variation of the drag coefficient at different Reynolds numbers .. 172

7.4 The time variation of the friction component of drag coefficient

at different Reynolds numbers 173

7.5 The time variation of the pressure component of drag coefficient at different Reynolds numbers 174

7.6 The time variation of pressure during one half of a complete oscillation for the case Re=100 176

7.7 The time variation of the surface vorticity during one half of a complete oscillation for the case Re=100 177

7.8 Comparison of the pressure distribution at t=20 for different Reynolds numbers 178

7.9 Instantaneous streamline and vorticity for the case Re=100 182

7.10 Time development of the separation angle 183

7.11 Time development of the wake length 184

7.12 Time averaged streamline and vorticity patterns over one full cycle for the case Re=5 186

الخلاصة

الإسم : رجائي سميح العصار
عنوان الرسالة : القوة الهيدروديناميكية المتغيرة مع الزمن على الأجسام الكروية وشبه الكروية
التخصص : الهندسة المدنية
تاريخ الشهادة : ديسمبر ١٩٩٦ م

تُعنى هذه الرسالة بدراسة سريان الموائع المتناظر محورياً حول الأجسام المتشكّلة نتيجة الدوران المحوري ؛ فقد تمّ حلّ معادلات نافير –ستوكس الثابتة والمتغيّرة مع الزمن للموائع غير القابلة للإنضغاط . واعتمد الحل على أنظمة المحاور الكرويّة وشبه الكرويّة بإعتبار عدّة أنظمة زمنيّة للتدفق البعيد عن الجسم الدوراني مع التركيز على الحركة الإهتزازيّة . إنّ طريقة الحل المستخدمة تعتبر طريقة شبه تحليليّة ؛ حيث تمّت عملية تمديد رياضي لدالّتي التدفق والدوران بوساطة دوال ليجندر . وتمّ بعد ذلك حل المعادلات التفاضليّة الناتجة بطريقة عدديّة . ومن الجدير بالذكر أنّه قد تمّت مُقارنة نتائج هذه الدراسة مع مثيلاتها المنشورة وذلك لإثبات كفاءة النموذج الرياضي المطوّر . وبعد التأكد من كفاءة هذا النموذج عُرضت نتائج هذه الدراسة على شكل خواص محدّدة كمعامل السحب والدوران السطحي وتوزيع الضغط السطحي بالإضافة إلى أنماط خطوط السريان والدوران المتماثل . وأخيراً تمّ عرض التحليلات المفصّلة لطول الدوران الراجع وزاوية الإنفصال .

درجة الدكتوراة في الفلسفة

جامعة الملك فهد للبترول والمعادن
الظهران - المملكة العربية السعودية

ديسمبر ١٩٩٦ م

ABSTRACT

NAME OF STUDENT : RAJAI SAMIH ALASSAR
TITLE OF STUDY : UNSTEADY HYDRODYNAMIC FORCES ON SPHEROIDAL BODIES
MAJOR FIELD : CIVIL ENGINEERING
DATE OF DEGREE : December, 1996

The problem of incompressible axisymmetric flow over spheroidal bodies is considered. The analysis covers steady and unsteady flows of inviscid and viscous fluids. The spheroidal bodies may take the shape of spheres, oblate or prolate spheroids. The study is based on analytical and numerical solutions of the mass and momentum conservation equations. Euler's equations are solved analytically for the case of inviscid flow while the full Navier-Stokes equations are solved numerically for the case of viscous flow. The study focuses on the time variation of the velocity field as well as the hydrodynamic forces due to free-stream oscillations. The method of solution of the full Navier-Stokes equations combines analytical and numerical techniques where the stream function and vorticity are approximated using Legendre functions whereas the resulting differential equations are solved numerically. The parameters involved in the viscous flow problem are the Reynolds number, Strouhal number, and the spheroidal body geometry. The study covers Reynolds numbers in the range from 0.1 to 200 and Strouhal numbers in the range from $\pi/4$ *to* 2π. *Results are presented in terms of the drag coefficient, surface vorticity and surface pressure distributions, and streamline and equi-vorticity patterns. Detailed analysis of the velocity field including the wake length and angle of separation is also presented.*

DOCTOR OF PHILOSOPHY DEGREE

KING FAHD UNIVERSITY OF PETROLEUM & MINERALS
DHAHRAN, SAUDI ARABIA

December, 1996

CHAPTER 1

INTRODUCTION

In the last few years, considerable research has been carried out to investigate the characteristics of flows over bodies of various shapes. Because of the related engineering applications, special interest has evolved in bodies of cylindrical, disk-shaped, or spherical geometry. For example, the analysis of viscous flow over inclined cylinders is motivated by the need to estimate the hydrodynamic forces on various components of submerged structures (columns and supports of off shore platforms, underwater cables and pipes, ... etc.). This analysis is also useful in the process of cooling hot wires and electronic components. Other components of these offshore structures and platforms which are subject to wave induced oscillatory motion can be of different shapes such as plates and disks which are sometimes used as damping devices. There is a need to characterize the hydrodynamic forces acting on these structural components for analysis and design. Flow over spheres has many applications in natural processes. Water droplets 300 μm in diameter settling in air remain spherical under the influence of surface tension and behave essentially as a rigid sphere. The corresponding Reynolds number is approximately 20 based on the diameter and terminal falling speed. An air bubble in water will behave as a sphere due to surface tension and the presence of surfactants with Reynolds number of about 10 as it rises under buoyancy, Chang and Maxey (1994). Flow over spheres is also encountered in particle-laden flows, such as pneumatic conveying systems and spray injection of liquid fuel in combustors and cyclone separators.

In many situations, the velocity field is time-dependent and details of the unsteady dynamics of the motion are required. Of particular interest is the oscillatory motion over particles which takes place when the main stream exhibits some velocity fluctuations. The

oscillatory motion of a particle at low Reynolds number is of interest in Brownian motion, suspension rheometry and the passage of sound waves through particulate systems. More general unsteady particle motions occur in colloidal suspensions and for particle motion in filters. Moreover, the rates of heat and mass transfer can be enhanced by the oscillation of the surrounding fluid. This phenomenon is useful in pulsed combustion, drying, and absorption of high-intensity sound in particle-laden flows, Drummond and Lyman (1990).

There are many situations where the particles are neither perfect spheres nor flat circular disks. Under real conditions, offshore structural members may be covered by marine fouling thus changing the shape. Furthermore, motion of particles suspended in a gas is common in the industry where there is active aerosols release. Most aerosol particles are not spherical and therefore it is of considerable interest to examine the effects of particle shapes. Generally, studying flows over oblate and prolate spheroids is important as the sphere and the flat circular disk are special cases of these generalized geometries. Thus, there is a strong need to obtain accurate solutions that can describe the characteristics of the flow over these geometries.

In the present study, an attempt is made to broaden the solutions available in the literature to suit the general spheroidal geometries. In this regard, the full steady and unsteady Navier-Stokes equations for incompressible fluids, written in terms of the stream function and vorticity, are solved using the spherical and spheroidal coordinates systems. Furthermore, time dependent free stream conditions are to be incorporated with concentration on oscillatory motions. While the main interest is to determine the characteristics of the viscous flow, it is also important to determine the potential flow solution for such motion. The potential flow solution provides a base for comparison with the viscous flow in the region adjacent to the solid surface and also provides the boundary conditions far away from the surface. In the past, simplifying assumptions were always used to solve the Navier-Stokes equations. These assumptions include neglecting inertia terms (Stokes solution), neglecting viscous terms (potential flows), and boundary layer

approximation. Such simplifications, of course, restrict the range of applicability of the solutions obtained. The cost of computations using numerical solutions have always been prohibitive. Reasonably accurate methods of solution have determined the characteristics of oscillatory flow over spheres up to Reynolds number of 16.7, Chang and Maxey (1994). Oscillatory flows over oblate and prolate spheroids have only been analyzed through Stokes linearized equations of motion, Lai and Mockros (1971).

1.1 Present Status of the Problem

The problem under consideration consists of two parts. The first is the flow over perfect spheres and the second is the flow over spheroids (oblate and prolate). The following summarizes the present knowledge of each problem.

1.1.1 Spheres

Considerable research has been carried out in this case. Steady flow over spheres is quite known and well established in the literature. The impulsively started flow describing the time development of the flow field has been studied by few researchers. Among those is the excellent study by Dennis and Walker (1972) where the full Navier-Stokes equations were solved. Studies related to oscillatory flow over spheres are scarce. The problem has been solved by neglecting the non-linear inertia terms in the equations of motion. The solution obtained is only valid for small Reynolds numbers due to the considerable effect that these terms have when Reynolds number increases. A recent attempt to solve the full Navier-Stokes equations for the oscillating flow over spheres was made by Chang and Maxey (1994) using spectral methods. The results were obtained up to Reynolds number of 16.7 and Strouhal number of 10. Fluctuating flow about a non-zero mean past spheres has only been considered by Mei et al. (1991) where attention was focused on the flow characteristics for very small fluctuations.

1.1.2 Spheroids

The only known solutions for steady flow over spheroids are those of Payne and Pell (1960) which were modified by Breach (1961). These solutions for oblate and prolate spheroids were obtained through solving the linearized Stokes equations. The literature lacks the solutions of the time-dependent flow problem. The oscillating flow solution over these geometries was obtained through Stokes equations, Lai and Mockros (1971).

1.2 Objectives

The objectives of the present study are as follows:

1. Obtain the steady and time-dependent potential flow solutions for oblate and prolate spheroids.

2. Develop a special mathematical method for solving the problem of steady and time-dependent flow over axisymmetric bodies including the following cases:

   A. Oscillating flow over spheres
   B. Fluctuating flow about a non-zero mean over spheres.
   C. Steady viscous flow over oblate spheroids
   D. The impulsively started flow over oblate spheroids.
   E. Oscillating flow over oblate spheroids.
   F. Oscillating flow over prolate spheroids.

3. Compare the obtained solutions with the previous available results.

CHAPTER 2

LITERATURE REVIEW

The literature published on the flow over spheres and sphere-like bodies is numerous. Perhaps, the best way to review these papers is through grouping them as presented below.

2.1 Spheres

2.1.1 Steady, Uniform, and Rotating Flows

Previous numerical solutions for the problem of steady flow over a sphere have been reported by Kawaguti (1950) at Reynolds number Re = 20, Lister (1953) at Re = 0, 1, 10, 20 and by Jenson (1959) at Re = 5, 10, 20, 40. Jenson (1959) concluded that separation took place as low as Re = 17 which was later criticized by many authors who found that separation does not take place below Re = 20. The method of solution adopted in the previous studies was the finite difference technique applied to the governing equations written in terms of the stream function and vorticity. Using finer grids, the same problem was solved by Hamielec et al. (1967), and Le Clair et al. (1970). The steady state solution obtained at large time when solving the impulsively started flow problem was reported by Rimon and Cheng (1969). Dennis and Walker (1964) used Fourier expansion for the flow variables to solve the problem for a wide range of Reynolds numbers. Later on (1971), they calculated the steady flow over a sphere by the series truncation method up to Re=40. Their method of solution was semi-analytical where the dependent variables were expanded in terms of Legendre polynomials. A third excellent paper by the same authors appeared in (1972) where they used the same method to determine the solution of the

impulsively started sphere for a wide range of Reynolds numbers. Matching techniques were used by Bentwich and Miloh (1978) to describe the flow past a sphere. Sano (1981) showed that the matching procedure used by Bentwich and Miloh (1978) was incomplete and presented a complete procedure for successful matching. The equations of motion for a small rigid sphere in a non-uniform flow were developed by Maxey and Riley (1983) from first principles. Oliver and Chung (1987) solved the steady flow problem over a fluid sphere through the series truncation method coupled with finite elements. The range of Reynolds numbers was from 0.5 to 50 while the range of viscosity ratio was from 0 (gas bubble) to 10^7 (solid sphere). Fornberg (1988) studied the steady flow over a sphere at high Reynolds numbers up to 5000. The wake was found to resemble a Hill's spherical vortex. An elementary treatment of Stokes flow was given by Klamkin (1989). A multigrid defect correction technique was used by Juncu and Mihail (1990) to solve the problem of incompressible steady flow past a sphere. The considered Reynolds numbers were 50, 100, 400, and 1000. A procedure for the calculation of the starting flow around a sphere in a uniform stream was presented by Lee (1991). In this procedure, the discrete vortices method was used where the vorticity filed was approximated by a number of discrete circular line vortices. The flow field over a sphere placed in a uniform flow was numerically analyzed by Shirayama (1992) on the basis of unsteady three dimensional structures in a separated flow field. He concluded that a topological transition suddenly takes place, and a periodical structure appears in the wake region. The instability of steady flow past a sphere was investigated by Natarajan and Acrivos (1993). The finite element method was used to compute the base flows, and to examine their linear instability to three-dimensional modal perturbations. The results showed that the first instability was through a regular bifurcation, and the critical number (based on the sphere radius) was 105. Kholeif and Kamel (1993) studied the deceleration of a sphere in an infinite viscous fluid. They considered two sources of retardation namely, by the action of a viscous shear on the sphere surface and by the action of the viscous shear with a plane shear flow at infinity. An exponential decay was shown in both cases.

Raman (1984) solved the problem of boundary-layer flow on a sphere rotating anticlockwise about its axis in a stagnant fluid using finite differences. He showed that the transverse velocity was positive in the upper hemisphere, zero in the equatorial plane and becomes negative in the lower hemisphere. Slow viscous rotating steady flow past a sphere was investigated by Raghavarao and Valli (1987) and by the same authors in (1989). A spinning sphere in a slowly rotating fluid at low Reynolds numbers was studied by Raghavarao and Sekhar (1993). They used an upwinding technique for the nonlinear inertia terms.

2.1.2 Oscillating and Accelerating Flows

One of the earliest attempts to analyze the motion of a sphere dates back to Basset (1888) who gave an analytical solution for the motion of a small spherical particle settling from rest under gravity in still fluid, based on the assumption of low particle Reynolds number. Odar and Hamilton (1964) proposed an equation for the force exerted by viscous fluid on a sphere which is accelerating arbitrarily and moving linearly in an otherwise quiet fluid. Odar (1966) later verified the equation through experiments. Riley (1966) investigated the flow induced by a sphere oscillating in a viscous fluid when the amplitude of oscillation is small compared with the radius of the sphere through perturbation methods. The flow induced by an oscillating sphere in a viscous fluid otherwise at rest was investigated by Higa and Takahashi (1987). Mass transfer from a sphere in an oscillating flow with zero mean velocity was studied by Drummond and Lyman (1990) using a pseudo-spectral method. Their main interest was to determine the best conditions for enhancing the mass transfer rate. Unsteady flow over a stationary sphere with small fluctuations in the free stream velocity at finite Reynolds numbers was investigated by Mei et. al (1991). Mei and Adrian (1992) investigated the same problem at small Reynolds numbers using a matched asymptotic solution. It was found that the acceleration dependent force was linearly proportional to the frequency. The Stokes flow solution was not appropriate at small frequencies. Mei et al. (1991) computed the unsteady drag on a

sphere at finite Reynolds number with small fluctuations in the free stream velocity. The finite-difference scheme showed that the force increases linearly with the square root of frequency. Mei (1994) used a numerical solution, together with a high-frequency asymptotic solution, to solve the unsteady Navier-Stokes equations for flow over a stationary sphere at finite Reynolds number with oscillating free stream velocity. The total unsteady drag compared well with Odar and Hamilton's (1964) experimental results at finite Reynolds numbers. Various unsteady drag components were examined. A general dynamic equation including the quasi-steady drag, history force and added-mass force in the time domain was proposed for particle motions at finite Reynolds number. An excellent paper about oscillatory motion was presented by Chang and Maxey (1994) using spectral methods. They investigated oscillating flow over a sphere for Strouhal numbers up to 10 and Reynolds numbers up to 16.7. It was found that at very low Reynolds numbers, separation took place during the deceleration period. This was attributed to the adverse pressure gradients during deceleration. No separation was found during the accelerating period. The accelerating and decelerating phases were not direct opposites of each other but created time-dependent streaming patterns. It was found that for a given phase angle, the length of the separation region decreases but encompasses more of the sphere at increasing Strouhal numbers. As the Strouhal number increases, the surface vorticity becomes more symmetric about the equator and increases in intensity. At very low Reynolds and Strouhal numbers, the shear stress was found to remain in phase with the free-stream velocity. Increasing Reynolds number acts to lengthen the recirculation region but reduces its breadth. Decreasing Reynolds number was found to delay separation. The pressure and viscous forces were shown to exhibit a phase lead over the free stream velocity. This was attributed to the acceleration effects which increase with the increase of the Strouhal number.

2.2 Oblate and Prolate Spheroids

The literature on the flow over oblate and prolate spheroids is scarce. The following papers are related to the present study.

Payne and Pell (1960) neglected the inertia terms and obtained formulas for the steady drag on bodies of various shapes including oblate and prolate spheroids. Breach (1961) modified these formulas by using two classical methods, those of Stokes (1851) and Oseen (1910) for finding approximations to viscous streaming at low Reynolds numbers. Upon investigating the Stokes flow generated by an oscillating spheroid, Kanwal (1955) obtained the general solution of the Stokes stream function. Kanwal, however, failed to numerically determine the constants of integration. Lai and Mockros (1971) used the linearized Stokes equations of motion to calculate the flow field generated by a spheroid executing axial translatory oscillations in an infinite, otherwise still, incompressible, viscous fluid. The flow field was expressed in terms of the wave function of order one. They integrated the drag formula over all frequencies to obtain a formula for the drag on a spheroid executing general axial translatory accelerations. The formula which is valid at low frequency consisted of three parts similar to those of the Basset solution (1888) for a sphere. These are the added mass, the steady Stokes drag, and the history term. Their solution was, however, criticized by Lawrence and Weinbaum (1988) who revealed significant differences between spheres and nearly spherical bodies. While investigating the oscillatory motion over oblate spheroids, Lawrence and Weinbaum (1986) found that the force was not a simple quadratic function in half-integer powers of the frequency as in the classical solution of Stokes for a sphere, and the force for an arbitrary velocity contained a new memory integral whose kernel differed from the classical behavior derived by Basset for a sphere. Barshinger and Geer (1984) studied Stokes flow past a thin body of revolution for the case of axially incident uniform flow. The part of the velocity and pressure fields due to the presence of the body was represented by a distribution of Stokelets and dipoles distributed over a disk which lies

entirely inside the body. Three-dimensional boundary layer on a spheroid at incidence was studied for the cases of laminar and turbulent flows by Patel and Baek (1985). The effect of deviation from sphericity on the deposition rate of aerosols on cold surfaces was found to be significant by Williams (1986). Rubel (1986) studied the axisymmetric shear flow over spheres and spheroids. An approximate boundary-layer method was used by Costis and Telionis (1988) to study the vortical wakes over a prolate spheroid. Turbulence effects on separated flow over a prolate spheroid were studied by Gee and Cummings (1992). Linear stability of the three-dimensional boundary layers over axisymmetric bodies at incidence was investigated by Spall and Malik (1992). Three-dimensional separation was also studied by Wu and Shen (1992) and by Su et al. (1993).

In the above-mentioned work on oblate and prolate spheroids, the linearized equations of motion were solved because the non-linearity in the Navier-Stokes equations renders the solutions of these problems extremely difficult. This, of course, imposes an upper limit on the range of validity of the obtained solutions. To obtain solutions that are valid at moderate or high Reynolds numbers, we recourse to the full Navier-Stokes equations.

CHAPTER 3

PROBLEM STATEMENT AND THE GOVERNING EQUATIONS

In this chapter, the Navier-Stokes equations are written in terms of the stream function and vorticity in any arbitrary coordinate system. These general equations are then used in subsequent chapters to obtain the appropriate governing relations for each specific coordinate system used.

3.1 Preliminaries

Consider any axisymmetric body whose geometry can be precisely described by a certain orthogonal coordinate system and assume that this coordinate system with coordinates labeled q_1 ,q_2 , and q_3 can be related to the Cartesian system (x,y,z) by the following relations:

$$x = x(q_1,q_2,q_3) \quad , \quad y = y(q_1,q_2,q_3) \quad , \quad \text{and} \quad z = z(q_1,q_2,q_3) \tag{3.1}$$

If it is further assumed that the arc length (ds) can be written in the new curvilinear coordinate system as

$$ds^2 = \sum_{i=1}^{3} (h_i\, dq_i)^2 \tag{3.2}$$

with h_i being some *scale factors,* it becomes standard mathematics to show that

$$h_i^2 = (\frac{\partial x}{\partial q_i})^2 + (\frac{\partial y}{\partial q_i})^2 + (\frac{\partial z}{\partial q_i})^2 \tag{3.3}$$

It follows that quantities such as arc length, gradients, laplacian, and the curl can be easily written in the new orthogonal curvilinear coordinate system once its scale factors are known. The arc length, then, takes the form

$$ds^2 = (h_1 dq_1)^2 + (h_2 dq_2)^2 + (h_3 dq_3)^2 \tag{3.4}$$

The gradient of a scalar function $\psi = \psi(q_1, q_2, q_3)$ is

$$\vec{\nabla}\psi = \frac{1}{h_1}\frac{\partial \psi}{\partial q_1}\vec{u}_1 + \frac{1}{h_2}\frac{\partial \psi}{\partial q_2}\vec{u}_2 + \frac{1}{h_3}\frac{\partial \psi}{\partial q_3}\vec{u}_3 \tag{3.5}$$

where $\vec{u}_1, \vec{u}_2$, and $\vec{u}_3$ are the unit vectors in the new orthogonal curvilinear coordinate system. The divergence of a vector field $(\vec{F})$ represented by

$$\vec{F} = F_1\vec{u}_1 + F_2\vec{u}_2 + F_2\vec{u}_2 \tag{3.6}$$

takes the following form:

$$\vec{\nabla} \bullet \vec{F} = \frac{1}{h_1 h_2 h_3}\left[\frac{\partial}{\partial q_1}(F_1 h_2 h_3) + \frac{\partial}{\partial q_2}(F_2 h_1 h_3) + \frac{\partial}{\partial q_3}(F_3 h_1 h_2)\right] \tag{3.7}$$

The laplacian then follows as

$$\nabla^2\psi = \frac{1}{h_1 h_2 h_3}\left[\frac{\partial}{\partial q_1}\left(\frac{h_2 h_3}{h_1}\frac{\partial \psi}{\partial q_1}\right) + \frac{\partial}{\partial q_2}\left(\frac{h_1 h_3}{h_2}\frac{\partial \psi}{\partial q_2}\right) + \frac{\partial}{\partial q_3}\left(\frac{h_1 h_2}{h_3}\frac{\partial \psi}{\partial q_3}\right)\right] \tag{3.8}$$

Finally the curl of a vector field can be written as

$$\vec{\nabla} \times \vec{F} = \frac{1}{h_1 h_2 h_3}\begin{vmatrix} h_1 u_1 & h_2 u_2 & h_3 u_3 \\ \dfrac{\partial}{\partial q_1} & \dfrac{\partial}{\partial q_2} & \dfrac{\partial}{\partial q_3} \\ F_1 h_1 & F_2 h_2 & F_3 h_3 \end{vmatrix} \tag{3.9}$$

3.2 Navier-Stokes Equations in the Stream Function and Vorticity Form

The Navier-Stokes equations for incompressible fluids in the most general form can be written in vector notation as

$$\rho\left[\frac{\partial \vec{w}}{\partial t} + (\vec{w} \bullet \vec{\nabla})\vec{w}\right] = -\vec{\nabla}p + \vec{F} + \mu\vec{\nabla}^2\vec{w} \tag{3.10}$$

where, $\vec{w}$ is the velocity vector, ρ is the fluid density, $\vec{F}$ is the body force vector, p is the pressure in the fluid, t is time, and μ is the dynamic viscosity. The assumptions inherent in these equations are the constant physical properties, the fluid does not develop any local

moment, and constant body forces. The continuity equation for incompressible fluids is simply a zero divergence of the velocity vector.

$$\vec{\nabla} \cdot \vec{w} = 0 \tag{3.11}$$

The vorticity (ς) is defined in the usual way as the curl of the velocity vector.

$$\vec{\varsigma} = \vec{\nabla} \times \vec{w} \tag{3.12}$$

If a stream function (ψ) is defined so that the continuity equation is satisfied, then its appropriate form is

$$h_2 h_3 w_1 = \frac{\partial \psi}{\partial q_2}, \qquad h_1 h_3 w_2 = -\frac{\partial \psi}{\partial q_1} \tag{3.13}$$

where q_1, q_2 are the space coordinates. It should be noted that we strictly speak of axisymmetric or two-dimensional problems. The vorticity is then a scalar and a stream function is an appropriate definition.

The quantity $(\vec{w} \cdot \vec{\nabla})\vec{w}$ in equation (3.10) is a pseudo-vector and can be expanded as

$$(\vec{w} \cdot \vec{\nabla})\vec{w} = \vec{\nabla}(w^2/2) - \vec{w} \times (\vec{\nabla} \times \vec{w}) \tag{3.14}$$

and, $$\vec{\nabla}^2 \vec{w} = \vec{\nabla}(\vec{\nabla} \cdot \vec{w}) - \vec{\nabla} \times (\vec{\nabla} \times \vec{w}) \tag{3.15}$$

Using the appropriate coordinate scale factors, the equations for any two-dimensional or three-dimensional axisymmetric flow in terms of the stream function and vorticity can be written as

$$\frac{\partial}{\partial q_1}\left(\frac{h_2}{h_1 h_3}\frac{\partial \psi}{\partial q_1}\right) + \frac{\partial}{\partial q_2}\left(\frac{h_1}{h_2 h_3}\frac{\partial \psi}{\partial q_2}\right) = -h_1 h_2 \varsigma \tag{3.16}$$

and,

$$h_1 h_2 \frac{\partial \varsigma}{\partial t} + \frac{\partial \psi}{\partial q_2}\frac{\partial}{\partial q_1}\left(\frac{\varsigma}{h_3}\right) - \frac{\partial \psi}{\partial q_1}\frac{\partial}{\partial q_2}\left(\frac{\varsigma}{h_3}\right) = \nu\left\{\frac{\partial}{\partial q_1}\left[\frac{h_2}{h_1 h_3}\frac{\partial}{\partial q_1}(h_3 \varsigma)\right] + \frac{\partial}{\partial q_2}\left[\frac{h_1}{h_2 h_3}\frac{\partial}{\partial q_2}(h_3 \varsigma)\right]\right\} \tag{3.17}$$

where ν is the coefficient of kinematic viscosity. The boundary conditions associated with these equations depend on the flow considered, whether uniform, oscillating or fluctuating and will be left for the specific cases considered.

3.3 The Spheroidal Bodies under Consideration

In this study, the full Navier-Stokes equations are solved for flows over three axially symmetric bodies, namely, a sphere, an oblate spheroid, and a prolate spheroid. To describe the geometries of these bodies, the spherical, oblate spheroidal, and prolate spheroidal coordinates are used.

3.3.1 The Sphere

The coordinate system that best describes the spherical geometry is the spherical coordinate system (r,θ,ϕ). The cartesian coordinate system is related to the spherical coordinate system by

$$\begin{aligned} x &= r\ \sin\theta\ \cos\phi \\ y &= r\ \sin\theta\ \sin\phi \\ z &= r\cos\theta \end{aligned} \qquad (3.18)$$

with corresponding scale factors

$$h_r = 1 \quad , \quad h_\theta = r \quad , \quad h_\phi = r\sin\theta \qquad (3.19)$$

Figure 3.1 shows the coordinate variables and the flow problem to be considered. The sphere has a diameter of 2a. The velocity of the fluid far away from the surface of sphere U is assumed to take any time dependent function U = U(t). In the case U(t) = constant, the problem reduces to that of the impulsively started flow. If time variations are ignored, only the steady version of equation (3.17) is to be solved.

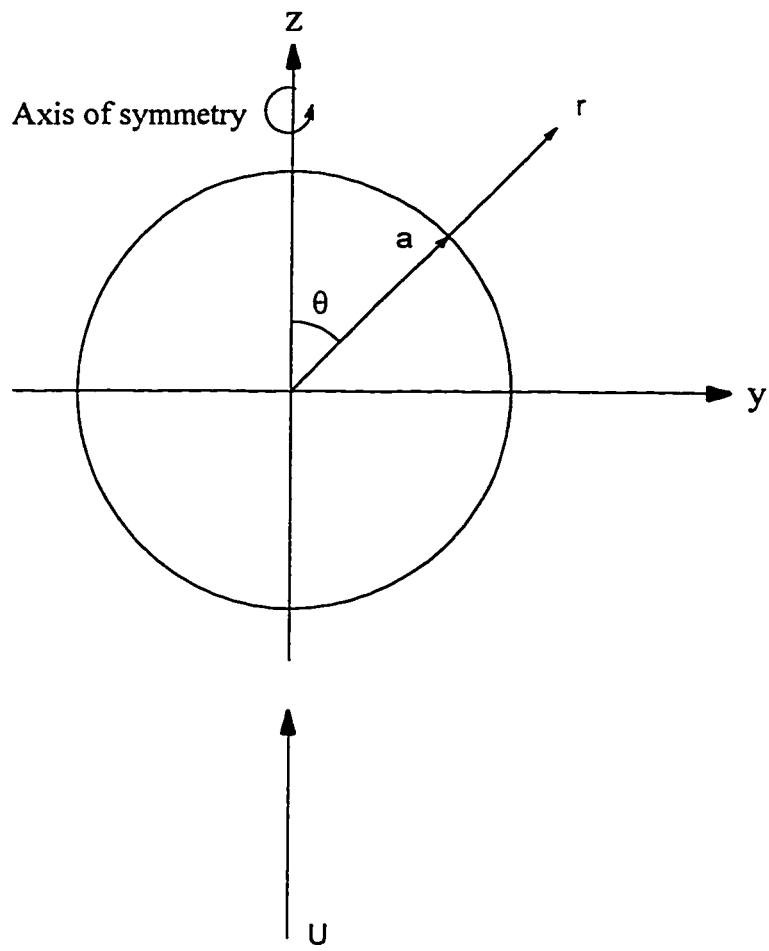

Figure 3.1 The spherical coordinate system

3.3.2 The Oblate and Prolate Spheroids

The oblate and prolate spheroids considered here have major and minor axes of 2a and 2b respectively. Figures 3.2 and 3.3 show the oblate and prolate spheroidal coordinate systems used. The oblate spheroidal coordinate system (ξ, η, ϕ) is related to the cartesian coordinate by

$$\begin{aligned} x &= c' \cosh\xi \sin\eta \cos\phi \\ y &= c' \cosh\xi \sin\eta \sin\phi \\ z &= c' \sinh\xi \cos\eta \end{aligned} \tag{3.20}$$

with corresponding scale factors:

$$h_\xi = h_\eta = c' \sqrt{\sinh^2\xi + \cos^2\eta} \qquad h_\phi = c' \cosh\xi \sin\eta \tag{3.21}$$

where c' is the focal distance. On the other hand, the prolate spheroidal coordinate system (ξ, η, ϕ) is related to the cartesian coordinate system by

$$\begin{aligned} x &= c' \sinh\xi \sin\eta \cos\phi \\ y &= c' \sinh\xi \sin\eta \sin\phi \\ z &= c' \cosh\xi \cos\eta \end{aligned} \tag{3.22}$$

with the corresponding scale factors given by:

$$h_\xi = h_\eta = c' \sqrt{\sinh^2\xi + \sin^2\eta} \qquad h_\phi = c' \sinh\xi \sin\eta \tag{3.23}$$

The oblate and prolate spheroidal coordinate systems, while they look like a mere rotation, are different. An oblate spheroid is generated by rotating an ellipse around its minor axis. A prolate spheroid, on the other hand, is generated by rotating an ellipse around its major axis. The limiting case for both coordinates as ξ_o (ξ_o defines the surface of the spheroid and is related to the axis ratio (b/a) by: $\xi_o = \tanh^{-1}(b/a)$) tends to infinity is a sphere. On the other hand, as ξ_o tends to zero, the oblate spheroid becomes a flat circular disk while the prolate spheroid becomes an infinitely thin needle. The velocity of the fluid far away from the surface of spheroids is assumed to take any time dependent function U = U(t).

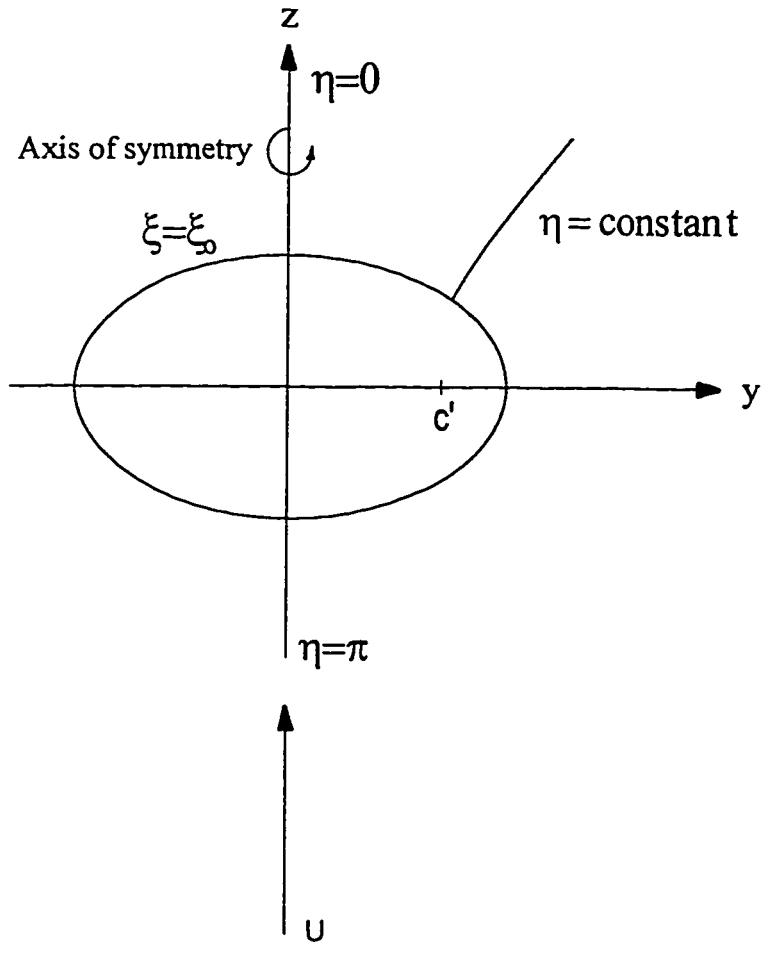

Figure 3.2 The oblate spheroidal coordinate system

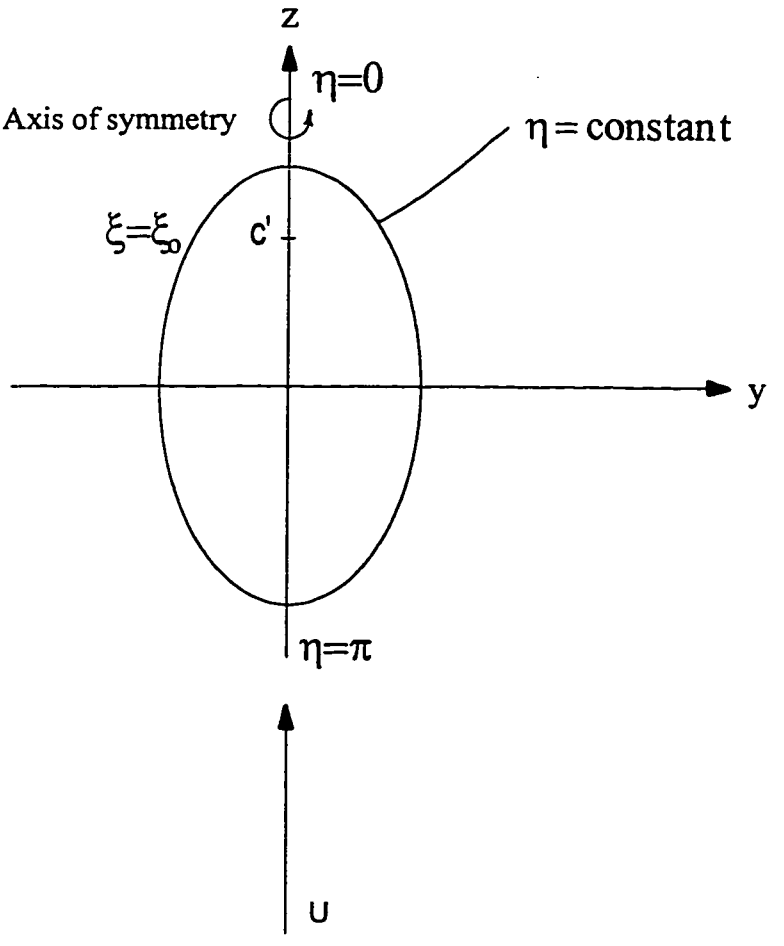

Figure 3.3 The prolate spheroidal coordinate system

CHAPTER 4

POTENTIAL FLOW OVER OBLATE AND PROLATE SPHEROIDS

The hydrodynamic forces acting on oblate and prolate spheroids placed in an oscillating free stream are obtained for the special case of inviscid flow. Analytical expressions are obtained for the potential and stream functions as well as the surface pressure distribution and the hydrodynamic force coefficient. The analysis is based on the solution of the unsteady equations of motion and continuity in spheroidal coordinate systems. The parameters involved are the major to minor axes ratio and the Strouhal number. The solutions for the two limiting cases of oscillating flows over disks and spheres can be easily obtained from the presented analytical solutions.

4.1 Potential Flow over Oblate Spheroids

The problem considered here is that of an oblate spheroid placed in a frictionless incompressible fluid of infinite extent. The fluid far a way from the spheroid moves in an oscillatory fashion along the spheroid axis of symmetry. The flow remains axisymmetric. In transferring from the cartesian coordinate system to the oblate spheroidal system, we use the transformation presented in chapter 3. The equations of conservation of momentum for inviscid incompressible axisymmetric flow can be written as

$$\rho\left[\frac{\partial w'_\xi}{\partial t'}+\frac{w'_\xi}{h_\xi}\frac{\partial w'_\xi}{\partial \xi}+\frac{w'_\eta}{h_\eta}\frac{\partial w'_\xi}{\partial \eta}-w'_\eta\left(\frac{w'_\eta}{h_\xi h_\eta}\frac{\partial h_\eta}{\partial \xi}-\frac{w'_\xi}{h_\xi h_\eta}\frac{\partial h_\xi}{\partial \eta}\right)\right]=-\frac{1}{h_\xi}\frac{\partial p'}{\partial \xi} \qquad (4.1)$$

$$\rho\left[\frac{\partial w'_\eta}{\partial t'}+\frac{w'_\xi}{h_\xi}\frac{\partial w'_\eta}{\partial \xi}+\frac{w'_\eta}{h_\eta}\frac{\partial w'_\eta}{\partial \eta}+w'_\xi\left(\frac{w'_\eta}{h_\xi h_\eta}\frac{\partial h_\eta}{\partial \xi}-\frac{w'_\xi}{h_\xi h_\eta}\frac{\partial h_\xi}{\partial \eta}\right)\right]=-\frac{1}{h_\eta}\frac{\partial p'}{\partial \eta} \qquad (4.2)$$

The continuity equation can be stated as

$$\frac{\partial}{\partial\xi}\left(h_\eta h_\phi w'_\xi\right)+\frac{\partial}{\partial\eta}\left(h_\xi h_\phi w'_\eta\right)=0 \tag{4.3}$$

and since the vorticity vanishes everywhere, one can write

$$\frac{\partial}{\partial\xi}\left(h_\eta w'_\eta\right)-\frac{\partial}{\partial\eta}\left(h_\xi w'_\xi\right)=0 \tag{4.4}$$

where w'_ξ, w'_η are the velocity components in the ξ and η directions respectively, t' is the time, and p' is fluid pressure. The velocity of the free stream varies with time according to

$$U' = U_o \sin(\omega\, t') \tag{4.5}$$

where ω is the frequency of oscillations and U_o is the amplitude. *The primes denote the dimensional quantities*. We introduce the following dimensionless variables:

$$w=\frac{w'}{U_o} \qquad ,t=\frac{U_o t'}{a} \qquad ,p=p'/\frac{1}{2}\rho U_o^2 \qquad ,S=\frac{a\,\omega}{U_o} \tag{4.6}$$

where S is the Strouhal number. Using these dimensionless variables and noting that $h_\xi = h_\eta$, the above equations can be written as:

$$-2H_\xi\left[\frac{\partial w_\xi}{\partial t}+\frac{w_\xi}{H_\xi}\frac{\partial w_\xi}{\partial\xi}+\frac{w_\eta}{H_\xi}\frac{\partial w_\xi}{\partial\eta}-\frac{w_\eta}{H_\xi^2}\left(w_\eta\frac{\partial H_\xi}{\partial\xi}-w_\xi\frac{\partial H_\xi}{\partial\eta}\right)\right]=\frac{\partial p}{\partial\xi} \tag{4.7}$$

$$-2H_\xi\left[\frac{\partial w_\eta}{\partial t}+\frac{w_\xi}{H_\xi}\frac{\partial w_\eta}{\partial\xi}+\frac{w_\eta}{H_\xi}\frac{\partial w_\eta}{\partial\eta}+\frac{w_\xi}{H_\xi^2}\left(w_\eta\frac{\partial H_\xi}{\partial\xi}-w_\xi\frac{\partial H_\xi}{\partial\eta}\right)\right]=\frac{\partial p}{\partial\eta} \tag{4.8}$$

$$\frac{\partial}{\partial\xi}\left(H_\xi H_\phi w_\xi\right)+\frac{\partial}{\partial\eta}\left(H_\xi H_\phi w_\eta\right)=0 \tag{4.9}$$

$$\frac{\partial}{\partial\xi}\left(H_\xi w_\eta\right)-\frac{\partial}{\partial\eta}\left(H_\xi w_\xi\right)=0 \tag{4.10}$$

where $H_\xi = c\sqrt{\sinh^2\xi+\cos^2\eta}$, $c=\frac{c'}{a}=\frac{1}{\cosh\xi_o}$, $H_\phi = c\cosh\xi\sin\eta$, and

$\xi_o = \tanh^{-1}\frac{b}{a}$. Let us now introduce the potential function (φ) defined by

$$\vec{w} = -\vec{\nabla}\varphi = -\frac{1}{H_\xi}\frac{\partial\varphi}{\partial\xi}\vec{e}_1 - \frac{1}{H_\eta}\frac{\partial\varphi}{\partial\eta}\vec{e}_2 \tag{4.11}$$

$$\text{where, } w_\xi H_\xi = -\frac{\partial\varphi}{\partial\xi} \quad \text{and} \quad w_\eta H_\xi = -\frac{\partial\varphi}{\partial\eta} \tag{4.12}$$

The continuity equation can be written as

$$\frac{\partial}{\partial\xi}\left(H_\phi \frac{\partial\varphi}{\partial\xi}\right) + \frac{\partial}{\partial\eta}\left(H_\phi \frac{\partial\varphi}{\partial\eta}\right) = 0 \tag{4.13}$$

$$\text{or, } \frac{\partial^2\varphi}{\partial\xi^2} + \frac{\partial^2\varphi}{\partial\eta^2} + \tanh\xi\frac{\partial\varphi}{\partial\xi} + \cot\eta\frac{\partial\varphi}{\partial\eta} = 0 \tag{4.14}$$

with boundary conditions being mainly the impermeability condition at the surface and the free stream conditions far a way. These can be expressed as

$$\frac{\partial\varphi}{\partial\xi} \to -\frac{c}{2}\sin(S\,t)\,e^{\xi}\cos\eta \qquad \text{as} \quad \xi \to \infty \tag{4.15}$$

$$\frac{\partial\varphi}{\partial\eta} \to \frac{c}{2}\sin(S\,t)\,e^{\xi}\sin\eta \qquad \text{as} \quad \xi \to \infty \tag{4.16}$$

$$\frac{\partial\varphi}{\partial\xi} = 0 \qquad \text{at} \quad \xi = \xi_o \tag{4.17}$$

The boundary conditions (4.15) and (4.16) can be combined to give

$$\varphi \to -\frac{c}{2}\sin(S\,t)\,e^{\xi}\cos\eta \qquad \text{as} \quad \xi \to \infty \tag{4.18}$$

The solution to equation (4.14) that satisfies boundary conditions (4.17) and (4.18) can be obtained by separation of variables where the resulting ordinary differential equations are the well known Legendre equations. The solution can be written as

$$\varphi = -c\sin(S\,t)\sinh\xi_o\cos\eta\, f_1(\xi) \tag{4.19}$$

The stream function ψ is related to the potential function φ through:

$$\frac{\partial\psi}{\partial\xi} = -H_\xi H_\phi w_\eta = H_\phi\frac{\partial\varphi}{\partial\eta} \qquad \text{and} \qquad \frac{\partial\psi}{\partial\eta} = H_\eta H_\phi w_\xi = -H_\phi\frac{\partial\varphi}{\partial\xi} \tag{4.20}$$

Equation (4.19) and the boundary condition $\psi = 0$ at $\xi = \xi_o$ can be used to obtain the following expression for ψ :

$$\psi = -\frac{c^2}{4}\sin(S\,t)\sinh\xi_o\cosh\xi\cos 2\eta\, f_2(\xi) + \frac{c^2}{4}\sin(S\,t)\sinh\xi_o\cosh\xi\, f_3(\xi) + \frac{c^2}{4}\sin(S\,t) \tag{4.21}$$

where $f_1(\xi)$, $f_2(\xi)$, and $f_3(\xi)$ are defined as follows:

$$f_1(\xi) = \left[\frac{\sinh\xi}{\sinh\xi_o} - \frac{\sinh\xi\coth^{-1}(\sinh\xi) - 1}{\sinh\xi_o\coth^{-1}(\sinh\xi_o) - \tanh^2\xi_o}\right] \tag{4.22}$$

$$f_2(\xi) = \left[\frac{\cosh\xi}{\sinh\xi_o} - \frac{\cosh\xi\ \coth^{-1}(\sinh\xi) - \tanh\xi}{\sinh\xi_o\coth^{-1}(\sinh\xi_o) - \tanh^2\xi_o}\right] \tag{4.23}$$

$$f_3(\xi) = \left[\frac{\sinh\xi\tanh\xi}{\sinh\xi_o} - \frac{\cosh\xi\ \coth^{-1}(\sinh\xi) - \tanh\xi}{\sinh\xi_o\coth^{-1}(\sinh\xi_o) - \tanh^2\xi_o}\right] \tag{4.24}$$

Using equations (4.8) and (4.12) , one can express the surface pressure gradient in terms of the potential function as

$$\left(\frac{\partial p}{\partial\eta}\right)_{\xi_o} = 2\frac{\partial}{\partial t}\left(\frac{\partial\varphi}{\partial\eta}\right) - \frac{2}{H_\xi}\frac{\partial\varphi}{\partial\eta}\frac{\partial}{\partial\eta}\left(\frac{1}{H_\xi}\frac{\partial\varphi}{\partial\eta}\right) \tag{4.25}$$

Using the expression of the potential function given in equation (4.19), the surface pressure gradient is

$$\left(\frac{\partial p}{\partial\eta}\right)_{\xi_o} = 2\,S\sin\eta\cos(St)\frac{f_4(\xi_o)}{\cosh\xi_o} - 2\sin^2(St)\frac{f_4{}^2(\xi_o)\sin\eta\cos\eta\cosh^2\xi_o}{(\sinh^2\xi_o + \cos^2\eta)^2} \tag{4.26}$$

where, $f_4(\xi)$ is defined as

$$f_4(\xi) = \sinh\xi_o\left[1 - \frac{\sinh\xi\coth^{-1}(\sinh\xi) - 1}{\sinh\xi_o\coth^{-1}(\sinh\xi_o) - \tanh^2\xi_o}\right] \tag{4.27}$$

We now define the dimensionless pressure as

$$P^* = \frac{p'_\eta - p'_\pi}{\frac{1}{2}\rho U_o^2} = p_\eta - p_\pi \tag{4.28}$$

Integrating Equation (4.26) between π and η results in the following expression for the dimensionless pressure:

$$P^* = -2\,S\cos(S\,t)\,(1+\cos\eta)\frac{f_4(\xi_o)}{\cosh\xi_o} - \sin^2(S\,t)\sin^2\eta\frac{f_4^{\,2}(\xi_o)}{(\sinh^2\xi_o+\cos^2\eta)} \qquad (4.29)$$

Since the flow is inviscid , the pressure forces are the only forces that act on the spheroid surface. The drag can be computed by

$$D = -\pi\,c'^2\cosh^2\xi_o\int_0^{\pi}\sin 2\eta\;\; p'_\eta d\eta \qquad (4.30)$$

The drag coefficient can be defined as

$$C_D = \frac{D}{\rho\,U_o^2 A} \qquad (4.31)$$

where $A = \pi\,c'^2\cosh^2\xi_o$ is the projected area of the oblate spheroid. The drag coefficient can be written as

$$C_D = -\frac{1}{2}\int_0^{\pi}\sin 2\eta\;\; p_\eta d\eta \qquad (4.32)$$

which upon performing the integration reduces to

$$C_D = \frac{4}{3}\,S\cos(S\,t)\frac{f_4(\xi_o)}{\cosh\xi_o} \qquad (4.33)$$

Equation (4.33) provides an analytical solution to the time variation of the drag coefficient in terms of the independent variables ξ_o , S, and t . In the limit as $\xi_o \to \infty$, the oblate spheroid becomes a sphere. One can show that

$$\lim_{\xi_o\to\infty}\frac{f_4(\xi_o)}{\sinh\xi_o} = \lim_{\xi_o\to\infty}\frac{f_4(\xi_o)}{\cosh\xi_o} = \frac{3}{2} \qquad (4.34)$$

which in the case of a sphere gives

$$P^* = -3\,S\cos(S\,t)\,(1+\cos\eta) - \frac{9}{4}\sin^2(S\,t)\sin^2\eta \qquad (4.35)$$

and the drag coefficient becomes

$$C_D = 2\;\; S\;\cos(S\,t) \qquad (4.36)$$

These equations agree with those obtained from the spherical coordinate system for the case of a sphere placed in an oscillating stream. The stream function obtained from such analysis takes the form

$$\psi = \frac{\sin(S\,t)}{2}\frac{a}{r}[(\frac{r}{a})^3 - 1]\sin^2\eta \qquad (4.37)$$

The oblate spheroid approaches a circular flat disk as $\xi_o \to 0$. In this case, one can easily show that

$$\lim_{\xi_o \to 0} \frac{f_4(\xi_o)}{\cosh\xi_o} = \frac{2}{\pi} \qquad (4.38)$$

Hence, the drag coefficient for the flat circular disk is

$$C_D = \frac{8}{3\pi} S\cos(S\,t) \qquad (4.39)$$

4.2 Potential Flow over Prolate Spheroids

The continuity equation associated with the prolate spheroidal coordinate system can be written as

$$\frac{\partial^2\varphi}{\partial\xi^2} + \frac{\partial^2\varphi}{\partial\eta^2} + \coth\xi\frac{\partial\varphi}{\partial\xi} + \cot\eta\frac{\partial\varphi}{\partial\eta} = 0 \qquad (4.40)$$

with boundary conditions, $\frac{\partial\varphi}{\partial\xi} = 0$ at $\xi = \xi_o$ (4.41)

and , $\varphi \to -\frac{c}{2}\sin(S\,t)\,e^{\xi}\cos\eta$ as $\xi \to \infty$ (4.42)

Equation (4.40) is separable. It separates into two associated Legendre equations (In the case of prolate spheroids , they reduce to Legendre equations), the solution of which is

$$\varphi = -c\sin(S\,t)\sinh\xi_o\cos\eta\, z_1(\xi) \qquad (4.43)$$

With the same definition of the stream function ψ as in the oblate spheroid case but using the appropriate scale factors, the expression for the stream function is

$$\psi = -\frac{c^2}{4}\sin(S\,t)\cosh\xi_o\,\cos 2\eta\, z_2(\xi) + \frac{c^2}{4}\sin(S\,t)\cosh\xi_o\, z_3(\xi) - \frac{c^2}{4}\sin(S\,t) \qquad (4.44)$$

where $z_1(\xi), z_2(\xi)$, and $z_3(\xi)$ are defined as

$$z_1(\xi) = \left[\frac{\cosh\xi}{\sinh\xi_o} - \frac{\cosh\xi\,\ln(\frac{\cosh\xi+1}{\cosh\xi-1}) - 2}{\sinh\xi_o\,\ln(\frac{\cosh\xi_o+1}{\cosh\xi_o-1}) - 2\coth^2\xi_o}\right] \qquad (4.45)$$

$$z_2(\xi) = \left[\frac{\sinh^2\xi}{\cosh\xi_o} - \frac{\sinh^2\xi\,\ln(\frac{\cosh\xi+1}{\cosh\xi-1}) - 2\cosh\xi}{\cosh\xi_o\,\ln(\frac{\cosh\xi_o+1}{\cosh\xi_o-1}) - 2\coth^2\xi_o}\right] \qquad (4.46)$$

$$z_3(\xi) = \left[\frac{\cosh^2\xi}{\cosh\xi_o} - \frac{\sinh^2\xi\,\ln(\frac{\cosh\xi+1}{\cosh\xi-1}) - 2\cosh\xi}{\cosh\xi_o\,\ln(\frac{\cosh\xi_o+1}{\cosh\xi_o-1}) - 2\coth^2\xi_o}\right] \qquad (4.47)$$

Using the expression of the potential function given in equation (4.43), the surface pressure gradient is

$$\left(\frac{\partial p}{\partial \eta}\right)_{\xi_o} = 2\,S\sin\eta\cos(St)\frac{z_4(\xi_o)}{\cosh\xi_o} - 2\sin^2(St)\frac{z_4^{\,2}(\xi_o)\sin\eta\cos\eta\sinh^2\xi_o}{(\sinh^2\xi_o+\sin^2\eta)^2} \qquad (4.48)$$

where, $z_4(\xi)$ is defined as

$$z_4(\xi) = \cosh\xi_o\left[\frac{\cosh\xi}{\cosh\xi_o} - \frac{\cosh\xi\,\ln(\frac{\cosh\xi+1}{\cosh\xi-1}) - 2}{\cosh\xi_o\,\ln(\frac{\cosh\xi_o+1}{\cosh\xi_o-1}) - 2\coth^2\xi_o}\right] \qquad (4.49)$$

The dimensionless pressure can be obtained by integrating equation (4.48) between π and η, the result of which can be written as

$$P^* = -2\,S\cos(S\,t)\,(1+\cos\eta)\frac{z_4(\xi_o)}{\cosh\xi_o} - \sin^2(S\,t)\sin^2\eta\frac{z_4^{\,2}(\xi_o)}{(\sinh^2\xi_o+\sin^2\eta)} \qquad (4.50)$$

The drag can be computed by

$$D = -\pi c'^2 \sinh^2 \xi_o \int_0^{\pi} \sin 2\eta \; p'_\eta d\eta \tag{4.51}$$

The projected area used in the definition of the drag coefficient in equation (4.31) is different in this case. It is equal to $\pi c'^2 \sinh^2 \xi_o$. The following expression for C_D is easily obtained:

$$C_D = \frac{4}{3} S \cos(S\,t) \frac{z_4(\xi_o)}{\cosh \xi_o} \tag{4.52}$$

In the limit as $\xi_o \to \infty$, the prolate spheroid becomes a sphere. It is easily shown that

$$\lim_{\xi_o \to \infty} \frac{z_4(\xi_o)}{\sinh \xi_o} = \lim_{\xi_o \to \infty} \frac{z_4(\xi_o)}{\cosh \xi_o} = \frac{3}{2} \tag{4.53}$$

By applying this limit to equations (4.50) and (4.52), the drag coefficient and the dimensionless pressure for the sphere can be obtained which are identical to those reduced from the oblate spheroid case.

4.3 Observations and Comments

The analytical expressions for the stream and potential functions given in equations (4.19), (4.21), (4.43), and (4.44) can fully describe the time variation of the flow pattern and the details of the velocity field for the cases of oscillating inviscid flows over oblate and prolate spheroids. Such a velocity field is essential in the understanding of the viscous flow problem and may also provide the far field boundary conditions outside the viscous flow region. The equations also describe the detailed structure of the streamline pattern and the velocity field in the special case of a sphere when placed in an oscillating inviscid flow. As a check of the accuracy of these equations , the results for the special case of a sphere were compared with those obtained from the analysis of oscillating flow over a sphere using the spherical coordinate system. The comparison shows an excellent

agreement. The expressions obtained for the fluid pressure in equations (4.29) and (4.50) provide the details of pressure variation on the spheroid surface at any given time. These expressions are essential in providing a base for comparison with the viscous flow solutions and also experimental measurements in such problems. The pressure distribution for the special case of the sphere was also given in equation (4.35). By equating the Strouhal number to zero, we obtain the pressure distribution in the case of steady free stream. The obtained expression is in total agreement with those obtained from solving the problem using spherical coordinates. A graphical representation of the pressure distributions calculated for the case of $S = \pi/4$, and b/a = 0.6 are shown in figure 4.1 for one half of a complete oscillation. The pressure distribution is sharper in the case of oblate spheroids than in the case of prolate spheroids. The oblate spheroid drag coefficient for the case $S = \pi/4$ over a full cycle is shown in figure 4.2. It is clear from the figure that the curves converge to that of a sphere as $\xi_o \to \infty$ and to the flat circular disk as $\xi_o \to 0$. The prolate spheroid drag coefficient is shown in figure 4.3 for the same case. The drag here represents the contribution of the fluid inertia only. The steady flow case when the Strouhal number is zero will result in a zero drag as would be expected from the potential flow theory.

It should be emphasized that the analytical expressions given are only exact in the case of inviscid flow. They may be accurate enough for use in engineering problems in cases of high Reynolds and Strouhal numbers in which vortex shedding is strongly suppressed. It is difficult to give numerical ranges for the Reynolds and Strouhal numbers for the applicability of the analytical expressions deduced in this work. However, this can be established either experimentally or theoretically by investigating the viscous flow problem over a wide range of Reynolds and Strouhal numbers as presented in chapters 6 and 7.

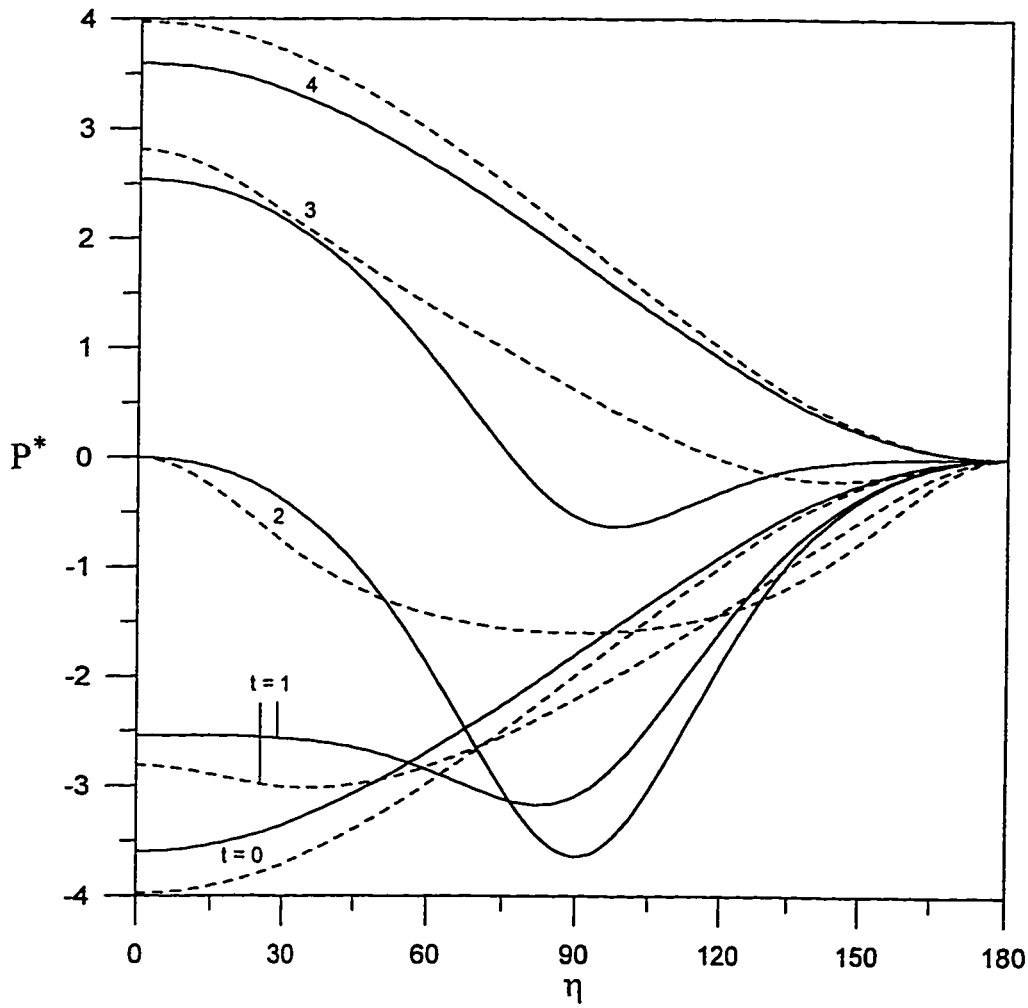

Figure 4.1 Inviscid surface pressure distribution for the spheroids when $S = \pi/4$, $b/a = 0.6$ during one-half of a complete cycle.

(_____) Oblate, (_ _ _ _) Prolate

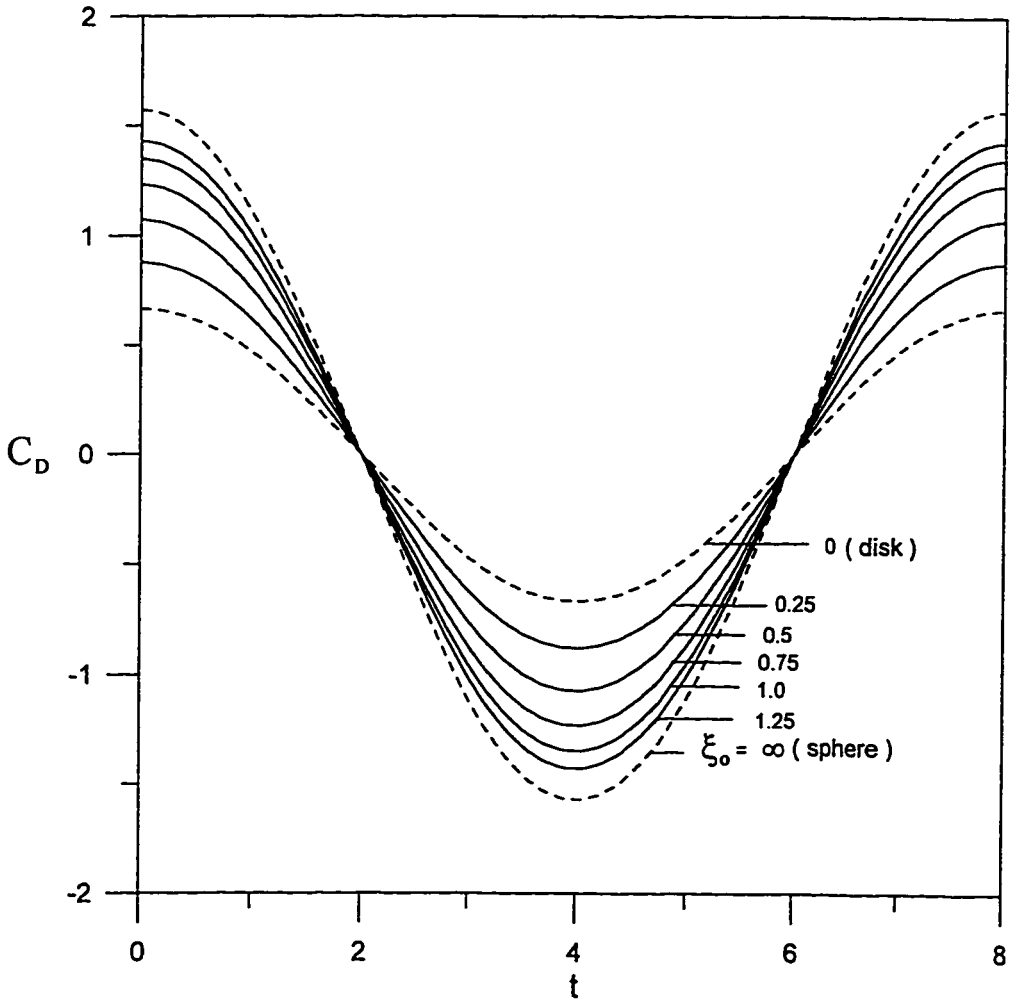

Figure 4.2 The inviscid drag coefficient of the oblate spheroid over one full cycle for the case $S = \pi/4$

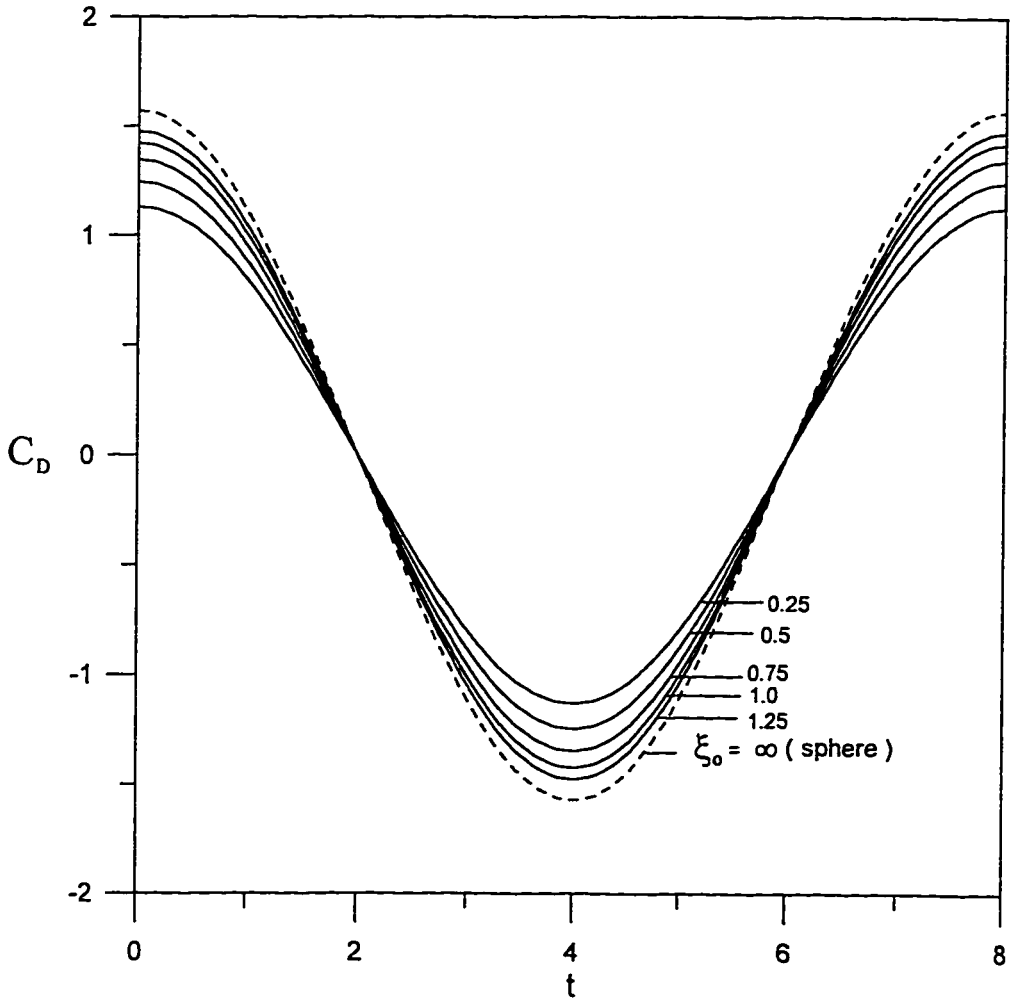

Figure 4.3 The inviscid drag coefficient of the prolate spheroid over one full cycle for the case $S = \pi/4$

CHAPTER 5

VISCOUS FLOW OVER SPHERES

The problem considered in this chapter is that of a sphere placed in an incompressible fluid of infinite extent. The free stream dimensionless velocity (U) changes with time according to

$$U = \frac{U'}{U_o} = F(t) \tag{5.1}$$

where U' is the dimensional free stream velocity and t is the dimensionless time which is related to the dimensional time t' by

$$t = U_o t' / a \tag{5.2}$$

and U_o is some constant that represents the amplitude of the free stream velocity for oscillating flows or the mean velocity for fluctuating flows. Two forms of the function F(t) are considered. The first corresponds to the oscillatory motion of the free stream which can be written as

$$F(t) = \cos(S\ t) \tag{5.3}$$

where S is the Strouhal number which is related to the Keulegan-Carpenter number (KC) by

$$S = \frac{a\omega}{U_o} = \frac{\pi}{KC} \tag{5.4}$$

with ω being the frequency of oscillations. The second form describes fluctuations of the free stream about a non zero mean and can be written as

$$F(t) = 1 + \gamma \cos(S\ t) \tag{5.5}$$

where γ represents the relative deviation from the mean value. Since the steady and the impulsively started flows over spheres are well documented in the literature, no attempt is

made here to obtain their corresponding solutions. These solutions are, however, indirectly obtained when solving the fluctuating flow problem.

5.1 Basic Equations and Method of Solution

Using the spherical coordinate system, the governing equations (3.16) and (3.17) can be written in dimensionless form as

$$e^{3\xi}\sin\theta\zeta+\frac{\partial^2\psi}{\partial\xi^2}+\frac{\partial^2\psi}{\partial\theta^2}-\frac{\partial\psi}{\partial\xi}-\cot\theta\frac{\partial\psi}{\partial\theta}=0 \tag{5.6}$$

$$e^{2\xi}\frac{\partial\zeta}{\partial t}+\frac{e^{-\xi}}{\sin\theta}\left[\frac{\partial\psi}{\partial\theta}\left(\frac{\partial\zeta}{\partial\xi}-\zeta\right)-\frac{\partial\psi}{\partial\xi}\left(\frac{\partial\zeta}{\partial\theta}-\cot\theta\zeta\right)\right]=\frac{2}{\mathrm{Re}}\left[\frac{\partial^2\zeta}{\partial\xi^2}+\frac{\partial^2\zeta}{\partial\theta^2}+\frac{\partial\zeta}{\partial\xi}+\cot\theta\frac{\partial\zeta}{\partial\theta}-\frac{\zeta}{\sin^2\theta}\right] \tag{5.7}$$

The parameter Re appearing in equation (5.7) is the Reynolds number based on the sphere diameter which is defined as

$$\mathrm{Re}=2aU_o/\nu \tag{5.8}$$

The variable ξ is used in place of r to insure a small step size near the sphere surface as compared to the step size in the free stream. It is defined through the following logarithmic transformation:

$$\xi=\ln(r/a) \tag{5.9}$$

The dimensionless variables ψ, and ζ in equations (5.6) and (5.7) are defined in terms of the usual dimensional quantities ψ', and ζ' as

$$\psi=\psi'/U_oa^2 \tag{5.10}$$

$$\zeta=\zeta'a/U_o \tag{5.11}$$

The boundary conditions to be satisfied are the no-slip and impermeability conditions on the surface of the sphere and the free stream conditions away from it. These can be expressed as

$$\psi=\frac{\partial\psi}{\partial\theta}=\frac{\partial\psi}{\partial\xi}=0 \quad \text{at} \quad \xi=0 \tag{5.12}$$

$$\frac{\partial \psi}{\partial \xi} = e^{2\xi} \sin^2\theta \ F(t) \quad \text{, and} \quad \frac{\partial \psi}{\partial \theta} = e^{2\xi} \sin\theta \cos\theta \ F(t) \quad \text{as } \xi \to \infty \tag{5.13}$$

The conditions in equation (5.13) lead to

$$\psi = \frac{e^{2\xi}}{2} \sin^2\theta \ F(t) \quad \text{as } \xi \to \infty \tag{5.14}$$

The flow away from the sphere surface is irrotational leading to

$$\zeta \to 0 \quad \text{as } \xi \to \infty \tag{5.15}$$

There is no explicit boundary condition for the vorticity on the sphere surface. In principle, the surface vorticity can be computed from the known stream function by applying equation (5.6), however, the large velocity gradient at the surface reduces the accuracy of such computations. This problem is overcome by introducing an integral condition which is used to predict the surface vorticity.

The method of solution is based on approximating ζ and ψ using Legendre polynomials. Accordingly, the stream function and vorticity are expressed in the form

$$\psi = e^{\xi/2} \sum_{n=1}^{\infty} f_n(\xi, t) \int_z^1 P_n(\lambda) \, d\lambda \tag{5.16}$$

$$\zeta = \sum_{n=1}^{\infty} g_n(\xi, t) \ P_n^1(z) \tag{5.17}$$

where $P_n(z)$ and $P_n^1(z)$ are the Legendre and first associated Legendre polynomials of order n respectively, and $z = \cos\theta$. These functions form a complete orthogonal set in the range z = -1 to z = 1. Substituting from equations (5.16) and (5.17) into equations (5.6) and (5.7) and integrating over z from -1 to 1 after multiplying by $P_m^1(z)$ (some useful integrals can be found in the appendix), the following expressions can be obtained by manipulation of the Legendre functions,

$$\frac{\partial^2 f_n}{\partial \xi^2} - (n + 1/2)^2 \ f_n = n(n+1) e^{5/2\xi} \ g_n \tag{5.18}$$

$$e^{2\xi}\frac{\partial g_n}{\partial t}=\frac{2}{Re}\left[\frac{\partial^2 g_n}{\partial \xi^2}+\frac{\partial g_n}{\partial \xi}-n(n+1)g_n\right]+S_n \tag{5.19}$$

where,

$$S_n=-e^{-\xi/2}\left[\sum_{i=1}^{\infty}\sum_{j=1}^{\infty}\alpha_{ij}^{n} f_i\left(\frac{\partial g_j}{\partial \xi}-g_j\right)+\sum_{i=1}^{\infty}\sum_{j=1}^{\infty}\beta_{ij}^{n} g_j\left(\frac{\partial f_i}{\partial \xi}+\frac{1}{2}f_i\right)\right] \tag{5.20}$$

The coefficients appearing in the series are defined as:

$$\alpha_{ij}^{n}=-(2n+1)\sqrt{\frac{j(j+1)}{n(n+1)}}\begin{pmatrix} n & i & j\\ -1 & 0 & 1\end{pmatrix}\begin{pmatrix} n & i & j\\ 0 & 0 & 0\end{pmatrix} \tag{5.21}$$

$$\beta_{ij}^{n}=(2n+1)\sqrt{\frac{j(j^2-1)(j+2)}{n(n+1)\,i(i+1)}}\begin{pmatrix} n & i & j\\ -1 & -1 & 2\end{pmatrix}\begin{pmatrix} n & i & j\\ 0 & 0 & 0\end{pmatrix} \tag{5.22}$$

where, $\begin{pmatrix} j_1 & j_2 & j_3\\ m_1 & m_2 & m_3\end{pmatrix}$ are the 3-j symbols.

The series truncation approach helps to reduce the independent space coordinates to only one coordinate (ξ) which results in avoiding the numerical difficulties and inaccuracy involved when obtaining derivatives with respect to the other coordinate (θ). Now, the solution of the original differential equations can be obtained by solving the differential equations corresponding to the modes of the truncated series. Equations (5.18) are treated as ordinary differential equations since they do not contain any time derivatives. On the other hand, equations (5.19) are partial differential equations to be solved in order to advance the solution of the g_n functions in time. The boundary conditions associated with these equations are

$$f_n(0,t)=\frac{\partial f_n}{\partial \xi}(0,t)=0 \qquad \text{on the surface of the sphere} \tag{5.23}$$

$$f_n(\xi,t)\to e^{3/2\xi}F(t)\,\delta_{n1},\quad \frac{\partial f_n(\xi,t)}{\partial \xi}\to\frac{3}{2}e^{3/2\xi}F(t)\,\delta_{n1},\quad g_n(\xi,t)=0 \ \text{ as } \ \xi\to\infty \tag{5.24}$$

where δ_{n1} is the Kronecker delta. Finally, we multiply equation (5.18) by $e^{-(n+1/2)\xi}$ and integrate by parts over ξ between the limits 0 and ∞. Making use of the boundary

conditions (5.23), and (5.24), one obtains the following integral condition to be satisfied by the functions g_n :

$$\int_0^\infty e^{(2-n)\xi} g_n \, d\xi = \frac{3}{2} F(t) \delta_{n1} \tag{5.25}$$

5.2 The Numerical Method

The solutions of the functions ψ and ζ are advanced in time by solving equation (5.19) using a Crank-Nicolson finite-difference scheme. At a typical time t, it is required to obtain the functions $g_n(\xi,t)$ to determine the vorticity distribution, and the functions $f_n(\xi,t)$ to determine the stream function provided that all these functions are known at time $(t-\Delta t)$, where Δt is the time increment. Equation (5.19) can be written as

$$\frac{\partial g_n}{\partial t} = q_n(\xi,t) \tag{5.26}$$

$$\text{where } q_n = e^{-2\xi}\left\{\frac{2}{Re}\left[\frac{\partial^2 g_n}{\partial \xi^2} + \frac{\partial g_n}{\partial \xi} - n(n+1) g_n\right] + S_n\right\} \tag{5.27}$$

The Crank-Nicolson finite-difference approximation of equation (5.26) results in

$$\frac{1}{\Delta t}\left[g_n(\xi,t) - g_n(\xi,t-\Delta t)\right] = \frac{1}{2}\left[q_n(\xi,t) + q_n(\xi,t-\Delta t)\right] \tag{5.28}$$

Using central differences for all derivatives in equation (5.27) and rearranging, one obtains

$$A(\xi,t) g_n(\xi-\Delta\xi,t) + B(\xi,t) g_n(\xi,t) + C(\xi,t) g_n(\xi+\Delta\xi,t) = D_n(\xi,t-\Delta t) + E_n(\xi,t) \tag{5.29}$$

where $\Delta\xi$ is the step size, A, B, and C are easily identifiable functions of ξ that can be calculated at each mesh point, $D_n(\xi,t-\Delta t)$ is a completely known function, and $E_n(\xi,t)$ is a function that depends on the solution at time t. Since the problem is solved numerically the conditions at ∞ are applied at $\xi = \xi_m$ where ξ_m defines the distance away from the sphere at which ζ has negligible value. Equation (5.29), when applied at

every mesh point in the range from $\xi = 0$ to $\xi = \xi_m$, will result in a set of algebraic equations that form a tridiagonal matrix problem which is solved for each value of n between 1 and N iteratively due to the dependence of the right hand side on values at time t. N designates the number of terms taken in the series defined in equations (5.16) and (5.17). The values of $g_n(0,t)$ which are needed to complete the integration procedure are obtained by writing the integral condition defined in equation (5.25) as a numerical quadrature formula which then relates the boundary value to values of the corresponding function at internal points of the computational domain. This gives the extra condition needed to determine the boundary values for g_n and thus the formulation of the solution of equation (5.19) is complete.

The solution for equations (5.18) is obtained using a step-by-step integration scheme. Denoting $n(n+1)e^{5/2\xi}g_n$ by $r_n(\xi)$, equation (5.18) splits into two first order equations by introducing the two functions H_n and Q_n such that

$$H_n = \frac{\partial f_n}{\partial \xi} - (n+1/2)f_n \tag{5.30}$$

and, $$Q_n = \frac{\partial f_n}{\partial \xi} + (n+1/2)f_n \tag{5.31}$$

The two functions satisfy

$$\frac{\partial H_n}{\partial \xi} + (n+1/2)H_n = r_n \tag{5.32}$$

$$\frac{\partial Q_n}{\partial \xi} - (n+1/2)Q_n = r_n \tag{5.33}$$

and consequently, $$f_n = \frac{Q_n - H_n}{2(n+1/2)} \tag{5.34}$$

with initial conditions

$$H_n = Q_n = \frac{\partial H_n}{\partial \xi} = \frac{\partial Q_n}{\partial \xi} = 0 \tag{5.35}$$

Equation (5.32) can now be integrated by a stable method in the direction of increasing ξ. One can write

$$H_n(\xi+h,t) = \lambda H_n(\xi,t) + \lambda e^{-(n+1/2)\xi} \int_{\xi}^{\xi+h} e^{(n+1/2)x} r_n(x,t)\,dx \tag{5.36}$$

where $\lambda = e^{-(n+1/2)h}$ and then a very simple step-by-step formula is obtained by assuming $r_n(x)$ to be constant in $\xi \le x \le \xi + h$ and equal to its value at $x = \xi$, for example. This gives

$$H_n(\xi+h,t) = \lambda H_n(\xi,t) + (1-\lambda)\, r_n(\xi,t)/(n+1/2) \tag{5.37}$$

which is stable since $\lambda < 1$. We can derive a more accurate formula than equation (5.37) by assuming that $r_n(\xi,t)$ is a linear function of ξ on the interval ξ to $\xi+h$ and evaluating the integral in equation (5.36) by parts. An even more accurate formula on the interval ξ to $\xi+2h$ can be found by assuming $r_n(\xi,t)$ to be represented by a second degree polynomial over the three grid points on the interval. This formula is

$$\begin{aligned} H_n(\xi+2h,t) = \lambda^2 H_n(\xi,t) &+ \left\{\frac{1-\lambda^2}{h^2(n+1/2)^3} - \frac{3\lambda^2+1}{2h(n+1/2)^2} - \frac{\lambda^2}{n+1/2}\right\} r_n(\xi,t) \\ &- \left\{\frac{2(1-\lambda^2)}{h^2(n+1/2)^3} - \frac{2(\lambda^2+1)}{h(n+1/2)^2}\right\} r_n(\xi+h,t) \\ &+ \left\{\frac{1-\lambda^2}{h^2(n+1/2)^3} - \frac{\lambda^2+3}{2h(n+1/2)^2} + \frac{1}{n+1/2}\right\} r_n(\xi+2h,t) \end{aligned} \tag{5.38}$$

We can improve on equation (5.37) for the first interval $\xi = 0$ to $\xi = h$ by using a parabolic approximation to $r_n(\xi,t)$ and fitting it to the three points at $\xi = 0, h, 2h$. Thus we calculate $H_n(h,t)$ from the formula

$$\begin{aligned} H_n(h,t) = \lambda H_n(0,t) &+ \left\{\frac{1-\lambda}{h^2(n+1/2)^3} + \frac{1-3\lambda}{2h(n+1/2)^2} - \frac{\lambda}{n+1/2}\right\} r_n(0,t) \\ &- \left\{\frac{2(1-\lambda)}{h^2(n+1/2)^3} - \frac{2\lambda}{h(n+1/2)^2} - \frac{1}{n+1/2}\right\} r_n(h,t) \\ &+ \left\{\frac{1-\lambda}{h^2(n+1/2)^3} - \frac{1+\lambda}{2h(n+1/2)^2}\right\} r_n(2h,t) \end{aligned} \tag{5.39}$$

Hence from a given approximation to $g_n(\xi,t)$ and hence $r_n(\xi,t)$ at a given time, we can generate a solution for H_n using first equation (5.39) and then equation (5.38), step by step.

Equation (5.33) is integrated in a similar fashion but in the backward direction from $\xi = \infty$ to $\xi = 0$. The far field condition on Q_n which is needed for the integration can be written as

$$Q_n(\infty,t) = 3e^{3/2\xi}F(t)\delta_{n1} \qquad (5.40)$$

The whole iterative numerical scheme can be summarized as follows:

1. At time t, the known solution at time $(t-\Delta t)$ is used as a starting solution. The tridiagonal system resulting from equation (5.29) is solved using the most recently available information of E_n to obtain the functions $g_n(\xi,t)$.
2. Apply the integral condition (5.25) to obtain a better approximation for $g_n(0,t)$.
3. Solve equation (5.18) using the stable step-by-step numerical procedure mentioned above to obtain $f_n(\xi,t)$.
4. Repeat steps 1,2 and 3 until convergence is reached. The condition set for convergence is $\left|g_n^{m+1}(\xi,t) - g_n^m(\xi,t)\right| < 10^{-5}$ where m denotes the iteration number.
5. Increment time and return to step 1.

The computational algorithm is schematically shown in figure 5.1 .

Following the start of fluid motion, very small time steps were used since the time variation of vorticity is quite fast. As time increases, the time step was gradually increased. Smaller time steps were used for higher Strouhal numbers. For example, the time steps used for $S = \pi/4$ were 0.001, 0.005, 0.01, and 0.02 whereas for $S = \pi$, the time steps 0.0005, 0.001, and 0.005 were used. The number of points in the ξ direction used is 201 with a space step of 0.025. This makes $\xi_m = 5$ which sets the outer boundary

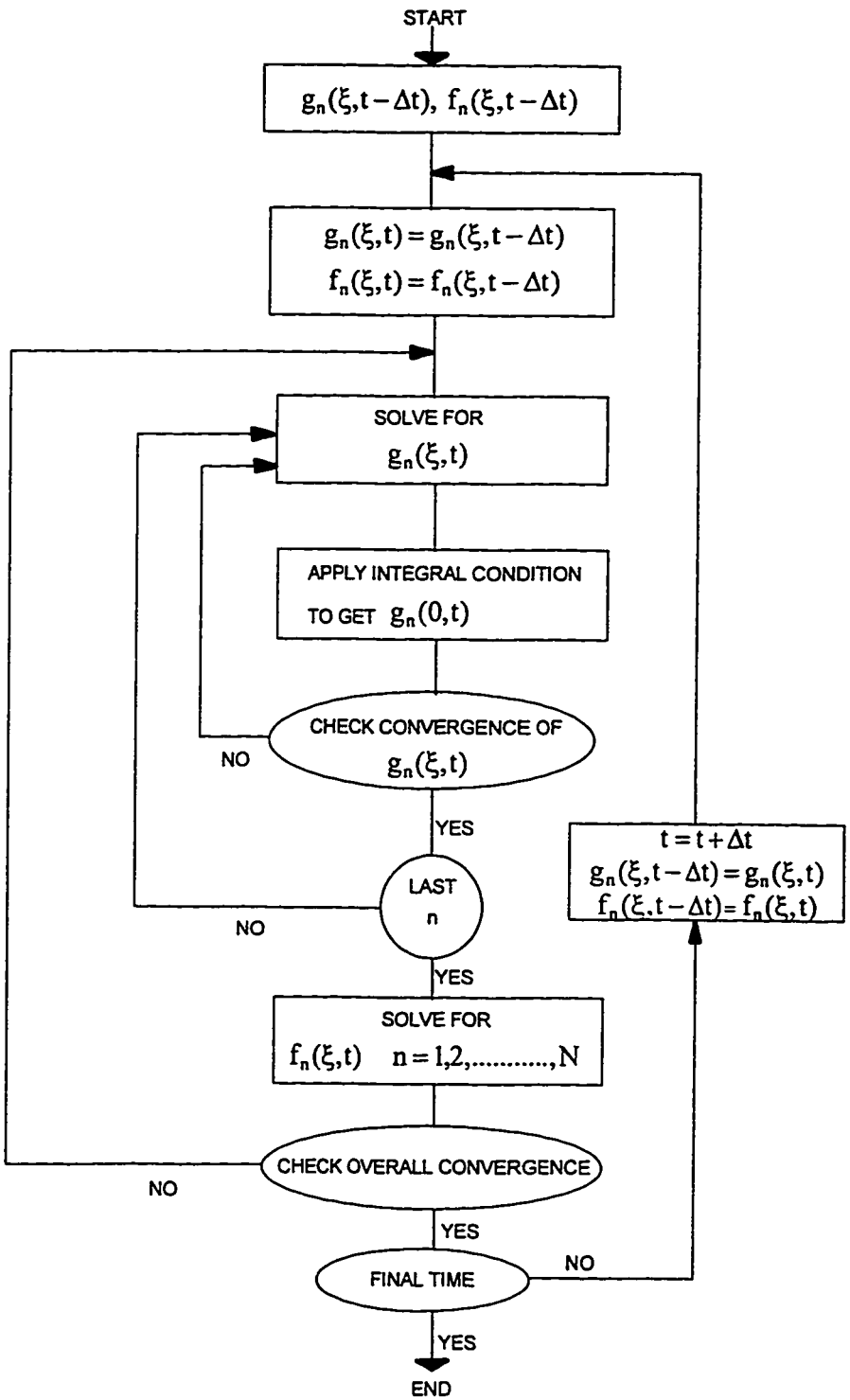

Figure 5.1 The Computational Algorithm

at a physical distance of approximately 148 times the radius of the sphere. This is necessary to ensure that the conditions at infinity are appropriately incorporated in the numerical solution. The number of terms taken in the series starts with only 3 terms. One more term is added when the last term in the series exceeds 10^{-6}. The total number of terms is dependent on Reynolds and Strouhal numbers, and the amplitude of oscillations in the case of fluctuating flow. For higher Reynolds and lower Strouhal numbers, more terms are needed than at lower Reynolds and higher Strouhal numbers. The number of terms needed in the case of oscillating flow for Re = 5 and S = π is 6 while for Re = 200 and S = $\pi/4$ is 28. In the case of fluctuating flow, the number of terms needed for the case $\mathrm{Re}=100, \mathrm{S}=\pi/4, \gamma=0.5$ is 29, and only 23 terms were needed for the case $\mathrm{Re}=100, \mathrm{S}=\pi/4, \gamma=0.1$.

The drag coefficient C_D defined in equation (4.31) is composed of two parts, one due to friction and the other due to pressure. We may then write

$$C_D = C_{DF} + C_{DP} \tag{5.41}$$

The projected area of the sphere is (πa^2). By integrating these forces over the surface of the sphere, one can show that

$$C_{DF} = -\frac{4}{\mathrm{Re}}\int_0^{\pi}\zeta(0,\theta)\sin^2\theta\, d\theta \tag{5.42}$$

$$C_{DP} = -\frac{1}{\rho U_o^2}\int_0^{\pi} p'(0,\theta)\sin 2\theta\, d\theta \tag{5.43}$$

By applying Navier-Stokes equations on the surface of the sphere, one can show that

$$\left(\frac{\partial p}{\partial \theta}\right)_{\xi=0} = \frac{4}{\mathrm{Re}}\left[\frac{\partial \zeta}{\partial \xi}+\zeta\right]_{\xi=0} \tag{5.44}$$

Using equation (5.44) together with equation (5.17), the drag components can be expressed as

$$C_{DF} = \frac{16}{3\,\mathrm{Re}} g_1(0,t) \tag{5.45}$$

$$C_{DP} = -\frac{8}{3\,\mathrm{Re}}\left[g_1(0,t) + \frac{\partial g_1}{\partial \xi}(0,t) \right] \tag{5.46}$$

The dimensionless pressure distribution around the sphere can be obtained by integrating equation (5.44) which results in

$$p^* = p_0 - p_\pi = \frac{4}{\mathrm{Re}} \int_{\pi}^{\theta} \left(\frac{\partial \zeta}{\partial \xi} + \zeta \right) d\theta \tag{5.47}$$

and by using equation (5.17), one can prove that

$$p^*(\theta,t) = \frac{4}{\mathrm{Re}} \sum_{n=1}^{N} \left[P_n(\cos\theta) - (-1)^n \right] \left[\frac{\partial g_n}{\partial \xi}(0,t) + g_n(0,t) \right] \tag{5.48}$$

5.3 Oscillating Flow

The accuracy of the method of solution for oscillatory flow will first be verified by comparing with the results of Chang and Maxey (1994), hereinafter referred to as the CM study, and the drag formula by Basset (1888) for Reynolds number 16.7 and Strouhal number 0.625. Figure 5.2 presents the drag coefficient over one full oscillation. The portion of the graph shown corresponds to a full cycle of the CM study where a negative sine curve for the free stream velocity was used instead of the cosine function used in the present study. It can be seen that an excellent agreement exists between the drag coefficient obtained in the present work and that obtained in the CM study who used a direct numerical simulation based on spectral methods for Reynolds numbers up to 16.7 and Strouhal numbers up to 10. The Basset solution which is shown is based on the assumption that the non-linear inertia terms are neglected, the form of which is

$$C_D = -2\,S\sin(St) + \frac{12}{\mathrm{Re}}\cos(St) - 12\sqrt{\frac{S}{2\,\mathrm{Re}}}\cos\left(St - \frac{3\pi}{4}\right) \tag{5.49}$$

The first term on the right hand side is equal to the potential flow drag. As Re tends to infinity, equation (5.49) converges to the potential flow drag as the two terms on the right hand side which are functions of Re tend to zero.

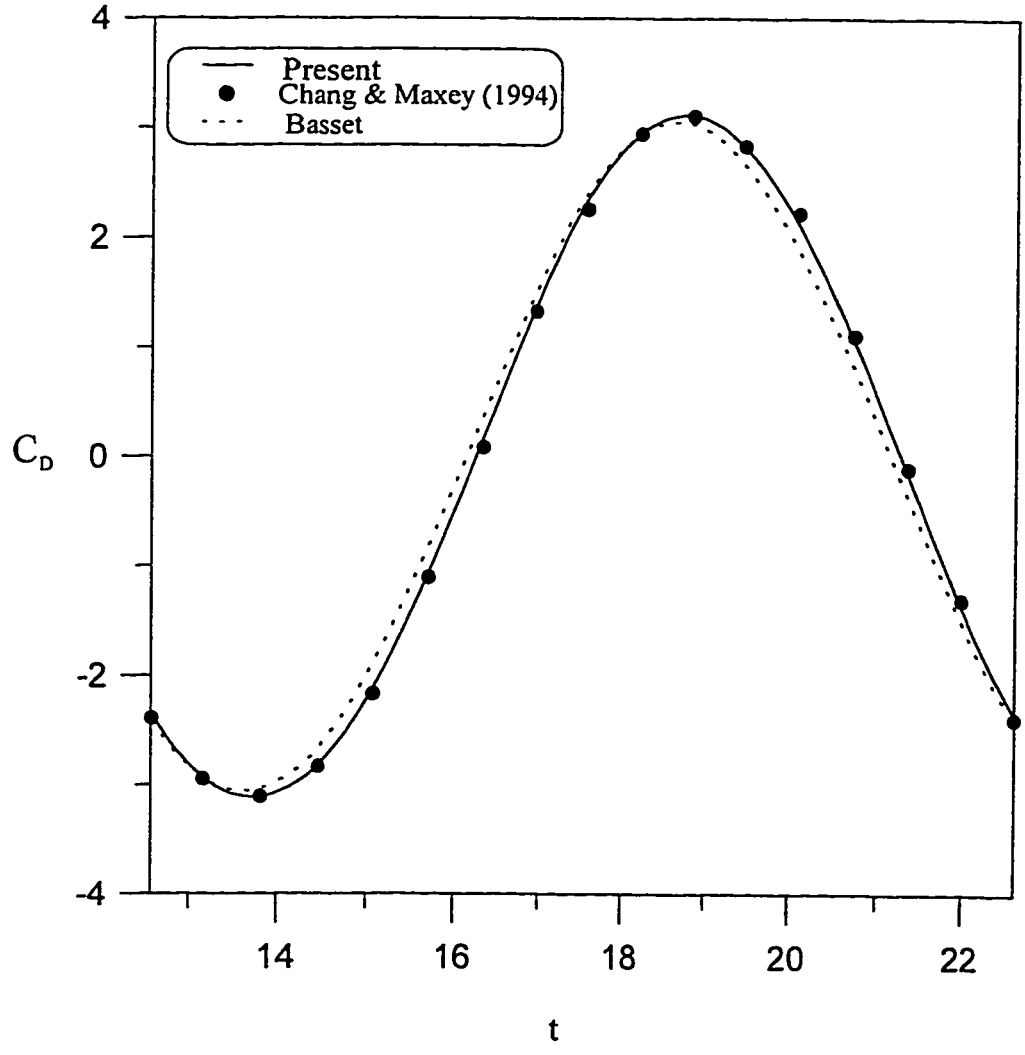

Figure 5.2 Drag Over an Oscillation Cycle, Re = 16.7, S=0.625

In this study, results are obtained for Reynolds numbers ranging from 5 to 200 and Strouhal numbers from $\pi/4$ to 2π. The time variation of the drag coefficients for Re =10, 20, 50, 100, and 200 when $S = \pi / 4$ are shown in figure 5.3. The corresponding potential flow solution is also plotted. It can be observed that the drag coefficient exhibits a phase lead over the free stream velocity profile. This is attributed to the separation of the flow during the decelerating period of the flow oscillation. This is significant because it indicates that under the right conditions, instead of retarding the flow, the presence of the sphere can act to maintain it, CM (1994). This phase lead increases at higher Reynolds numbers. The pressure and friction components of the drag for the same cases are plotted in figures 5.4 and 5.5. They also exhibit phase lead over the free-stream velocity. The figures show that the effect of Re on C_{DF} amplitude is considerable while its effect on C_{DP} is much less. This is quite expected since the pressure distribution follows closely the potential flow solution except for the separated flow region. On the other hand, the frictional drag is influenced by the boundary-layer thickness as well as the fluid viscosity. Both elements have direct relation with Reynolds number. Table 5.1 presents the phase angles $\Phi(\Phi = St)$ at which the drag components change sign. The free stream changes sign at $\Phi = \pi / 2$ and $3\pi / 2$. The phase lead of the drag components increases as Reynolds and Strouhal numbers increase. Theoretically, the frictional component of drag will be in phase with the free-stream velocity as Strouhal number decreases, and will lead the free-stream velocity by $\pi / 4$ as Reynolds and Strouhal numbers increase. The pressure component of drag will lead the free-stream velocity by $\pi / 2$ as Strouhal number increases. The results presented in table 5.1 for higher Reynolds numbers than those treated by the CM study are confined within these limits. Badr et al. (1995) observed that the pressure component of drag approaches that of the potential flow as Strouhal number increases in the case of cylinders in an oscillating free-stream. Figure 5.6 shows the same trend for a sphere in an oscillating flow. The figure presents the drag components for the case of Re = 50 and S = $\pi / 4$, $\pi / 2$, π, and 2π. Obviously, the pressure dominates the drag and C_{DP} tends to the potential flow value as S increases.

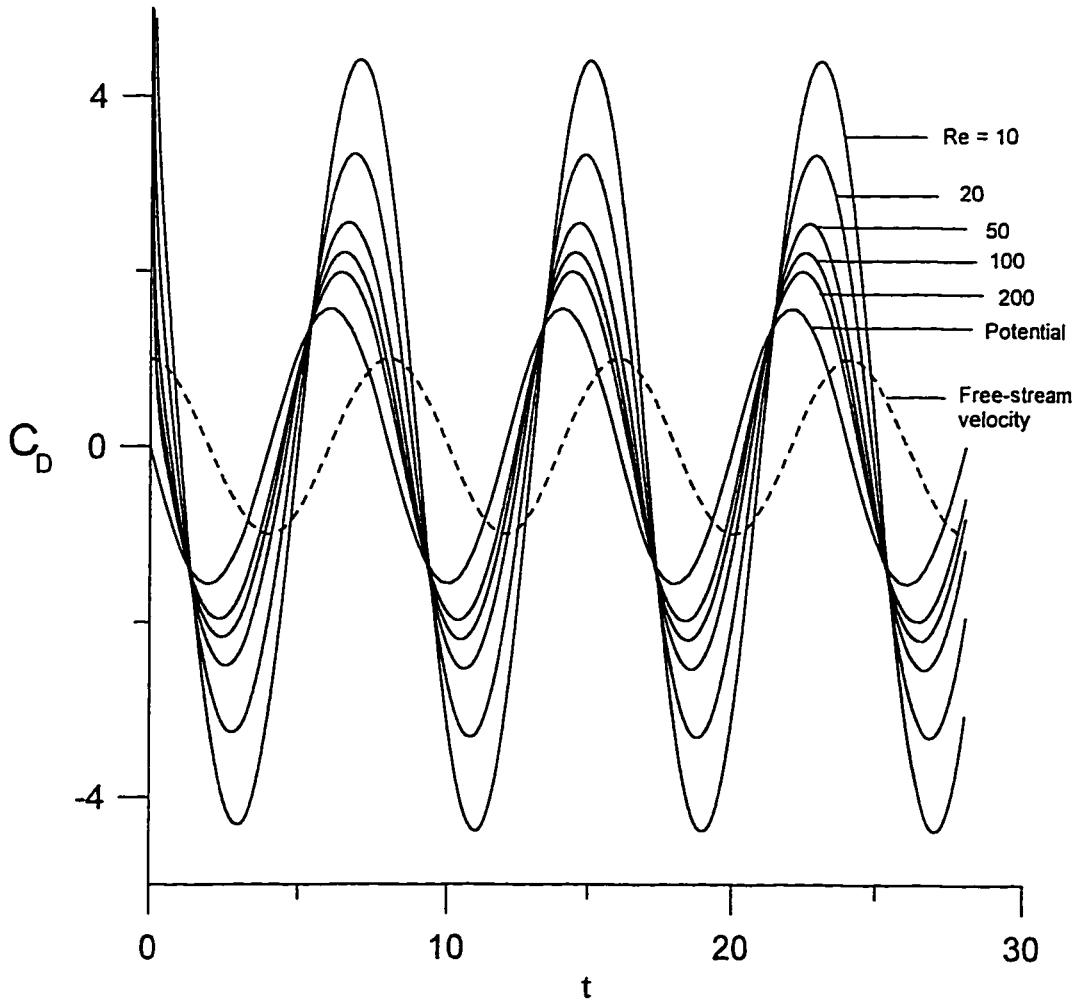

Figure 5.3 The time variation of the drag coefficient for the case $S = \frac{\pi}{4}$ at different Reynolds numbers.

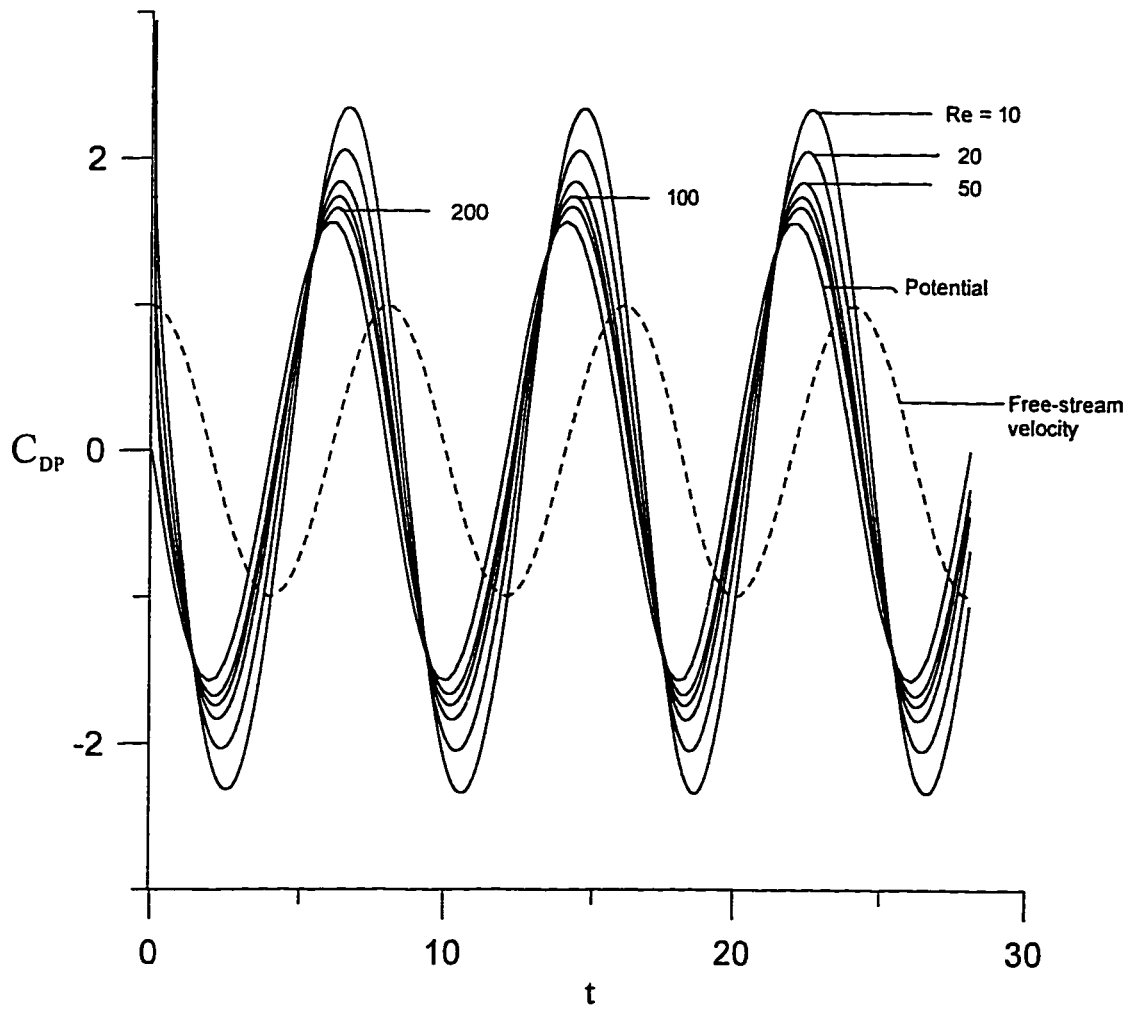

Figure 5.4 The time variation of the pressure component of drag for the case $S = \frac{\pi}{4}$ at different Reynolds numbers.

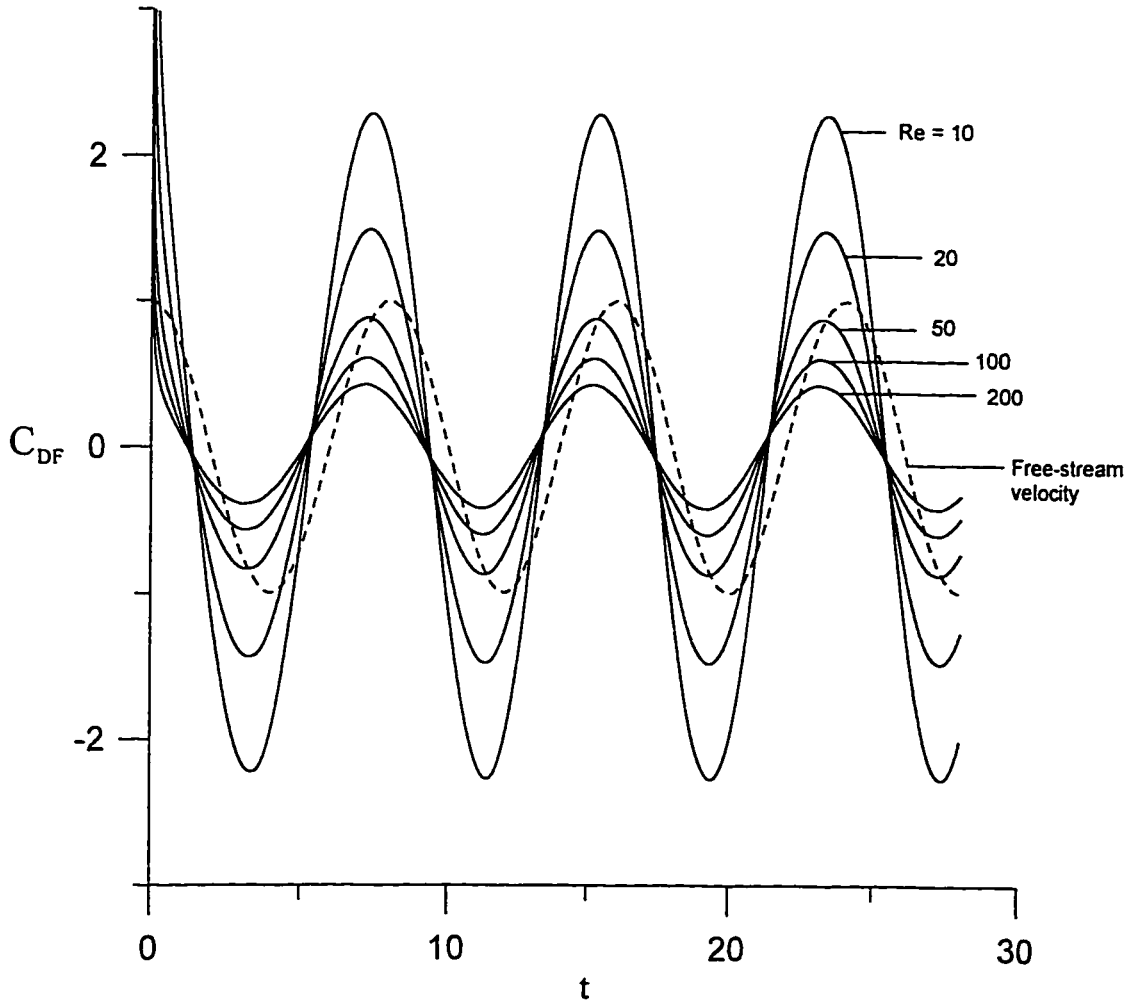

Figure 5.5 The time variation of the friction component of drag for the case, $S = \frac{\pi}{4}$ at different Reynolds numbers.

Table 5.1 Phase angles at which drag components change sign

Re	S	Φ	Φ	Φ
10	π	.770	1.078	.471
10	π	.596	1.001	.313
10	π	.451	.942	.211
50	π	.479	.978	.247
50	π	.333	.913	.152
50	π	.242	.870	.108
50	2	.193	.845	.096
100	π	.376	.935	.191
100	π	.258	.886	.120
100	π	.197	.851	.098
200	π	.295	.893	.154
200	π	.210	.864	.108

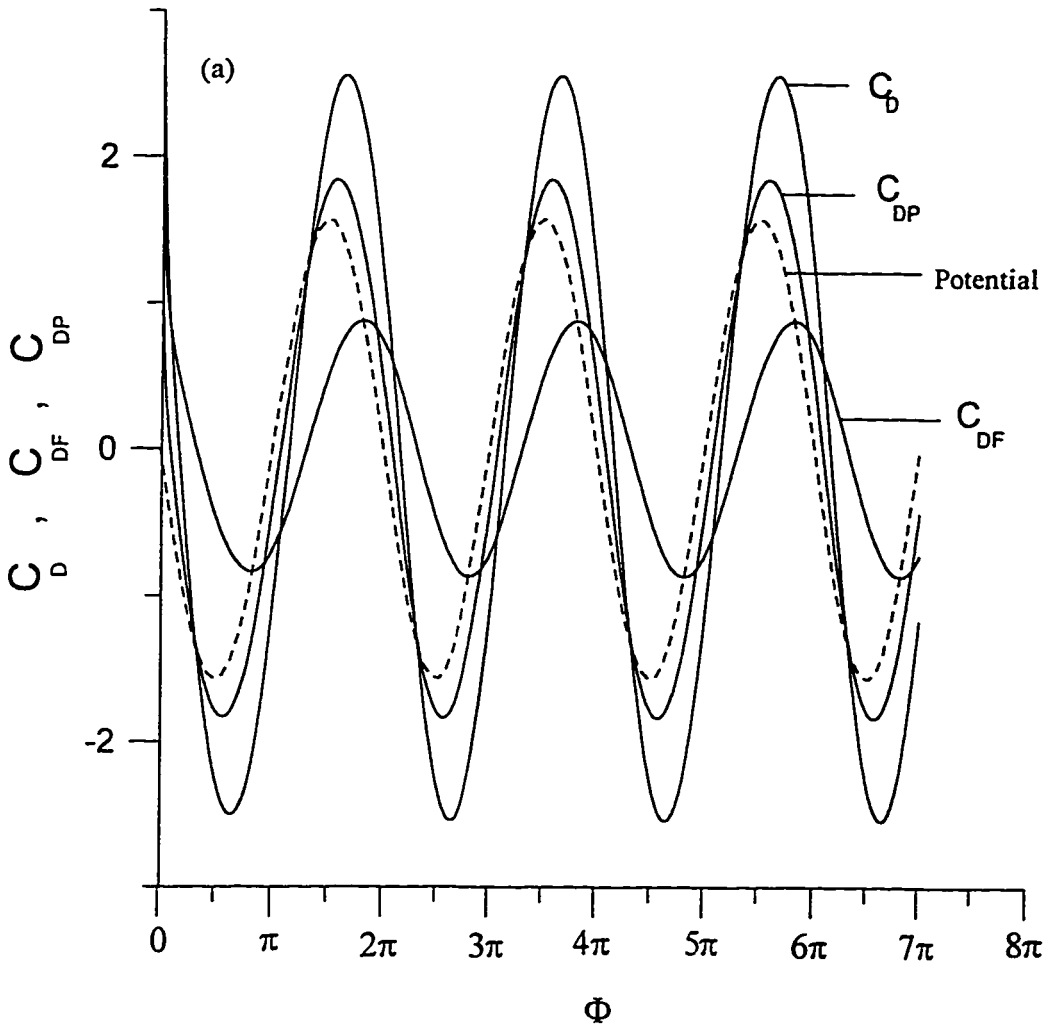

Figure 5.6a

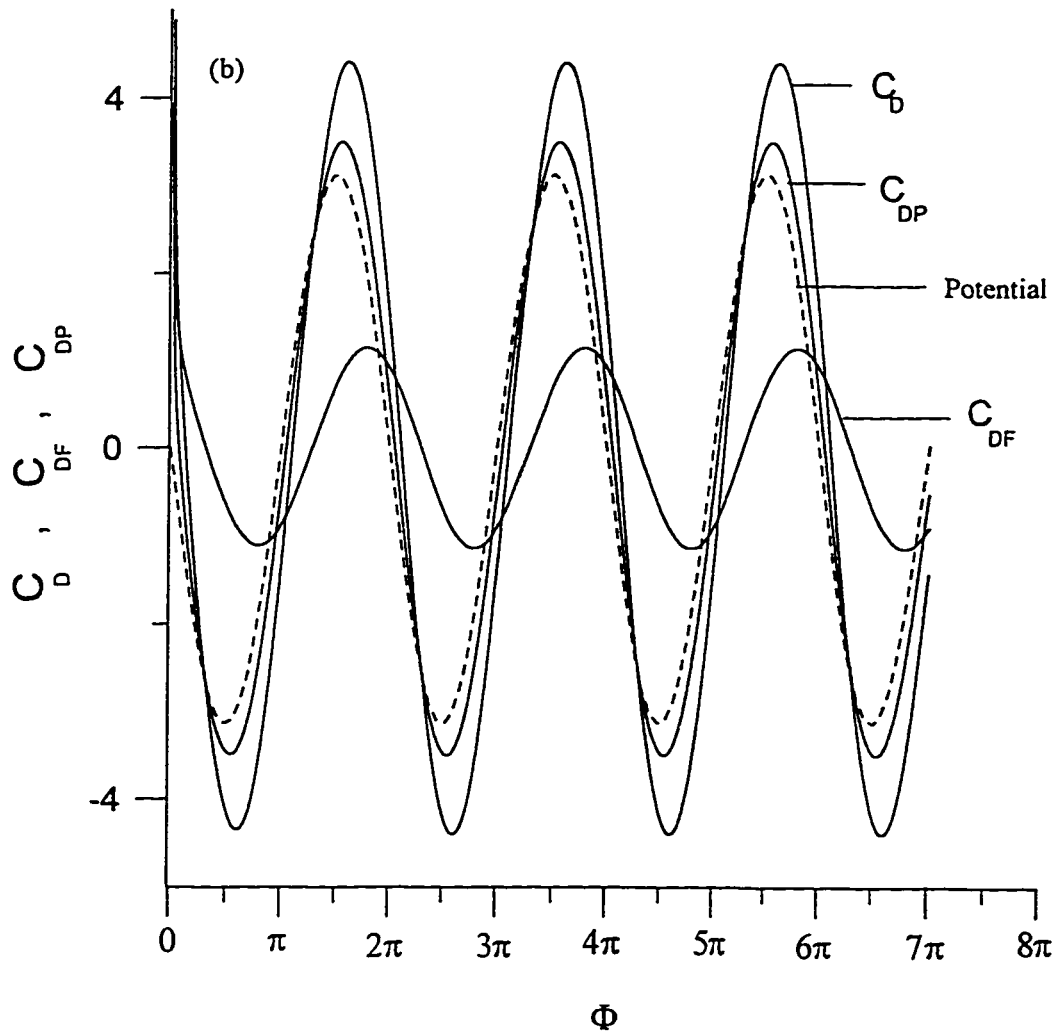

Figure 5.6b

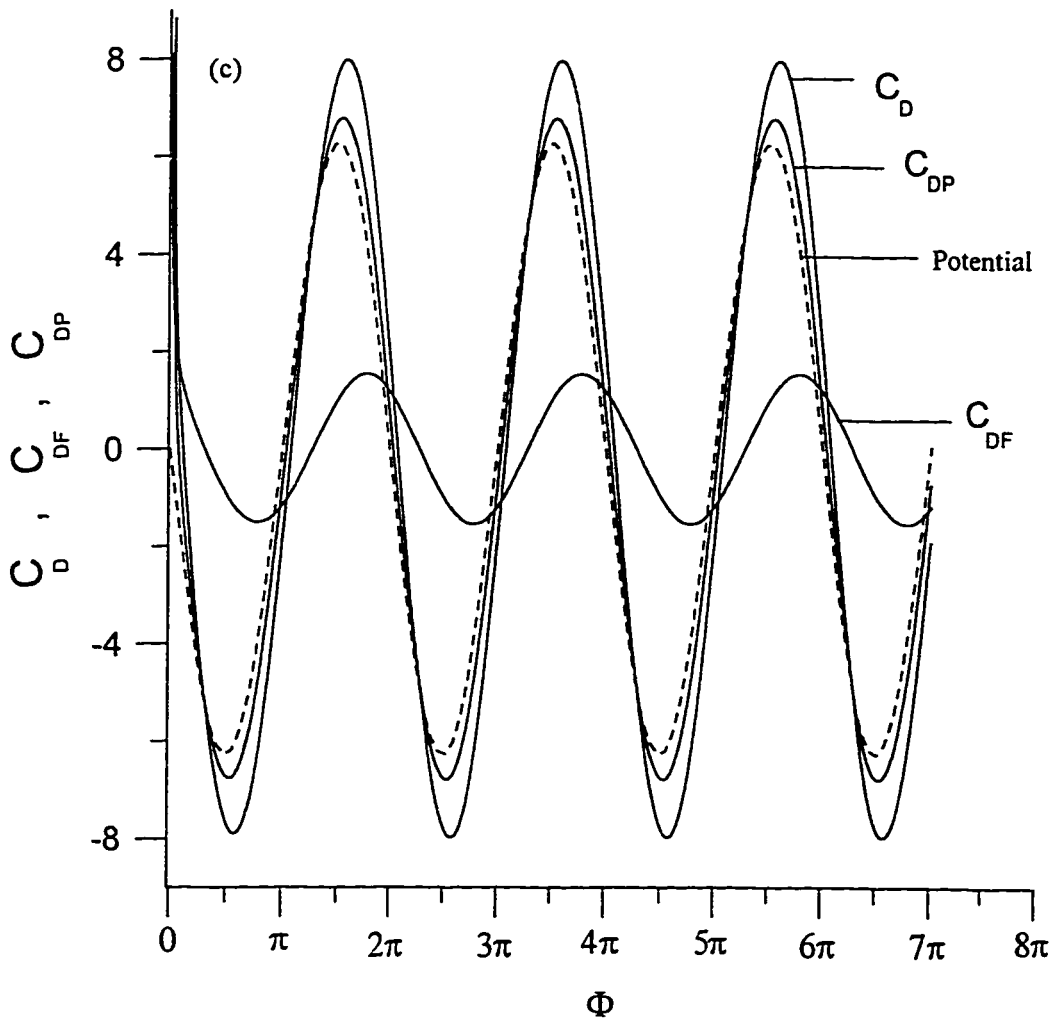

Figure 5.6c

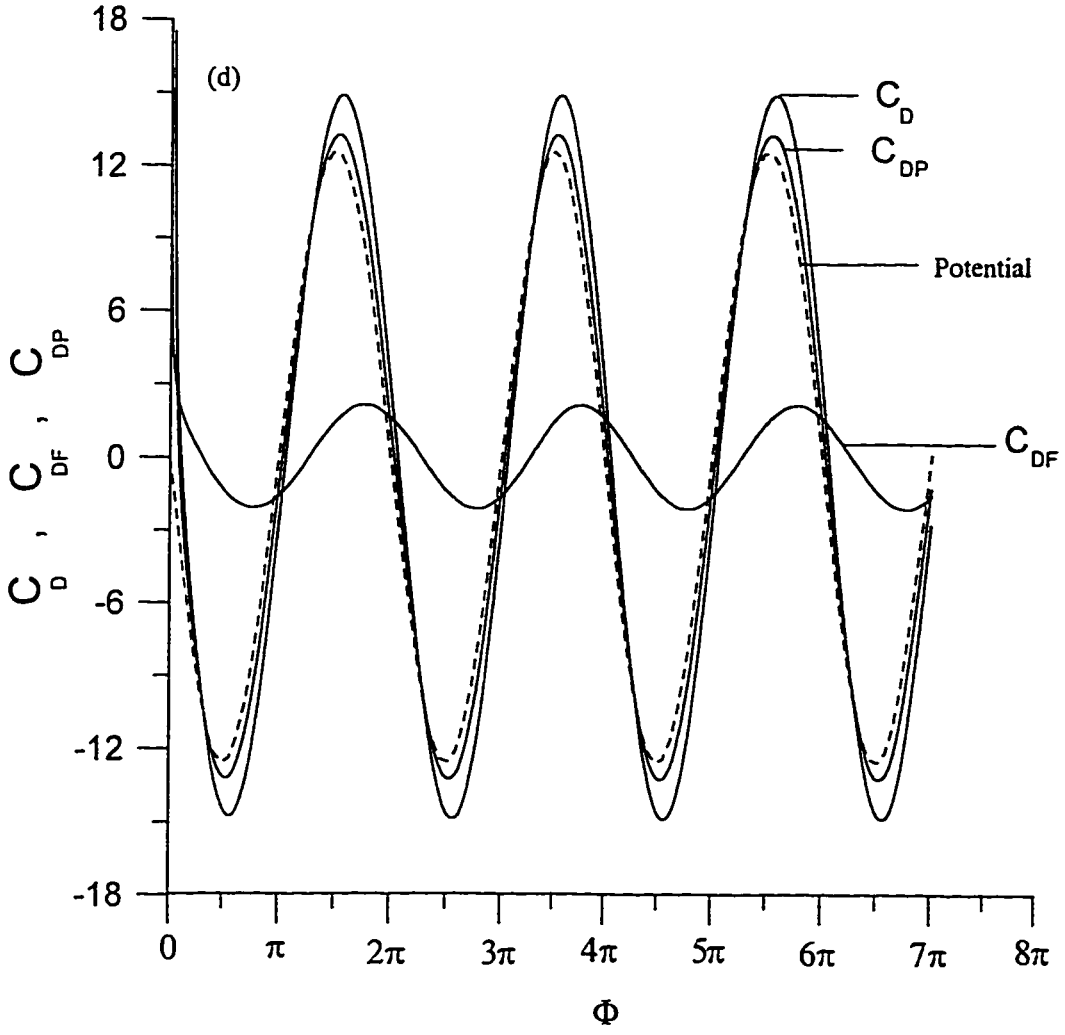

Figure 5.6d

Figure 5.6 The time variation of the total, pressure, and friction drag for the case Re = 50, (a) S= $\frac{\pi}{4}$, (b) S= $\frac{\pi}{2}$, (c) S= π , (d) S= 2π .

Figure 5.7 shows the time variation of the surface pressure distribution for the case of $S = \pi / 4$ at Reynolds numbers 50 and 200 for one-quarter of a complete oscillation. It is important to note that the curve of $\Phi = 0$ corresponds to $U = U_{max}$ at which the inertia effect is zero and that for $\Phi = \pi / 2$ corresponds to $U = 0$ at which the inertia effect is maximum. On the same figure, the corresponding inviscid flow pressure distributions are plotted. The later takes the form

$$p^*(\theta,t) = 3\,S\,\sin(S\,t)(1+\cos\theta) - \frac{9}{4}\cos^2(S\,t)\,\sin^2\theta \qquad (5.50)$$

As can be seen in figure 5.7, the viscous and inviscid flow pressure distributions are in good agreement at $\Phi = \pi / 4$ except for the region close to the rear stagnation point ($\theta = 0$) where the flow is characterized by vortical motion. It can also be observed that the curves for higher Reynolds numbers are closer to the inviscid flow pressure distribution curves than for lower Reynolds numbers.

The time variation of the surface vorticity distributions during one-half of an oscillation cycle for the case $S = \pi / 4$ and Reynolds numbers of 50 and 200 are shown in figures 5.8 and 5.9 respectively. The figures show that higher Reynolds number flows have higher surface vorticity. An interesting feature of figure 5.9 is that the curve for $\Phi = 0$ crosses the x-axis which indicates that separation has already started during the acceleration part of the motion. This is not observed in figure 5.8 which is for the case Re = 50. In the CM study, separation was only observed during the decelerating part of the motion due to the low Reynolds numbers considered in their study. In this study, for the range of Reynolds and Strouhal numbers considered, separation during the accelerating part was observed for the two cases of Re =100, and Re =200 and $S = \pi / 4$ which indicates that for higher Reynolds and lower Strouhal numbers separation can occur during the accelerating as well as the decelerating parts of motion.

Figure 5.10 shows the time development of the streamline patterns over one-half of a complete oscillation for the case Re = 200 and $S = \pi / 4$. At low frequencies, the

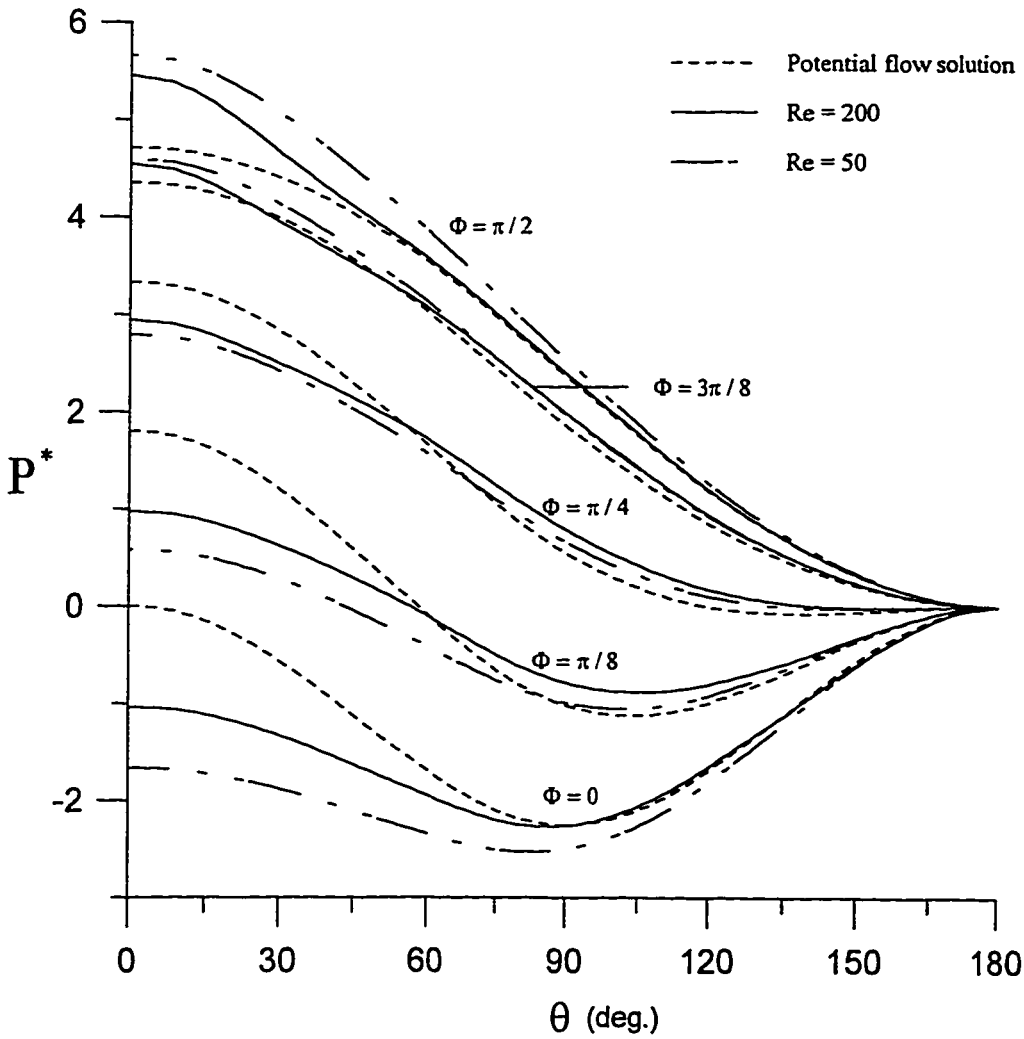

Figure 5.7 The time variation of the pressure coefficient during one quarter of a complete oscillation for the case $S = \pi / 4$.

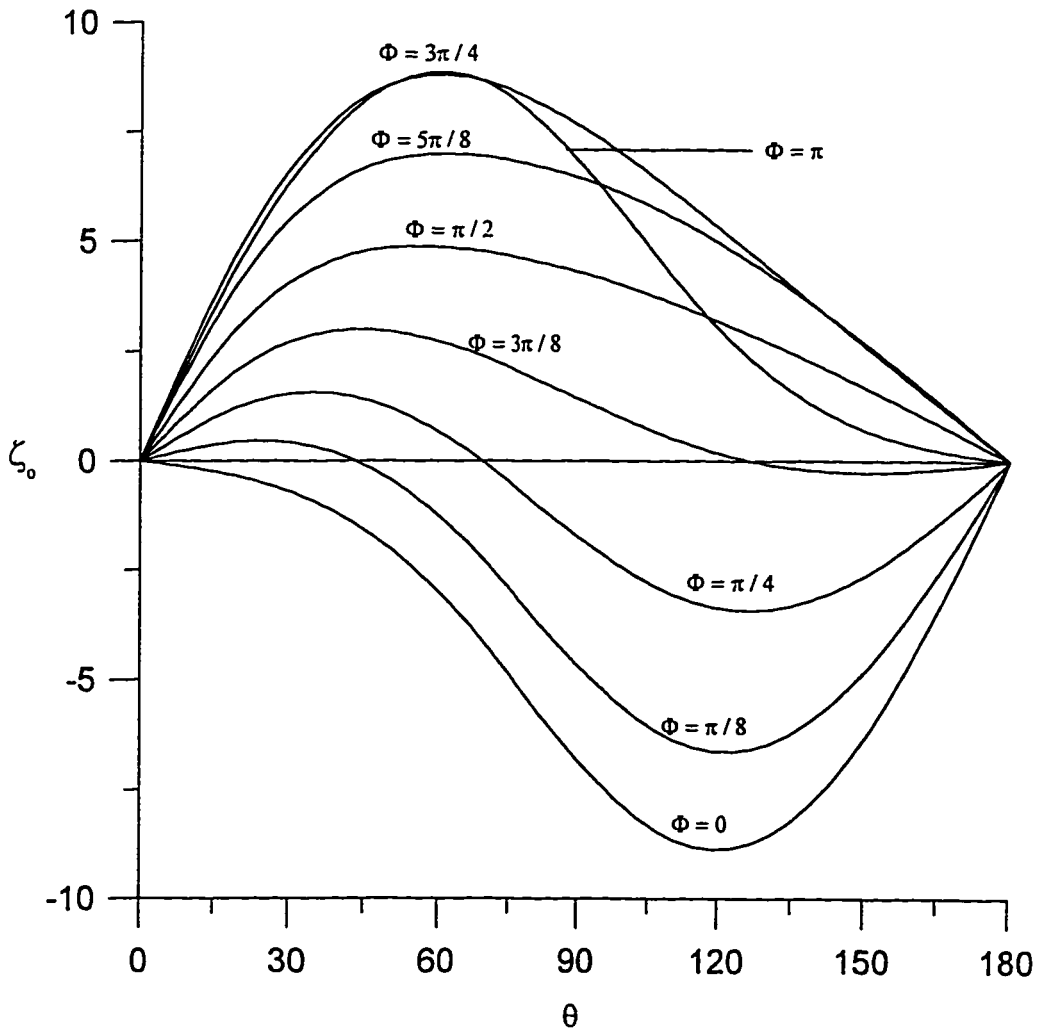

Figure 5.8 The time variation of the surface vorticity distribution during one-half of a complete oscillation for the case Re = 50, S = π / 4 .

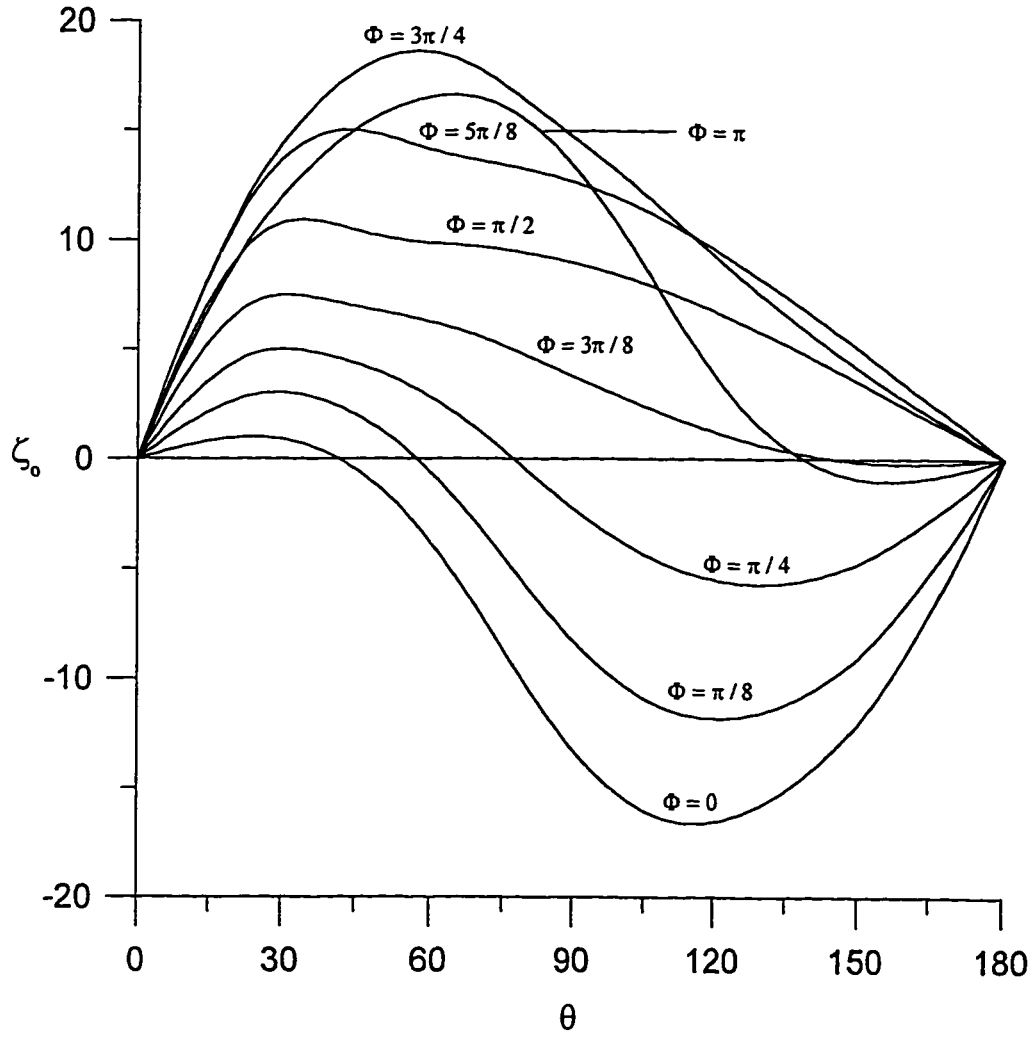

Figure 5.9 The time variation of the surface vorticity distribution during one-half of a complete oscillation for the case Re =200, S = $\pi/4$.

convective acceleration term is the dominant inertia effect while the temporal accelerations dominate any convective inertial effects at high frequencies. Furthermore, the flow is highly diffusive in nature at low frequencies and the vorticity extends throughout much of the flow field. It can be observed that in figure 5.10a (t = 24.0) which corresponds to $\Phi = 0$, separation has already occurred. The separated flow region started to form during the accelerating part of motion. As time progresses, the separation bubble grows until it eventually surrounds the sphere even before the free-stream velocity reverses direction. When the free-stream velocity is zero, the streamline pattern will be as shown in figure 5.10d where two vortices are counter rotating near the sphere. The streamlines will then follow the new direction of motion and the counter rotating vortices die out as the flow accelerates in the other direction. The streamlines will then become similar to potential flow until a separation bubble is formed on the other end of the sphere causing a mirror-image behavior in the second half of the oscillation. The corresponding vorticity patterns are shown in figure 5.11. There are two regions of opposite vorticity close to the sphere. As the flow decelerates, the outer region detaches and the inner one grows. The detachment of the outer region takes place even before the free-stream velocity reverses direction. As the flow reverses direction and starts to accelerate, the detached region subsides and the inner one grows until the velocity peaks again causing another inner vorticity region to be created on the surface and the process is repeated.

When the free-stream velocity decelerates, the point of separation travels upstream until the recirculation region encompasses the whole sphere. Figure 5.12 compares the time development of the separation angle (θ_s) for different Reynolds numbers. It is evident from the figure that for higher Re, separation occurs earlier and the bubble takes longer time to encompass the whole sphere. There is no definable angle of separation for Stokes flow. The effect of nonlinear convective acceleration by the flow is to introduce phase variations in the reversal of surface vorticity at different locations on the sphere. Figure 5.13 compares the separation angle for the same Reynolds number at different Strouhal numbers. At small phase angles, the separation angle is higher for lower Strouhal

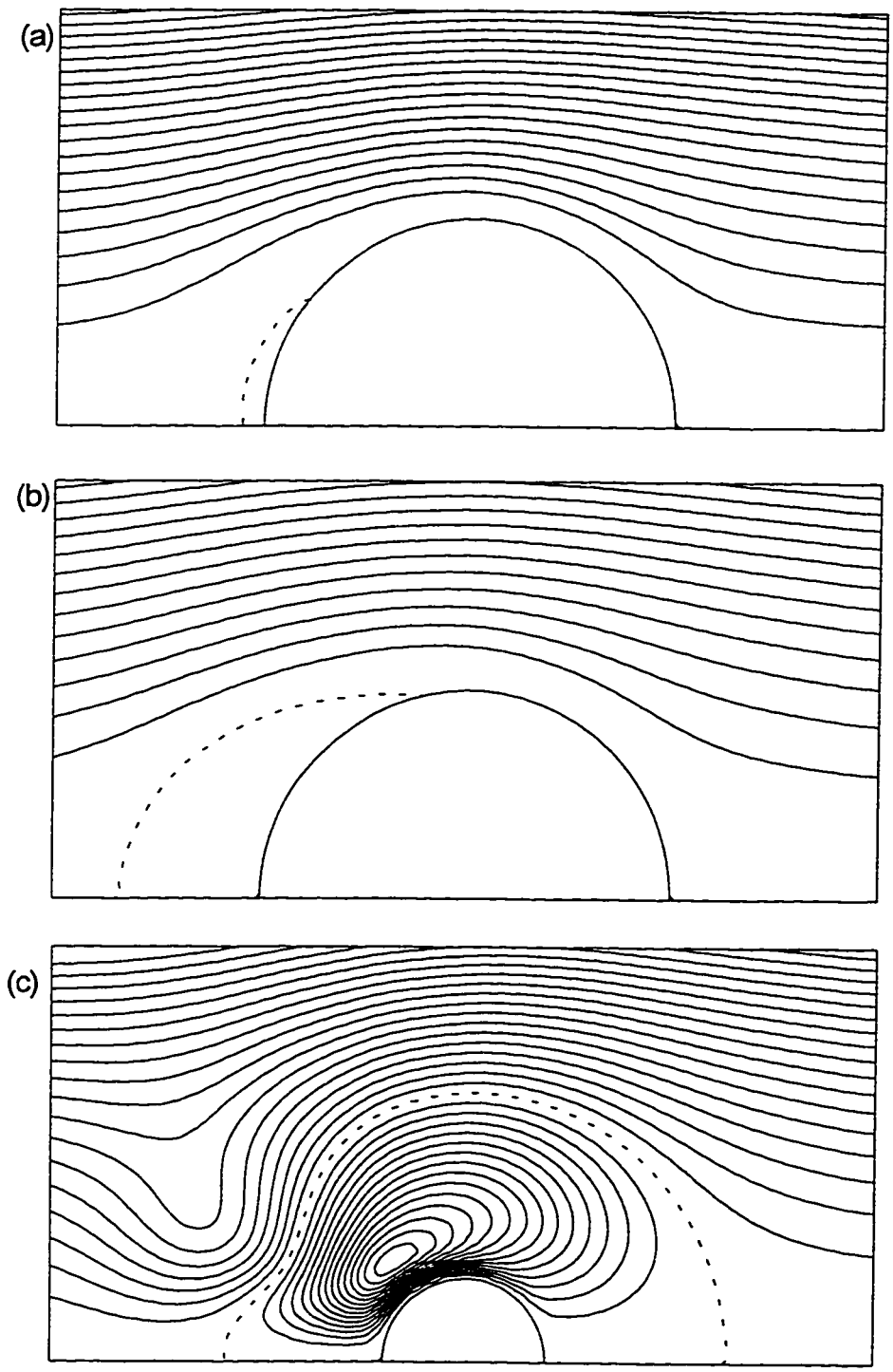

Figure 5.10a-c

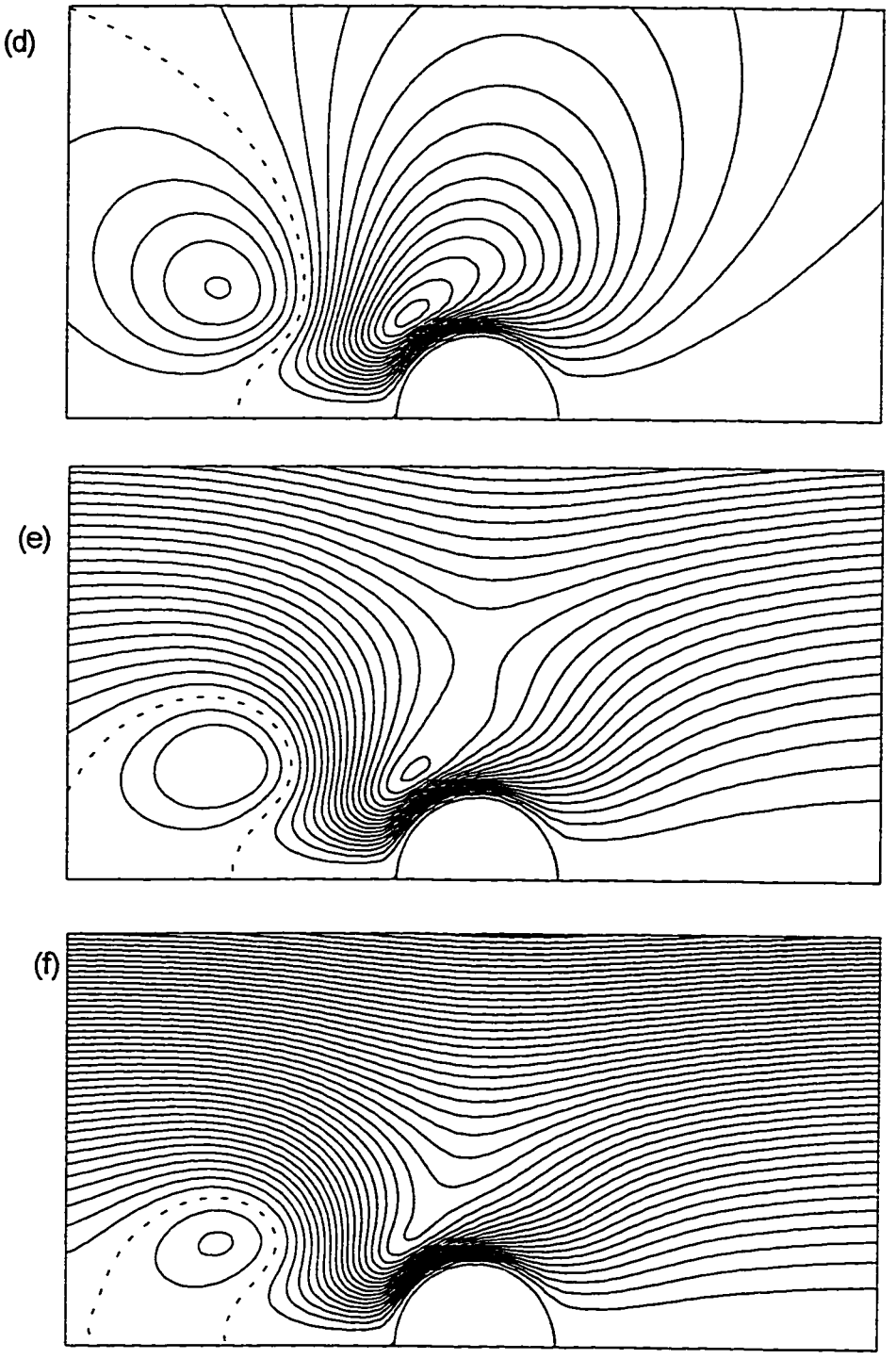

Figure 5.10d-f

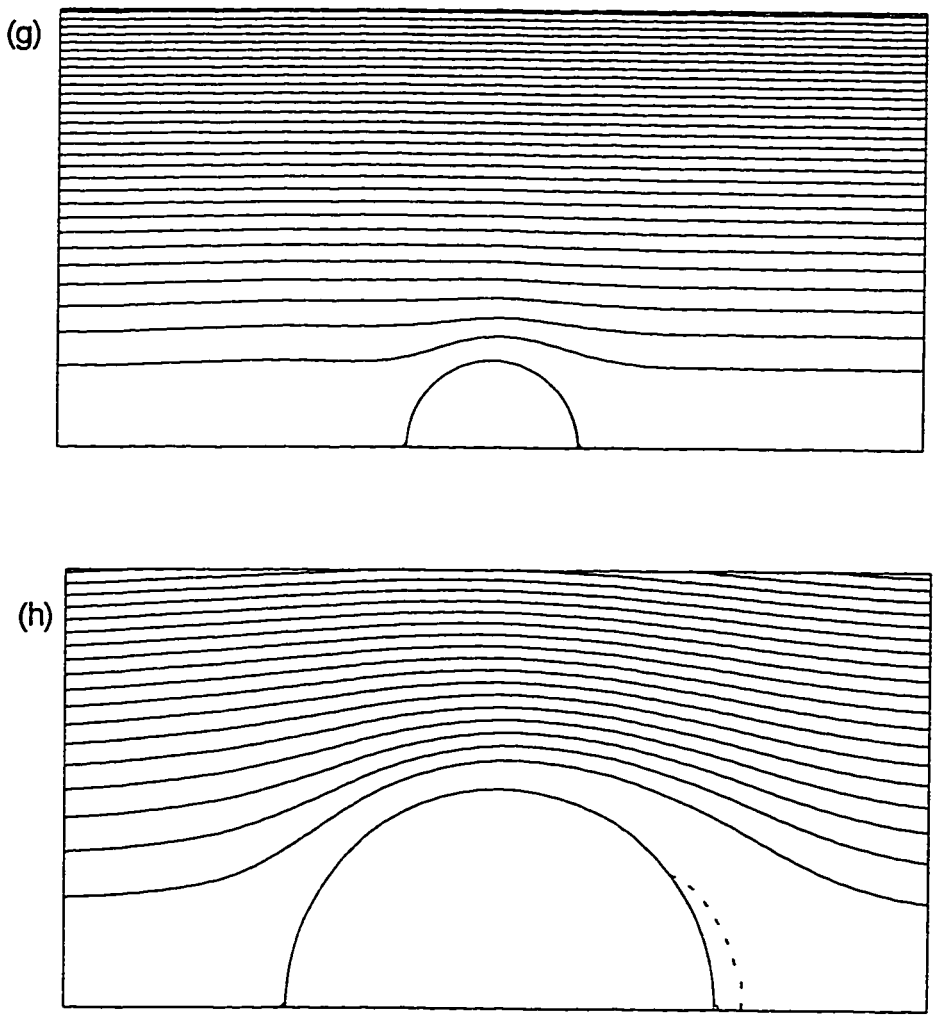

Figure 5.10 g-h

Figure 5.10 Instantaneous streamlines for the case Re = 200, $S = \pi/4$.
(a) t=24.00 ($\Delta\psi = 0.10$), (b) t=25.00 ($\Delta\psi = 0.10$),
(c) t=25.98 ($\Delta\psi = 0.01$), (d) t=26.00 ($\Delta\psi = 0.01$),
(e) t=26.02 ($\Delta\psi = 0.01$), (f) t=26.04 ($\Delta\psi = 0.01$),
(g) t=27.00 ($\Delta\psi = 0.30$), (h) t=28.00 ($\Delta\psi = 0.1$).
Dotted lines indicate zero streamlines.

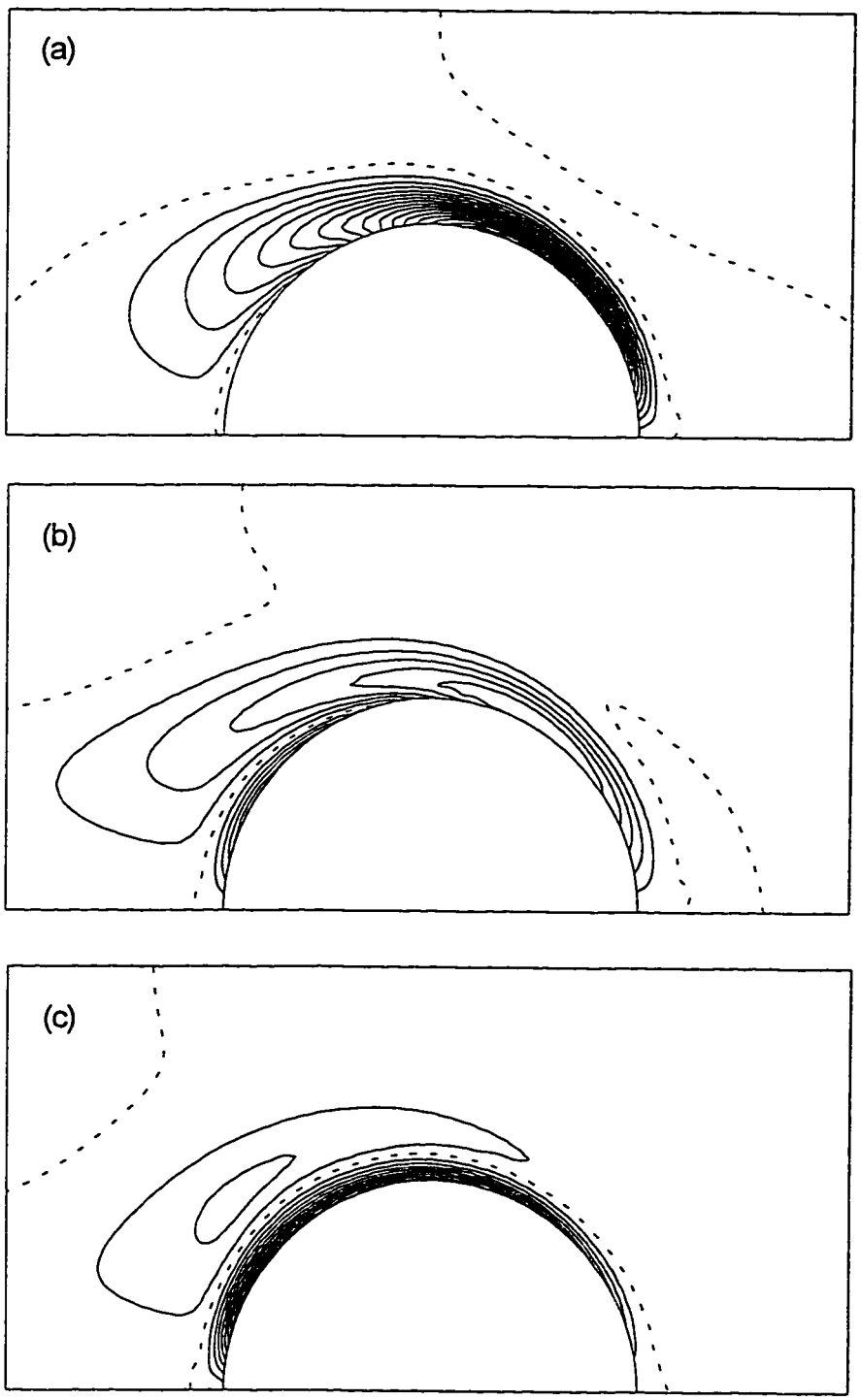

Figure 5.11a-c

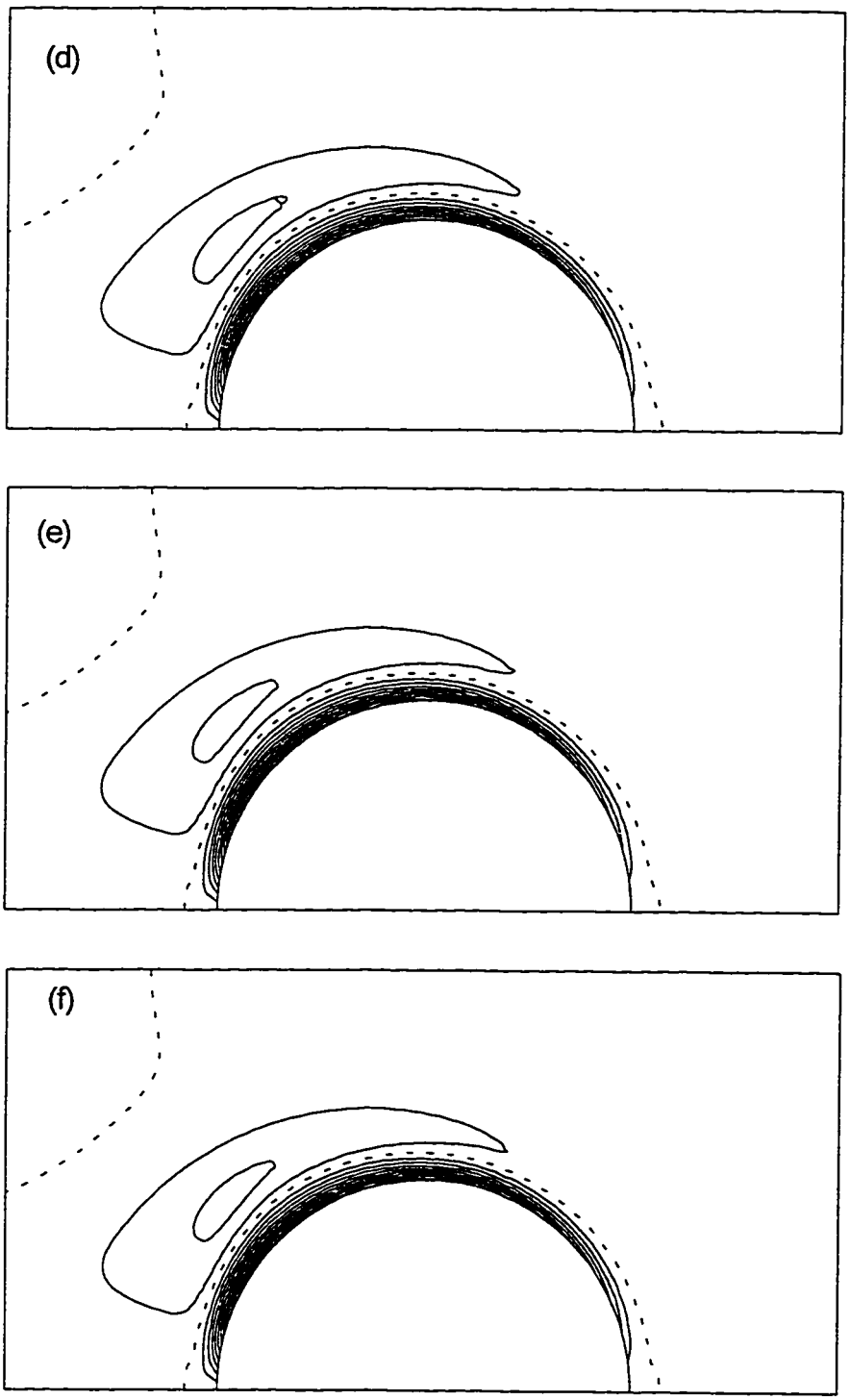

Figure 5.11d-f

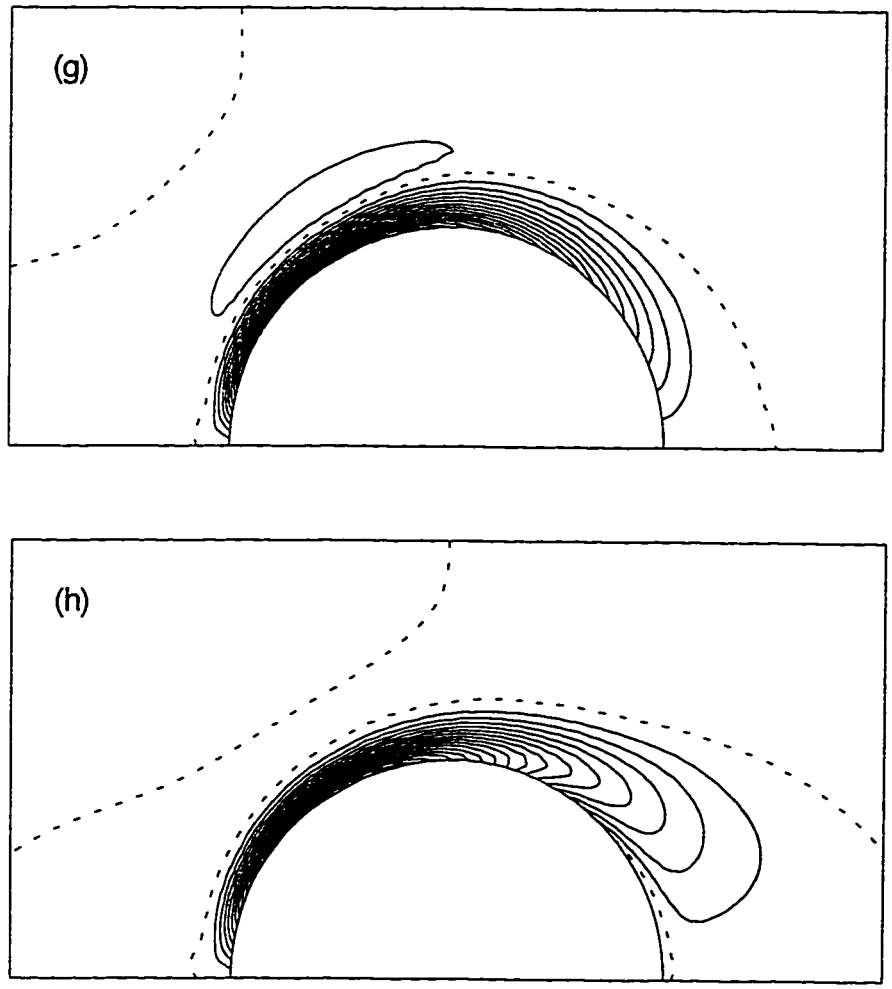

Figure 5.11 g-h

Figure 5.11 Instantaneous vorticity distribution for the case Re = 200, $S = \pi/4$. (a) t=24.0, (b) t=25.0, (c) t=25.98, (d) t=26.0, (e) t=26.02, (f) t=26.04, (g) t=27.0, (h) t=28.0 . Dotted lines indicate zero vorticity. $\Delta\varsigma$ =1.0 for all curves

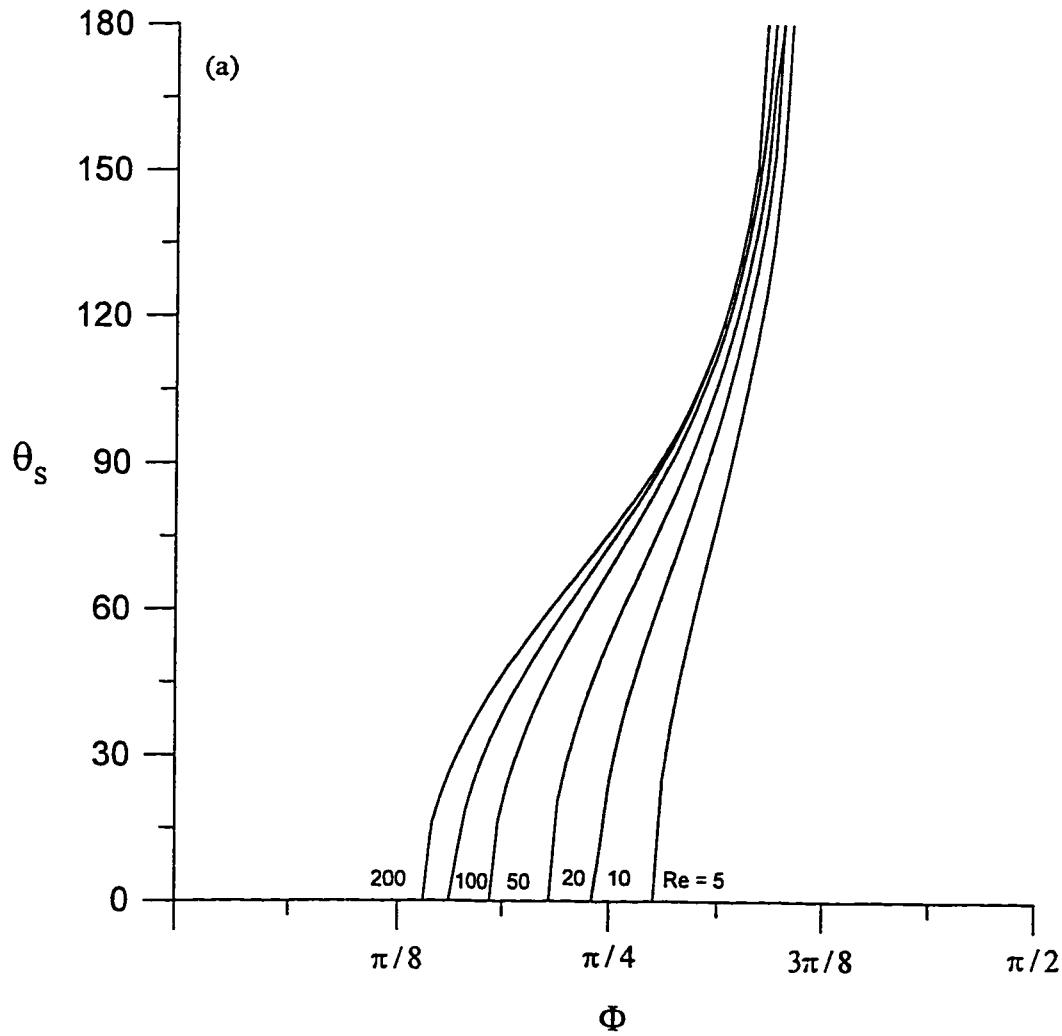

Figure 5.12a

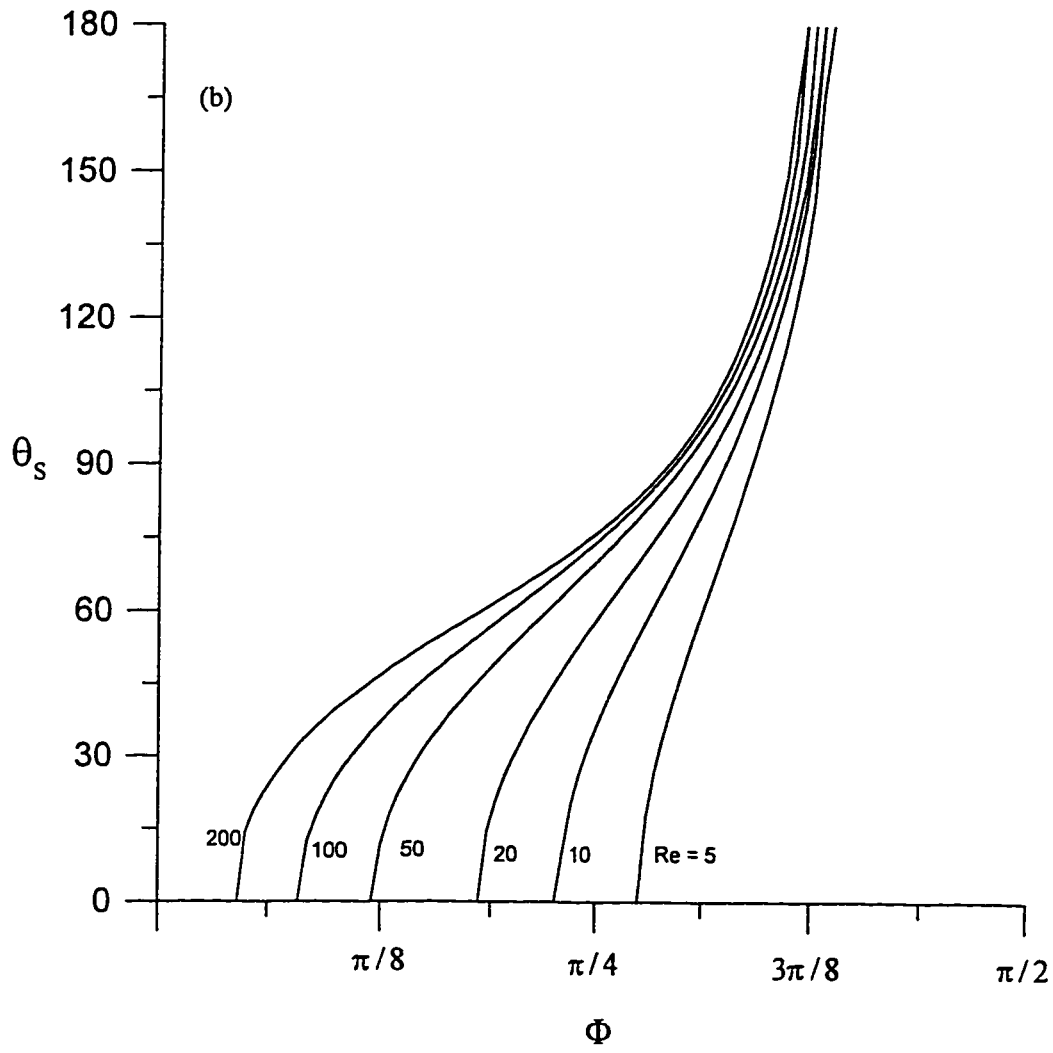

Figure 5.12b

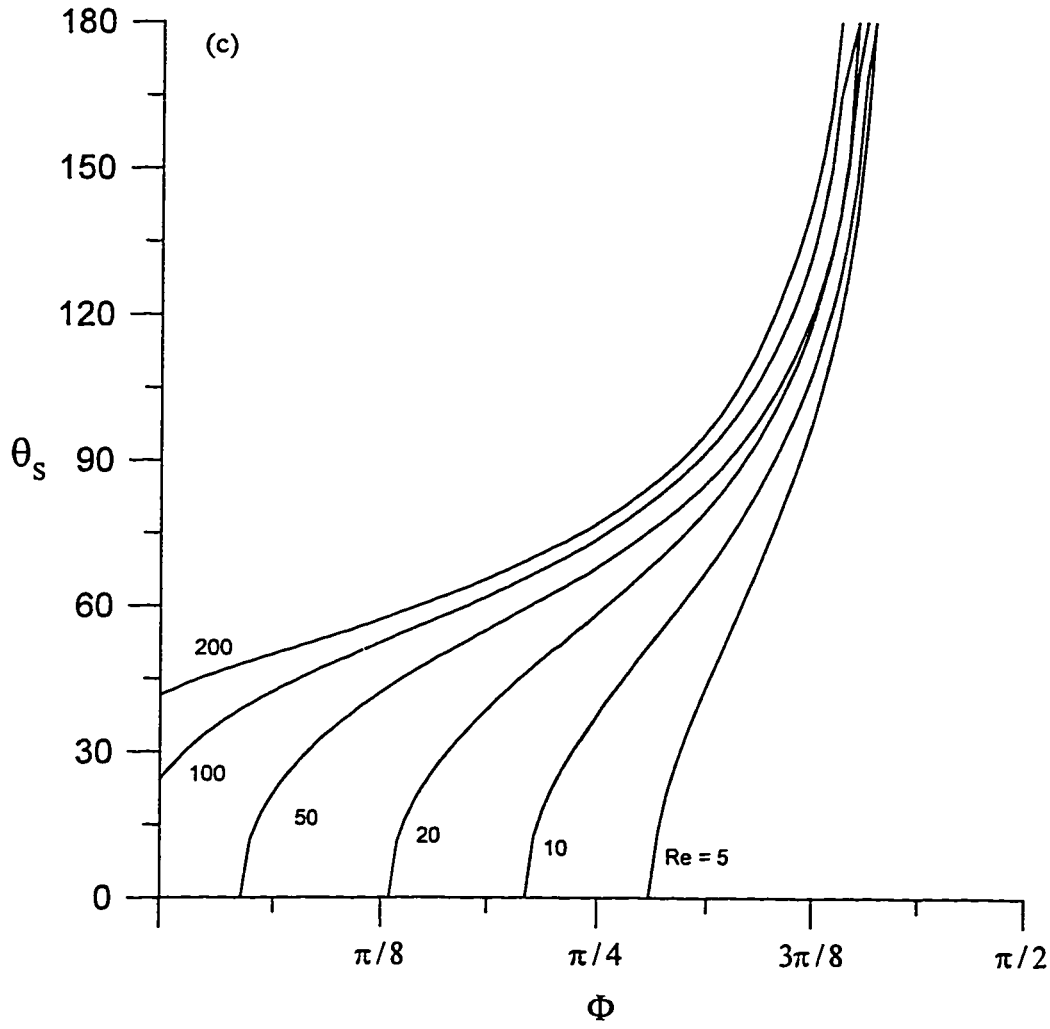

Figure 5.12c

Figure 5.12 The time variation of the separation angle
(a) S=π , (b) S=π/2, (c) S=π/4

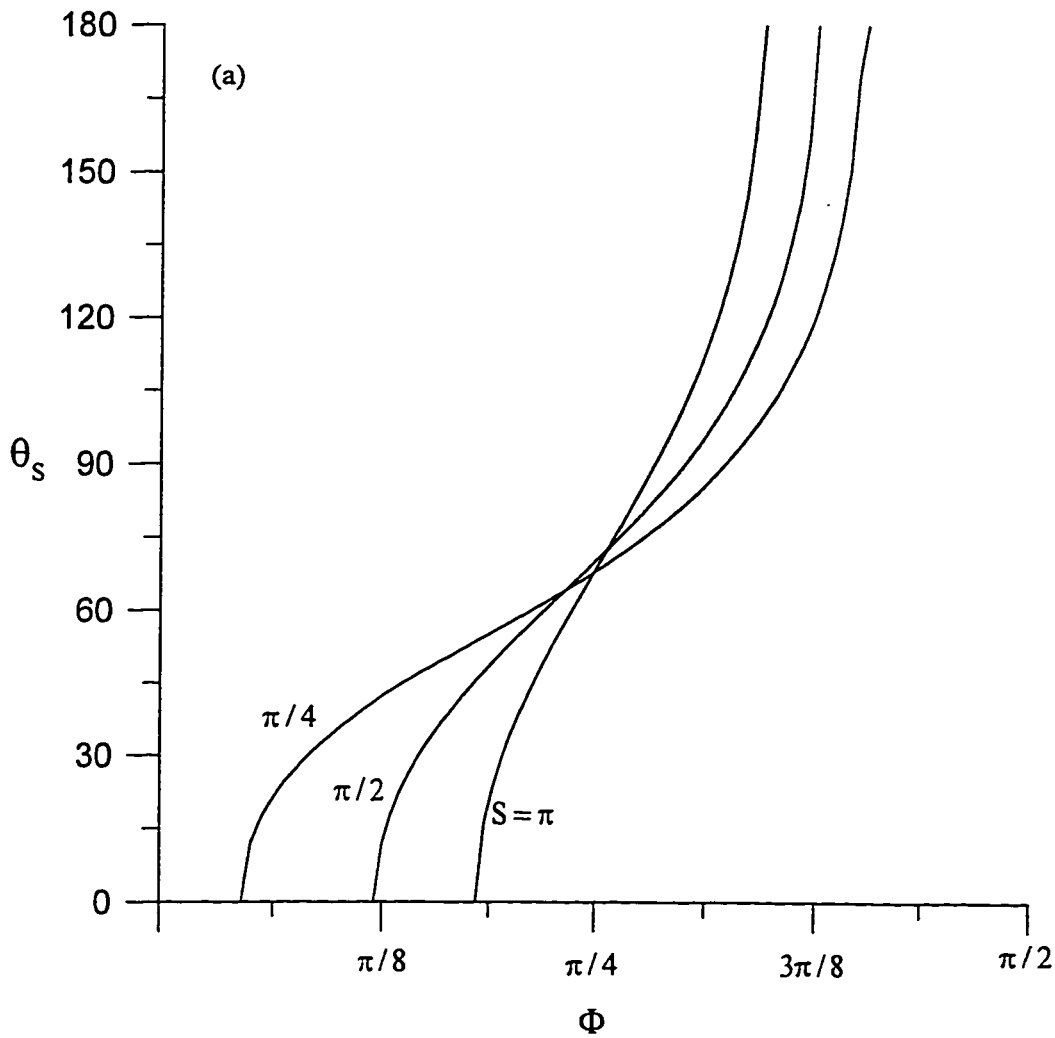

Figure 5.13a

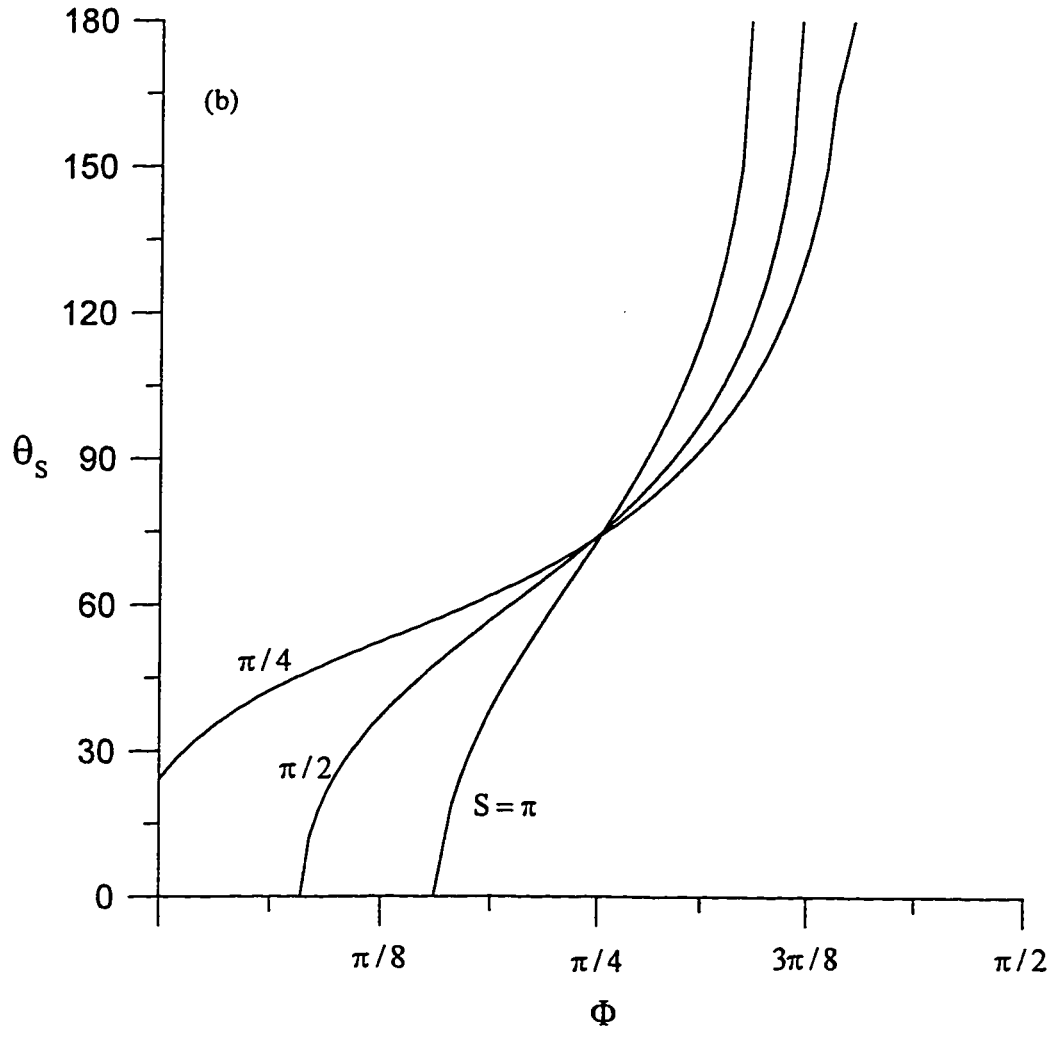

Figure 5.13b

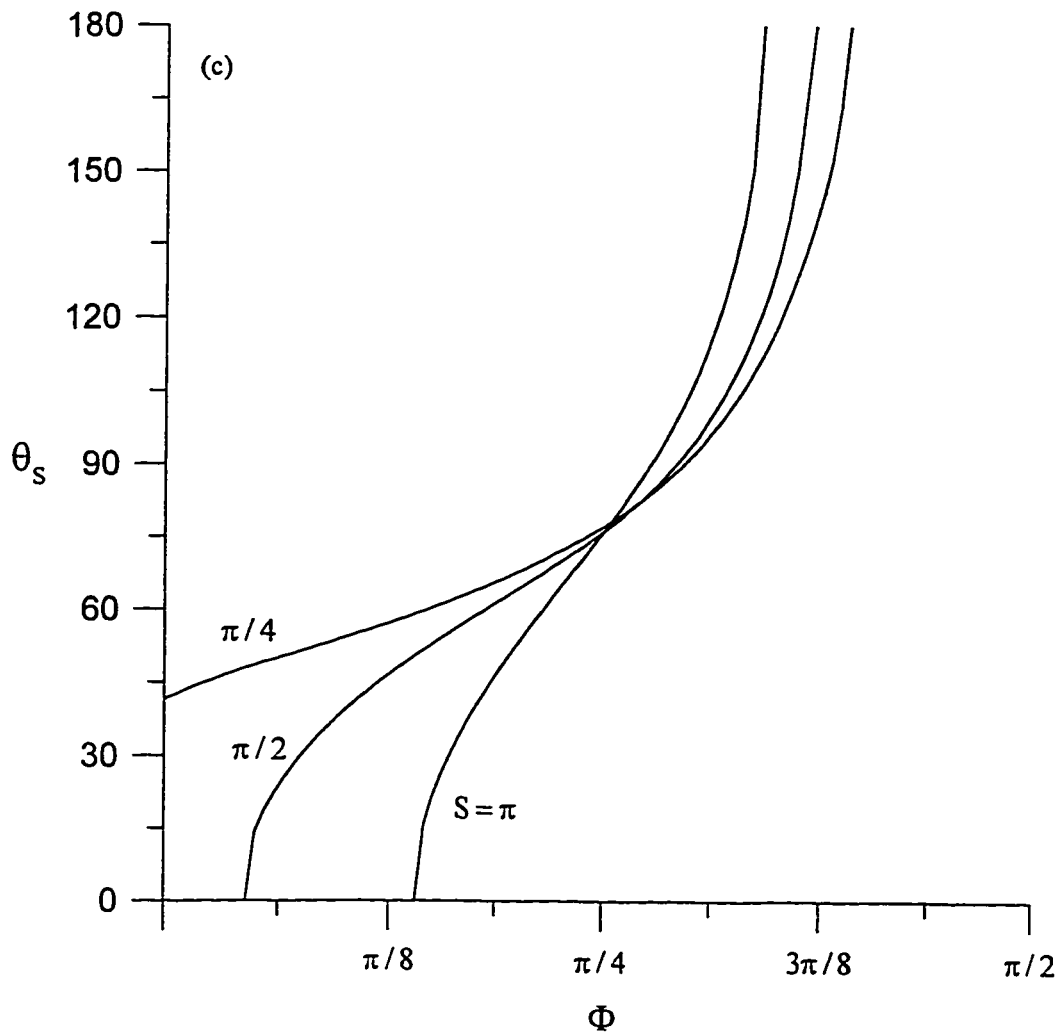

Figure 5.13c

Figure 5.13 The time variation of the separation angle
(a) Re = 50, (b) Re = 100, (c) Re = 200

numbers. As time progresses, higher Strouhal number-flows exhibit larger separation angles. The figure shows that at $\Phi = \pi / 4$ the separation angle for a fixed Reynolds number is not a function of the Strouhal number.

The length of the separation bubble (L) measured from the sphere surface at $\theta = 0$ for different cases are plotted in figure 5.14. The wake length can be obtained by locating where the velocity along the line of symmetry is zero. This condition can be mathematically written as

$$\sum_{n=1}^{\infty} f_n(\xi, t) = 0 \qquad (5.51)$$

It is clear from the curves that lower Strouhal numbers will result in longer separated regions. The behavior at the same Strouhal number but different Reynolds numbers is not as simple as described by the CM study which evaluated the length of the separated region at $\Phi = 3\pi / 10$. Figure 5.15 shows the length of the separated region for Re of 50, 100, and 200 at the same $S = \pi / 4$. At early phase angles, higher Re will produce longer recirculation regions. The trend is reversed at later times. The reversal of the trend takes place before the bubble surrounds the sphere (indicated by the stars on the curves). The same trend was observed for other Strouhal numbers.

The time-averaged stream function and vorticity over the fourth oscillation cycle are shown in figure 5.16 for the case Re = 200 and $S = \pi / 4$. The double boundary layer structure noted by the CM study is amply confirmed. The symmetry of the counter rotating eddies is slightly distorted. This is due to the fact that the solution was advanced only to the fourth cycle and the velocity field is not yet periodic. Figure 5.17 shows the time development of the time-averaged stream function for the case Re = 50 and $S = \pi / 4$ over the second, fourth, and sixth oscillation cycle. The symmetry gets better as time progresses. By comparison with figure 5.16, it can be concluded that the symmetry is achieved faster for higher Reynolds numbers.

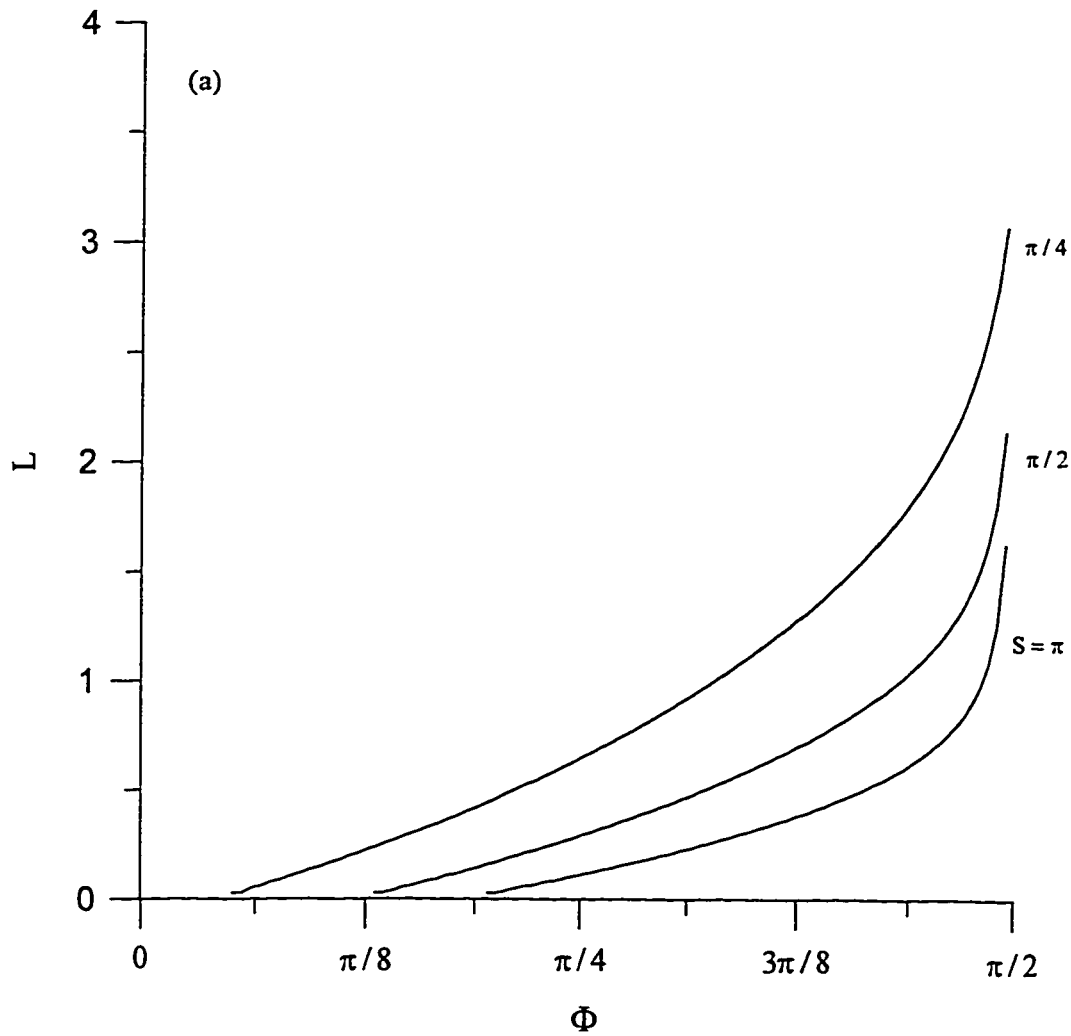

Figure 5.14a

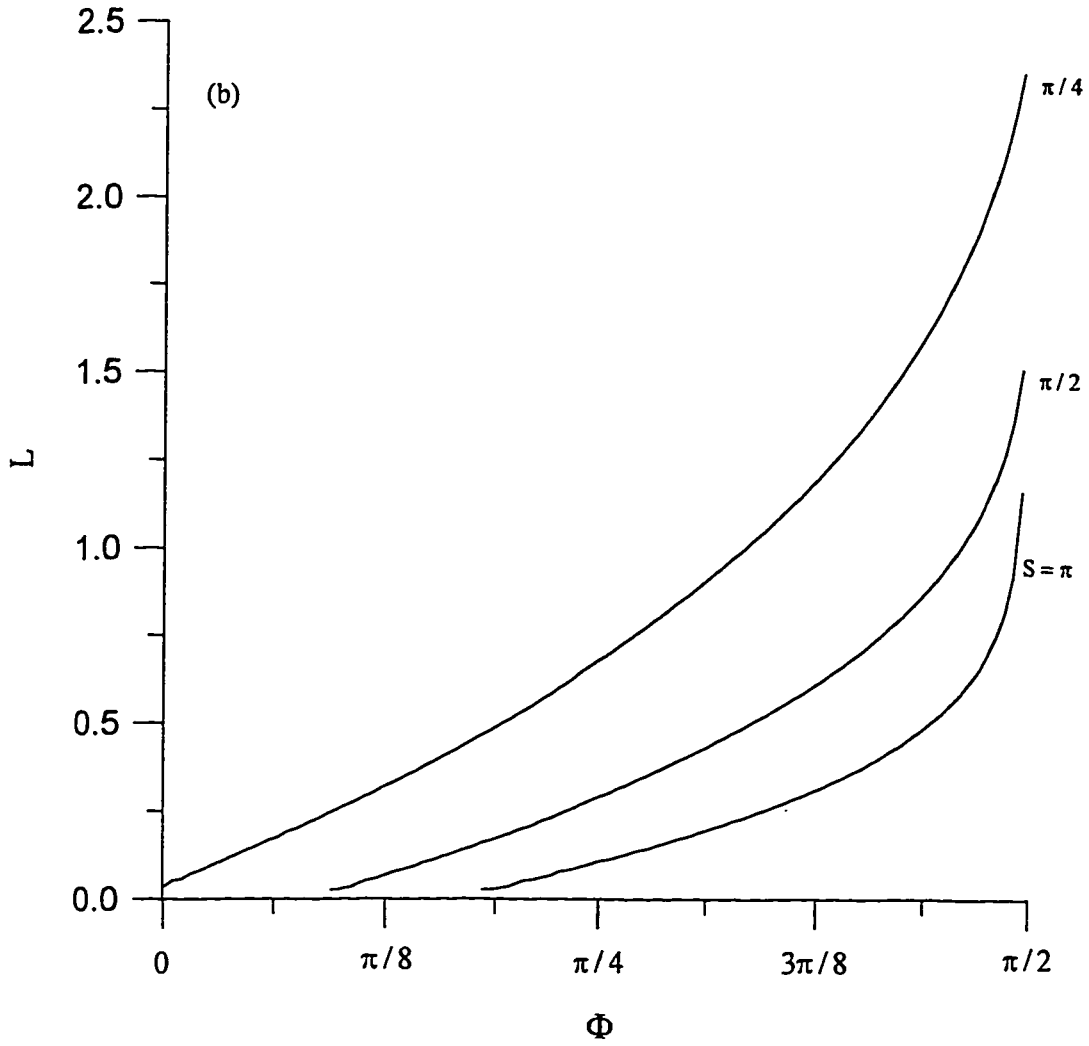

Figure 5.14b

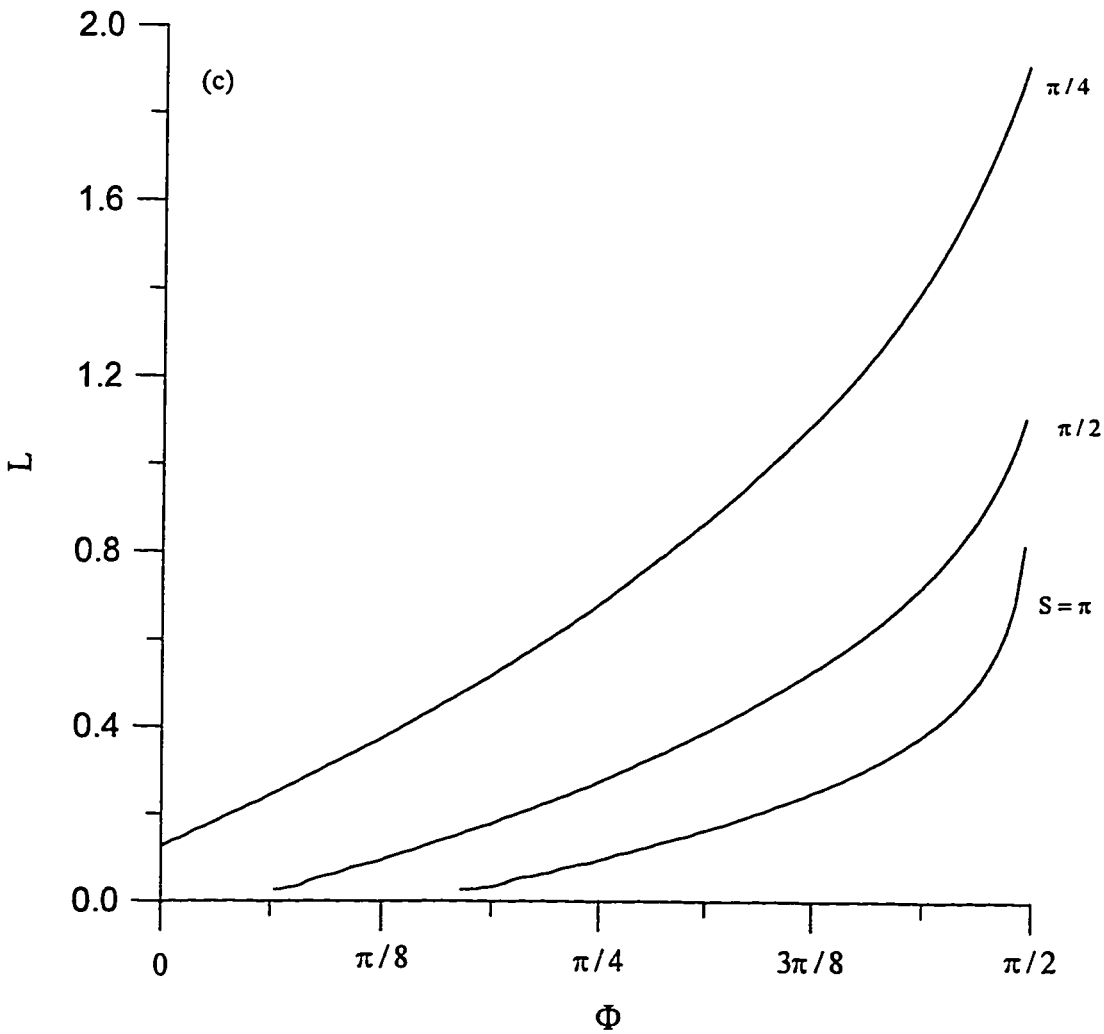

Figure 5.14c

Figure 5.14 The time variation of the wake length for the case S=π/4, (a) Re = 50, (b) Re = 100, (c) Re = 200.

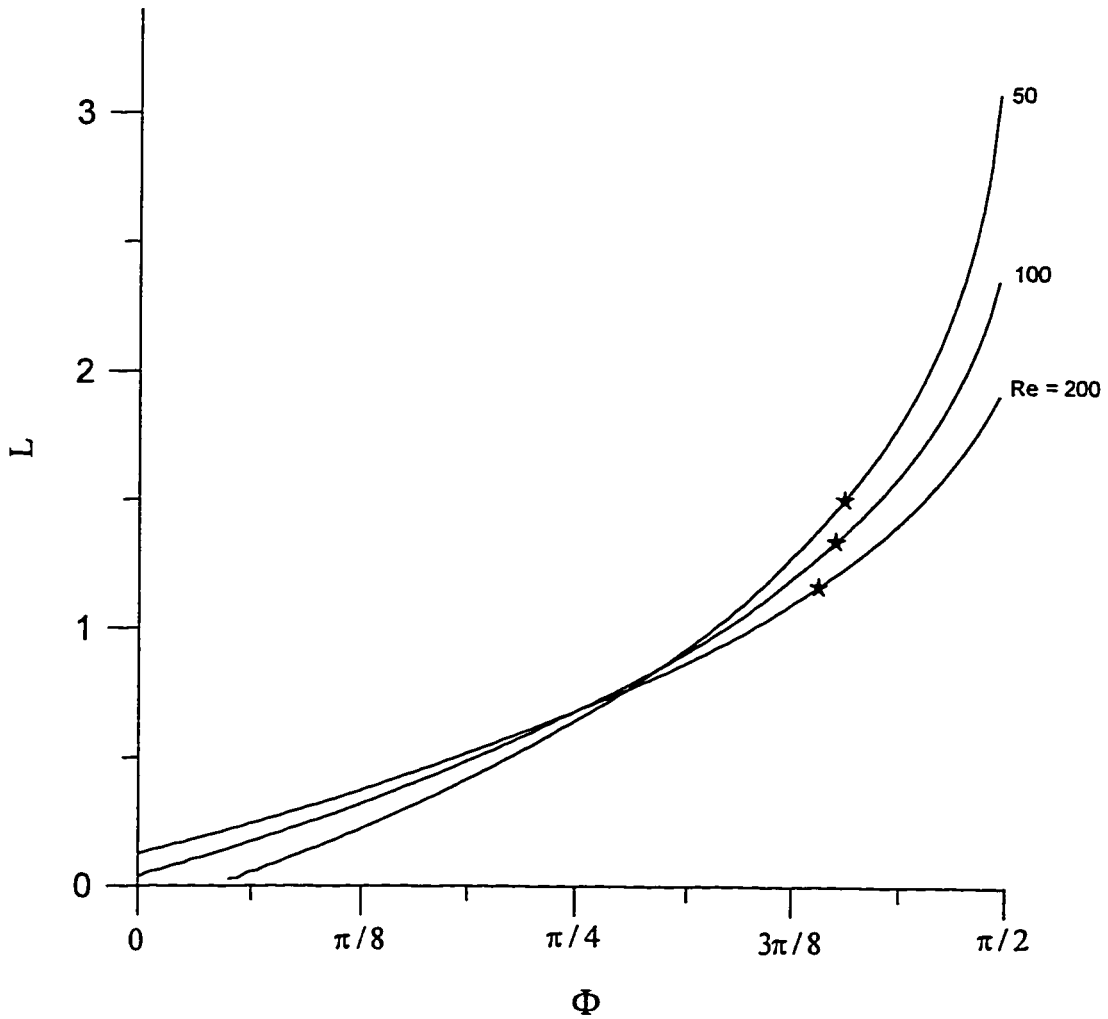

Figure 5.15 The time variation of the wake length for the case S=π/4
The stars indicate where the bubble surrounds the sphere

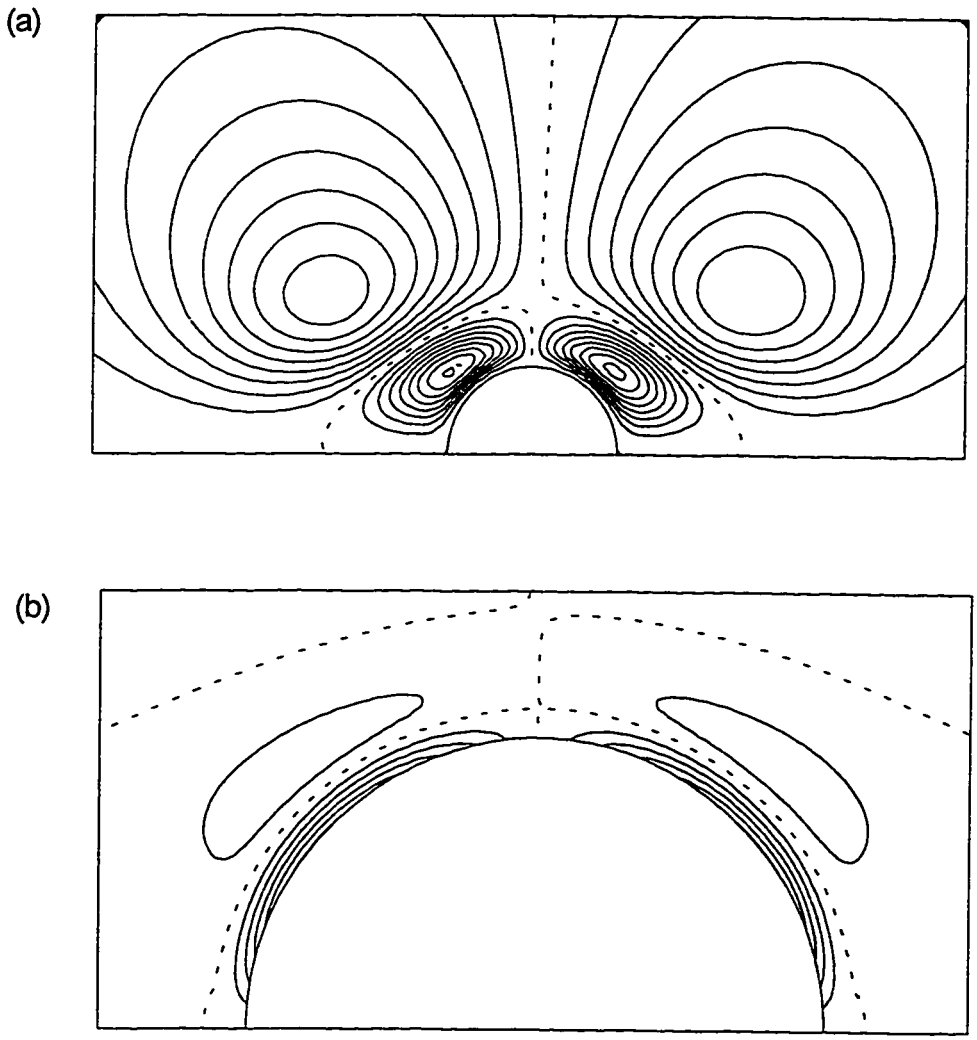

Figure 5.16 Time-averaged patterns over the fourth cycle of oscillation for the case Re = 200, S = $\pi/4$, (a) stream function, (b) vorticity.

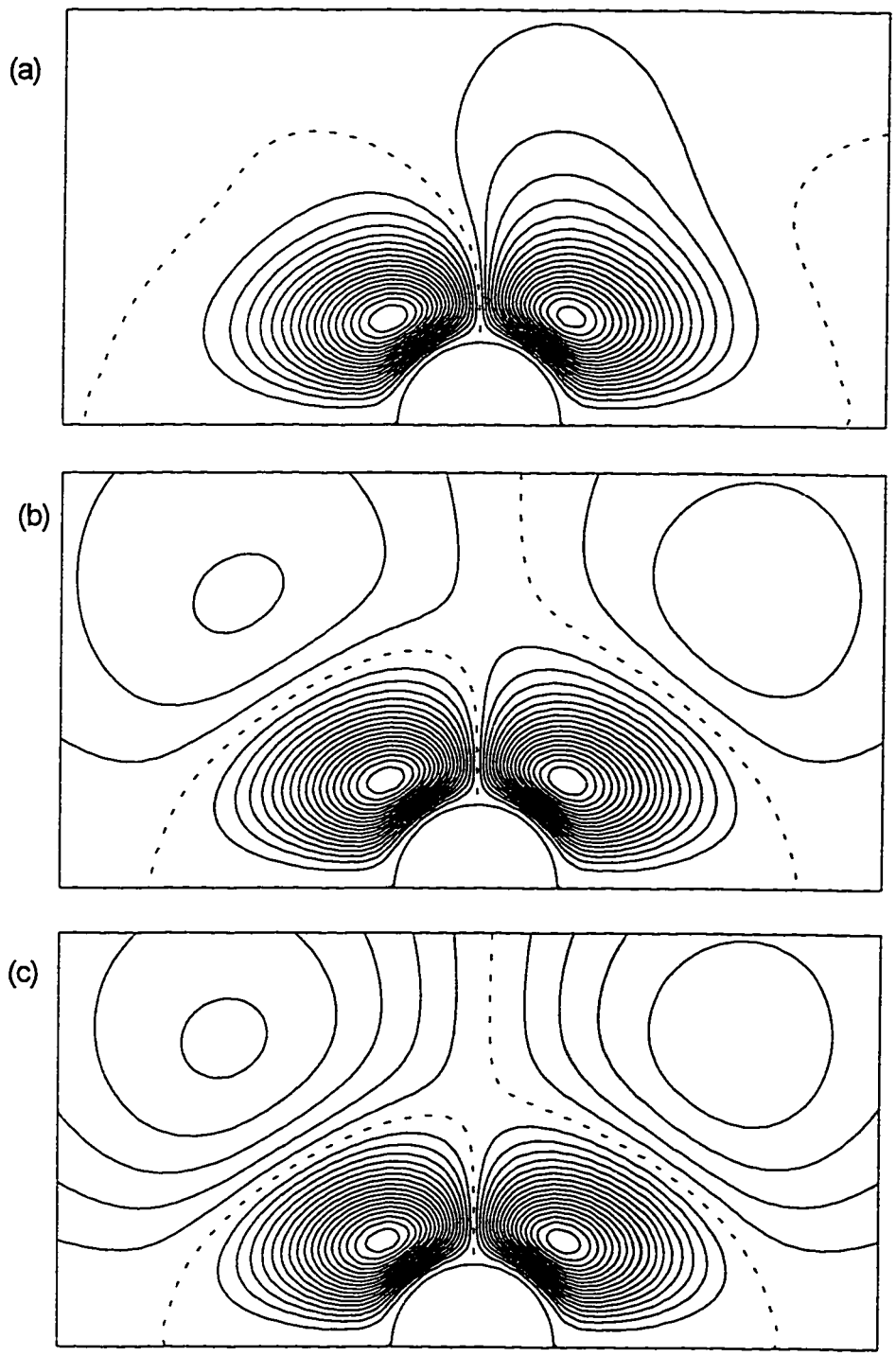

Figure 5.17 The time development of averged stream function for the case $Re = 50$, $S = \pi/4$,
(a) second cycle, (b) fourth cycle, (c) sixth cycle

5.4 Fluctuating Flow

The time variation of C_D for Re = 5, 10, 20, 40, and 100 when $S = \pi/4$, and γ = 0.5 is shown in figure 5.18. The corresponding potential flow solution is also plotted. The later takes the form:

$$C_D = -2\,\gamma\,S\sin(St) \qquad (5.52)$$

It is clear that as Re increases, the viscous drag is closer to the potential flow solution. A negative force is possible for higher Reynolds numbers due to the large recirculation region which also contributes to the large deviation of the pressure distribution from its potential values. Similar to the case of purely oscillating free stream, it can be observed that the viscous drag exhibits a phase lead over the free stream velocity profile. This phase lead is higher at higher Reynolds numbers. The potential flow drag leads the free stream velocity profile by a phase angle Φ ($\Phi = St$) of $\pi/2$. This phase lead is exhibited by both C_{DP} and C_{DF} shown in figures 5.19 and 5.20. The drag coefficient for S = $\pi/4, \pi/2, \pi$ when Re = 40 and γ = 0.5 is presented in figure 5.21. To make it possible to compare different Strouhal numbers, the phase angle Φ has been used for the abscissa. It can be observed that at higher Strouhal numbers, the drag coefficient phase lead over the free stream velocity increases. Finally, the effect of γ on C_D is shown in figure 5.22. The figure presents results for γ = 0.0, 0.1, 0.25, and 0.5 when Re = 100 and $S = \pi/4$. As γ is reduced, the amplitude of the drag coefficient is reduced until reaching that of the uniform flow (γ = 0.0). As γ increases, the phase lead over the free stream velocity profile also increases.

The time variation of the surface vorticity distribution during one complete cycle (the forth cycle) for the case Re = 40, $S = \pi/4$, and γ = 0.5 is shown in figure 5.23. The corresponding pressure distribution is shown in figure 5.24. At peak free stream velocity (t = 24, 32), the surface vorticity crosses the abscissa which indicates that separation has

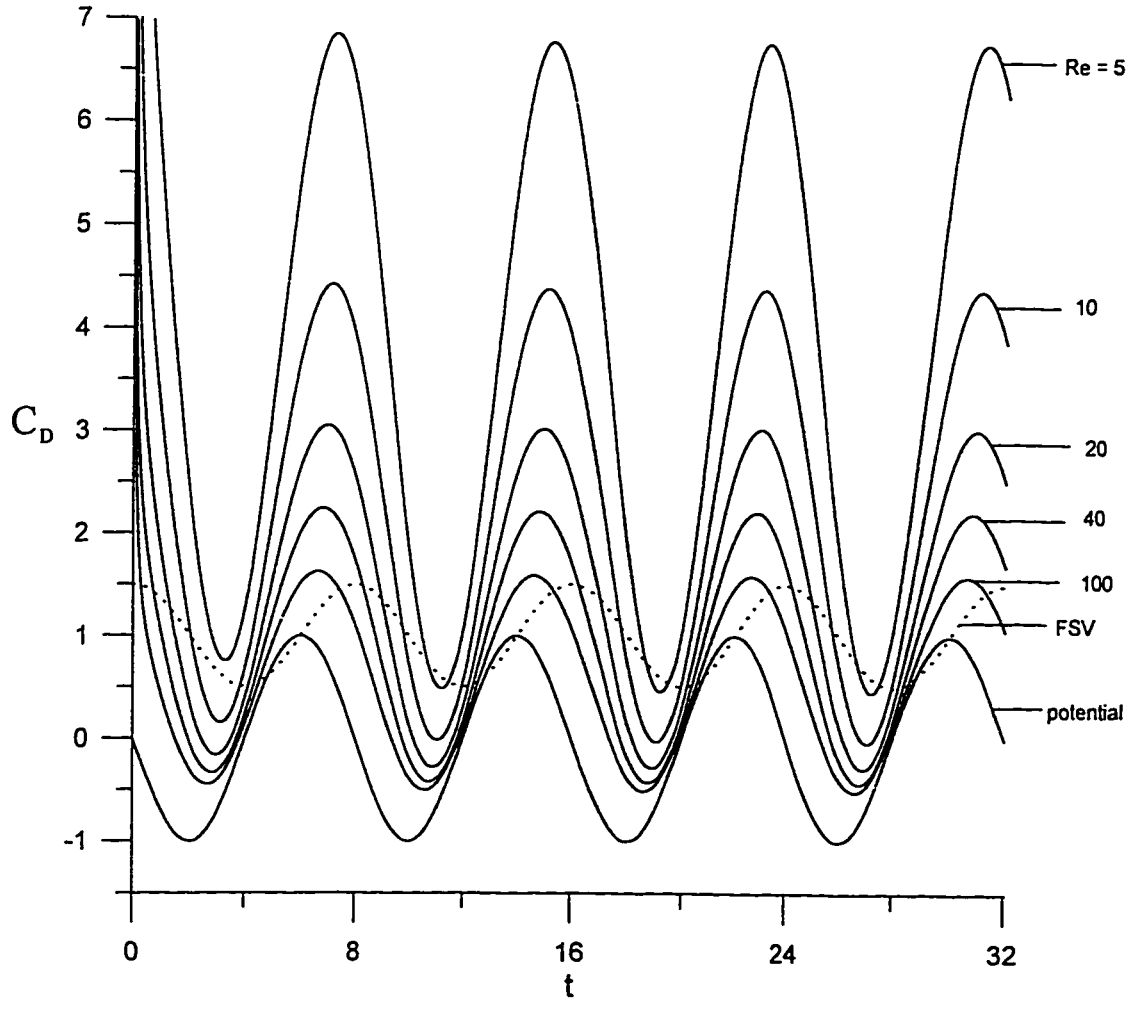

Figure 5.18 The time variation of C_D for the case of $S = \pi/4, \gamma = 0.5$
(FSV = Free-Stream Velocity)

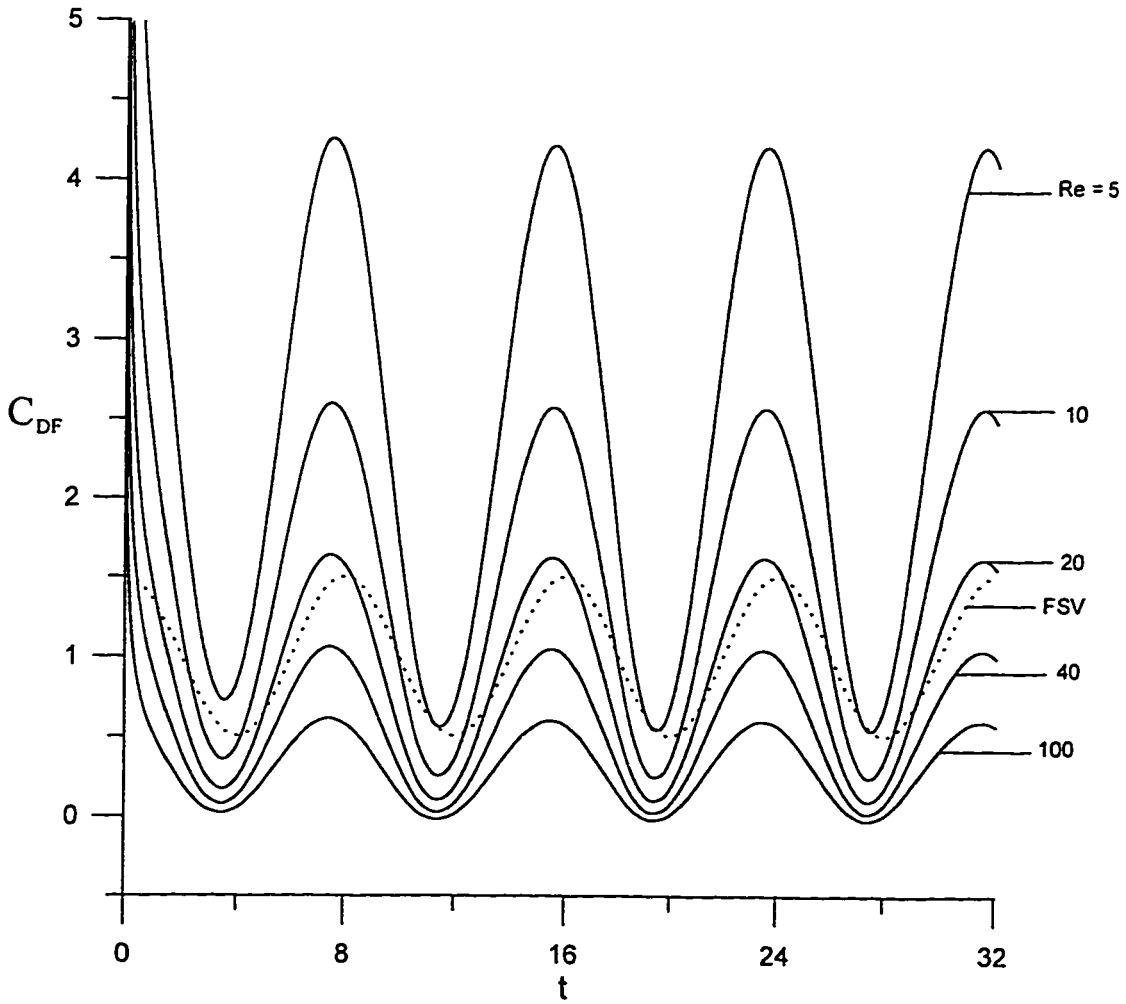

Figure 5.19 The time variation of C_{DF} for the case of $S = \pi/4$, $\gamma = 0.5$ (FSV = Free-Stream Velocity)

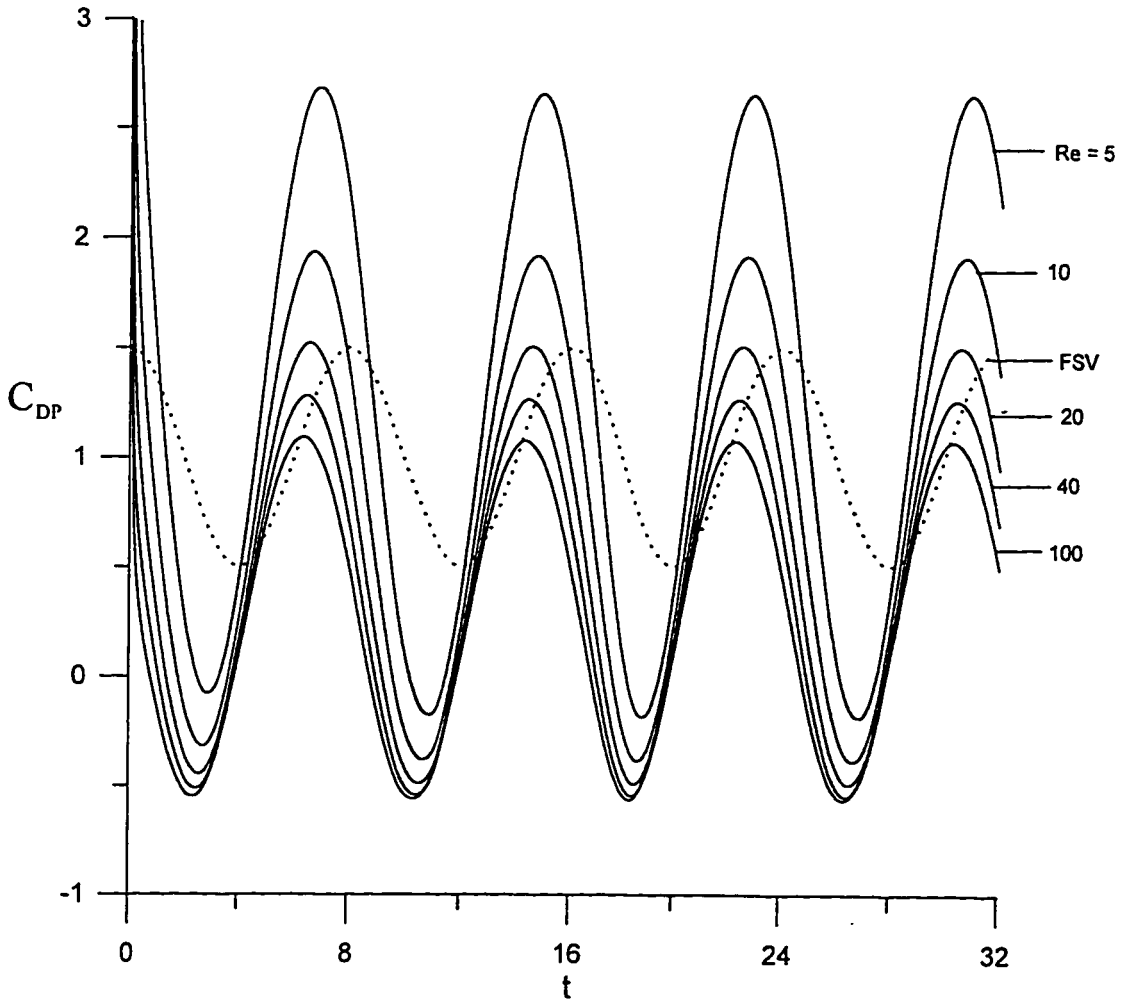

Figure 5.20 The time variation of C_{DP} for the case of $S = \pi/4$, $\gamma = 0.5$ (FSV = Free-Stream Velocity)

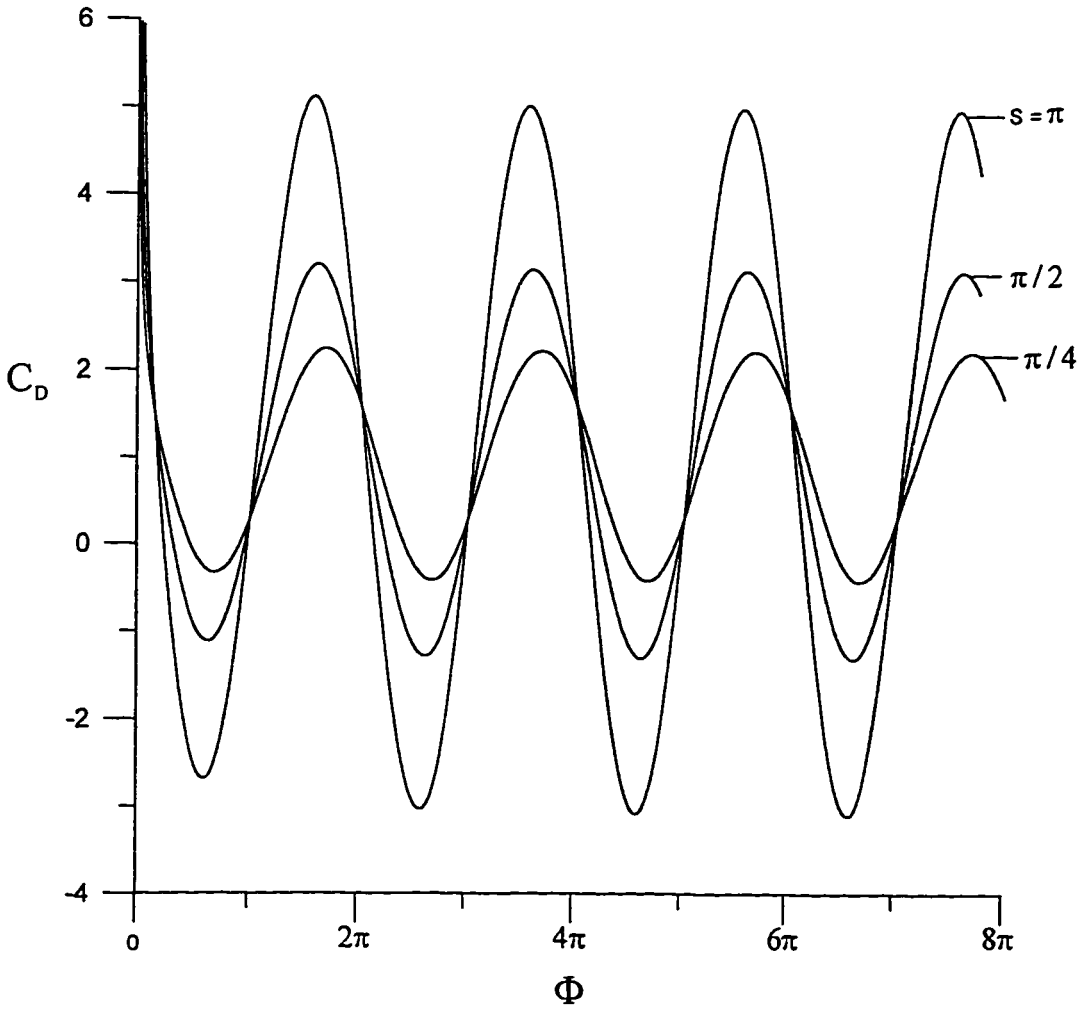

Figure 5.21 The time variation of C_D for the case of $Re = 40, \gamma = 0.5$

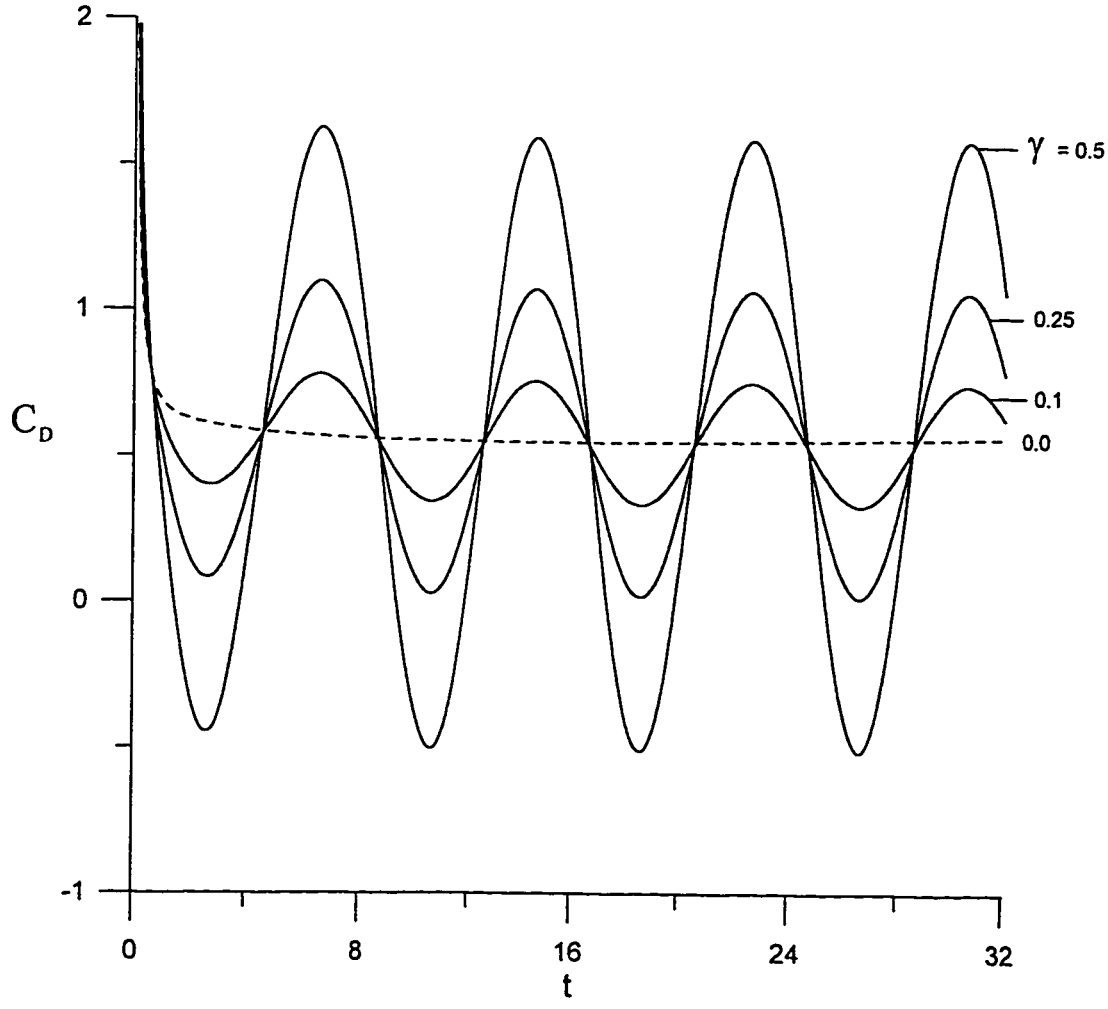

Figure 5.22 The time variation of C_D for the case of $S = \pi/4$, $Re = 100$

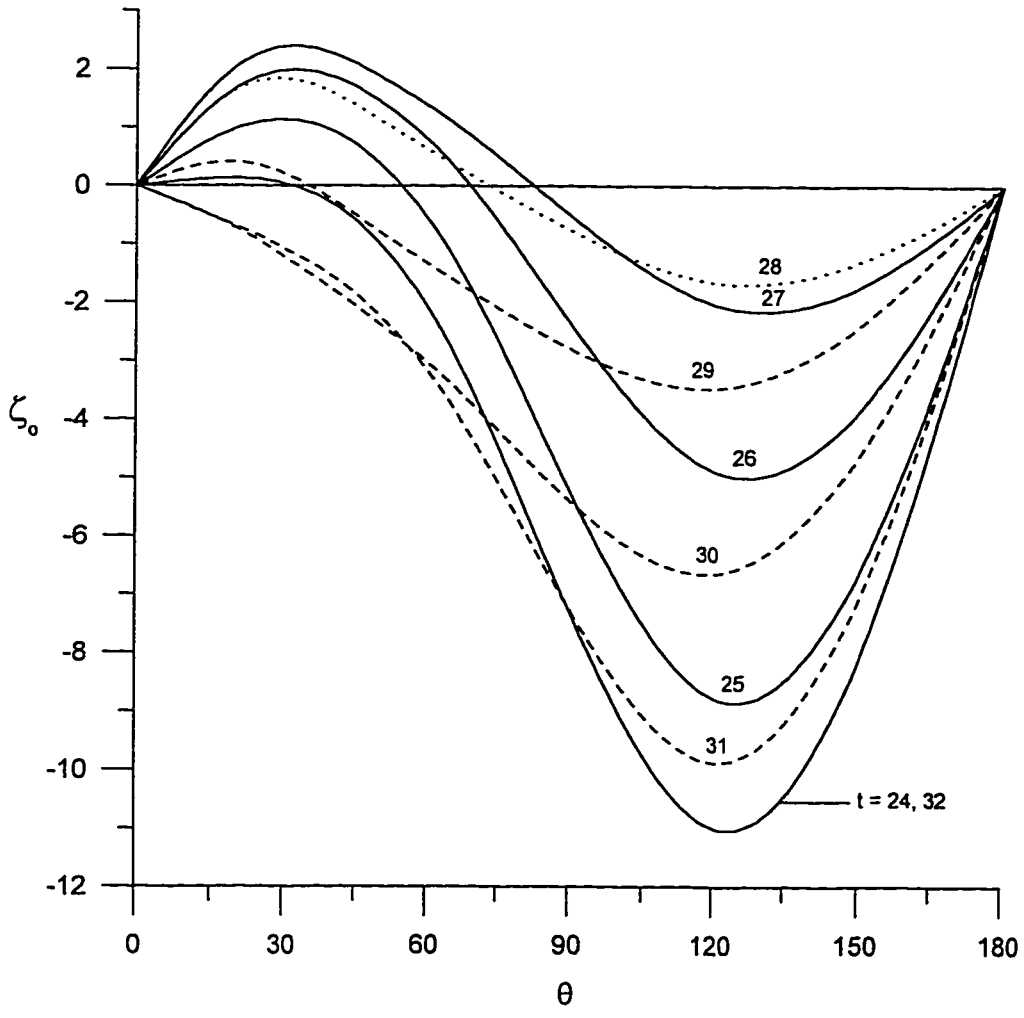

Figure 5.23 The time variation of surface vorticity for the case Re = 40, $S = \pi/4$, $\gamma = 0.25$

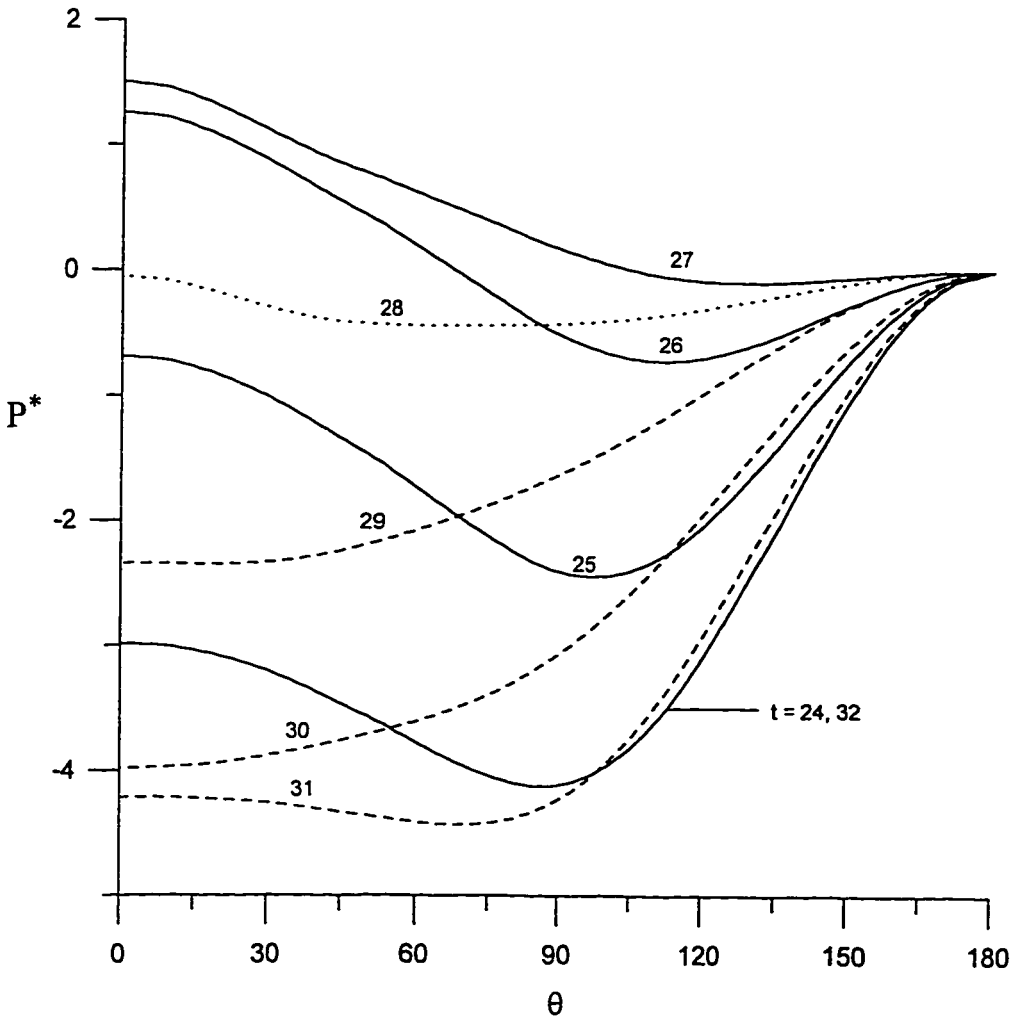

Figure 5.24 The time variation of P^* for the case of Re = 40, $S = \pi/4$, $\gamma = 0.5$

already occurred during the acceleration part of the previous cycle. This behavior is only observed for higher Reynolds numbers and lower Strouhal numbers. As time progresses, this recirculating region grows due to the deceleration effects and the point of separation travels upstream until the free stream velocity becomes minimum at which the separated region starts shrinking. The curves for t = 30, and 31 show no region of separation. The pressure distribution shown in figure 5.24 indicates that an adverse pressure gradient is possible (the curves at t = 26, and 27) due to the deceleration effects. Figure 5.25 shows the surface vorticity distributions for the case of Re = 100, S = $\pi/4$, and γ = 0.1 while figure 5.26 shows the surface vorticity for the same case when γ = 0.5. An interesting feature of figure 5.25 is that the recirculating region does not disappear during the whole cycle. Figure 5.26, on the other hand, indicates that the recirculation region disappears due to the large amplitude of fluctuations

The time development of the streamline patterns over one complete cycle for the case Re = 40, S = $\pi/4$, and γ = 0.5 is shown in figure 5.27. At t = 24.0, a separated region has already occurred during the accelerating period of the previous cycle. As time progresses, this region grows and travels upstream towards the front stagnation point at $\theta = \pi$. In cases of lower Reynolds numbers, the bubble completely surrounds the sphere. This was evident in the case of Re = 5. The wake length keeps increasing until the velocity of the free stream becomes minimum. In fact, the wake length peaks before the free stream velocity drops to its minimum value. The recirculating region, then, shrinks as the free stream starts accelerating. At this point, two cases are possible. The first is as shown in figure 5.27 where the recirculation region detaches and the vortex is shed away. The other possible case is when the recirculating region disappears before it can detach from the sphere surface. The later case was evident in low Reynolds number flows. As the flow accelerates, the streamlines becomes parallel until another recirculation region is formed during the same cycle or during the decelerating period of the following cycle. The corresponding vorticity contours are plotted in figure 5.28. At the start of the cycle at

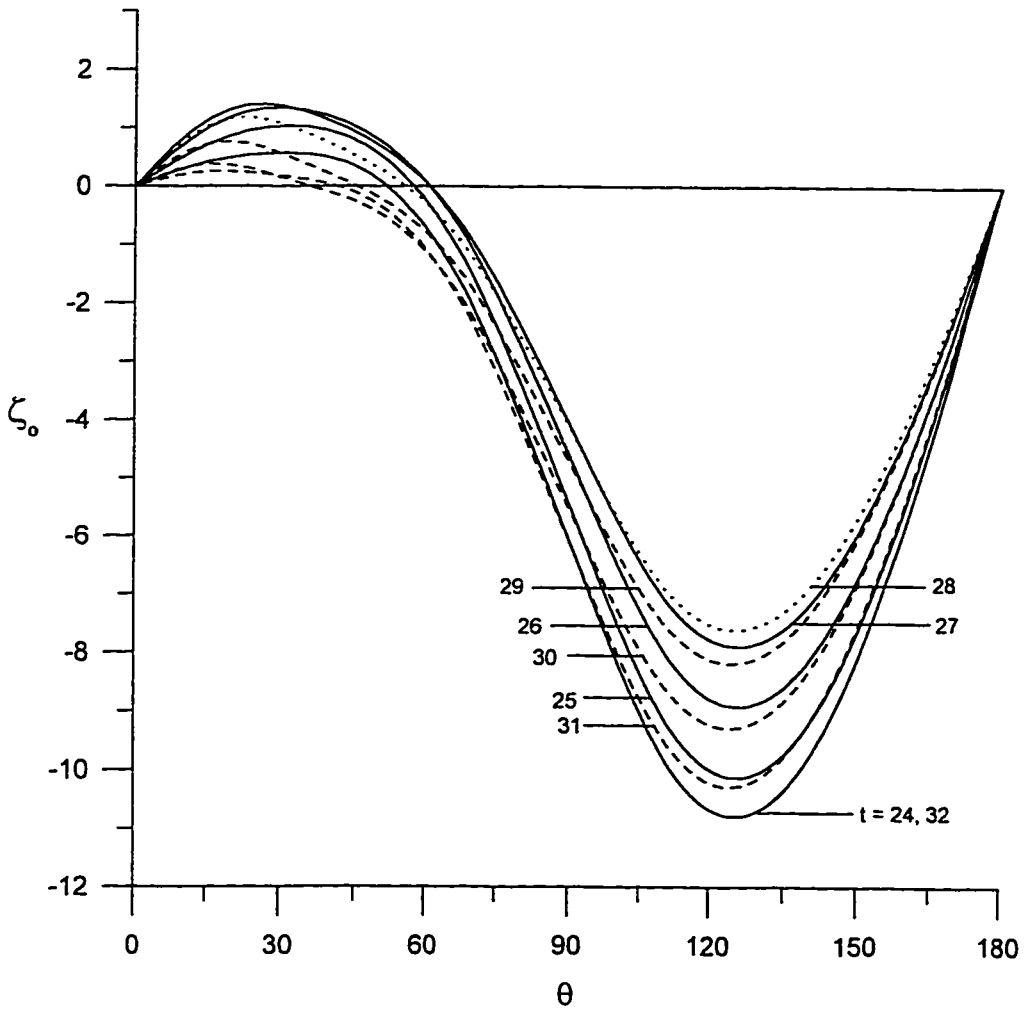

Figure 5.25 The time variation of surface vorticity for the case Re = 100, $S = \pi/4, \gamma = 0.1$

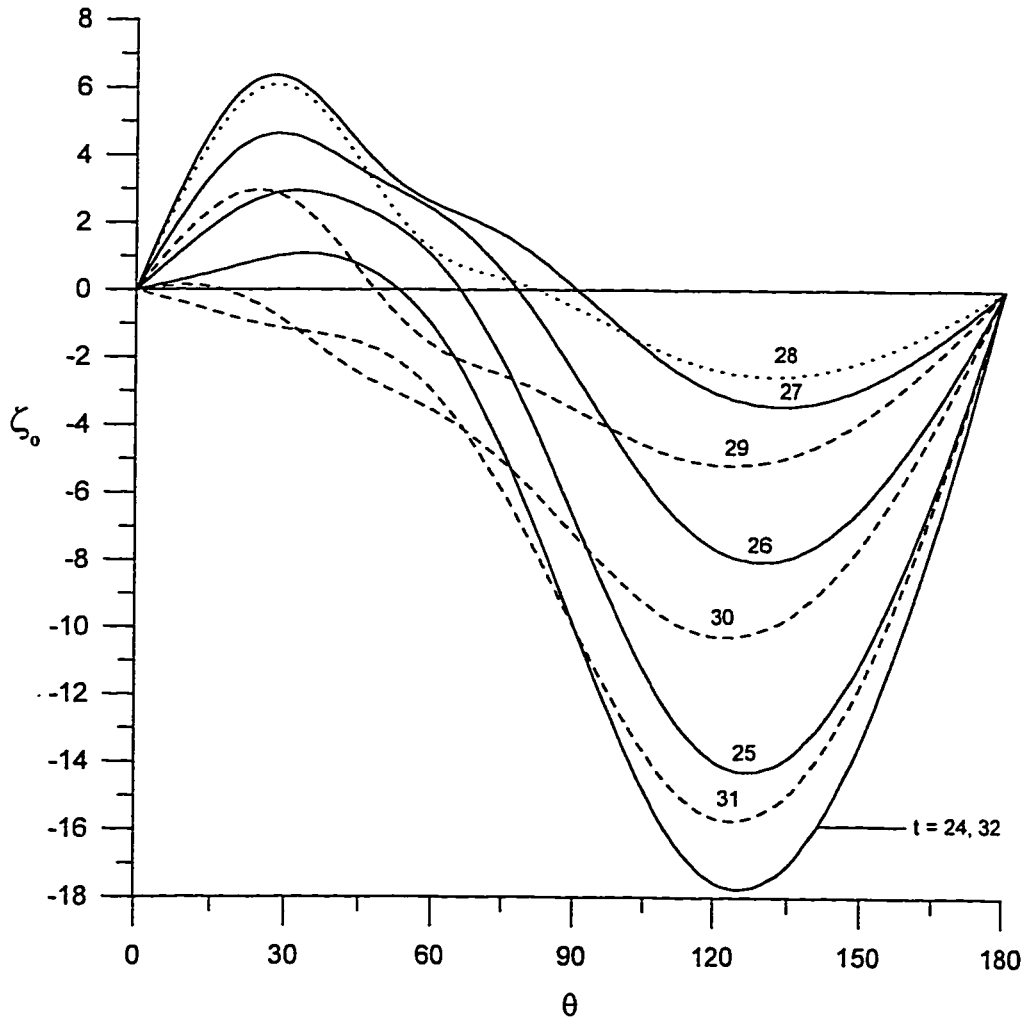

Figure 5.26 The time variation of surface vorticity for the case Re = 100, $S = \pi/4$, $\gamma = 0.5$

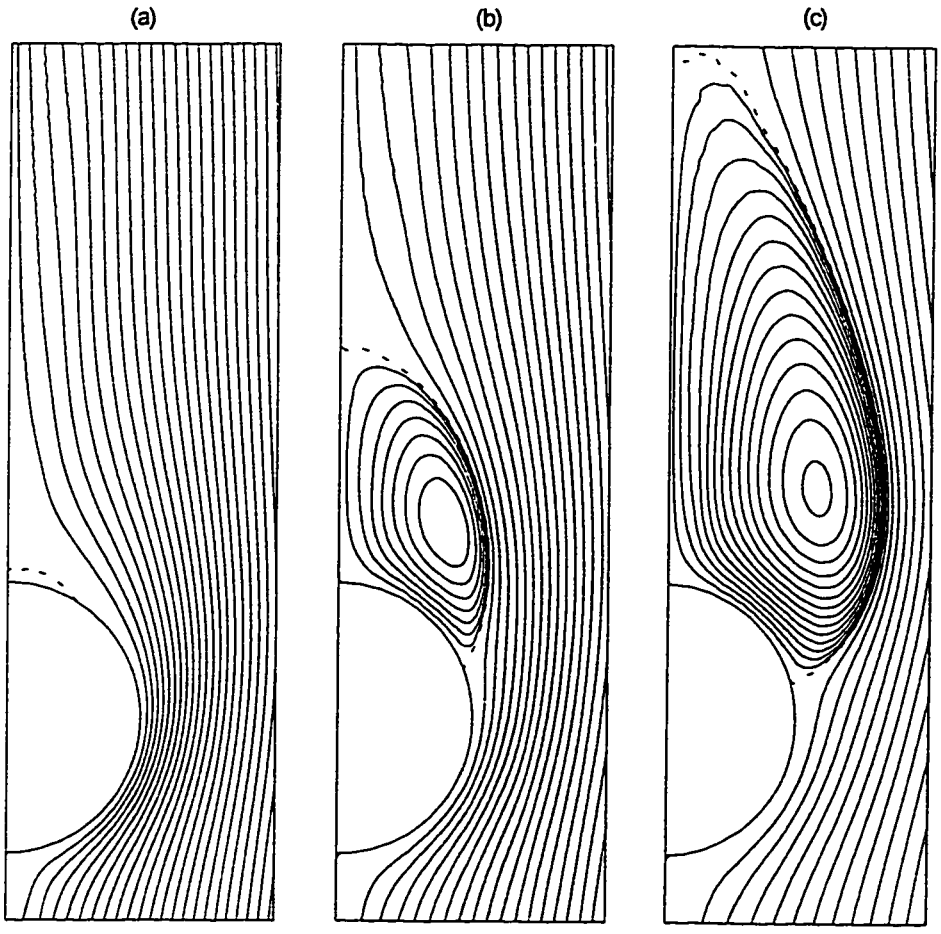

Figure 5.27 (a,b,c)

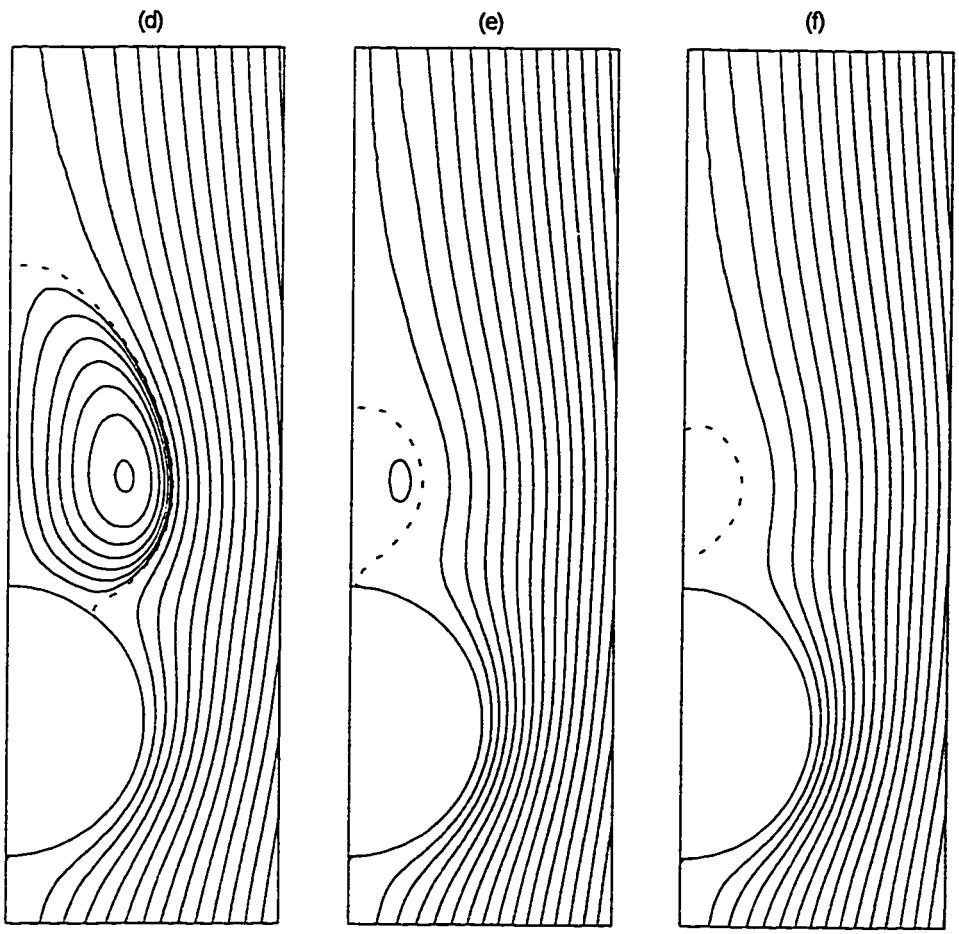

Figure 5.27 (d,e,f)

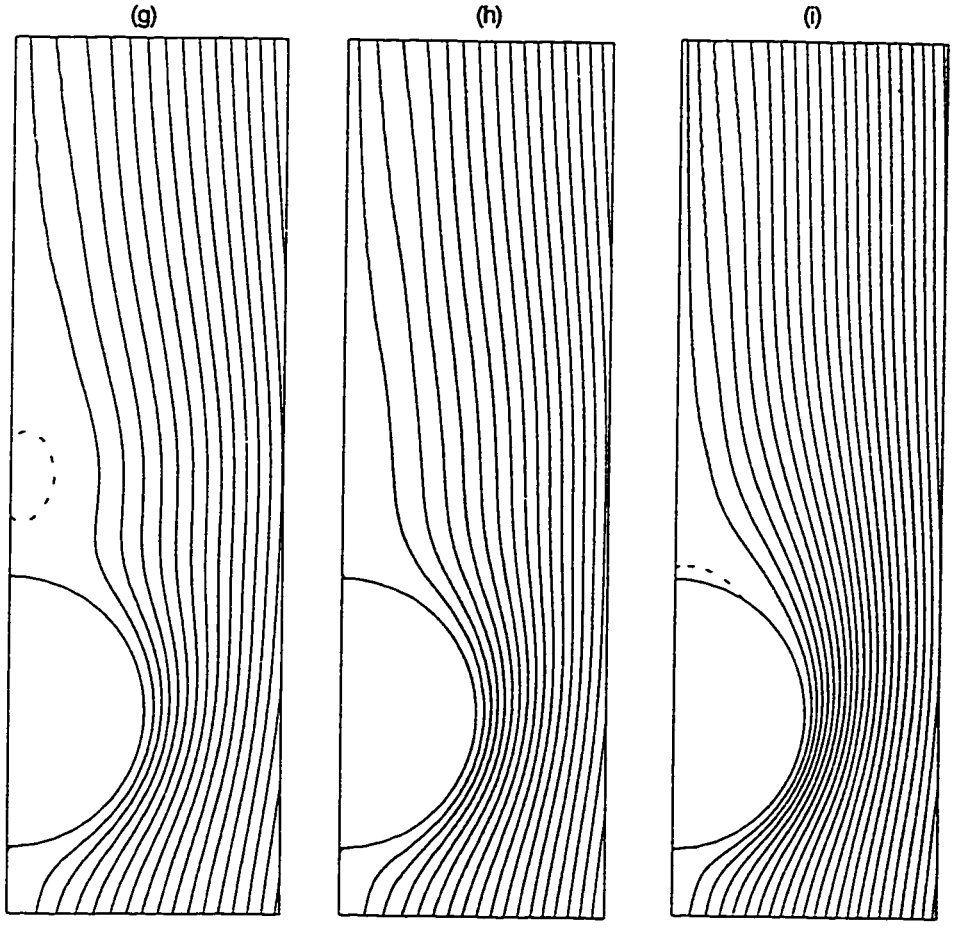

Figure 5.27 (g,h,i)

Figure 5.27 Time development of streamline patterns for the case of Re = 40, S = $\pi/4$, γ = 0.5.
(a) t = 24.0, (b) t = 26.0, (c) t = 28.0, (d) t = 29.0
(e) t = 29.5, (f) t = 29.54, (g) t = 29.58
(h) t = 30.0, (i) t = 32.0

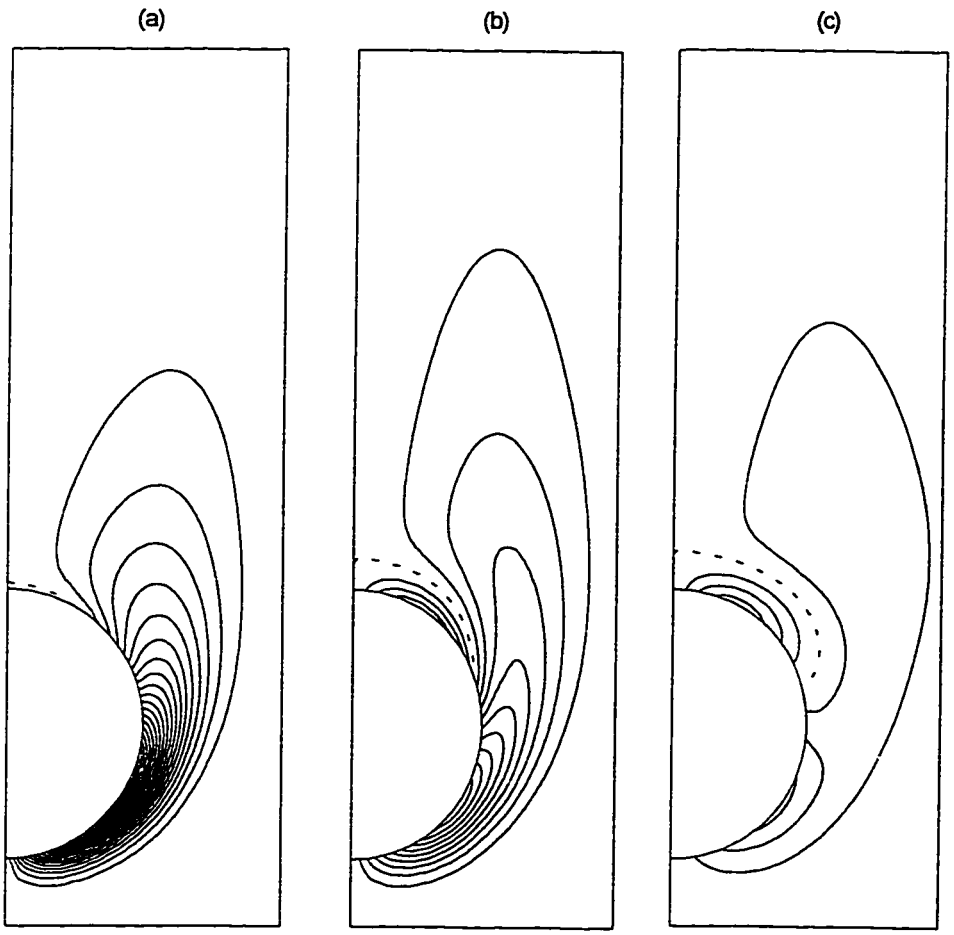

Figure 5.28 (a,b,c)

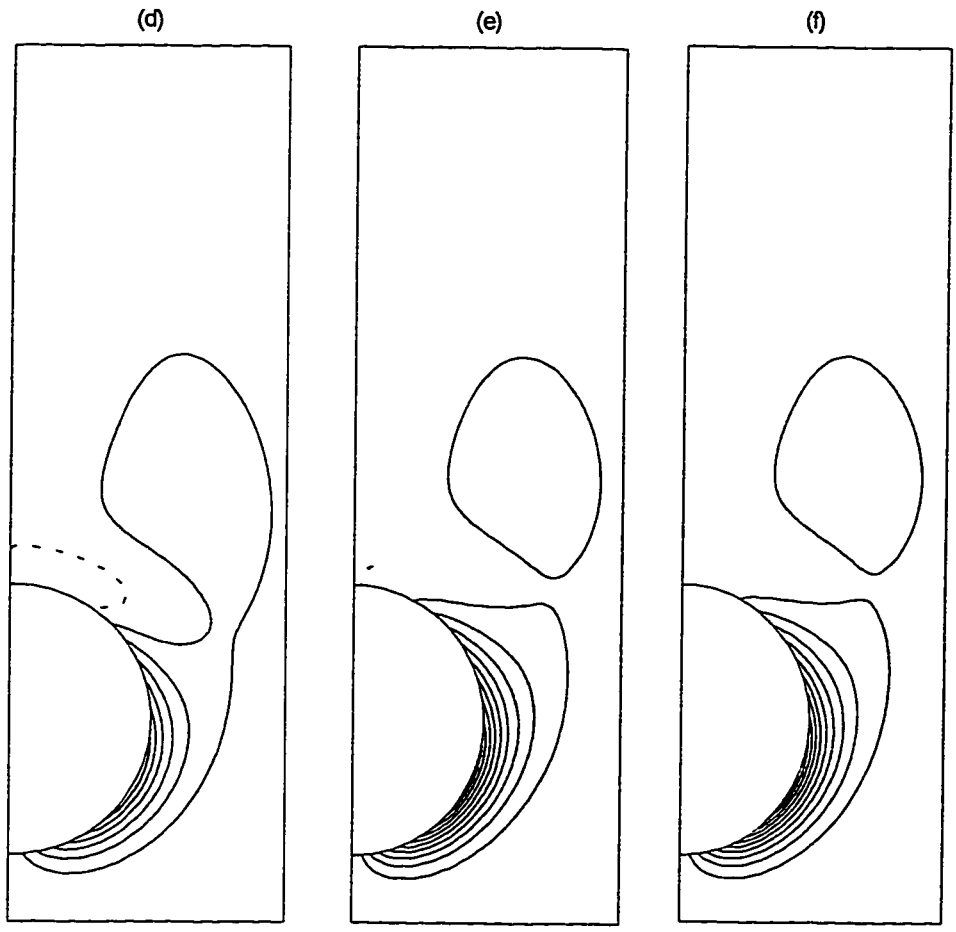

Figure 5.28 (d,e,f)

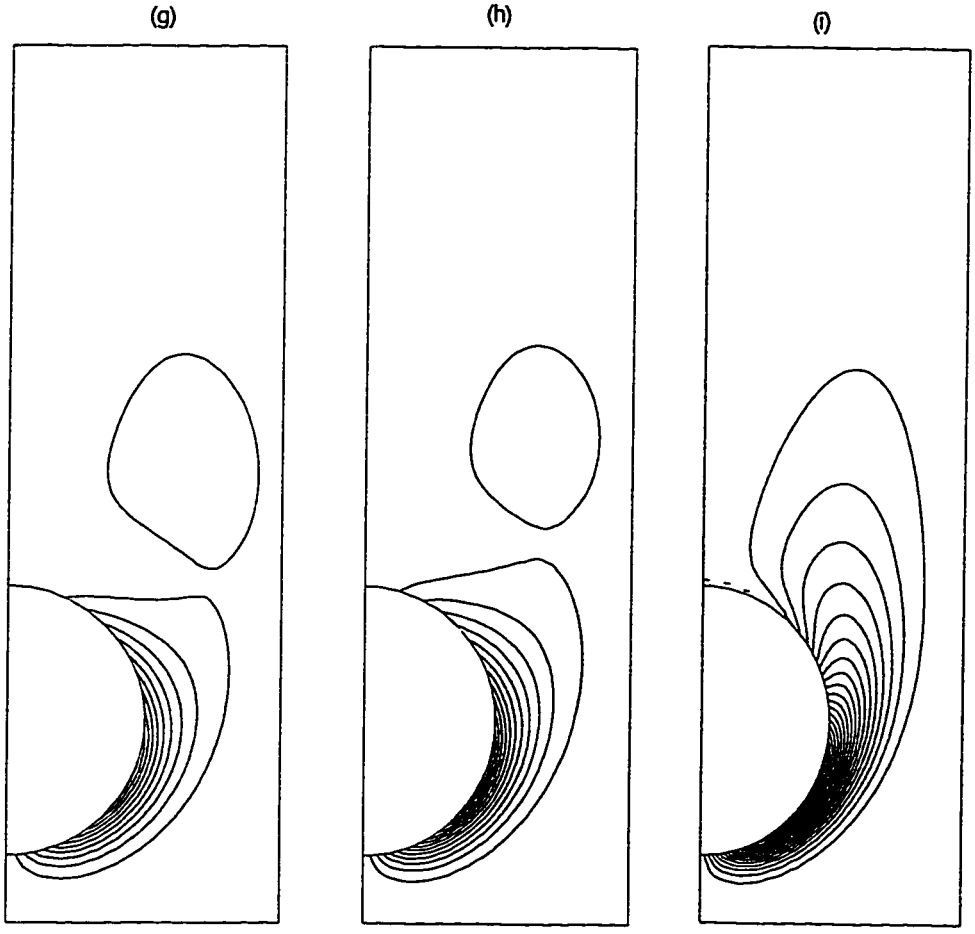

Figure 5.28 (g,h,i)

Figure 5.28 Time development of equi-vorticity patterns for the case of Re = 40, S = $\pi/4$, γ = 0.5.
(a) t = 24.0, (b) t = 26.0, (c) t = 28.0, (d) t = 29.0
(e) t = 29.5, (f) t = 29.54, (g) t = 29.58
(h) t = 30.0, (i) t = 32.0

t = 24.0, a region of negative vorticity that is confined to the surface of the sphere dominates with a small region of positive vorticity growing next to the back stagnation point at $\theta=0$. As the free stream decelerates, the negative vorticity diffuses longer into the bulk fluid and the region of positive vorticity grows. This growth of the positive vorticity is prohibited by the acceleration of the free stream velocity during the acceleration part of the cycle. At this point, part of the negative vorticity detaches and diminishes while the positive region shrinks back. The story is repeated in the following cycle.

The length of the recirculation region measured from the sphere surface at the back stagnation point (L) for Re = 5, 10, 20, 40, and 100 when $\gamma = 0.5$ and $S = \pi / 4$ is shown in figure 5.29. As the free stream decelerates, the recirculation region expands until it peaks. The peak takes place before the free stream velocity drops to its minimum value. This region, then, shrinks and at a certain time it detaches from the surface of the sphere. This is indicated by the stars on the figures. For low Reynolds numbers, this region does not detach. Instead, the region disappears completely until the next cycle. It can be observed that vortex shedding is delayed for higher Reynolds numbers. It is also noticed that for higher Reynolds numbers, a recirculation region during the acceleration part of the cycle is possible. Figure 5.30 shows that vortex shedding is expected for higher Strouhal numbers. The figure which shows the wake length for the case of $S = \pi / 4, \pi / 2, \pi, 2\pi,$ and 4π when Re = 10 and $\gamma = 0.5$, indicates that the effect of increasing Strouhal number is to reduce the wake length. The parameter γ has a significant effect on the wake length. Higher amplitude fluctuations have longer wakes. As γ is reduced, the wake length tends to be more uniform. $\gamma = 0.0$ represents the impulsively started uniform velocity profile. Vortex shedding is motivated by increasing γ. Figure 5.31 shows the wake length for $\gamma = 0.0, 0.1, 0.25,$ and 0.5 when Re = 100, and $S = \pi / 4$. Vortex Shedding takes place at earlier phase angles for $\gamma = 0.5$ than for $\gamma = 0.25$. Vortex shedding is not observed for lower values of γ. Table 5.2 lists the flow characteristics for

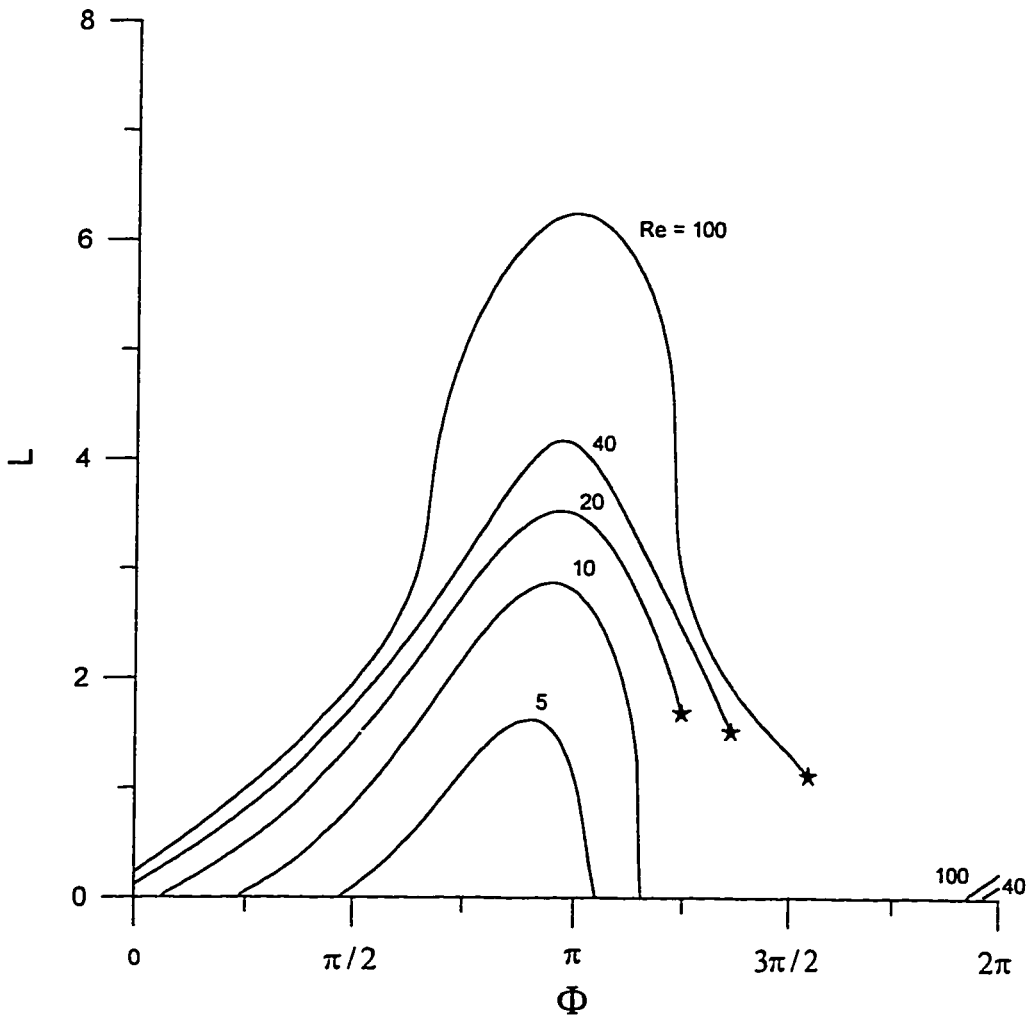

Figure 5.29 The time variation of the wake length for the case of $S = \pi/4$, $\gamma = 0.5$

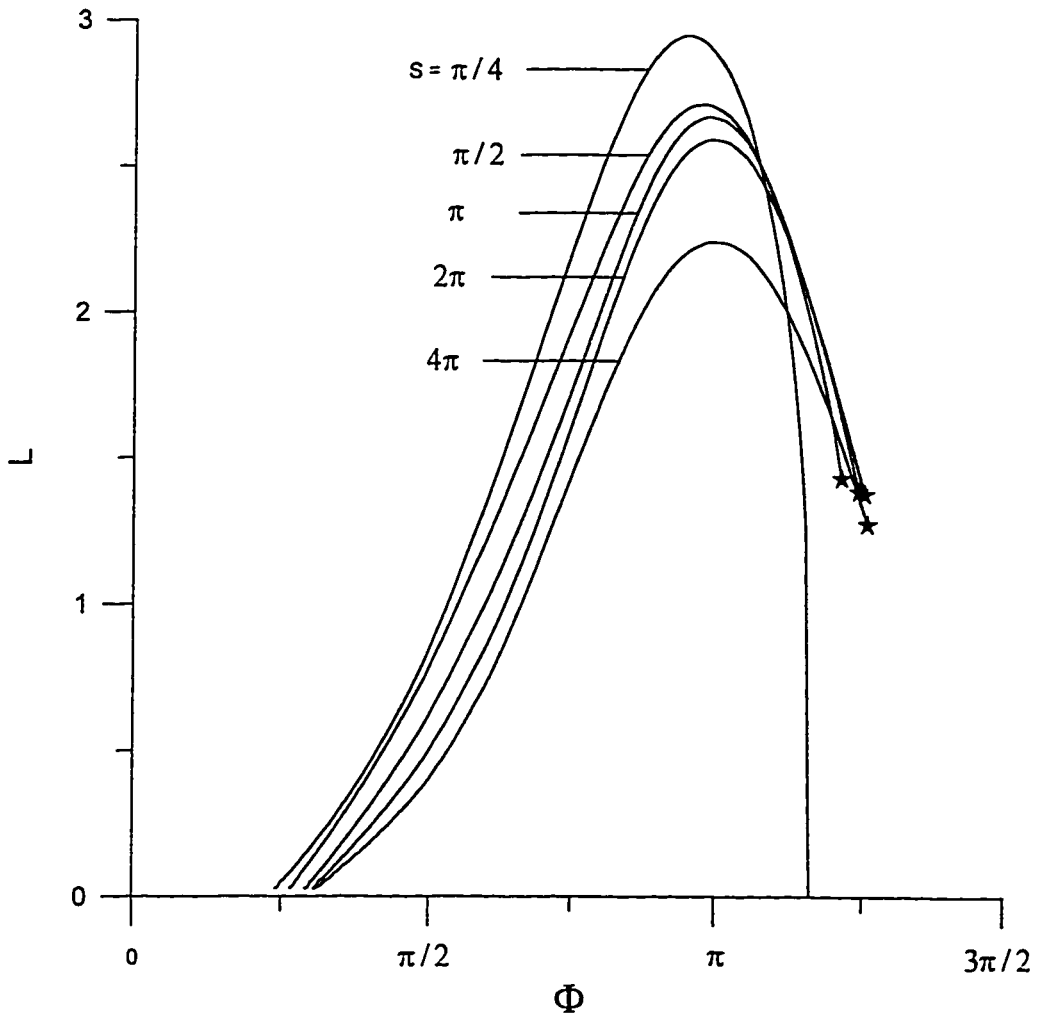

Figure 5.30 The time variation of the wake length for the case of Re = 10, γ = 0.5

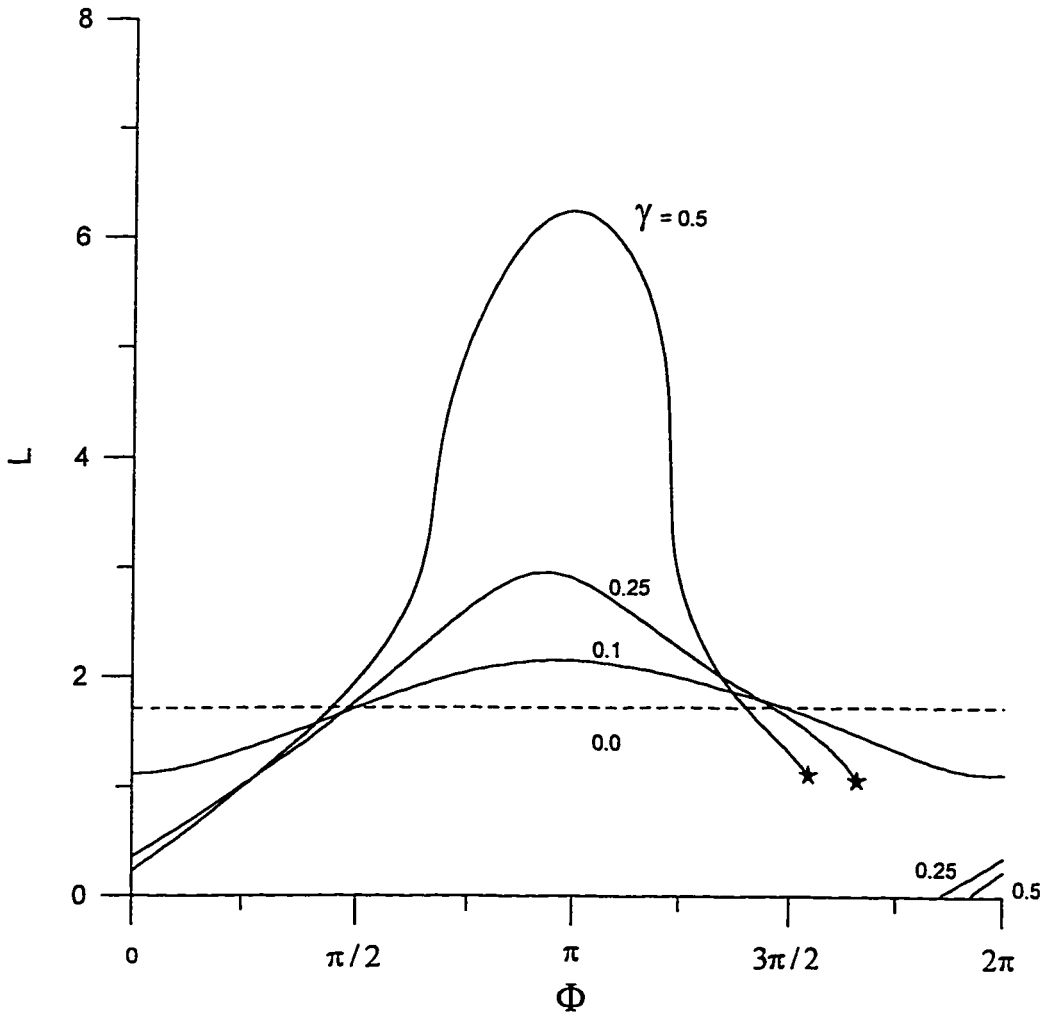

Figure 5.31 The time variation of the wake length for the case of Re = 100, S = π/4

Table 5.2 Flow characteristics for the range of parameters considered in the present study

	$\gamma = 0$	$\gamma = 0.1$			$\gamma = 0.25$			$\gamma = 0.5$		
		$S = \pi/4$	$S = \pi/2$	$S = \pi$	$S = \pi/4$	$S = \pi/2$	$S = \pi$	$S = \pi/4$	$S = \pi/2$	$S = \pi$
Re = 100	S	S	S	S	VS	VS	VS	VS	VS	VS
Re = 40	S	S	S	S	VS	VS	VS	VS	VS	VS
Re = 20	NS	S	S	S	S	VS	VS	VS	VS	VS
Re = 10	NS	NS	NS	S	S	S	S	S	VS	VS
Re = 5	NS	NS	NS	NS	NS	S	S	S	S	VS

S = Separation, NS = No Separation, VS = Vortex Shedding

the range of parameters considered in this study. The table indicates that vortex shedding is motivated by increasing γ, Strouhal number, and Reynolds number. For the case of γ = 0.0, Separation is only possible for Re>20. Separation, however, takes place well below this value by increasing γ or Strouhal number. It is possible for a flow with Re = 5 to exhibit vortex shedding when $S = \pi$, and $\gamma = 0.5$.

As the free stream velocity decelerates, the recirculation region travels upstream towards the front stagnation point. The separation angles (θ_s) measured from the rear stagnation point for Re = 5, 10, 20, 40, and 100 when $\gamma = 0.5$ and $S = \pi/4$ are plotted in figure 5.32. For higher Reynolds numbers, the recirculation region travels longer on the surface of the sphere. The separation angle peaks before the free stream velocity reaches its minimum value. Figure 5.33 shows that higher Strouhal numbers have longer separation angles. The figure which shows the separation angle for the case of Re = 10, γ = 0.5, and $S = \pi/4, \pi/2, \pi, 2\pi,$ and 4π indicates that as S increases, the bubble may encompass the whole sphere. Figure 5.34 presents the separation angles for different γ when Re = 100, and $S = \pi/4$. While the curves for $\gamma = 0.5$, and 0.25 drop to zero when vortex is shed, that of $\gamma = 0.1$ exhibits maximum and minimum separation angles which indicates that the recirculation region does not disappear. As γ tends to zero, the separation region is constant over the whole cycle.

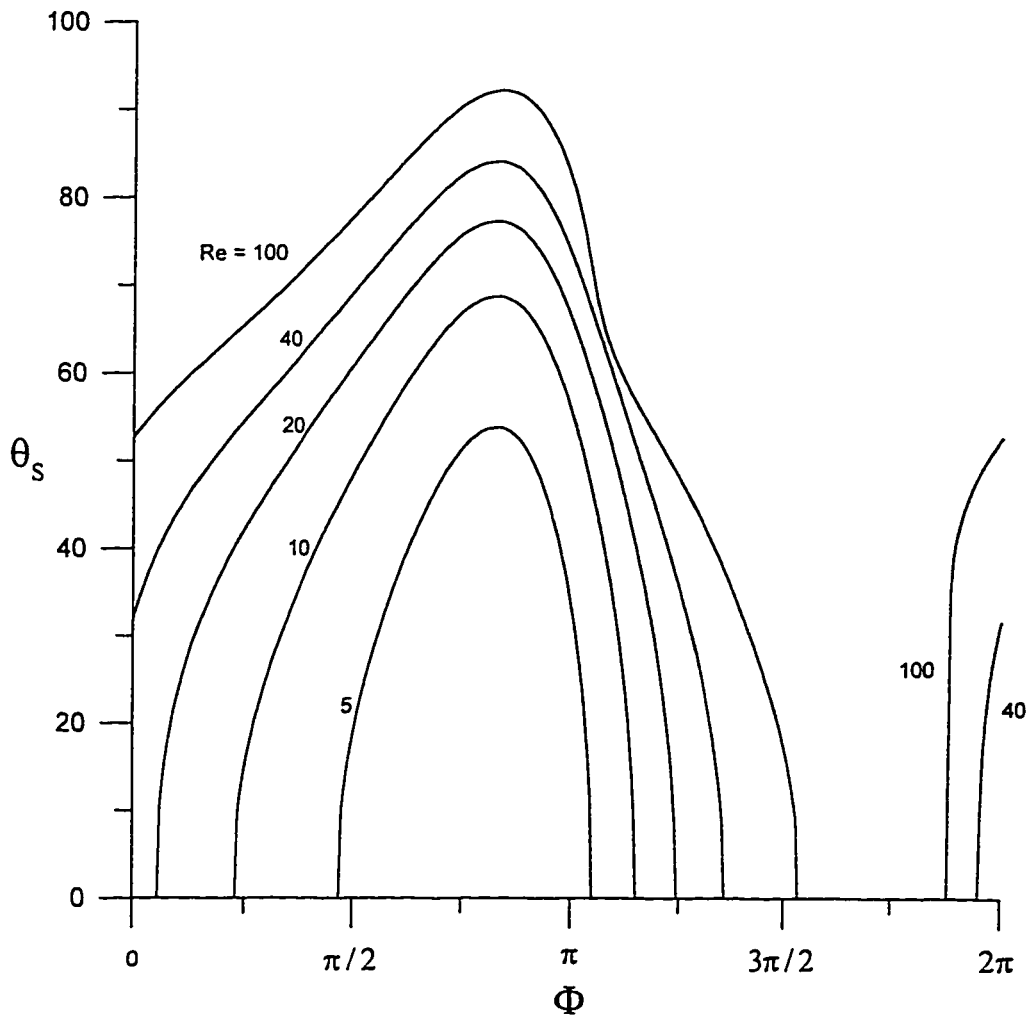

Figure 5.32 The time variation of the sparation angle for the case of $S = \pi/4, \gamma = 0.5$

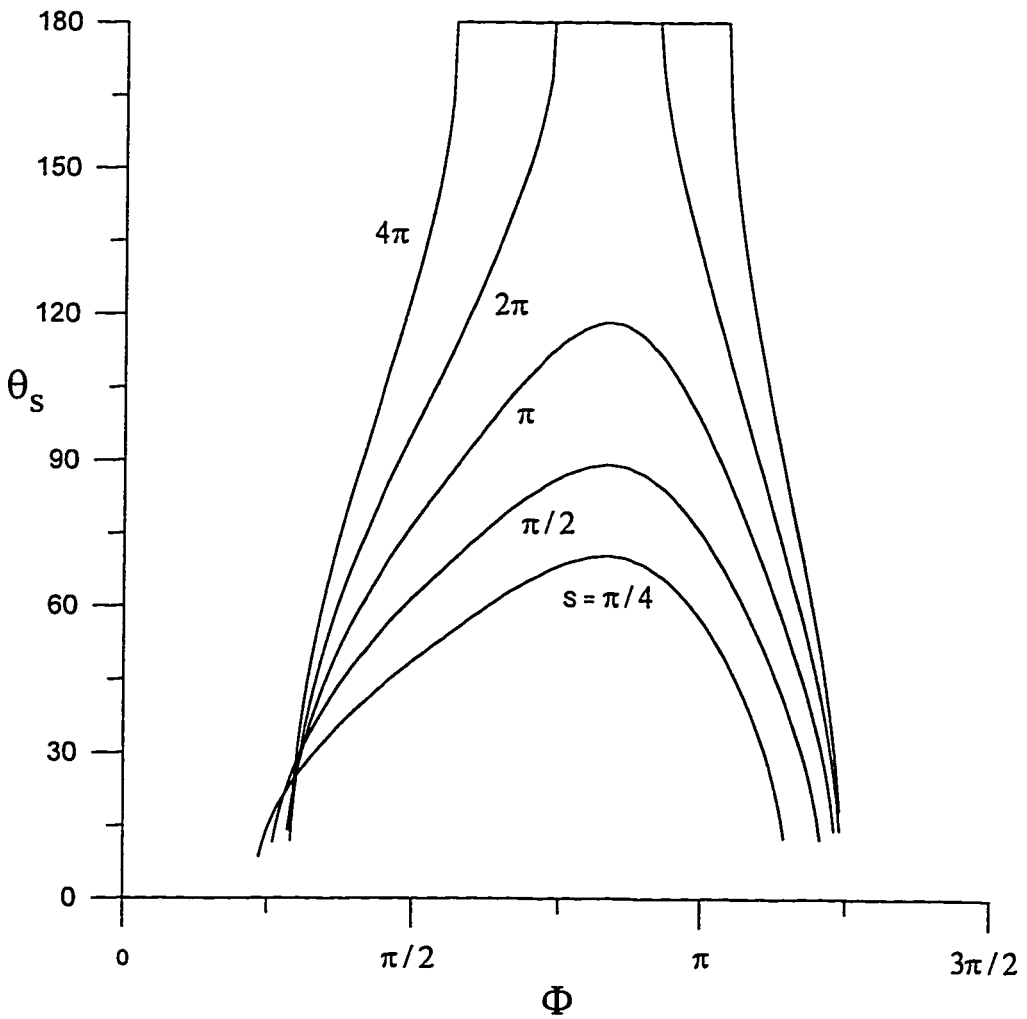

Figure 5.33 The time variation of the separation angle for the case of Re = 10, γ = 0.5

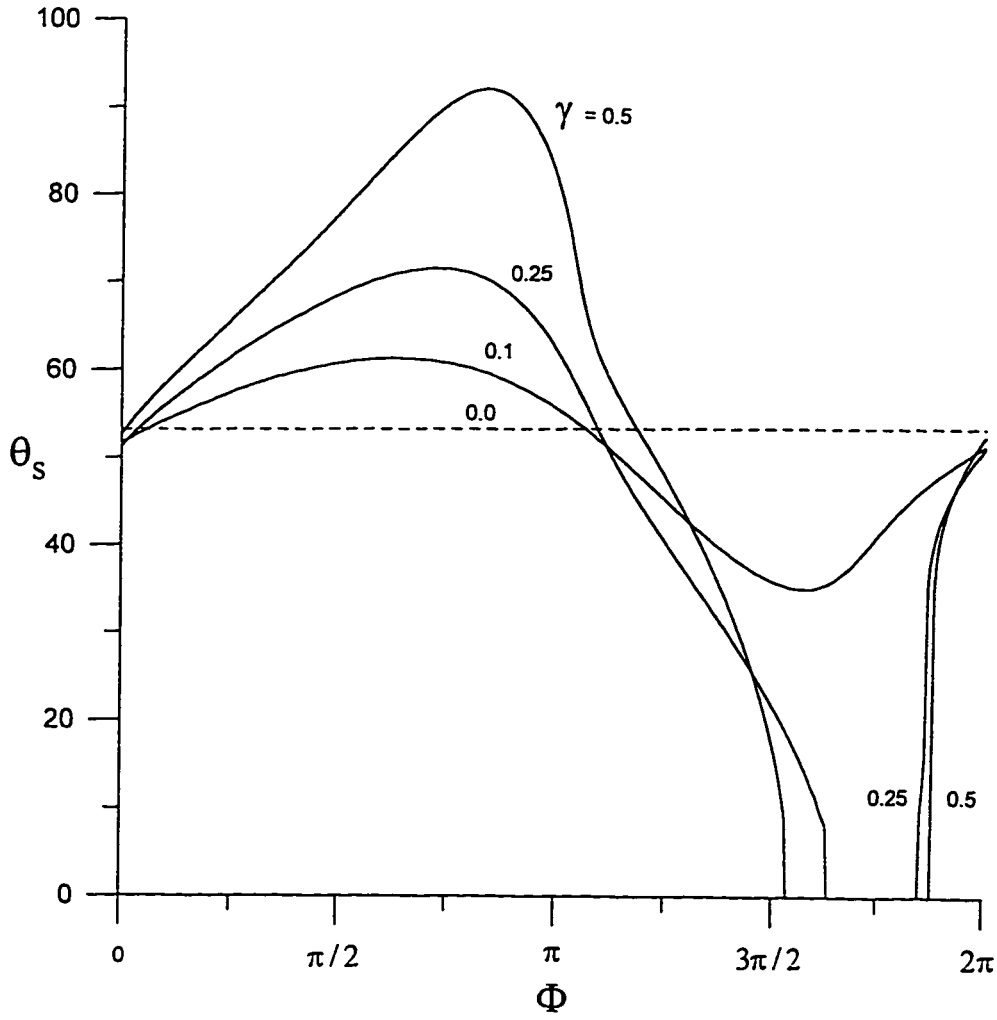

Figure 5.34 The time variation of the separation angle for the case of Re = 100, S = π/4

CHAPTER 6

VISCOUS FLOW OVER OBLATE SPHEROIDS

In this chapter, the series truncation method of solution is extended to the case of the axisymmetric flow over an oblate spheroid.

6.1 Steady Flow

The steady incompressible flow over an oblate spheroid with major and minor axes of 2a and 2b is considered. The full Navier-Stokes equations are solved in an attempt to specify a range of validity for the drag formulas obtained by Payne and Pell (1960) and by Breach (1961). These formulas are based on the solution of the linearized Stokes equations of motion. It is expected that as Reynolds number increases, the effect of the neglected nonlinear inertia terms in the equations of motion becomes pronounced.

6.1.1 Formulation of the Problem and the Method of Solution

The steady dimensionless forms of the governing equations (3.16) and (3.17) upon using the oblate spheroidal coordinate system are as follows:

$$\cosh\xi \sin\eta\,(\sinh^2\xi+\cos^2\eta)\zeta+\cosh\xi\frac{\partial}{\partial\xi}\left(\frac{1}{\cosh\xi}\frac{\partial\psi}{\partial\xi}\right)+\sin\eta\frac{\partial}{\partial\eta}\left(\frac{1}{\sin\eta}\frac{\partial\psi}{\partial\eta}\right)=0 \quad (6.1)$$

$$\frac{\partial\psi}{\partial\eta}\frac{\partial}{\partial\xi}\left(\frac{\zeta}{\cosh\xi\sin\eta}\right)-\frac{\partial\psi}{\partial\xi}\frac{\partial}{\partial\eta}\left(\frac{\zeta}{\cosh\xi\sin\eta}\right)=\frac{2}{\mathrm{Re}}\left\{\frac{\partial}{\partial\xi}\left[\frac{1}{\cosh\xi}\frac{\partial}{\partial\xi}(\cosh\xi\,\zeta)\right]+\frac{\partial}{\partial\eta}\left[\frac{1}{\sin\eta}\frac{\partial}{\partial\eta}(\sin\eta\,\zeta)\right]\right\} \quad (6.2)$$

In the above equations, the dimensionless variables are related to the dimensional ones by

$$\psi = \frac{\psi'}{U_o c'^2}, \qquad \zeta = \frac{\zeta' c'}{U_o}, \qquad \text{and} \quad Re = \frac{\rho U_o (2c')}{\mu} \tag{6.3}$$

The parameter Re is the Reynolds number based on the focal length. The focal length is used here instead of the major axis used in chapter 4 for convenience. The boundary conditions to be satisfied are the no-slip and impermeability conditions on the surface of the spheroid and the free stream conditions away from it. These can be expressed as

$$\psi = \frac{\partial \psi}{\partial \theta} = \frac{\partial \psi}{\partial \xi} = 0 \quad \text{at} \quad \xi = \xi_o \tag{6.4}$$

$$\frac{\partial \psi}{\partial \xi} = \frac{1}{2}\sinh 2\xi \, \sin^2 \eta \quad , \text{and} \quad \frac{\partial \psi}{\partial \eta} = \frac{1}{2}\cosh^2 \xi \, \sin 2\eta \qquad \text{as } \xi \to \infty \tag{6.5}$$

The conditions in equation (6.5) lead to,

$$\psi = \frac{1}{2}\cosh^2 \xi \, \sin^2 \eta \qquad \text{as } \xi \to \infty \tag{6.6}$$

The flow away from the oblate spheroid is irrotational leading to,

$$\zeta \to 0 \qquad \text{as } \xi \to \infty \tag{6.7}$$

Consider the following expansions for ψ and ζ:

$$\psi = \sum_{n=1}^{\infty} f_n(\xi) \int_z^1 P_n(\gamma)\, d\gamma \tag{6.8}$$

$$\zeta = \sum_{n=1}^{\infty} g_n(\xi)\, P_n^1(z) \tag{6.9}$$

When these expansions, which are slightly modified here from those used in chapter 5, are substituted into equations (6.1) and (6.2) and integrating over z from -1 to 1, give the following expressions,

$$\frac{d^2 f_n}{d\xi^2} - \tanh\xi \frac{df_n}{d\xi} - n(n+1) f_n = \cosh\xi \, n(n+1)\left[\sinh^2 \xi + \frac{2n^2 + 2n - 3}{(2n-1)(2n+3)}\right] g_n + \cosh\xi \frac{n(n+1)(n+2)(n+3)}{(2n+3)(2n+5)} g_{n+2} + \cosh\xi \frac{n(n-1)(n-2)(n+1)}{(2n-1)(2n-3)} g_{n-2} \tag{6.10}$$

$$\frac{d^2 g_n}{d\xi^2} + \tanh\xi \frac{dg_n}{d\xi} + \left[\frac{1}{\cosh^2\xi} - n(n+1)\right] g_n = \frac{Re}{2} S_n \tag{6.11}$$

$$\text{where, } S_n = \frac{1}{\cosh\xi}\left[\sum_{i=1}^{\infty}\sum_{j=1}^{\infty} \alpha_{ij}^n f_i \left(\frac{dg_j}{d\xi} - \tanh\xi\, g_j\right) + \sum_{i=1}^{\infty}\sum_{j=1}^{\infty} \beta_{ij}^n g_j \frac{df_i}{d\xi}\right] \tag{6.12}$$

The coefficients appearing in the series are the same as those defined in chapter 5. It is also understood that g_{-1} , $g_0 = 0$. The boundary conditions associated with these equations are

$$f_n(\xi_o) = \frac{df_n}{d\xi}(\xi_o) = 0 \tag{6.13}$$

$$f_n(\xi) \to \cosh^2\xi\ \delta_{n1}, \quad \frac{df_n(\xi)}{d\xi} \to \sinh 2\xi\ \delta_{n1}, \quad g_n(\xi) \to 0 \quad \text{as} \quad \xi \to \infty \tag{6.14}$$

The solutions of the functions ψ and ζ are obtained through the following steps:

1. Denoting the right hand side of equation (6.10) by $r_n(\xi)$, it can be rewritten as

$$\frac{d^2 f_n}{d\xi^2} - \tanh\xi \frac{df_n}{d\xi} - n(n+1) f_n = r_n(\xi) \tag{6.15}$$

If central differences are used to approximate the space derivatives, the functions f_n can be obtained sequentially from n = 1 to N (N denotes the maximum number of terms taken in the series) by solving the resulting tridiagonal systems of equations.

2. The tridiagonal systems corresponding to equations (6.11) are then solved for the functions $g_n(\xi)$.

3. The values of the functions g_n on the surface of the spheroid required to complete the integration procedure are obtained from equation (6.10) by approximating the space derivative $\frac{d^2 f_n}{d\xi^2}$ by central differences as

$$\frac{d^2 f_n}{d\xi^2} = \frac{2 f_n(\xi_o + h)}{h^2} \qquad (6.16)$$

This approximation was successfully used for the elliptic cylinder case by Patel (1981) and for the sphere case by Drummond and Lyman (1990). The appearance of the functions g_{n-2} and g_{n+2} in equation (6.10) when solving for g_n on the surface of the spheroid does not present any problems. The functions with subscript (n-2) are known from the solution of the previous terms; however, functions with subscript (n+2) are unknown. These unknown functions were initially assumed and then updated through an iterative procedure.

4. As each new mode is determined, a solution which can be denoted by $g_n^{m+1/2}(\xi)$ is obtained. To obtain the solution with iterate (m+1), we take the weighted average:

$$g_n^{m+1}(\xi) = K g_n^{m+1/2}(\xi) + (1-K) g_n^{m}(\xi) \qquad (6.17)$$

where $g_n^{m}(\xi)$ are the solutions obtained from the previous iteration, and $0 < K < 1$. This averaging process was found necessary to achieve convergence.

5. Repeat all steps until convergence is reached. The condition set for convergence is $\left|g_n^{m+1}(\xi) - g_n^{m}(\xi)\right| < 10^{-10}$.

The number of points in the ξ direction used is 201 with a space step of 0.025. This sets the outer boundary at a physical distance that ensures that the conditions at infinity are appropriately incorporated in the numerical solution. The effect of the step size on the flow field near the spheroid was examined by comparing the results when using different values. No significant changes in the values of the drag or the surface vorticity were detected by reducing the step size further than the given value. As there is no intrinsic way to determine them, the total number of terms taken in the series was found by numerical experiments. The total number of terms depends on Reynolds number and ξ_o. For higher Reynolds numbers and lower ξ_o, more terms are needed. One way to check the convenience of the number of terms taken in the series is to observe the difference in the

values of the drag. Figure 6.1 shows the surface vorticity for the case Re = 0.1 and ξ_o = 0.25 at different values of N. In this case, the drag values for the cases N = 6, 8, 10, 12, and 16 are respectively, 102.913, 103.105, 103.155, 103.169, and 103.175 which differ at the maximum by 0.8%. The parameter K which is used in the averaging process of the vorticity calculations is higher for higher Reynolds numbers and is not sensitive to the parameter ξ_o. The parameters of calculations K, N, and the number of iterations required for convergence at a tolerance of 10^{-10} are given in table 6.1.

6.1.2 Results and Discussions

In a typical engineering problem of this nature, the quantities sought are the drag, surface vorticity, surface pressure distribution, and the stream function and vorticity patterns. In what follows, we present these for Reynolds numbers of 0.1, 0.5, and 1.0 at ξ_o of 0.25, 0.5, 0.75, 1.0, 1.25, and 1.5.

The projected area of the oblate spheroid is $\pi c'^2 \cosh^2 \xi$. By integrating forces over the surface of the spheroid, one can show that

$$C_{DF} = -\frac{4 \tanh \xi_o}{Re} \int_0^{\pi} \zeta(\xi_o, \eta) \sin^2 \eta \, d\eta \tag{6.18}$$

$$C_{DP} = -\frac{1}{\rho U_o^2} \int_0^{\pi} p'(\xi_o, \eta) \sin 2\eta \, d\eta \tag{6.19}$$

By applying Navier-Stokes equations on the surface of the spheroid, one can show that:

$$\left(\frac{\partial p}{\partial \eta}\right)_{\xi=\xi_o} = \frac{4}{Re}\left[\frac{\partial \zeta}{\partial \xi} + \tanh \xi \, \zeta\right]_{\xi=\xi_o} \tag{6.20}$$

Using equation (6.20) together with equation (6.9), the drag components can be expressed as

$$C_{DF} = \frac{16 \tanh \xi_o}{3 Re} g_1(\xi_o, t) \tag{6.21}$$

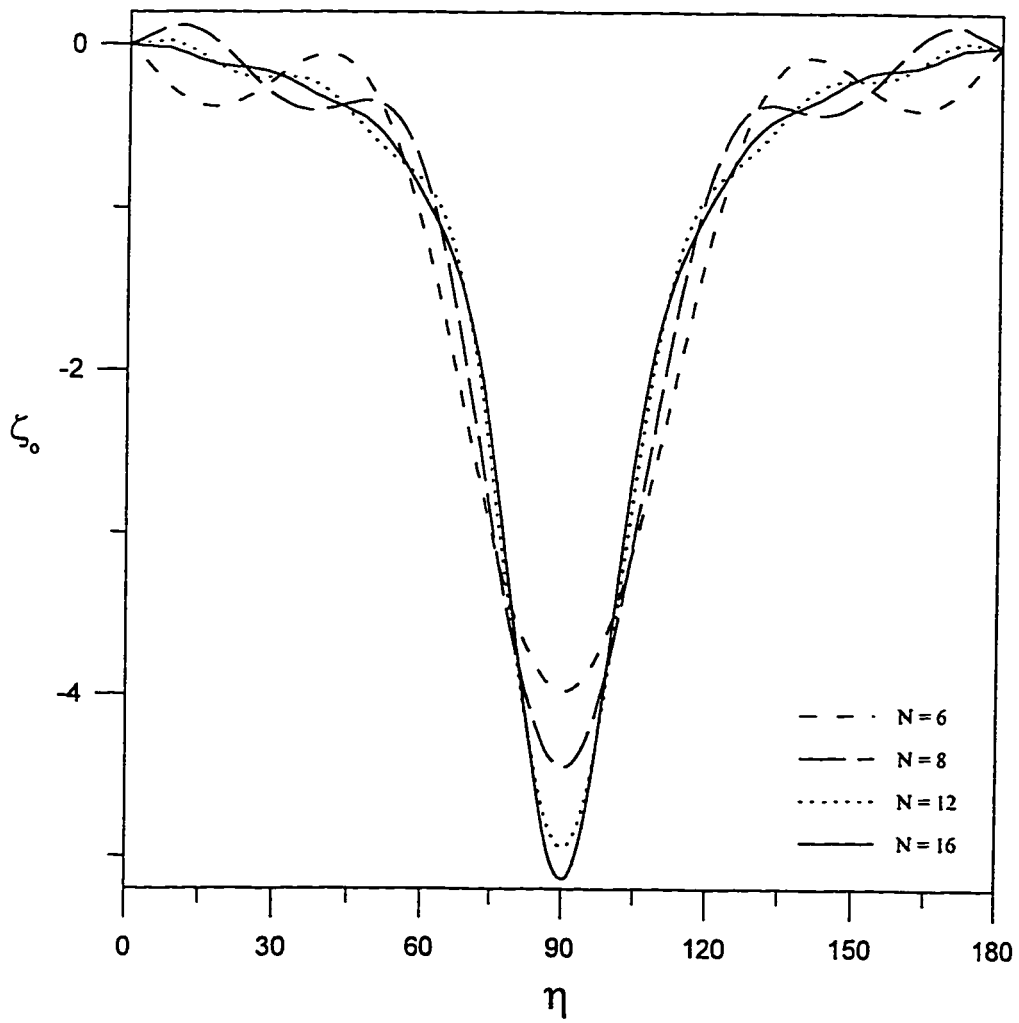

Figure 6.1 Surface vorticity distribution for the case Re = 0.1, ξ_0 = 0.25 at different N values.

Table 6.1 Parameters of Calculations

Re	ξ_o	K	N	No. Of Iterations
0.1	0.25	10^{-3}	16	10398
0.1	0.50	10^{-3}	10	5728
0.1	0.75	10^{-3}	10	3309
0.1	1.00	10^{-3}	8	2511
0.1	1.25	10^{-3}	8	2169
0.1	1.50	10^{-3}	8	1986
0.5	0.25	$9x10^{-4}$	18	7393
0.5	0.50	$9x10^{-4}$	11	6771
0.5	0.75	$9x10^{-4}$	11	6660
0.5	1.00	$9x10^{-4}$	9	6523
0.5	1.25	$9x10^{-4}$	9	6464
0.5	1.50	$9x10^{-4}$	9	6540
1.0	0.25	10^{-4}	20	7255
1.0	0.50	10^{-4}	12	6739
1.0	0.75	10^{-4}	12	6762
1.0	1.00	10^{-4}	10	6958
1.0	1.25	10^{-4}	10	6810
1.0	1.50	10^{-4}	10	8825

$$C_{DP} = -\frac{8}{3\,Re}\left[\tanh\xi_o\; g_1(\xi_o,t) + \frac{\partial g_1}{\partial \xi}(\xi_o,t)\right] \tag{6.22}$$

As indicated by equations (6.21) and (6.22), the drag depends on the first mode of the series in equation (6.9) which, in turn, depends on the other modes. The first 8 modes of the series at the surface of the oblate spheroid are given in table 6.2 for the different cases considered in this study. The drag formula given by Payne and Pell (1960) takes the form:

$$C_{D1} = \frac{4B}{3\,Re\;\cosh\xi_o} \tag{6.23}$$

and that modified by Breach (1961) is:

$$C_{D2} = \frac{4B}{3\,Re\;\cosh\xi_o}\left[1 + \frac{B\,Re}{48} + \frac{B^2\,Re^2}{1440}\log(Re/2) + O(Re^2)\right] \tag{6.24}$$

$$\text{where } B = \frac{12}{\cosh\xi_o\left[\sinh\xi_o + (1-\sinh^2\xi_o)\cot^{-1}(\sinh\xi_o)\right]} \tag{6.25}$$

The dimensionless pressure distribution around the oblate spheroid can be obtained by integrating equation (6.20) which results in:

$$p^* = p_\eta - p_\pi = \frac{4}{Re}\int_\pi^\eta \left(\frac{\partial \zeta}{\partial \xi} + \tanh\xi\;\zeta\right)_{\xi=\xi_o} d\eta \tag{6.26}$$

and by using equation (6.9), one can prove that

$$p^*(\eta,t) = \frac{4}{Re}\sum_{n=1}^{N}\left[P_n(\cos\eta) - (-1)^n\right]\left[\frac{\partial g_n}{\partial \xi}(\xi_o,t) + \tanh\xi_o\; g_n(\xi_o,t)\right] \tag{6.27}$$

Figure 6.2 shows the drag components for the case $\xi_o = 1.0$ when Re = 0.1, 0.2, 0.3, 0.4, 0.5, 0.6, 0.7, 0.8, 0.9, and 1.0. The drag values computed from equations (6.23) and (6.24) are also plotted. As Re increases, the drag coefficients decrease with both C_{D1} and C_{D2} underestimating the drag at higher Reynolds numbers. C_{D2} which modifies the Stokes drag presented by C_{D1} is closer to the present numerical solution. Figure 6.3 shows the corresponding surface pressure and surface vorticity distributions for the same cases. At low Reynolds numbers, the difference in the pressure between the front and the back stagnation points is considerable as compared to the difference at higher Reynolds

Table 6.2 Vorticity modes on the surface of the oblate spheroid

(- < 0.001)

Re	ξ_o	$g_1(\xi_O)$	$g_2(\xi_O)$	$g_3(\xi_O)$	$g_4(\xi_O)$	$g_5(\xi_O)$	$g_6(\xi_O)$	$g_7(\xi_O)$	$g_8(\xi_O)$
0.1	0.25	2.305	-0.013	-0.793	0.005	0.374	-0.003	-0.192	0.001
0.1	0.50	1.791	-0.013	-0.366	0.003	0.104	-0.001	-0.032	-
0.1	0.75	1.408	-0.012	-0.172	0.002	0.030	-	-0.006	-
0.1	1.00	1.110	-0.012	-0.082	0.001	0.008	-	-0.001	-
0.1	1.25	0.875	-0.012	-0.039	0.001	0.002	-	-	-
0.1	1.50	0.690	-0.012	-0.018	-	0.001	-	-	-
0.5	0.25	2.414	-0.062	-0.831	0.026	0.392	-0.013	-0.202	0.007
0.5	0.50	1.889	-0.060	-0.386	0.015	0.110	-0.005	-0.034	0.001
0.5	0.75	1.499	-0.058	-0.183	0.009	0.031	-0.002	-0.006	-
0.5	1.00	1.196	-0.057	-0.088	0.005	0.009	-	-0.001	-
0.5	1.25	0.956	-0.055	-0.042	0.003	0.003	-	-	-
0.5	1.50	0.765	-0.053	-0.021	0.002	0.001	-	-	-
1.0	0.25	2.542	-0.121	-0.874	0.051	0.413	-0.025	-0.212	0.013
1.0	0.50	1.998	-0.115	-0.408	0.029	0.116	-0.009	-0.036	0.003
1.0	0.75	1.597	-0.110	-0.195	0.017	0.033	-0.003	-0.006	0.001
1.0	1.00	1.286	-0.106	-0.094	0.010	0.010	-0.001	-0.001	-
1.0	1.25	1.040	-0.102	-0.046	0.006	0.003	-	-	-
1.0	1.50	0.845	-0.097	-0.023	0.003	0.001	-	-	-

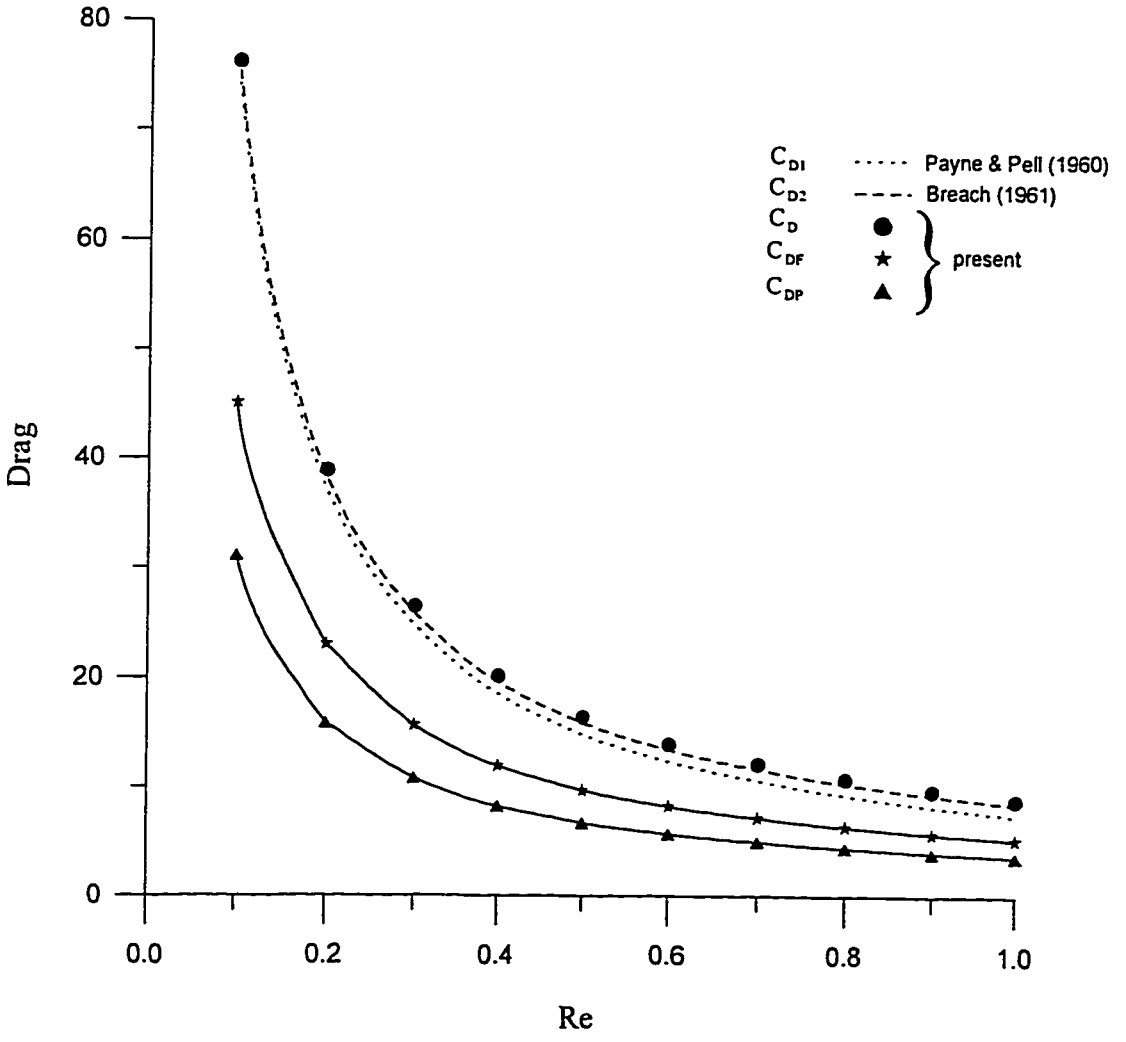

Figure 6.2 The drag components for the case $\xi_o = 1.0$ at different Reynolds numbers

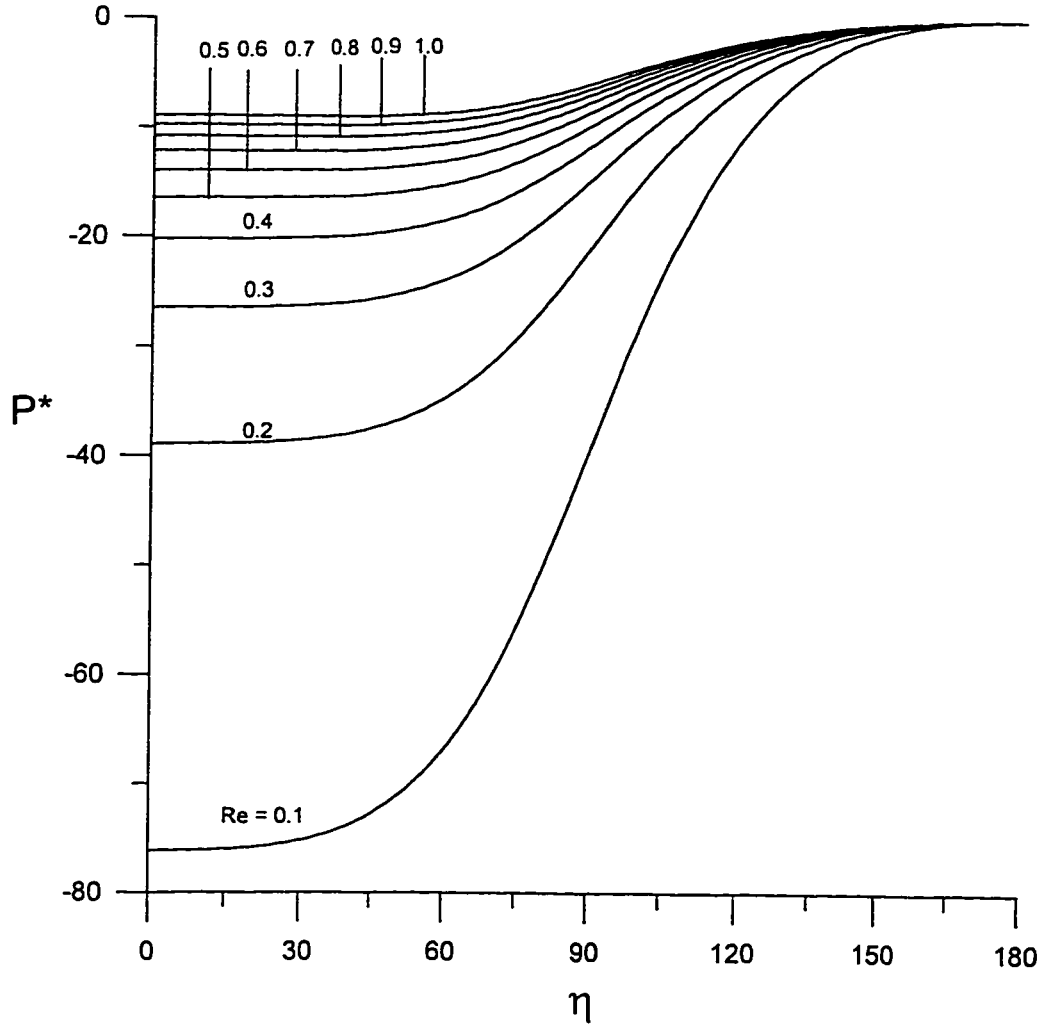

Figure 6.3 Surface pressure distribution for the case $\xi_o = 1.0$, at different Reynolds numbers.

numbers. Figure 6.4 shows the variation of the corresponding surface vorticity. The drag coefficients for the range of parameters considered in this study along with those from equations (6.23) and (6.24) are listed in table 6.3. It is useful to investigate the quantities $1-\frac{C_{D1}}{C_D}$ and $1-\frac{C_{D2}}{C_D}$ which measure the relative deviation of the drag formulas given by Payne and Pell (1960), and by Breach (1961) from the present study, respectively. Figures 6.5a and 6.5b show these quantities for the range of parameters considered. At low Re, there is a good agreement between C_{D1}, C_{D2}, and C_D. As Re increases, the values depart from each other with C_{D2} being closer to C_D. If an error of 5% can be accepted, a range of validity for C_{D1}, and C_{D2} can be stated. The formula for C_{D1} is valid for Re ≤ 0.3 while that of C_{D2} is valid for higher Reynolds numbers provided that a proper restriction on ξ_o is imposed. The dotted lines in figures 6.5a and 6.5b indicate the upper bound for the range of validity.

The effect of ξ_o on the pressure distribution and the surface vorticity can be seen in figures 6.6 and 6.7. The figures which show the results at Re = 1.0 when ξ_o = 0.25, 0.5, 0.75, 1.0, 1.25, and 1.5 indicate that when ξ_o decreases, the surface vorticity increases and a positive pressure gradient may be expected. ξ_o=0 corresponds to the circular disk case at which a singular behavior of the pressure gradient is expected.

Figure 6.8 shows the stream line and vorticity patterns for the cases Re = 0.1 and 1.0 when ξ_o = 0.25. No separation is expected at these low Re values. The symmetry of the vorticity at Re = 0.1 is slightly distorted at Re = 1.0.

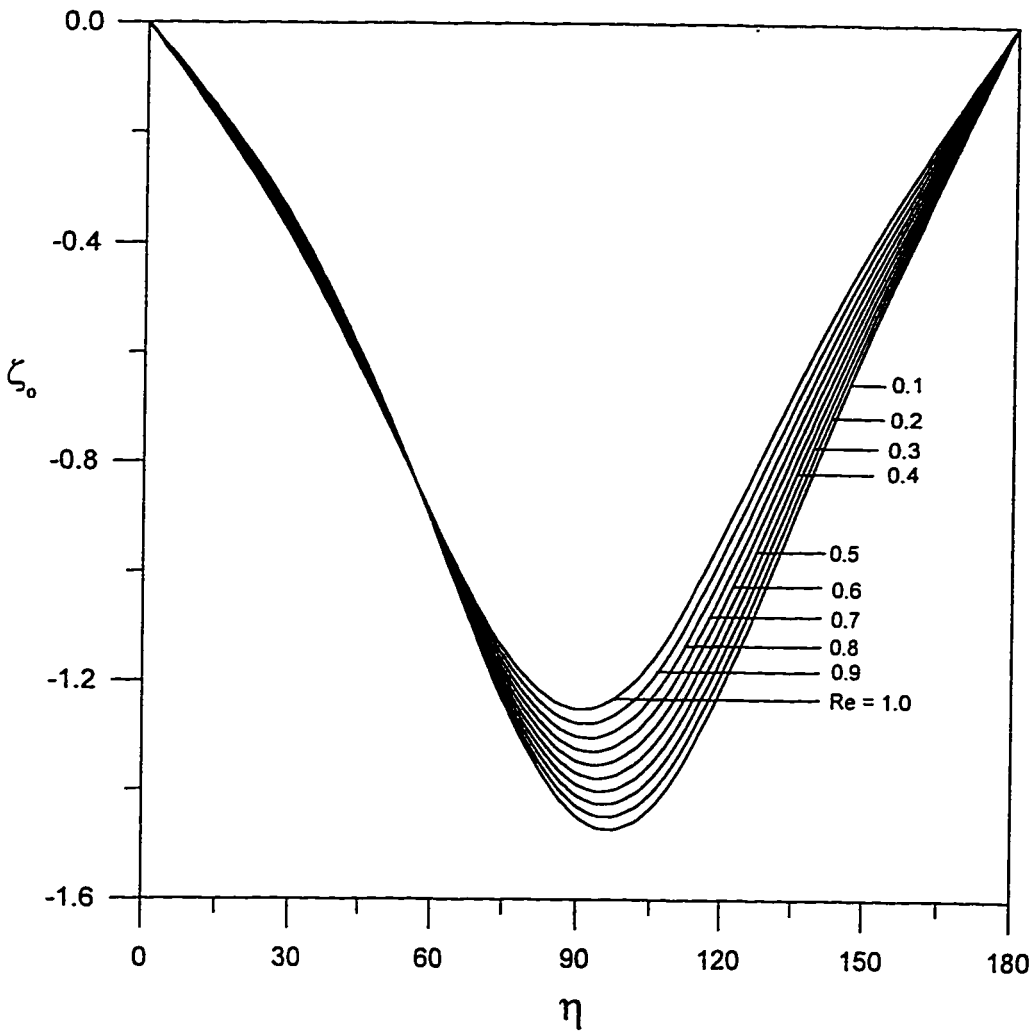

Figure 6.4 Surface vorticity distribution for the case $\xi_o = 1.0$, at different Reynolds numbers.

Table 6.3 Comparison of C_D with equations (6.23) and (6.24)

Re	ξ_o	C_{DF}	C_{DP}	C_D	C_{D1} Eq(6.23)	C_{D2} Eq(6.24)
0.1	0.25	30.107	73.068	103.175	100.838	102.349
0.1	0.50	44.136	53.732	97.868	95.659	97.141
0.1	0.75	47.706	40.571	88.277	86.142	87.518
0.1	1.00	45.106	31.101	76.207	74.125	75.336
0.1	1.25	39.608	24.065	63.673	61.637	62.660
0.1	1.50	33.304	18.738	52.041	50.05	50.890
0.5	0.25	6.308	15.318	21.626	20.168	21.511
0.5	0.50	9.31	11.345	20.655	19.132	20.443
0.5	0.75	10.156	8.649	18.805	17.228	18.439
0.5	1.00	9.713	6.711	16.424	14.825	15.887
0.5	1.25	8.647	5.27	13.917	12.327	13.222
0.5	1.50	7.388	4.176	11.563	10.01	10.743
1.0	0.25	3.321	8.078	11.399	10.084	11.427
1.0	0.50	4.925	6.015	10.94	9.566	10.877
1.0	0.75	5.409	4.622	10.031	8.614	9.825
1.0	1.00	5.225	3.628	8.853	7.413	8.475
1.0	1.25	4.706	2.888	7.594	6.164	7.059
1.0	1.50	4.077	2.327	6.404	5.005	5.738

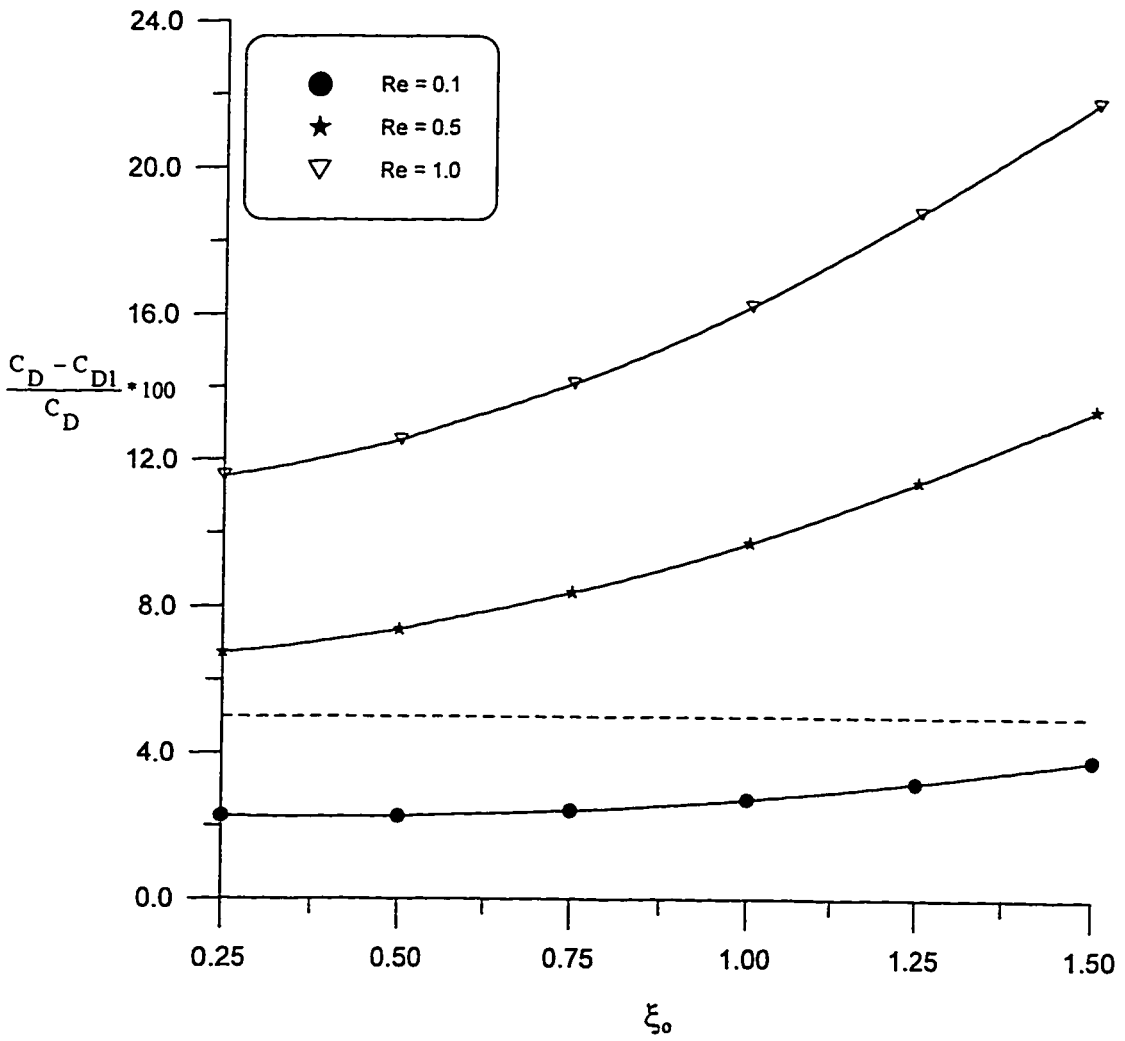

Figure 6.5a Comparison of the present drag with the formula of Payne and Bell (1960).

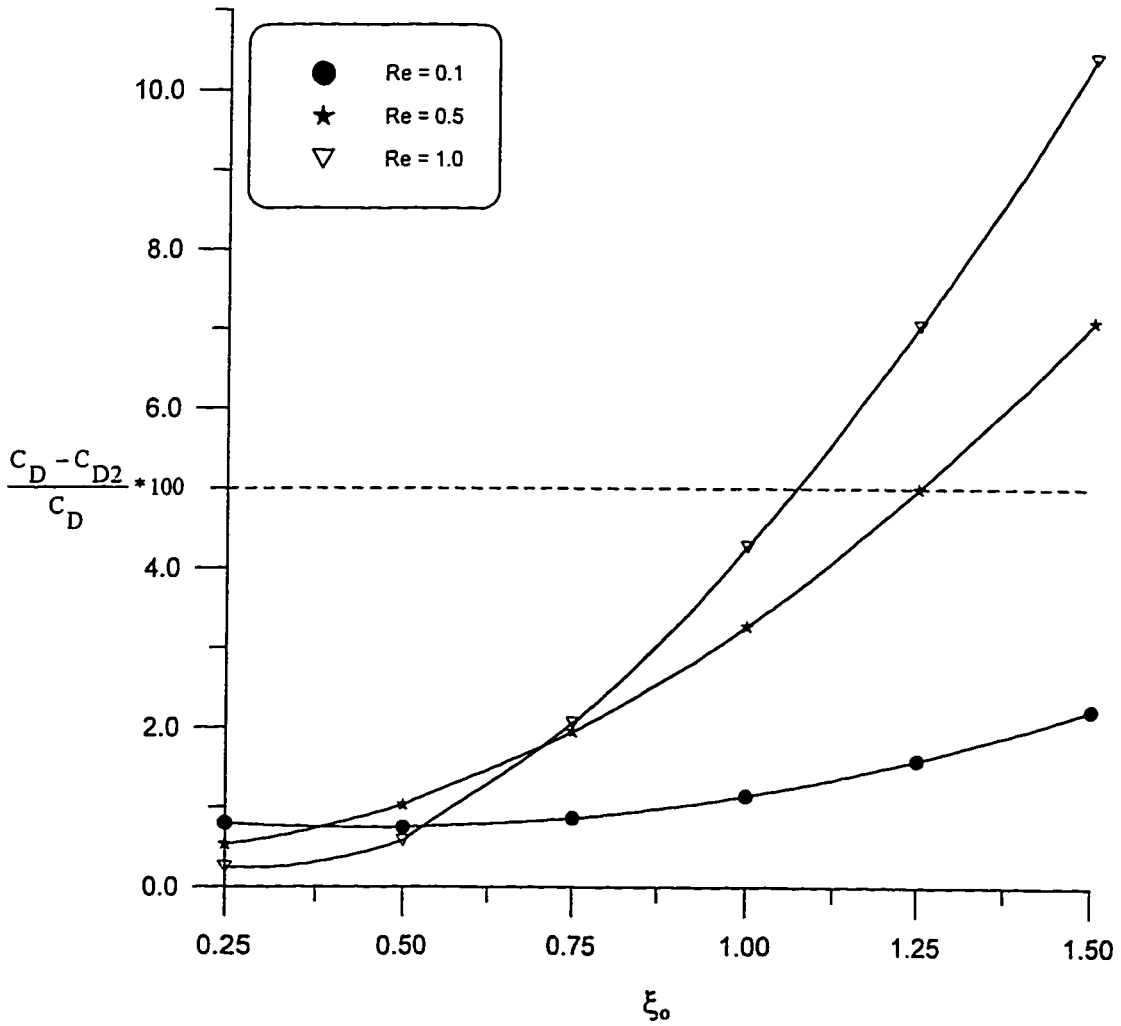

Figure 6.5b Comparison of the present drag with the formula of Breach (1961).

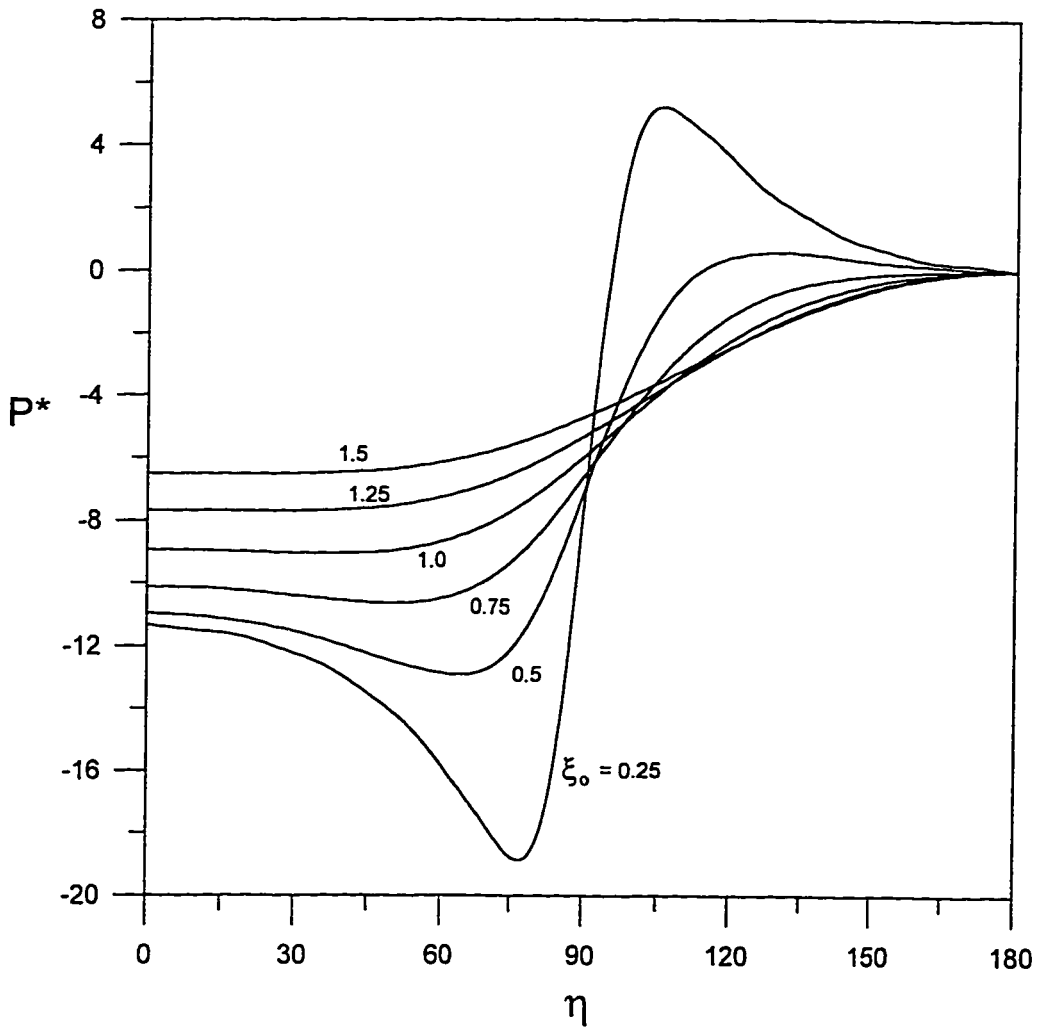

Figure 6.6 Surface pressure distribution for the case Re = 1.0 at different ξ_o values

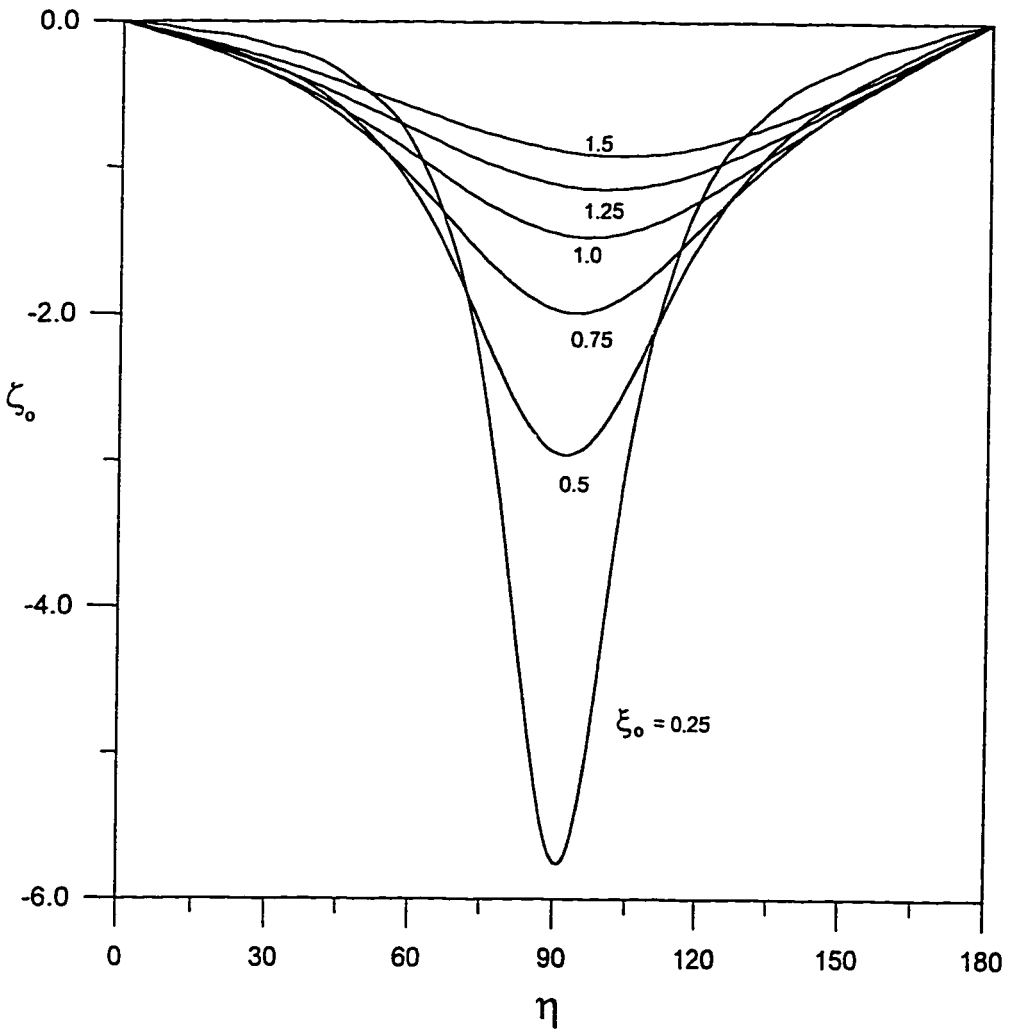

Figure 6.7 Surface vorticity distribution for the case Re = 1.0 at different ξ_o values

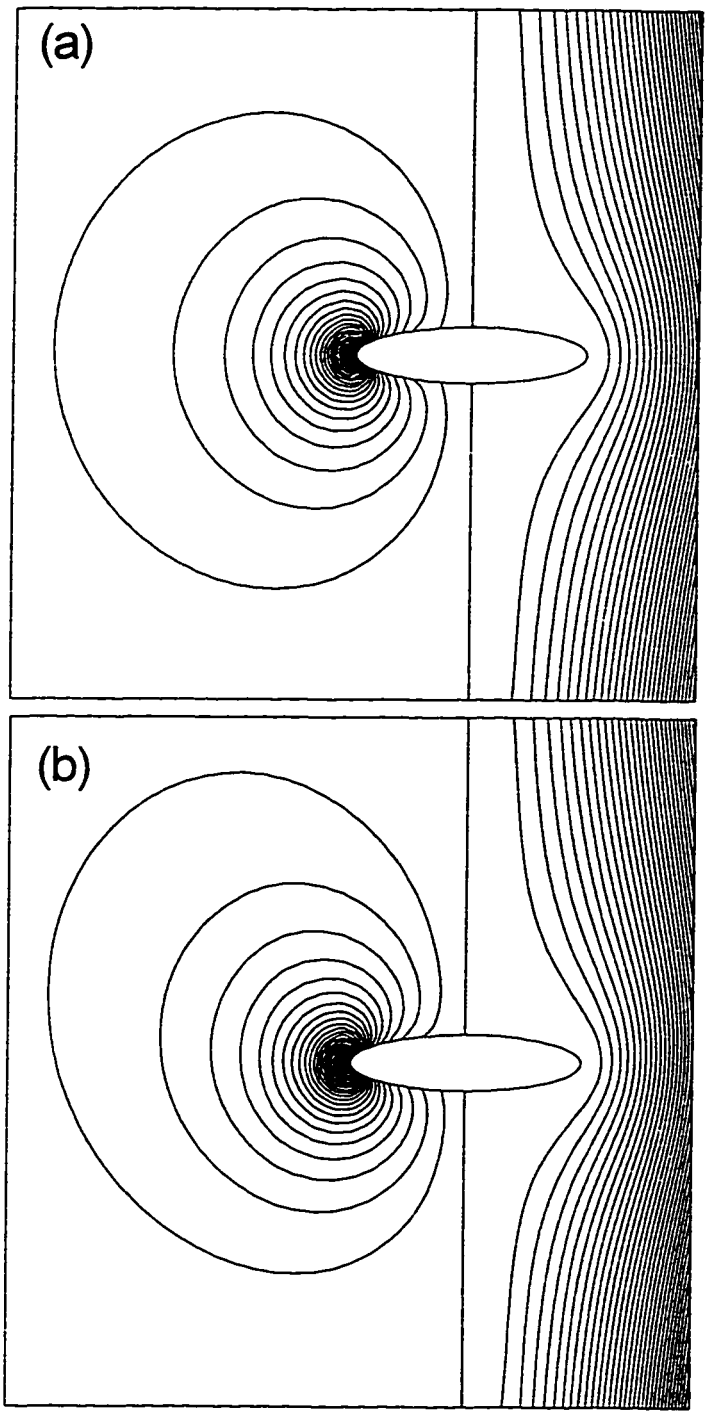

Figure 6.8 Streamlines (right) and vorticity (left) for the case $\xi_o = 0.25$
(a) Re = 0.1, (b) Re = 1.0. $\Delta\psi = 0.05, \Delta\zeta = 0.1$

6.2 Unsteady Flow

This part deals with the time development of the flow field in the neighborhood of an oblate spheroid placed in an infinite body of fluid. The variation of the free stream velocity with time can be expressed through the function F(t) defined in equation (5.1). Two forms of the function F(t) are considered. The first is when the free stream starts impulsively from rest and the resulting flow field is axisymmetric and time dependent. In this case the function F is time independent and assumes a value of unity. The second corresponds to the oscillatory motion of the free stream which can be written as $F(t) = \sin(S\ t)$.

6.2.1 Formulation of the Problem and the Method of Solution

The time dependent version of equation (6.2) assumes the following dimensionless form:

$$(\sinh^2\xi+\cos^2\eta)\ \frac{\partial\zeta}{\partial t}+\frac{\partial\psi}{\partial\eta}\frac{\partial}{\partial\xi}\left(\frac{\zeta}{\cosh\xi\ \sin\eta}\right)-\frac{\partial\psi}{\partial\xi}\frac{\partial}{\partial\eta}\left(\frac{\zeta}{\cosh\xi\ \sin\eta}\right)=$$
$$\frac{2}{\mathrm{Re}}\left\{\frac{\partial}{\partial\xi}\left[\frac{1}{\cosh\xi}\frac{\partial}{\partial\xi}(\cosh\xi\ \zeta)\right]+\frac{\partial}{\partial\eta}\left[\frac{1}{\sin\eta}\frac{\partial}{\partial\eta}(\sin\eta\ \zeta)\right]\right\} \tag{6.28}$$

In the above equation, the dimensionless time is related to the dimensional time by

$$t=\frac{t'U_o}{c'} \tag{6.29}$$

The boundary conditions to be satisfied are

$$\psi=\frac{\partial\psi}{\partial\theta}=\frac{\partial\psi}{\partial\xi}=0 \quad \text{at} \quad \xi=\xi_o \tag{6.30}$$

$$\frac{\partial\psi}{\partial\xi}\to\frac{1}{2}\sinh 2\xi\ \sin^2\eta\ F(t) \quad \text{, and} \quad \frac{\partial\psi}{\partial\eta}\to\frac{1}{2}\cosh^2\xi\ \sin 2\eta\ F(t) \quad \text{as } \xi\to\infty \tag{6.31}$$

The conditions in equation (6.31) lead to,

$$\psi \to \frac{1}{2}\cosh^2\xi \sin^2\eta \;\; F(t) \quad \text{as } \xi \to \infty \tag{6.32}$$

The series expansions used in section 6.1 are used here. Along with equations (6.10), the time dependent equations can be written as

$$\left[\sinh^2\xi + \frac{2n^2+2n-3}{(2n-1)(2n+3)}\right]\frac{\partial g_n}{\partial t} + \frac{(n+2)(n+3)}{(2n+3)(2n+5)}\frac{\partial g_{n+2}}{\partial t} + \frac{(n-1)(n-2)}{(2n-1)(2n-3)}\frac{\partial g_{n-2}}{\partial t}$$
$$= \frac{2}{Re}\left[\frac{\partial^2 g_n}{\partial \xi^2} + \tanh\xi\frac{\partial g_n}{\partial \xi} + \left\{\frac{1}{\cosh^2\xi} - n(n+1)\right\}g_n\right] + S_n \tag{3.33}$$

The boundary conditions are

$$f_n(\xi_o, t) = \frac{\partial f_n}{\partial \xi}(\xi_o, t) = 0 \tag{6.34}$$

$$f_n(\xi,t) \to \cosh^2\xi \;\; F(t)\delta_{n1}, \quad \frac{\partial f_n(\xi,t)}{\partial \xi} \to \sinh 2\xi \;\; F(t)\delta_{n1}, \quad g_n(\xi,t) = 0 \quad \text{as} \quad \xi \to \infty \tag{6.35}$$

The solutions of the functions ψ and ζ are advanced in time by solving equation (6.33) using a Crank-Nicolson finite-difference scheme. The method is similar to that used in chapter 5 for a sphere and need not be written in detail again. The only difference is the appearance of the derivatives $\frac{\partial g_{n-2}}{\partial t}$ and $\frac{\partial g_{n+2}}{\partial t}$. When solving for g_n, the functions with subscript (n-2) are known from the solution of the previous terms, however, functions with subscript (n+2) are unknown. These unknown functions were taken care of by approximating their values at time $(t+\Delta t)$ to be initially the same as time t and then updating these values through an iterative procedure. The method of solution of the other equations (equations (6.10)) was discussed in section 6.1.

6.2.2 The Impulsively Started Flow

The flow development near an oblate spheroid placed in an impulsively started infinite fluid is investigated for Reynolds numbers Re = 5, 10, 20, 40, and 100. The spheroid axis ratios considered are A_r = 0.6 and 0.76. In order to verify the accuracy of the method of solution and the computational scheme, the problem of steady flow over a sphere was approximated using the present computational scheme by considering the case of a spheroid with axis ratio $b/a = 0.99$ which corresponds to $\xi_o = 2.647$. The unsteady flow solution following the sudden velocity increase continued until the final steady solution was reached. Table 6.4 shows a comparison between the values of C_D obtained from this study and those reported by Dennis and Walker (1971) and (1972), LeClair et al. (1970), and Jenson (1959). The variables in these studies are made dimensionless by referring to the diameter of the sphere whereas the variables in the present study are referred to the focal length. The Reynolds number based on the focal length used in this study (Re) is related to the Reynolds number based on the diameter of the sphere (Re_s) by $Re = \frac{Re_s}{\cosh\xi_o}$. Therefore, the values Re_s = 20, and 40 correspond to Re = 2.821, and 5.643, respectively. An excellent agreement between the present study drag coefficient and the other studies can be observed. Figure 6.9 shows a comparison of the surface vorticity (ς_o') for the cases Re_s = 20, and 40 obtained from the present study and that obtained from the study of Dennis and Walker (1971). The surface vorticity ς_o' defined for the sphere is related to ς_o by $\varsigma_o = \frac{\varsigma_o'}{\cosh\xi_o}$. The difference between the two results is attributed to two reasons. The first is that the axis ratio in this study can not take the value of unity due to the obvious numerical reasons. The second is that the work by Dennis and Walker (1971) is based on solving the steady equations. In the present study, however, time was advanced to a value of t = 35.444 which corresponds to t_s = 5 (t_s is the dimensionless time based on the diameter of the sphere). The value of t_s = 5 is chosen

Table 6.4 Comparison of C_D for the sphere

Re_s	Jenson (1959)	LeClair et al. (1970)	Dennis&Walker (1971)	Dennis&Walker (1972)	Present
20	1.473	1.356	1.365	1.42	1.415
40	0.930	0.930	0.904	0.94	0.935

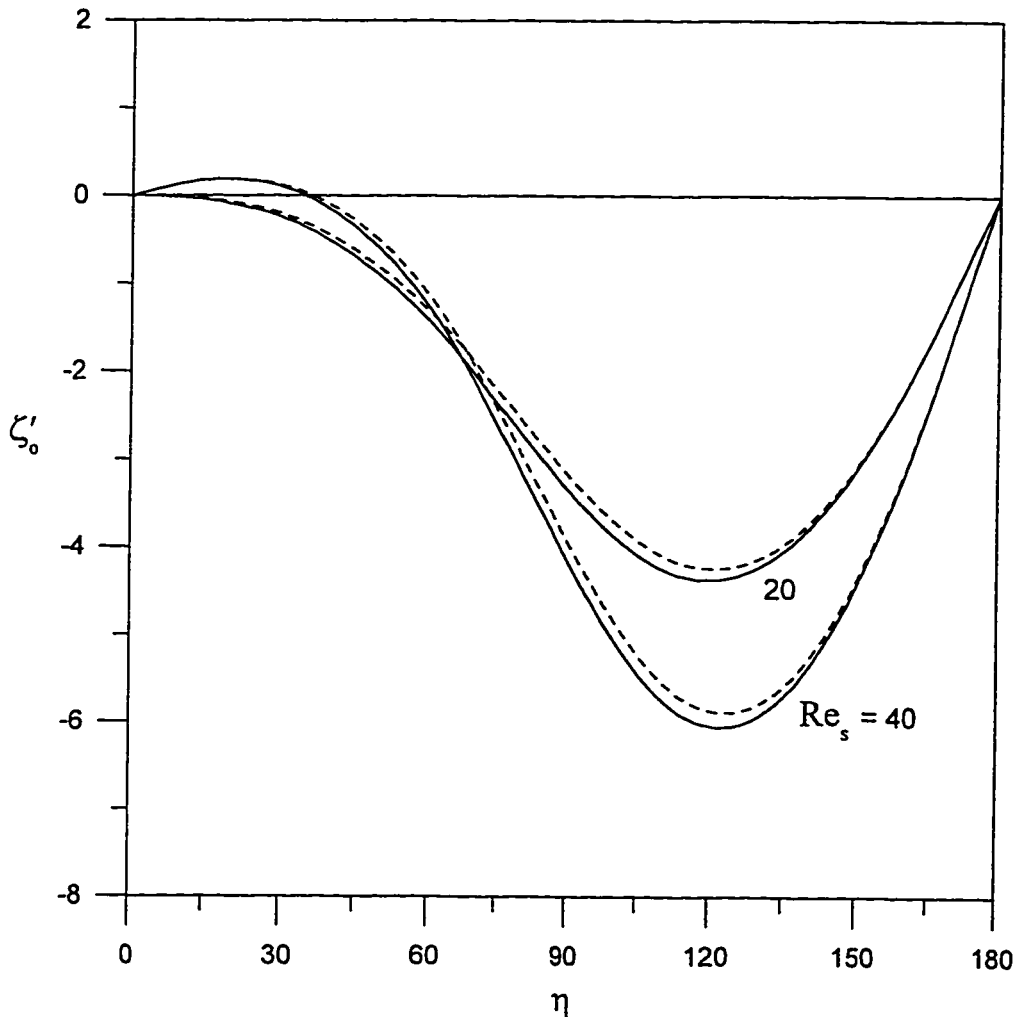

Figure 6.9 Surface vorticity distributions for the cases of $Re_s = 20$ and 40

——— Present with b/a = 0.99

- - - - - Dennis and Walker (1971)

because it corresponds to the time at which the computations of the impulsively started flow over a sphere by Dennis and Walker (1972) were terminated.

The time variation of the surface vorticity and pressure distributions for the case $A_r = 0.6$ and Re = 20 are shown in figures 6.10 and 6.11. Figure 6.10 shows that the maximum surface vorticity, ς_o, occurs as expected near $\eta = 90$ while separation starts to occur at time $t > 1$. At small times, $|\varsigma_o|$ is higher and decreases with the increase of t because of the growth of the boundary layer thickness. The same trend was reported earlier for the case of a cylinder by Patel (1981) and for the case of a sphere by Dennis and Walker (1972). Figure 6.11 shows the time development of the surface pressure distribution, p^* for the same case. The maximum pressure is at the forward stagnation point ($\eta = 180$) while the minimum occurs near $\eta = 70$ which precedes the point of separation as expected. The surface vorticity distributions at large times (steady cases) are shown in figure 6.12a for $A_r = 0.6$ and in figure 6.12b for $A_r = 0.76$. The corresponding surface pressure distributions are shown in figure 6.13. Figure 6.12a shows that flow separation occurs earlier as Re increases leading to a larger size separation bubble. The trend is very much the same for the case of $A_r = 0.76$ (see figure 6.12b) except that $|\varsigma_o|$ is smaller on almost all the spheroid surface. The same figures (6.12a and 6.12b) show that separation only occurs for values of Re = 20, 40, and 100 but not for the low Re cases of 5 and 10. The location of the separation point and its time variation is shown in figure 6.14 for Re = 20, 40, and 100 and for the two geometries ($A_r = 0.6$ and $A_r = 0.76$).

The time variation of the frictional and total drag coefficients (C_{DF} and C_D) are plotted in figures 6.15a and 6.15b for all Reynolds numbers and axis ratios considered. The figures show that C_{DF} and C_D reached their steady values with higher total drag for low axis ratio geometry. The effect of geometry on C_{DF} is insignificant.

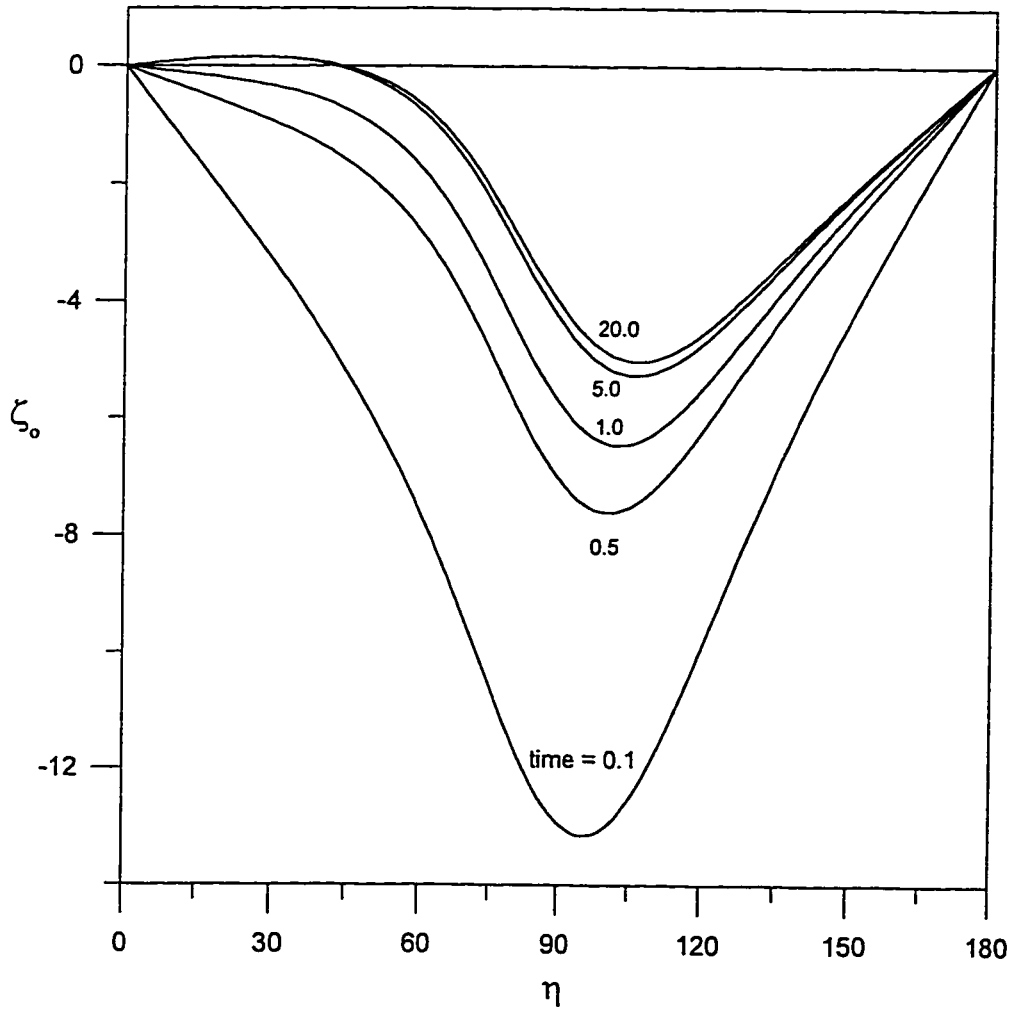

Figure 6.10 Time development of surface vorticity distribution for the case of $A_r = 0.6$ and Re = 20.

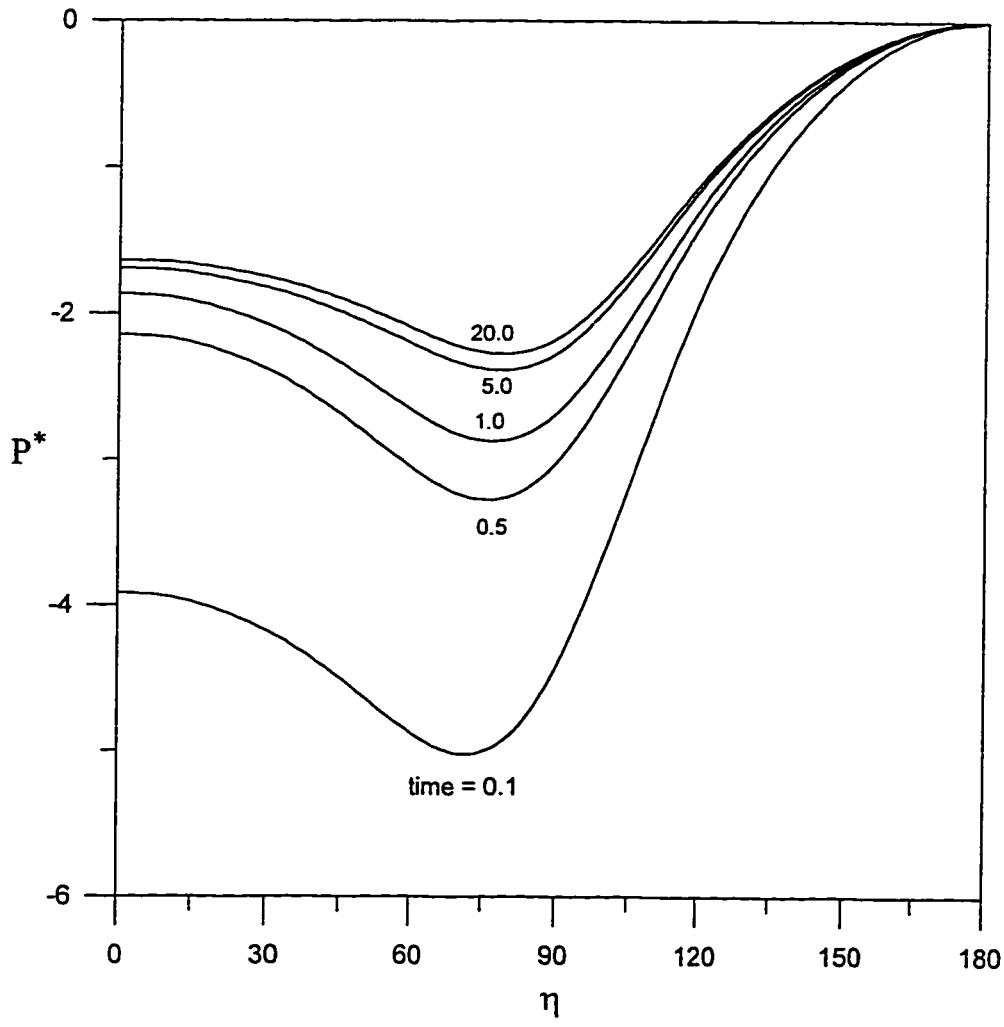

Figure 6.11 Time development of surface pressure distribution for the case of A_r = 0.6 and Re = 20.

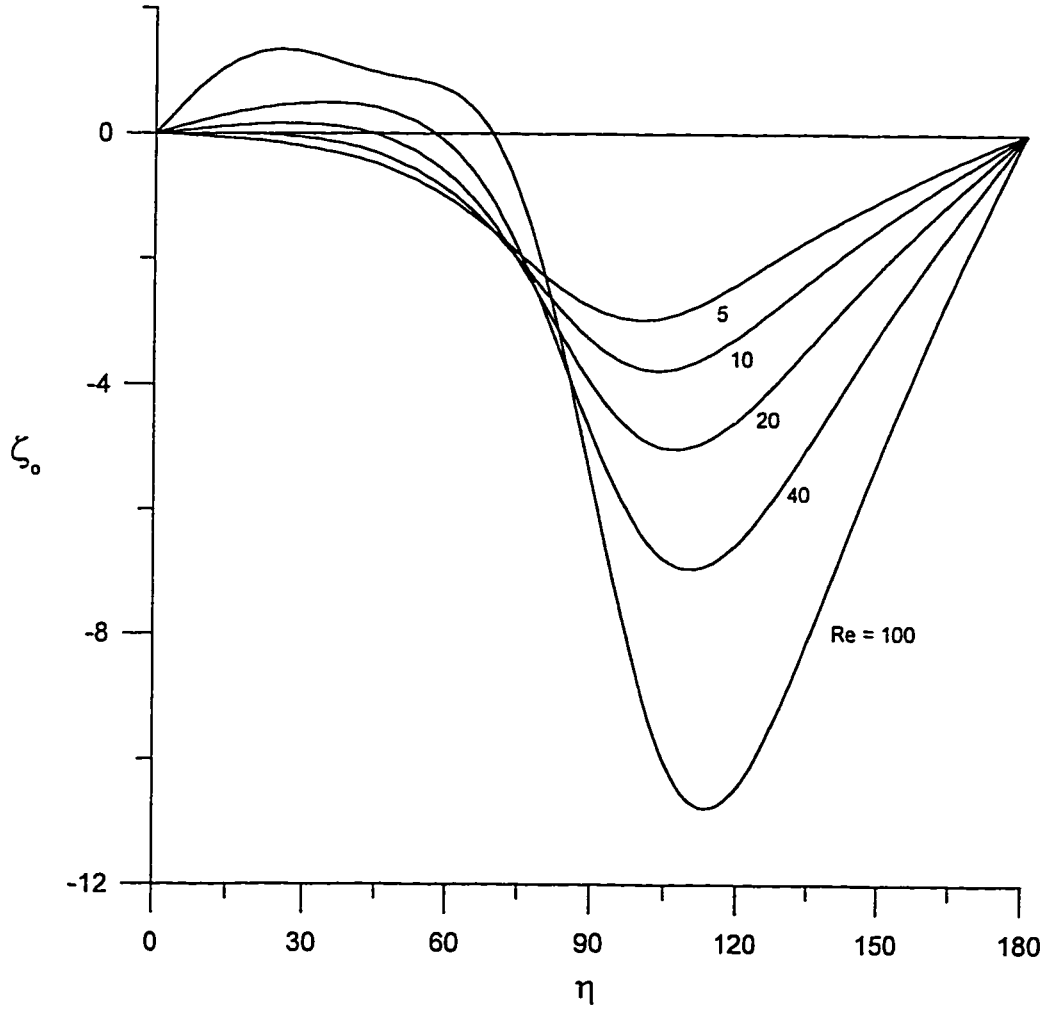

Figure 6.12a Surface vorticity distributions for the case of $A_r = 0.6$ at different Reynolds numbers.

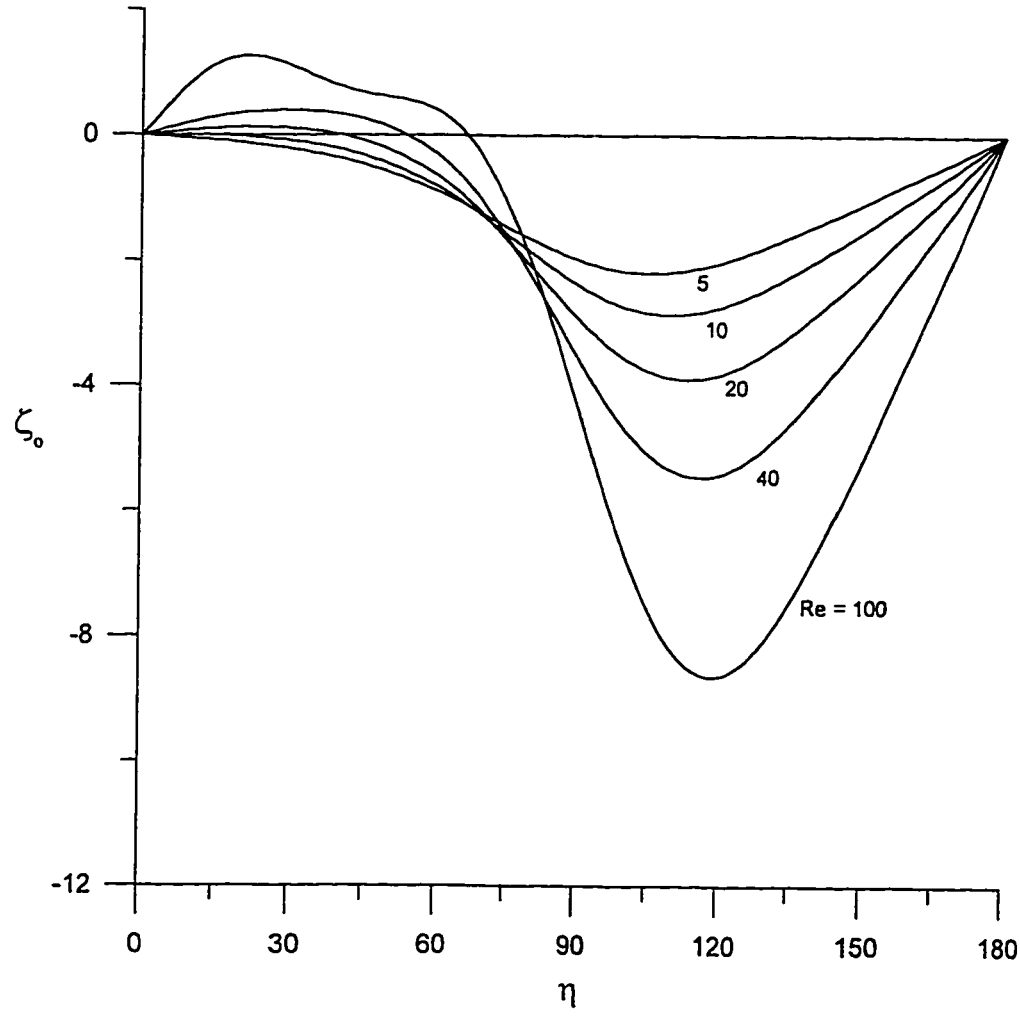

Figure 6.12b Surface vorticity distributions for the case of $A_r = 0.76$ at different Reynolds numbers.

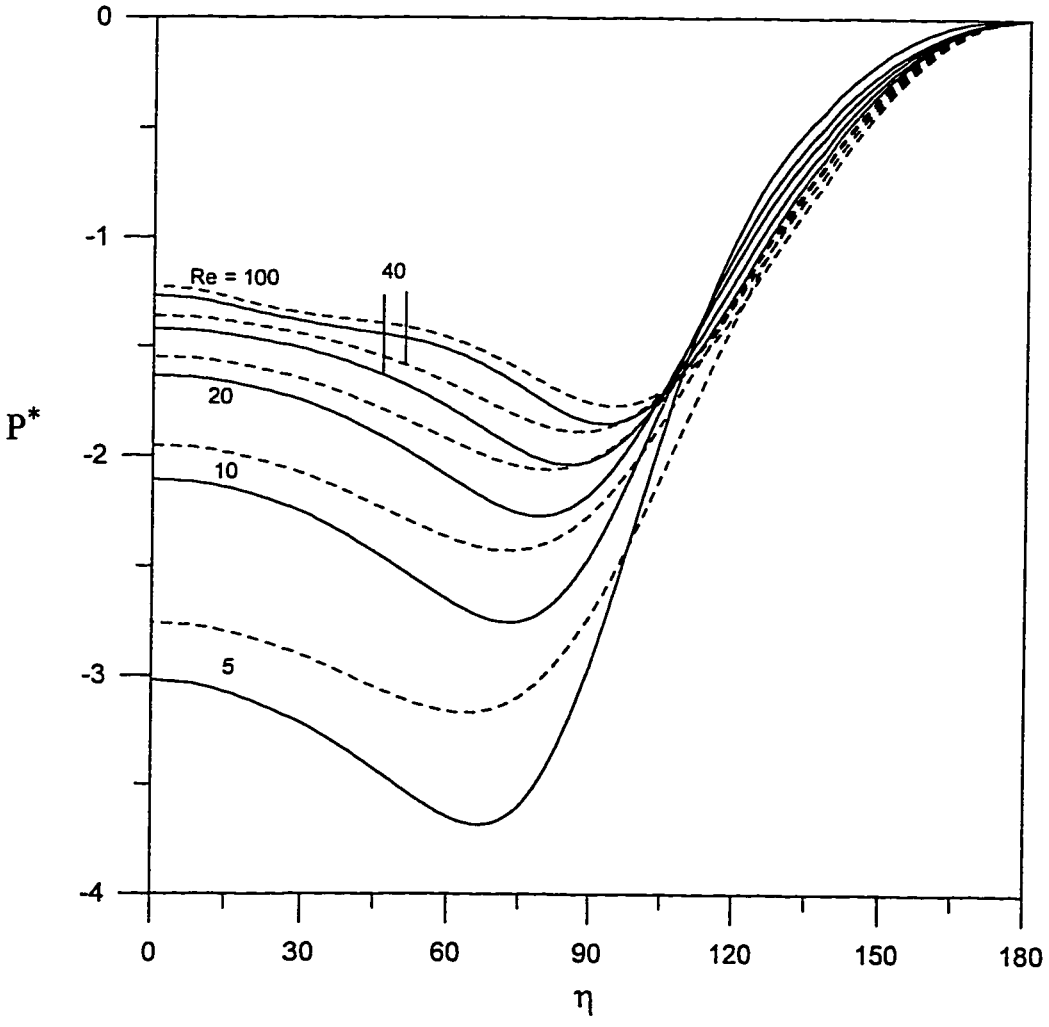

Figure 6.13 Surface pressure distributions for the cases of $A_r = 0.6$ (solid lines) and $A_r = 0.76$ (dotted lines) at different Reynolds numbers.

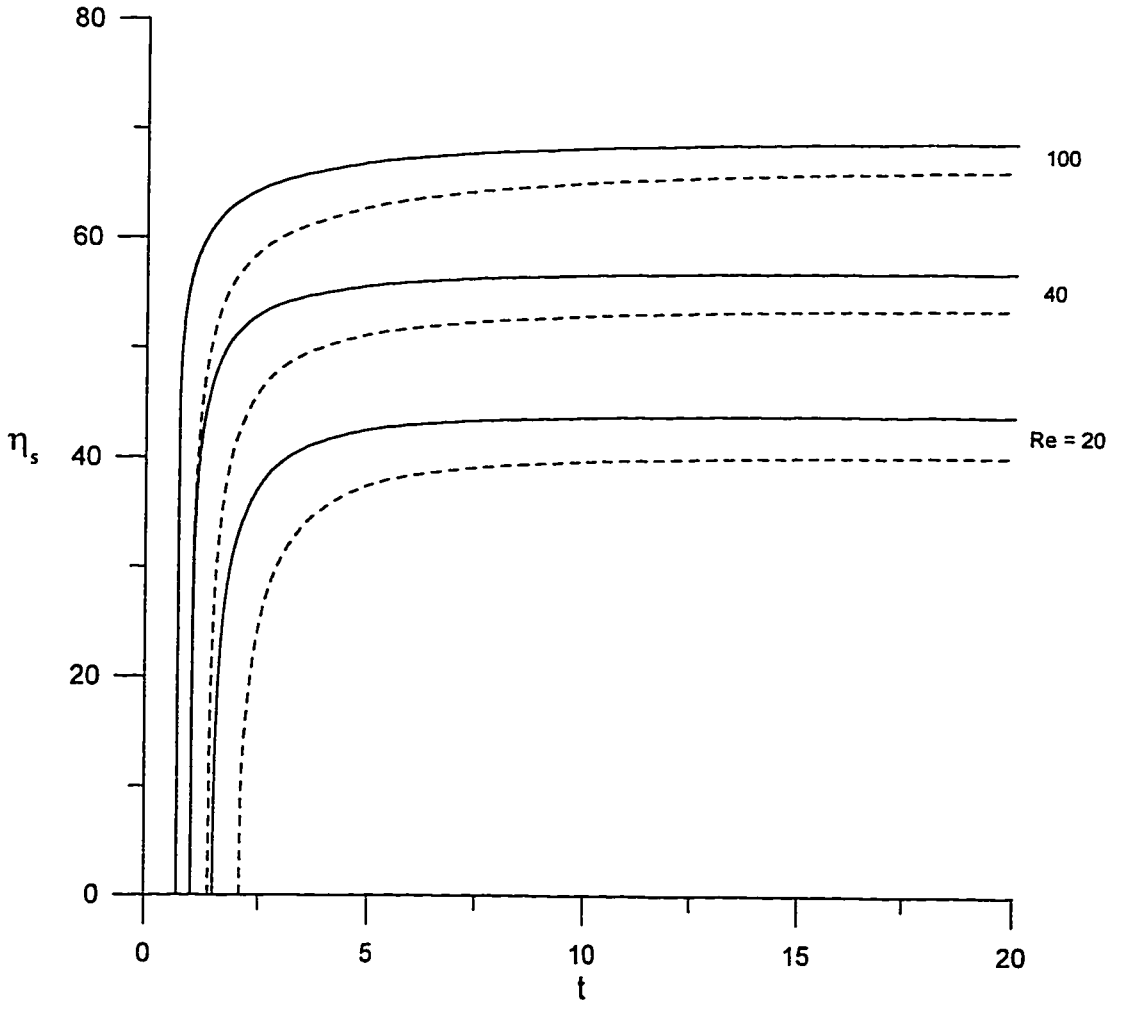

Figure 6.14 The time variation of the separation angle for the cases of $A_r = 0.6$ (solid lines) and $A_r = 0.76$ (dotted lines) at different Reynolds numbers.

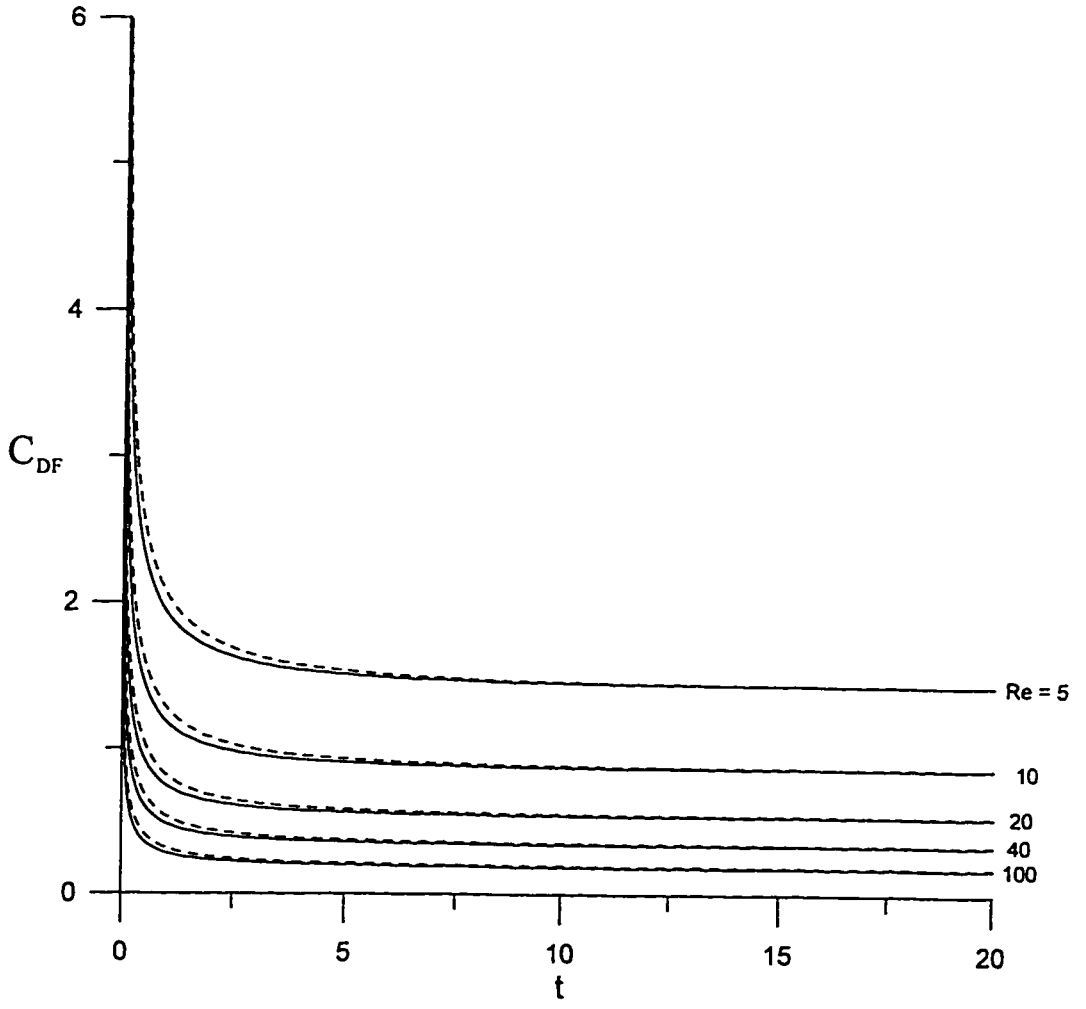

Figure 6.15a The time variation of the friction drag coefficient for the cases of $A_r = 0.6$ (solid lines) and $A_r = 0.76$ (dotted lines) at different Reynolds numbers.

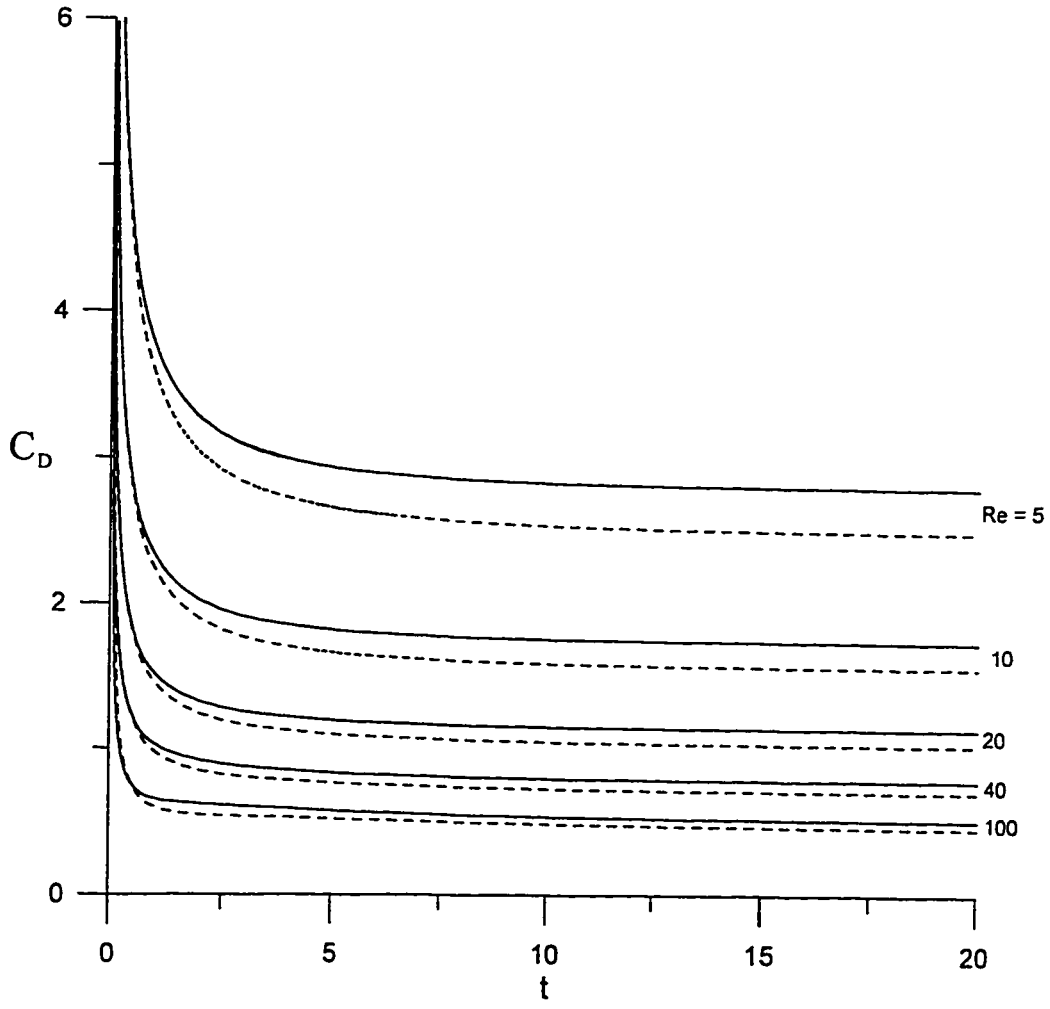

Figure 6.15b The time variation of the total drag coefficient for the cases of $A_r = 0.6$ (solid lines) and $A_r = 0.76$ (dotted lines) at different Reynolds numbers.

The time development of the flow structure near the spheroid surface is shown in figures 6.16a-6.16h for the case of Re = 100, $A_r = 0.6$. The lower half of each figure shows streamlines while the upper half shows equi-vorticity lines. At small times, the viscous effects are limited to the boundary layer region very close to the surface. As time increases, the boundary layer region becomes thicker and the separation bubble starts to appear at approximately t = 1.0 (see figure 6.16c). This separation bubble continued to grow until computations were terminated but with no appreciable change of ς_o or p^* at large times. The growth of the separation bubble with time is represented by the increase of the dimensionless wake length L (L = L′/a, where L′ is the dimensional wake length). Figure 6.17 shows the variation of L with time for the cases of Re = 20, 40, and 100 and for the two geometries ($A_r = 0.6$ and $A_r = 0.76$). Although the wake length reached a constant value for the cases of Re = 20 and 40, it continued to grow for the case of Re = 100 until computations were terminated at t = 20.

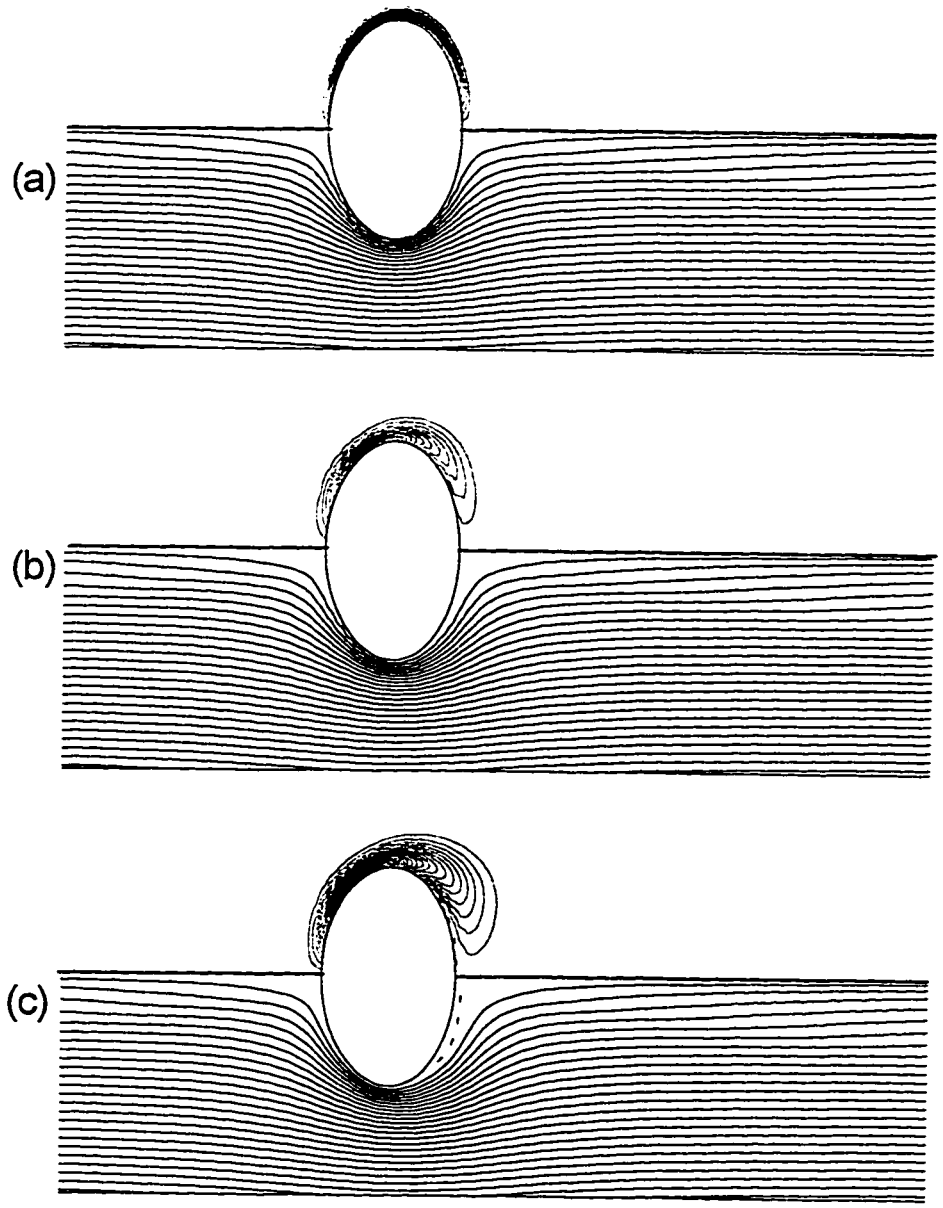

Figure 6.16 (a-c)

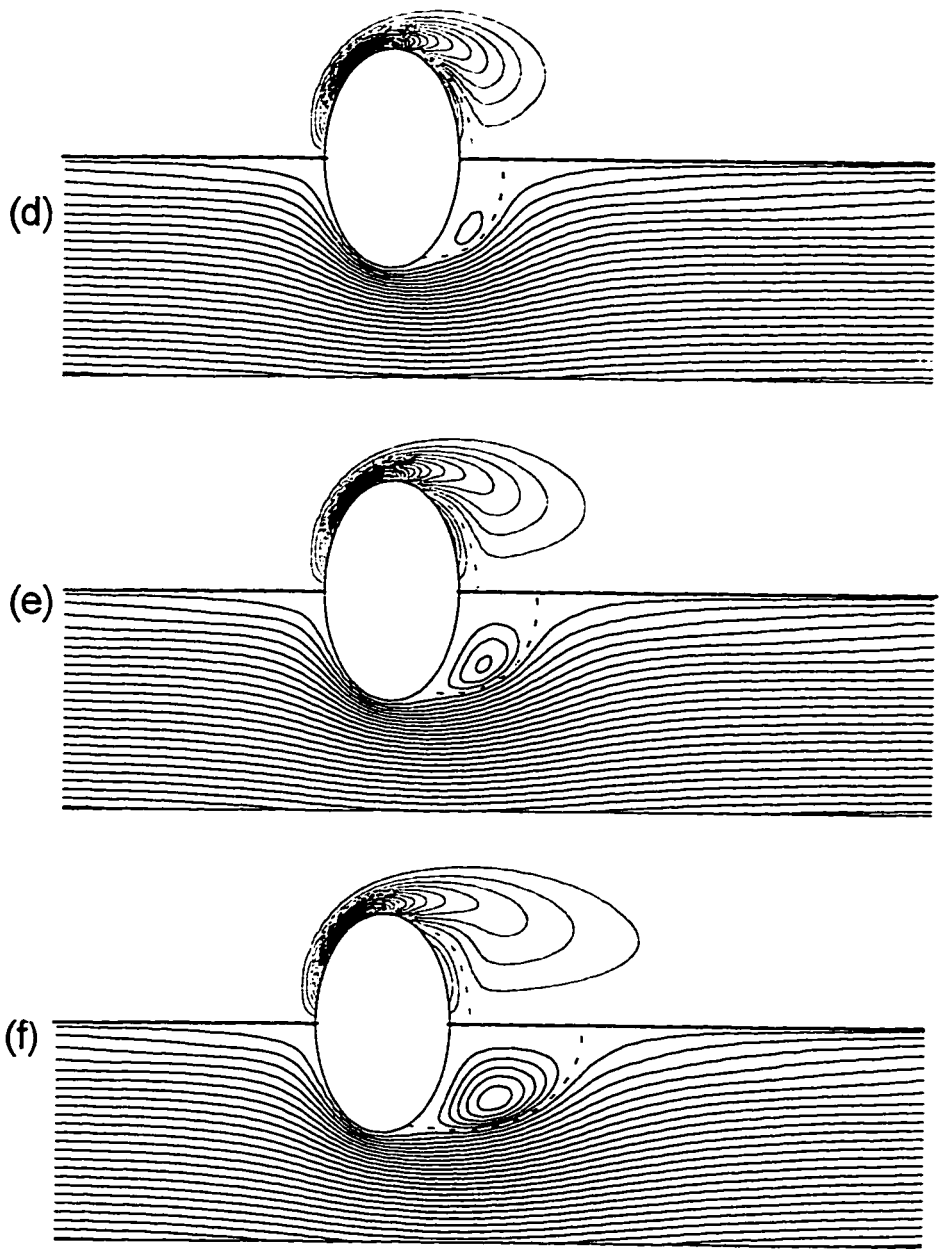

Figure 6.16 (d-f)

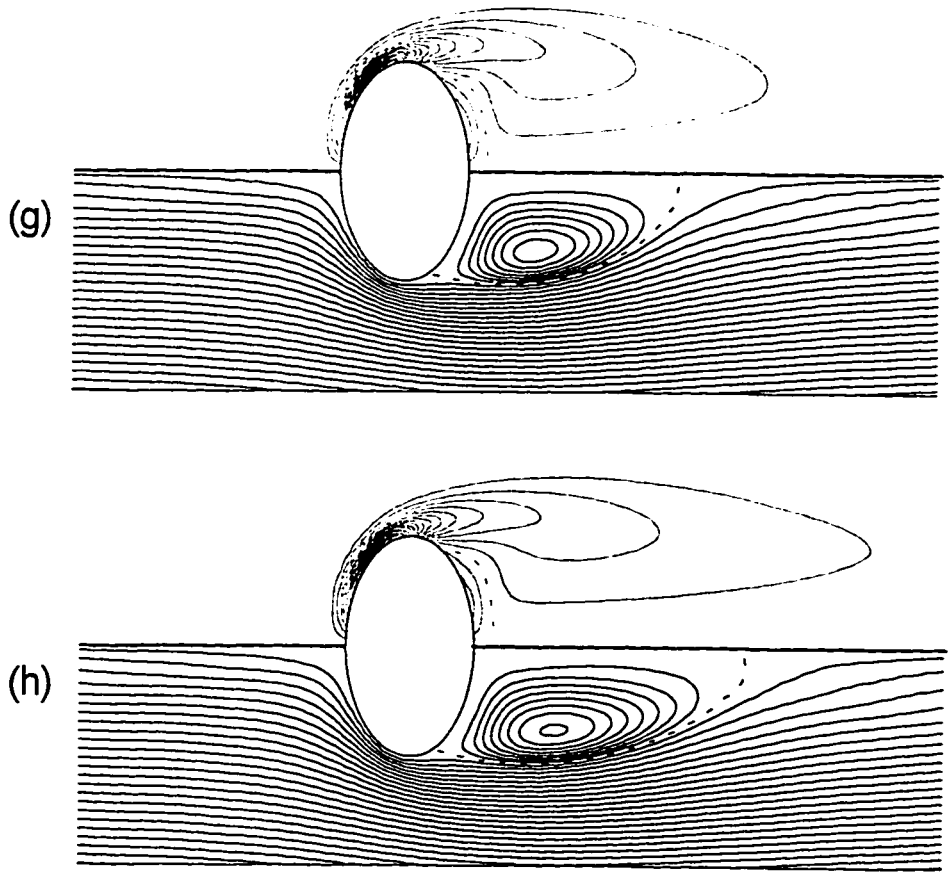

Figure 6.16 (g-h)

Figure 6.16 The streamlines and equi-vorticity lines for the case of Re = 100, A_r = 0.6 at times:
(a) t = 0.1, (b) t = 0.5, (c) t = 1.0, (d) t = 2.0,
(e) t = 3.0, (f) t = 5.0, (g) t = 10.0, (h) t = 20.0.

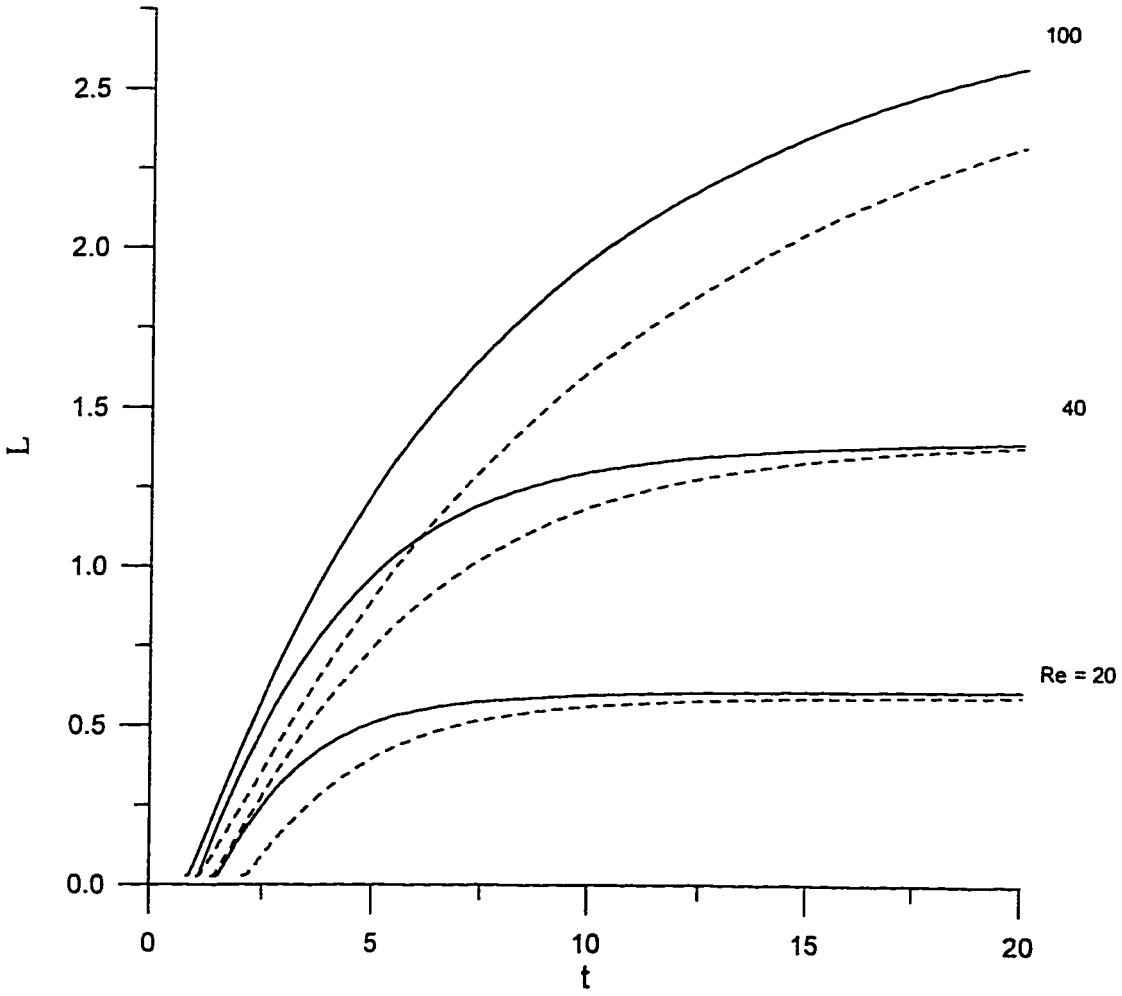

Figure 6.17 The variation of the wake length with time for the cases of $A_r = 0.6$ (solid lines) and $A_r = 0.76$ (dotted lines) at different Reynolds numbers.

6.2.3 Oscillating Flow

This section deals with the problem of oscillating viscous flow over an oblate spheroid that has an axes ratio of 0.6. The effects of the Reynolds and Strouhal numbers on the flow characteristics are studied and compared with previous available solutions. Results are presented for the periodic variation of the drag coefficient, surface vorticity and pressure distributions for Reynolds numbers ranging from 5 to 100 and Strouhal numbers of $\pi/4$, $\pi/2$, and π.

The series truncation method is further tested here in the context of oscillating flow over oblate spheroids by comparing the present results against the analytical unsteady Stokes flow solution given by Lai and Mockros (1972), hereinafter referred to as the LM study. The approximate force given by the LM study for an oblate spheroid moving with an arbitrary velocity u(t) along its axis of symmetry in a viscous fluid takes the form

$$-\frac{4}{3}\pi a^2 b\rho\left[\frac{(\lambda_o^2+1)q_1}{1-(\lambda_o^2+1)q_1}\right]\frac{du}{dt}-\frac{8\pi\mu bu}{\lambda_o\kappa}-\frac{32\pi a^2\rho}{3(\lambda_o^2+1)\kappa^2}\left(\frac{\nu}{\pi}\right)^{1/2}\int_{-\infty}^{t}\frac{du(\tau)/d\tau}{(t-\tau)^{1/2}}d\tau \qquad (6.36)$$

where $\lambda_o=\sinh\xi_o$, $q_1=1-\lambda_o\cot^{-1}\lambda_o$, and $\kappa=\lambda_o-(\lambda_o^2-1)\cot^{-1}\lambda_o$.

Equation (6.36), when written in terms of the notation in the present study and regarding the flow as oscillating and the spheroid at rest, takes the form

$$C_{DLM}=\frac{4}{3}F_1(\lambda_o)S\cos(St)+\frac{16}{Re}F_2(\lambda_o)\sin(st)-\frac{64}{3}F_3(\lambda_o)\sqrt{\frac{S}{2Re}}\cos(St+\frac{3\pi}{4}) \qquad (6.37)$$

where $F_1(\lambda_o)=\dfrac{\lambda_o}{\sqrt{1+\lambda_o^2}\left[1-(1+\lambda_o^2)q_1\right]}$, $F_2(\lambda_o)=\dfrac{1}{\kappa(1+\lambda_o^2)}$, and $F_3(\lambda_o)=\dfrac{1}{\kappa^2(1+\lambda_o^2)}$

C_{DLM} is the dimensionless pressure coefficient corresponding to the LM study. The first term on the right hand side of equation (6.37) is the potential flow drag, the second is the viscous drag, and the third is the history term. The formula is very similar to that derived

by Basset (1888) for the sphere case. In fact, in the limit as $\xi_o \to \infty$, the two formulas are identical.

The time variations of C_D and C_{DLM} for Re = 5, and 10 when $S = \pi / 4$ are shown in figure 6.18. An excellent agreement between the present results and the LM study can be observed. The agreement is better for lower Reynolds numbers as expected. Figure 6.19 shows that the difference between the two formulas for Re = 5 at the three levels of the Strouhal numbers considered in this study is sinusoidal. Lawrence and Weinbaum (1988) noted that the LM formula is valid for small frequency. Figure 6.19 confirms this by showing a larger relative deviation from the LM study for higher Strouhal numbers. Figure 6.20 shows the time variation of C_D for Re = 5, 10, 20, 40, and 100 when $S = \pi / 4$ over the first three cycles. The corresponding potential flow solution is also plotted. The two components of the drag C_{DF} and C_{DP} are shown in figures 6.21 and 6.22. It can be observed that C_D, C_{DF}, and C_{DP} exhibit phase lead over the free stream velocity profile. This is, similar to the sphere case, attributed to the separation of the flow during the decelerated period of the flow oscillation. This phase lead increases at higher Reynolds numbers. The figures also show that the effect of Re on C_{DF} amplitude is considerable while its effect on C_{DP} is much less. Table 6.5 presents the phase angle at which the drag components change sign. The free stream changes sign at $\Phi = \pi$. The phase lead of the drag components increases as Reynolds and Strouhal numbers increase. The same conclusions drawn in the case of the sphere can be made here for oblate spheroids. Figures 6.23 and 6.24 show the drag coefficient for the case Re = 40 at the three levels of S considered in this study, and the relative deviation from the potential flow drag, respectively. Obviously, the deviation is less for increasing Strouhal number.

Figure 6.25 shows the time variation of the surface pressure distribution for the case $S = \pi / 4$ and Re = 100 during one-half of a complete oscillation. It is important to note that the curve $\Phi = \pi / 2$ corresponds to $U = U_{max}$ at which the inertia effect is zero

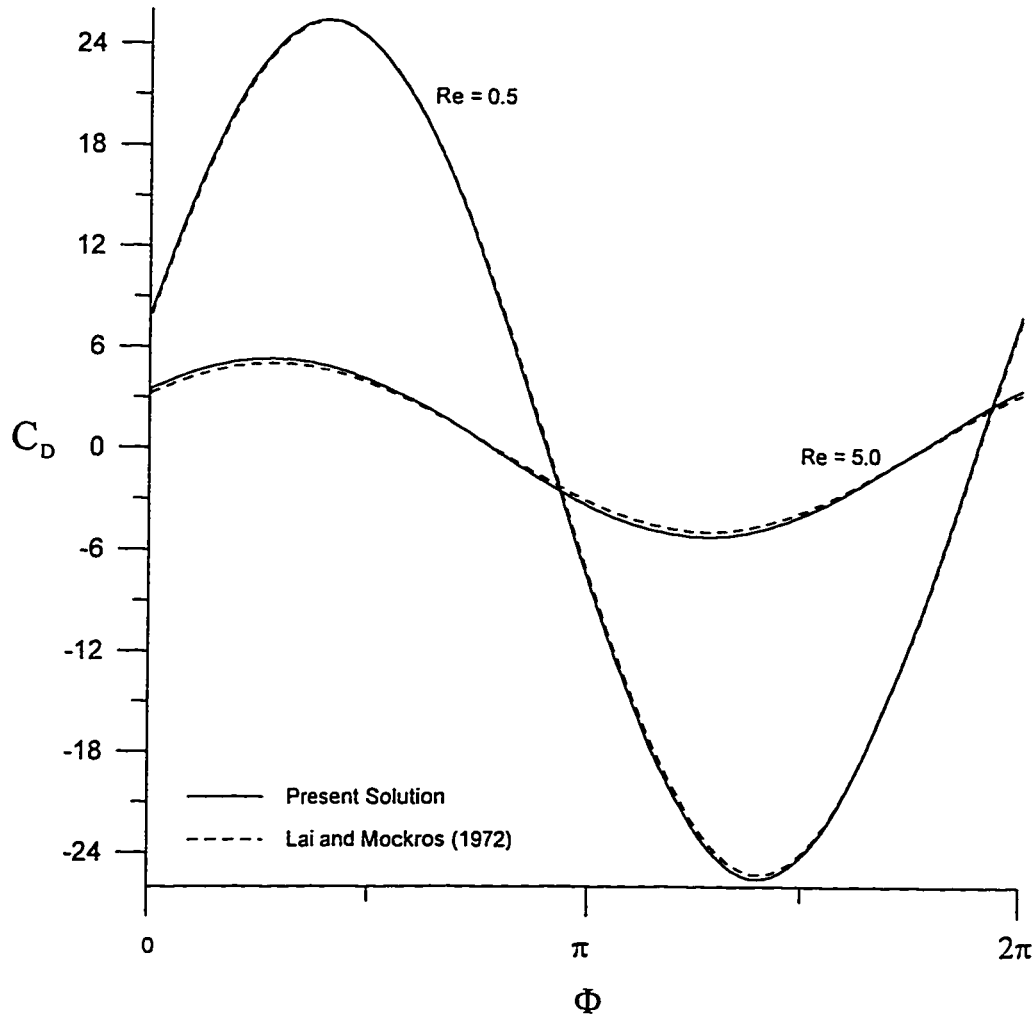

Figure 6.18 The time variation of the drag coefficient for the cases Re = 0.5, and 5.0 at $S = \pi/4$.

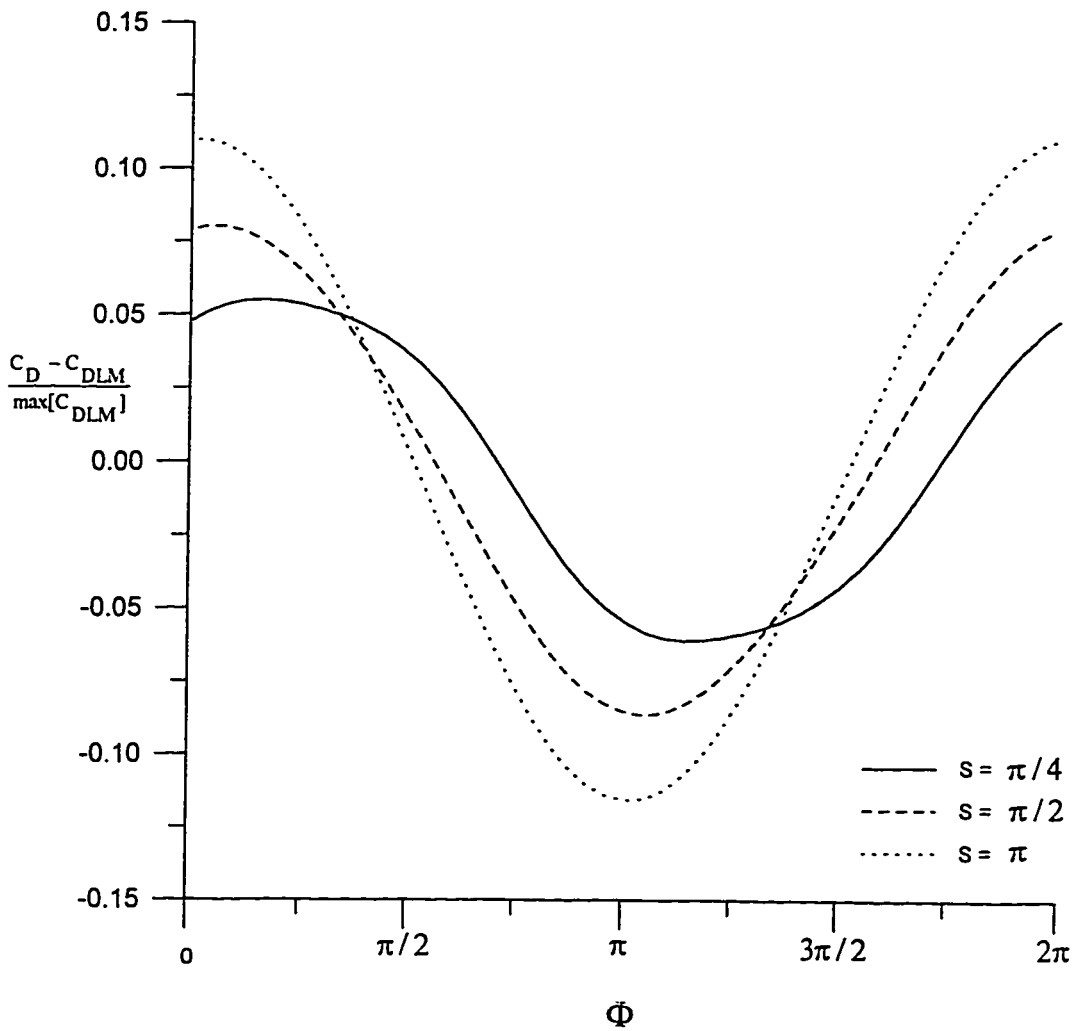

Figure 6.19 $\frac{C_D - C_{DLM}}{max[C_{DLM}]}$ versus Φ for the case , Re = 5

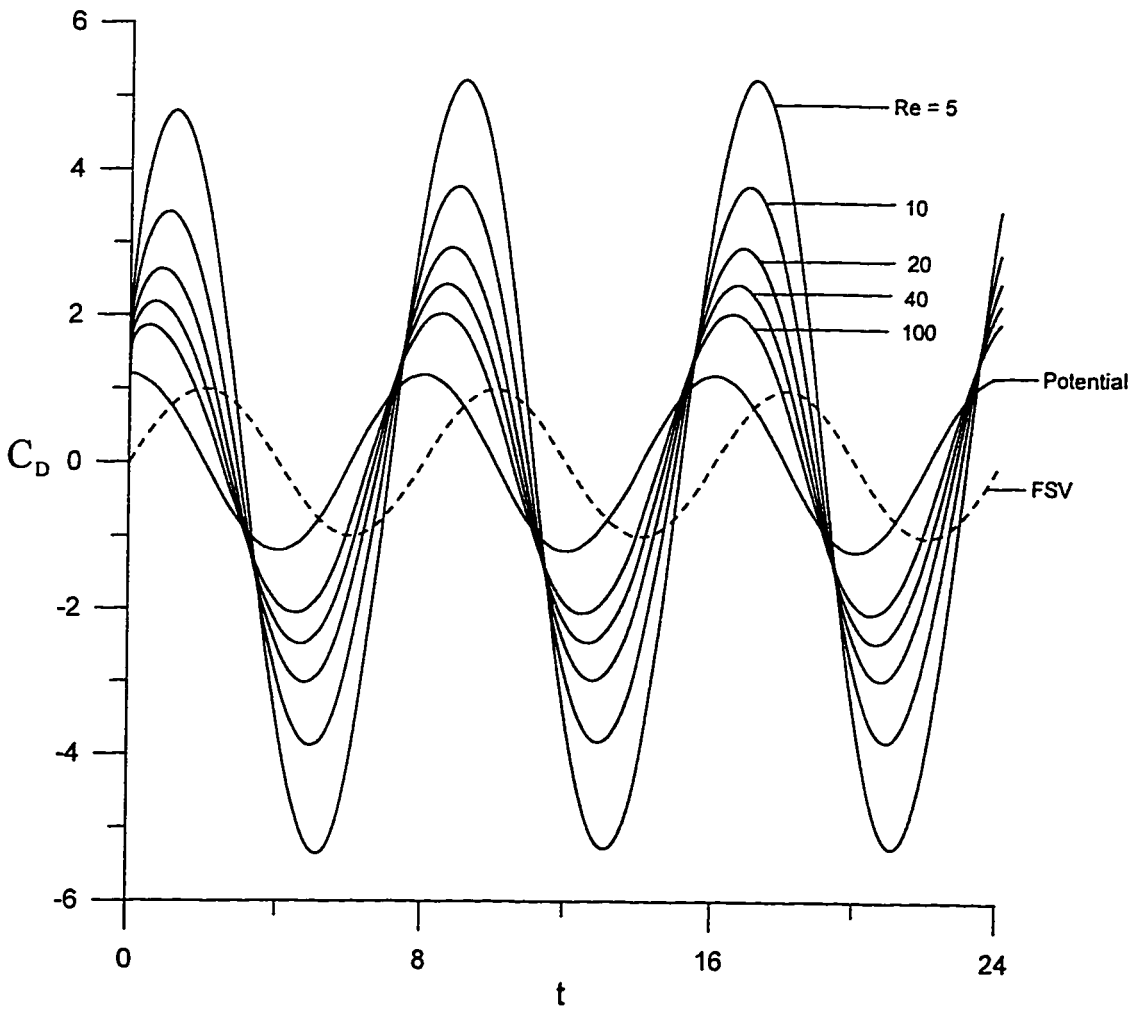

Figure 6.20 The time variation of the drag coefficient for the case, $S = \pi/4$ at different Reynolds numbers (FSV = Free Stream Velocity)

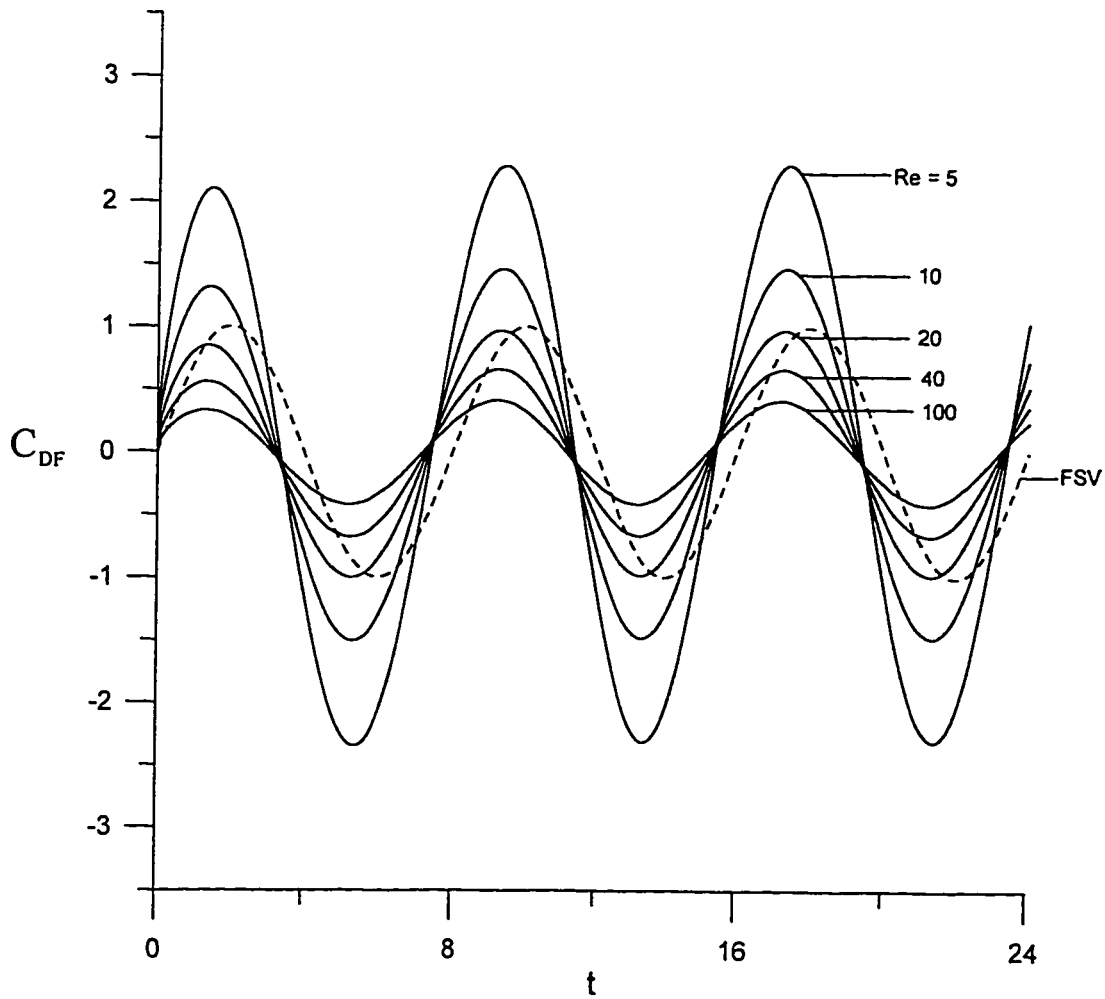

Figure 6.21 The time variation of the friction component of drag for the case, S = $\pi/4$ at different Reynolds numbers (FSV = Free Stream Velocity)

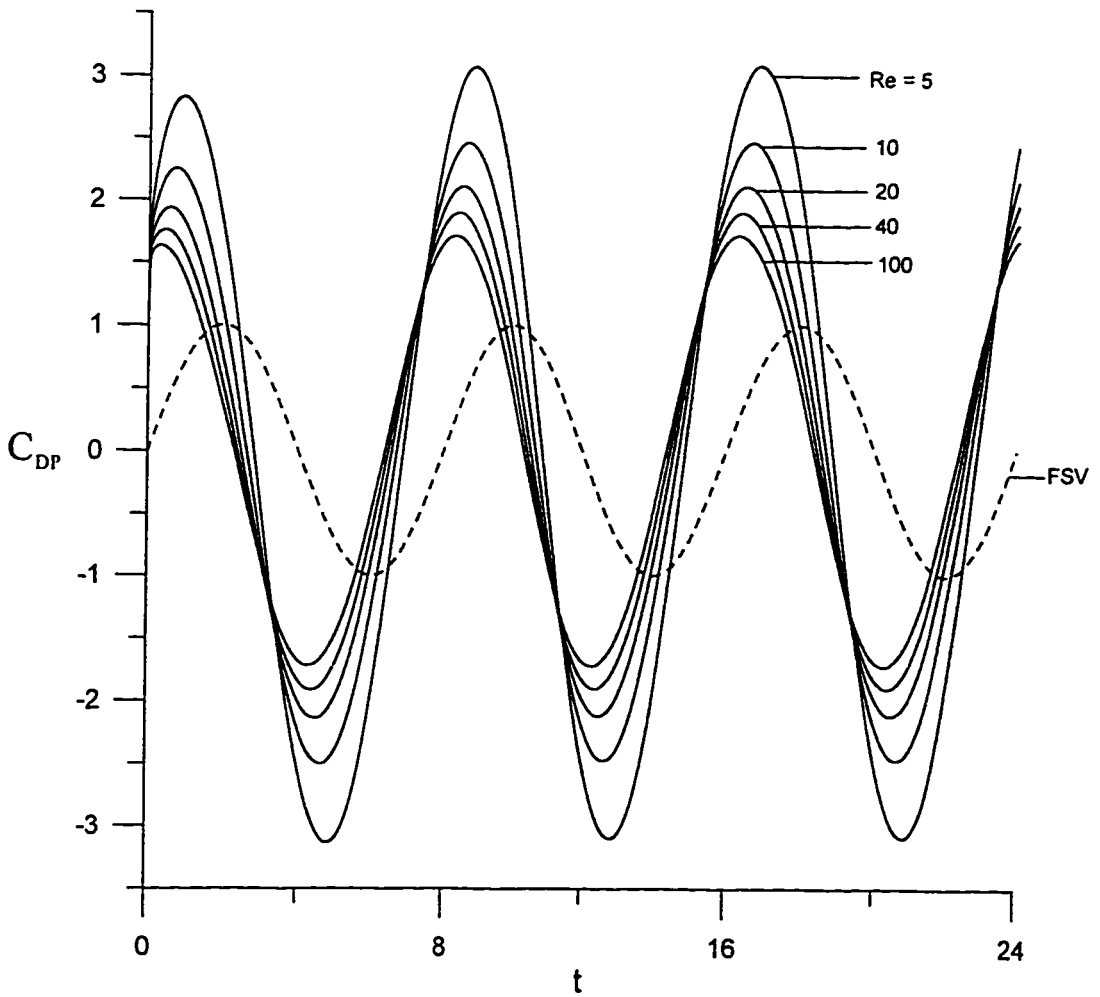

Figure 6.22 The time variation of the pressure component of drag for the case, $S = \pi/4$ at different Reynolds numbers (FSV = Free Stream Velocity).

Table 6.5 Phase angles at which drag components change sign

Re	S	Φ_D	Φ_{DF}	Φ_{DP}	Φ_S
5	π	2.102	2.535	1.914	2.231
10	π	1.982	2.494	1.820	2.199
20	π	1.885	2.463	1.754	2.152
40	π	1.812	2.440	1.710	2.089
100	π	1.754	2.420	1.684	2.026
5	$\pi / 2$	2.255	2.597	2.056	2.183
10	$\pi / 2$	2.122	2.551	1.934	2.089
20	$\pi / 2$	2.009	2.515	1.845	1.979
40	$\pi / 2$	1.916	2.485	1.782	1.885
100	$\pi / 2$	1.836	2.448	1.745	1.773
5	$\pi / 4$	2.424	2.673	2.240	2.183
10	$\pi / 4$	2.295	2.625	2.101	1.916
20	$\pi / 4$	2.177	2.585	1.995	1.744
40	$\pi / 4$	2.072	2.545	1.915	1.587
100	$\pi / 4$	1.951	2.478	1.833	1.335

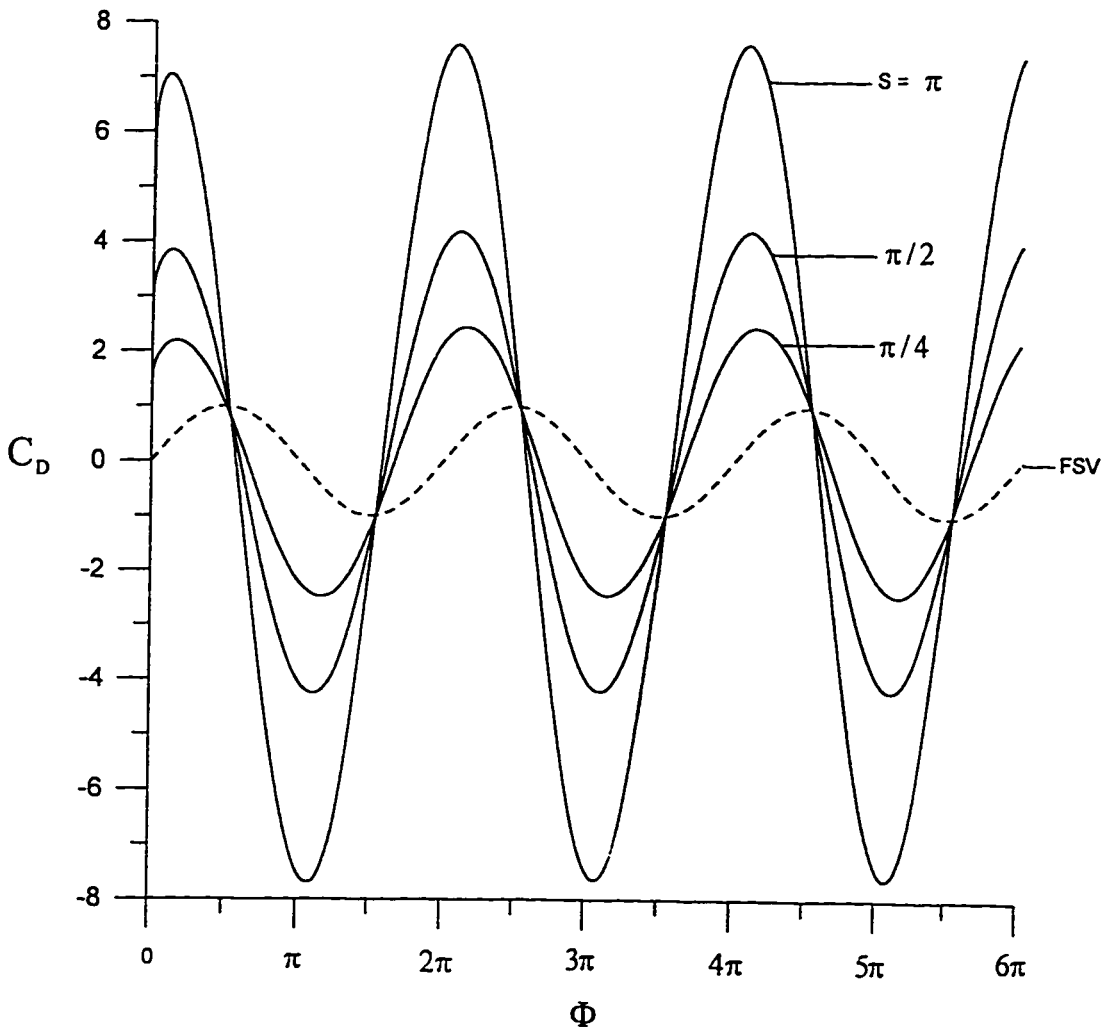

Figure 6.23 The time variation of the drag coefficient for the case, Re = 40 at different Strouhal numbers (FSV = Free Stream Velocity)

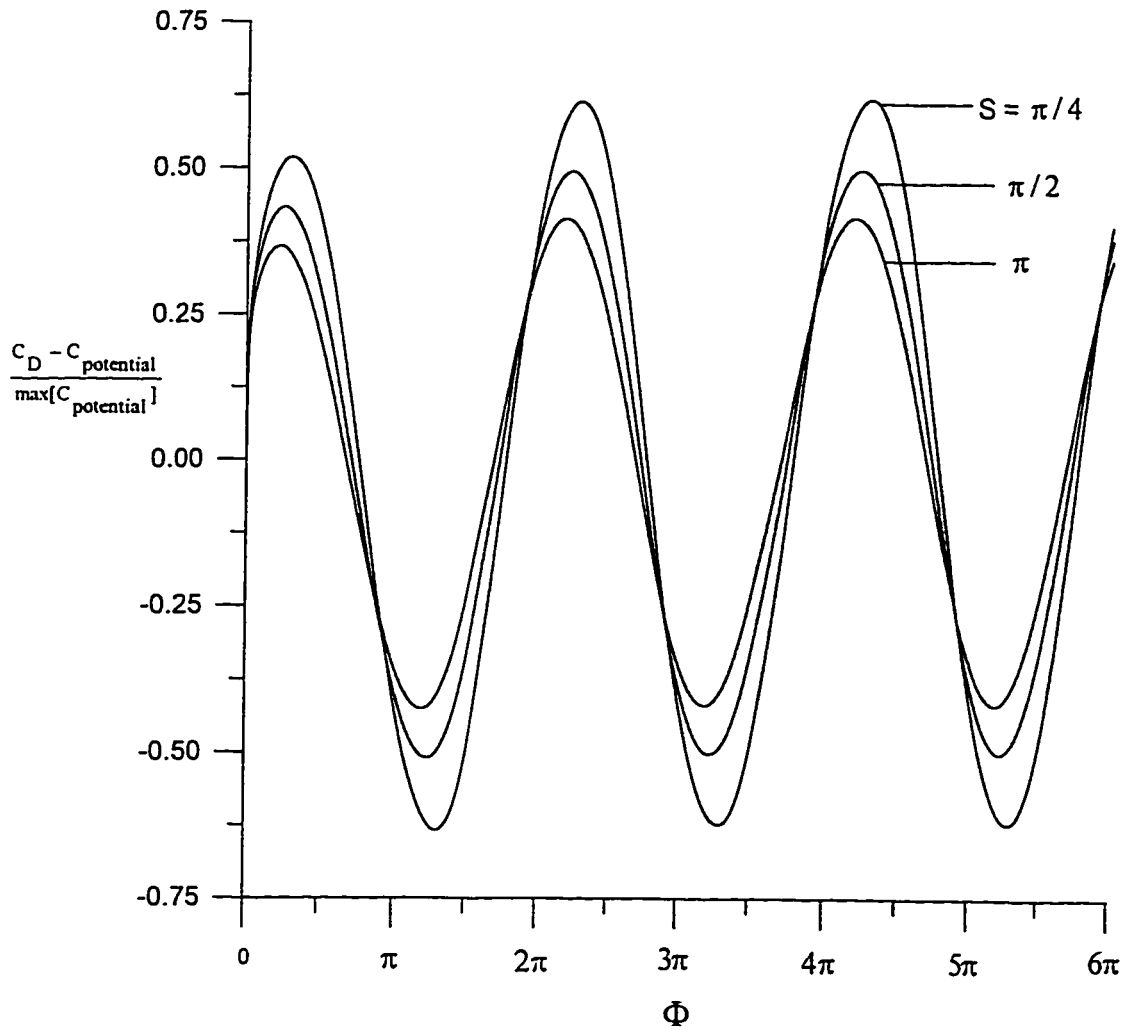

Figure 6.24 The relative difference between the drag coefficient for the case, Re = 40 and the potential flow drag at different Strouhal numbers

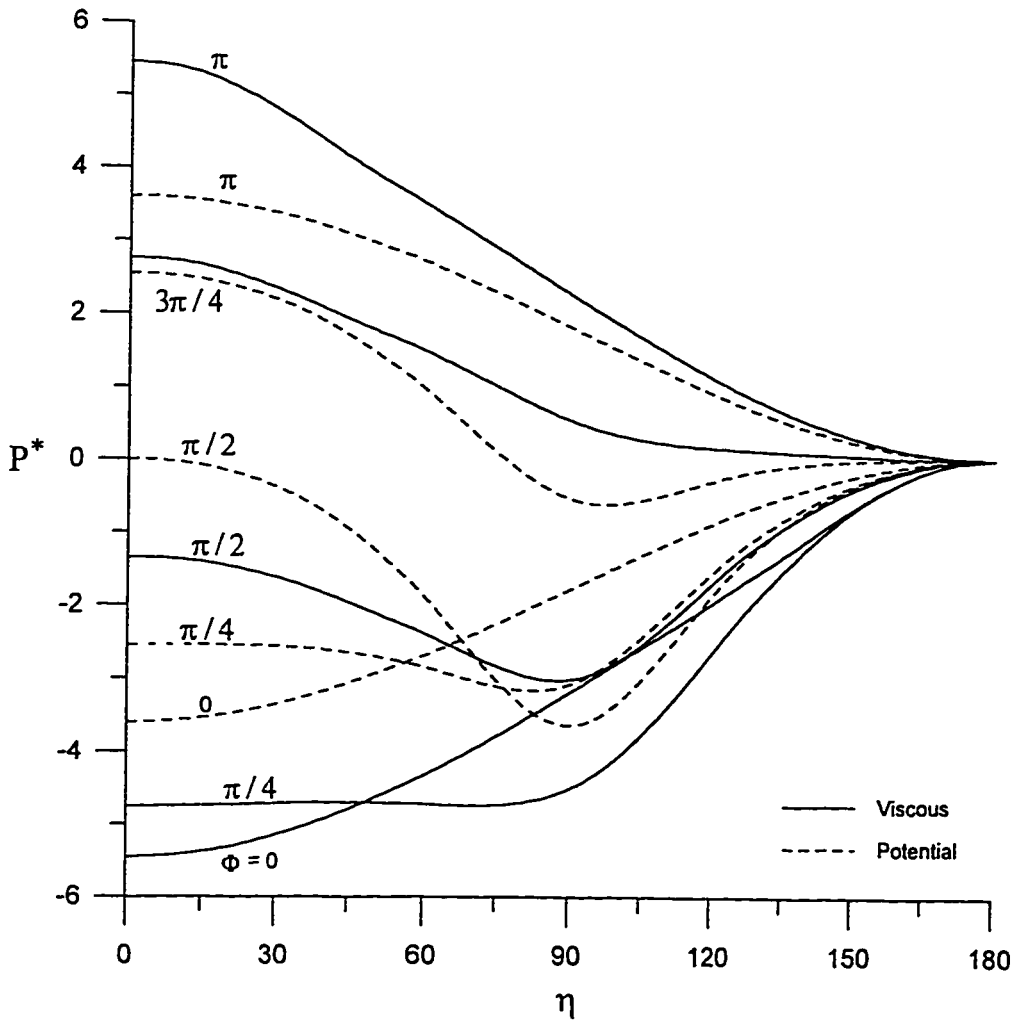

Figure 6.25 The time variation of the pressure coefficient during one half of a complete oscillation for the case Re = 100, S = $\pi/4$.

and those at $\Phi = 0, \pi$ correspond to $U = 0$ at which the inertia effect is maximum. On the same figure, the corresponding inviscid flow pressure distributions are plotted. As can be seen in figure 6.25, the viscous and inviscid flow pressure distributions are in their best agreement at $\Phi = 3\pi / 4$. The corresponding surface vorticity distribution during one-half of an oscillation cycle is shown in figure 6.26. An interesting feature of figure 6.26 is that the curve for $\Phi = \pi / 2$ crosses the x-axis which indicates that separation has already started during the acceleration part of the motion. In the CM study, separation was only observed during the decelerating part of the motion due to the low Reynolds numbers considered in their study. In this study, for the range of Reynolds and Strouhal numbers considered, separation during the accelerating part was only observed for the case of Re =100, and $S = \pi / 4$ which indicates that for higher Reynolds and lower Strouhal numbers separation can occur during the accelerating as well as the decelerating parts of motion. Figure 6.27 compares the surface vorticity for different Reynolds numbers when $S = \pi / 4$ at $\Phi = 3\pi / 4$. While the separation region for Re = 100 has traveled a long distance towards the front stagnation point ($\eta = 0$), the separated region for Re = 5 has just started. Figure 6.28 indicates that the effect of the Strouhal number on surface vorticity of the case Re = 20 is limited at $\Phi = 3\pi / 4$ as compared to its effect at other phase angles. The same trend was observed at other Reynolds numbers.

Figure 6.29 shows the time development of the streamline patterns over one-half of a complete oscillation for the case Re = 100 and $S = \pi / 4$. The half cycle shown starts at the maximum velocity ($\Phi = \pi / 2$) and ends at the minimum velocity ($\Phi = 3\pi / 2$). It is chosen such that the deceleration effects are clearly observed. Figure 6.29a (t=18.0) which corresponds to $\Phi = \pi / 2$, shows a small separated region near the rear stagnation point. A small positive vorticity is also observed next to the dominating negative vorticity. This means that the separated flow region started to form during the accelerating part of motion. As time progresses, the separation bubble grows until it eventually surrounds the oblate spheroid even before the free-stream velocity reverses direction. Simultaneously, the positive vorticity grows and the negative outer region of vorticity detaches from the

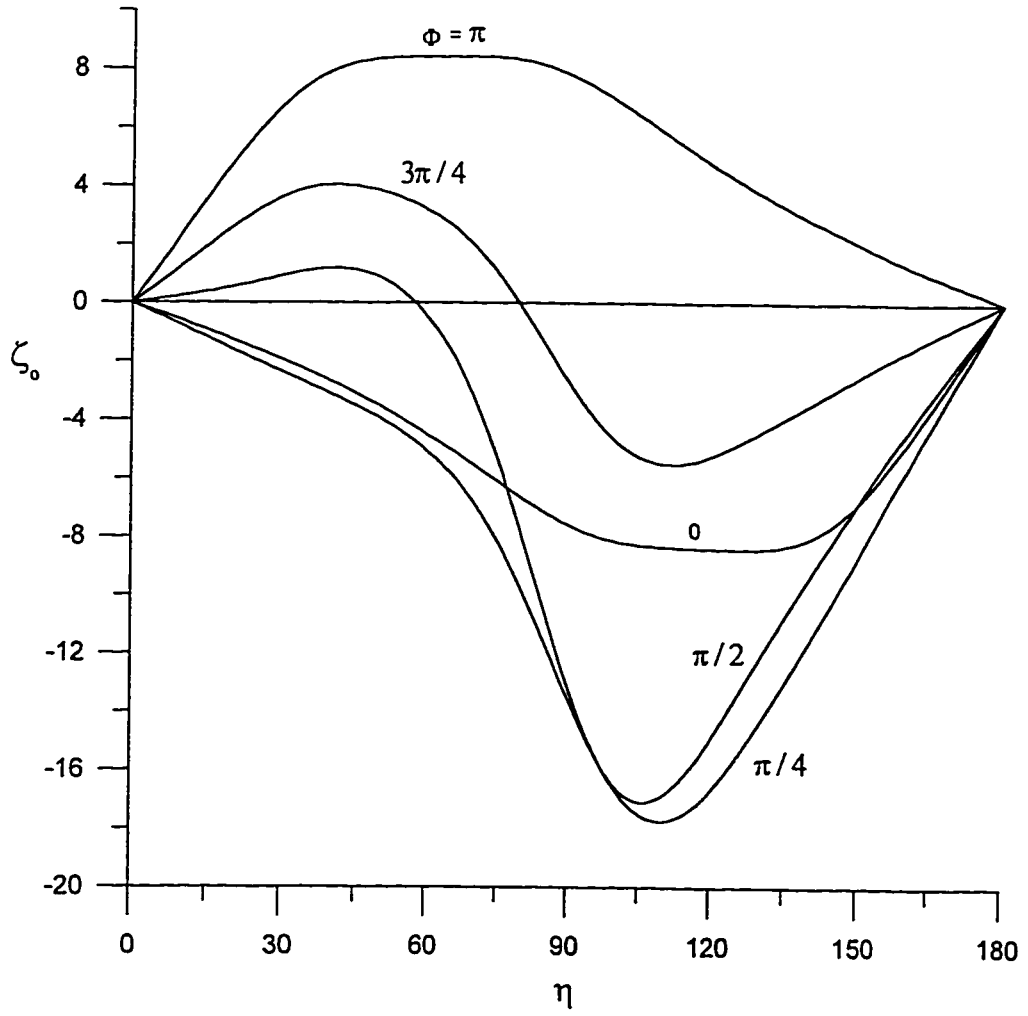

Figure 6.26 The time variation of the surface vorticity during one half of a complete oscillation for the case Re = 100, S = $\pi/4$.

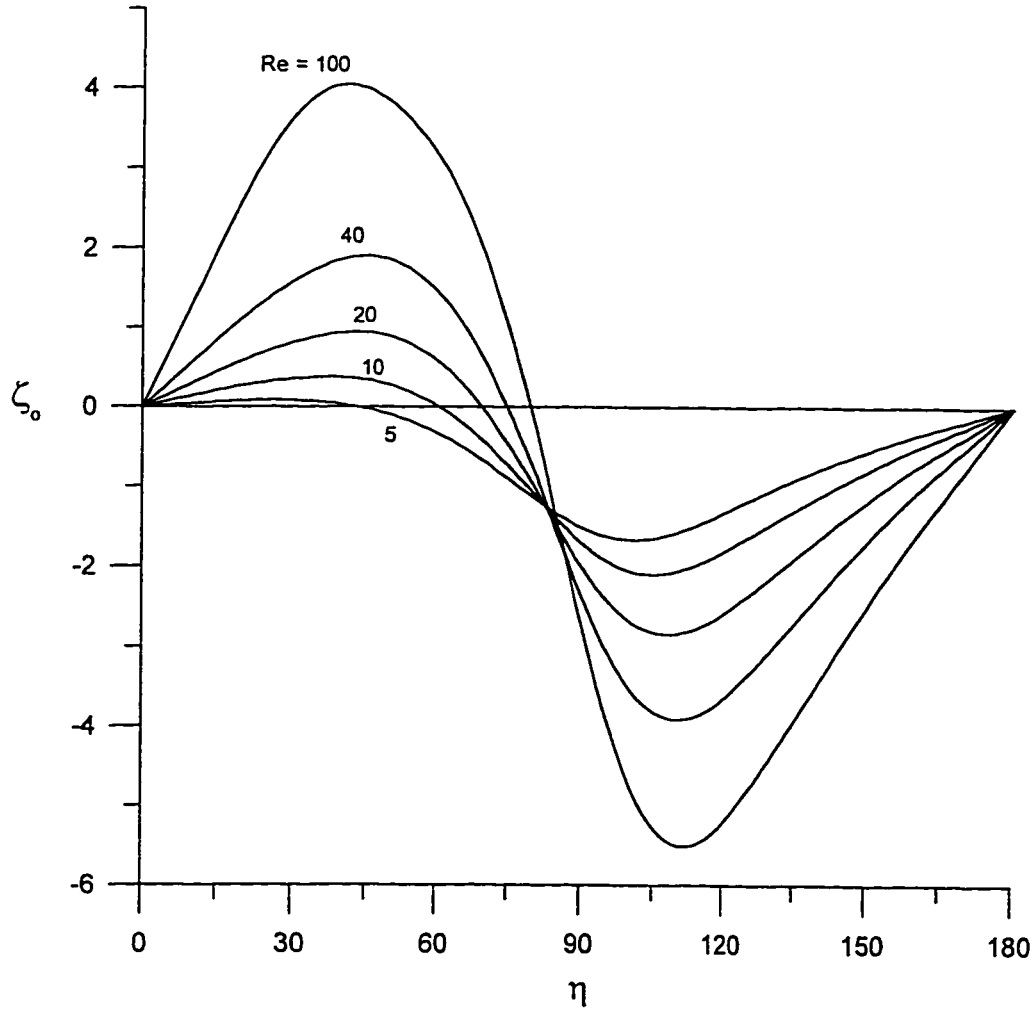

Figure 6.27 Comparison of the surface vorticity at phase angle = $\pi/4$ for the case S = $3\pi/4$.

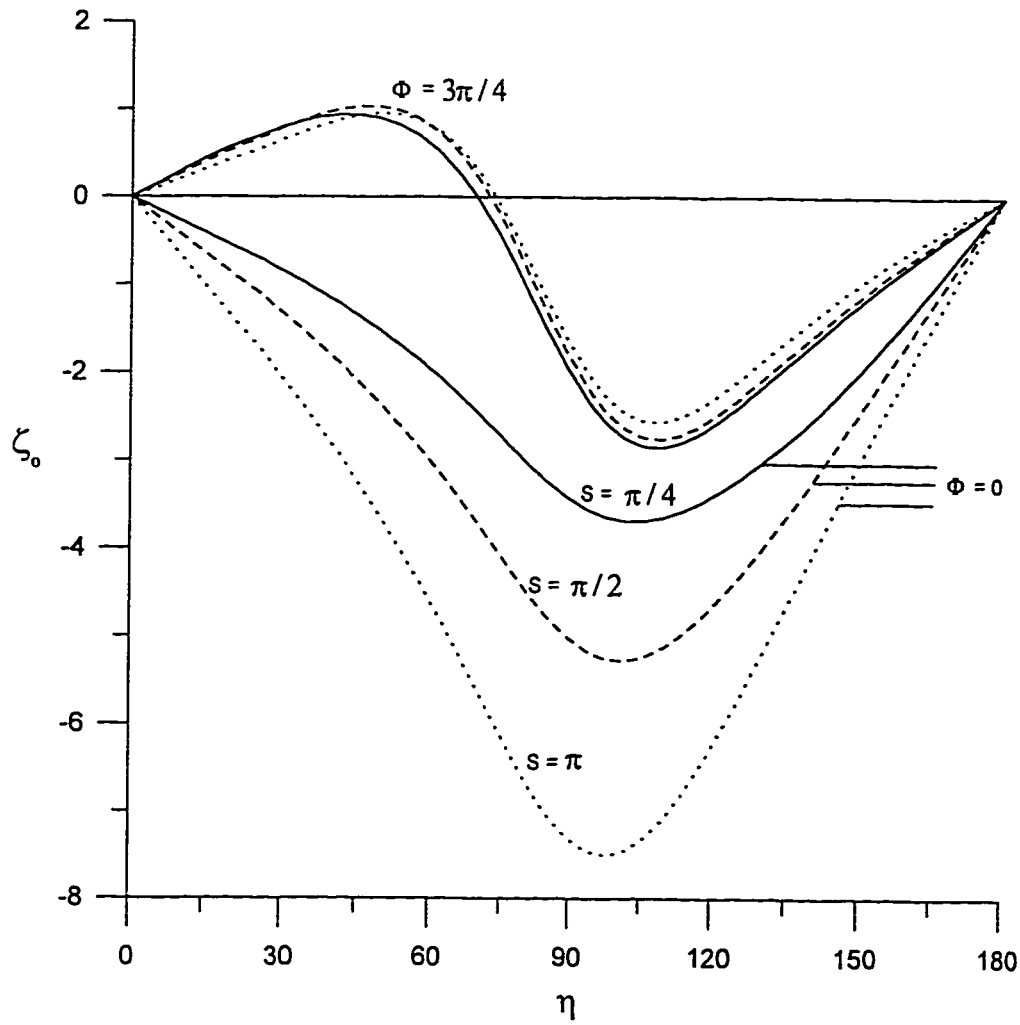

Figure 6.28 Comparison of the surface vorticity at phase angles of 0, and $3\pi/4$ for the case Re = 20 at different S values.

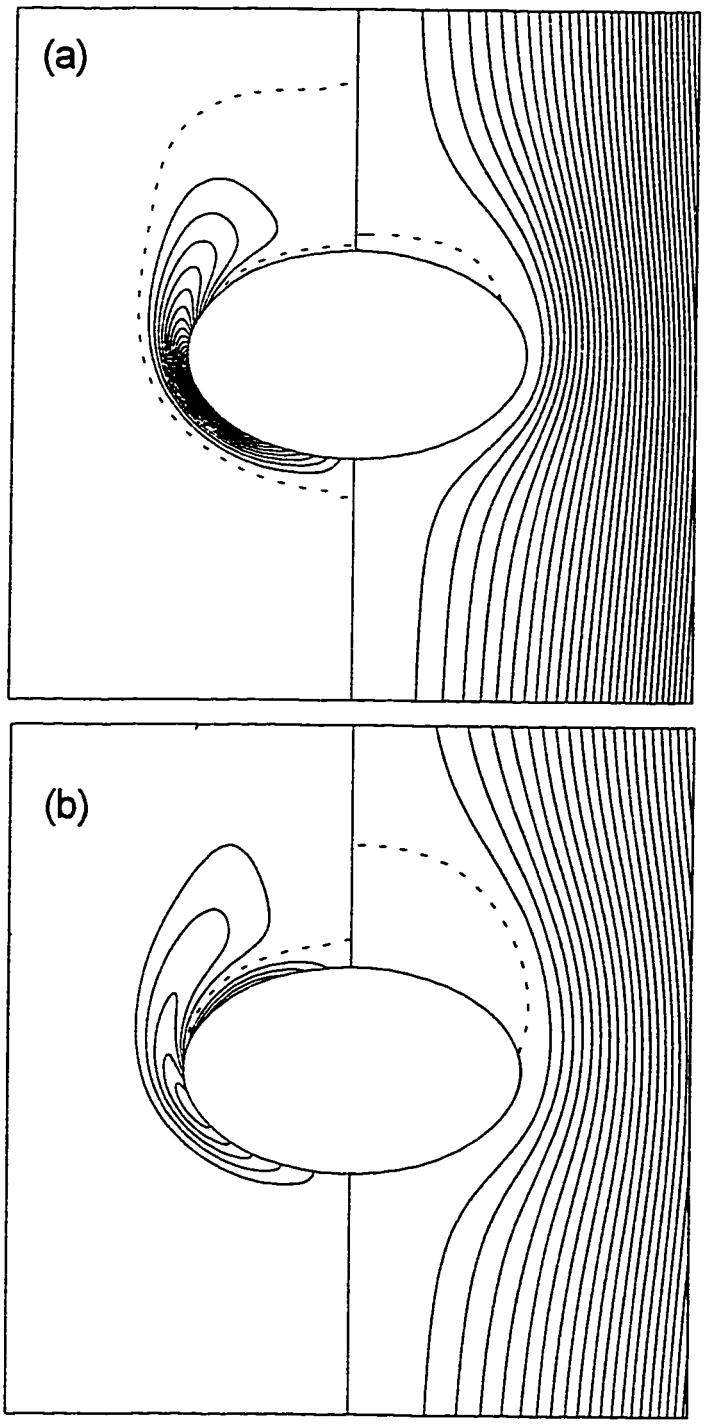

Figure 6.29 (a, b)

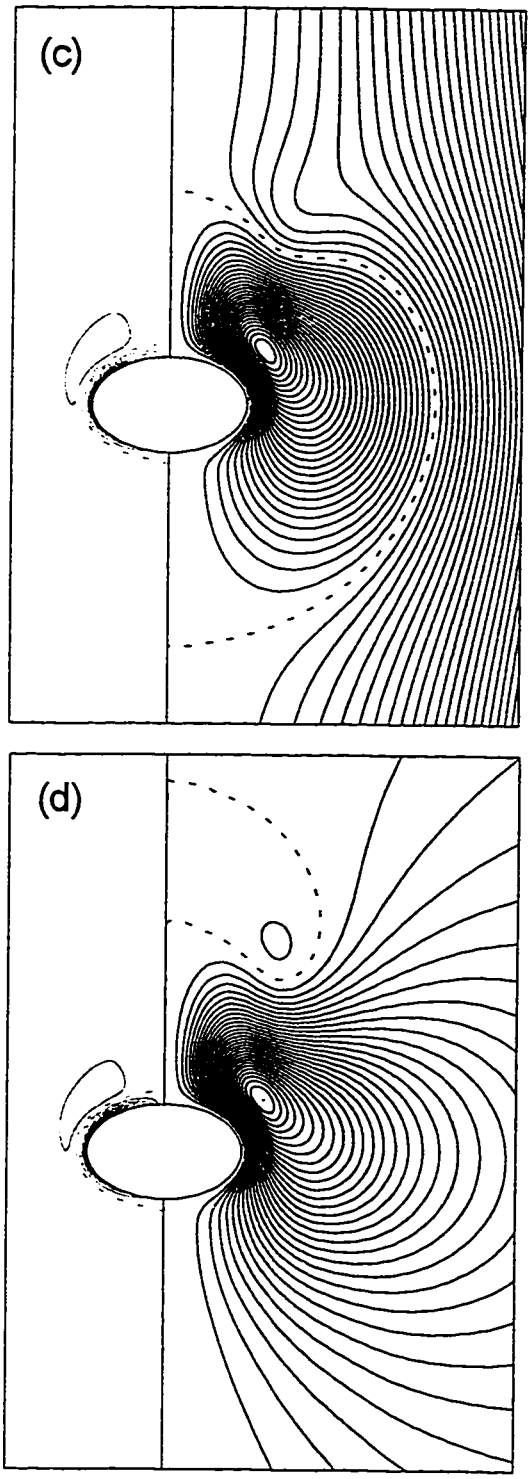

Figure 6.29 (c, d)

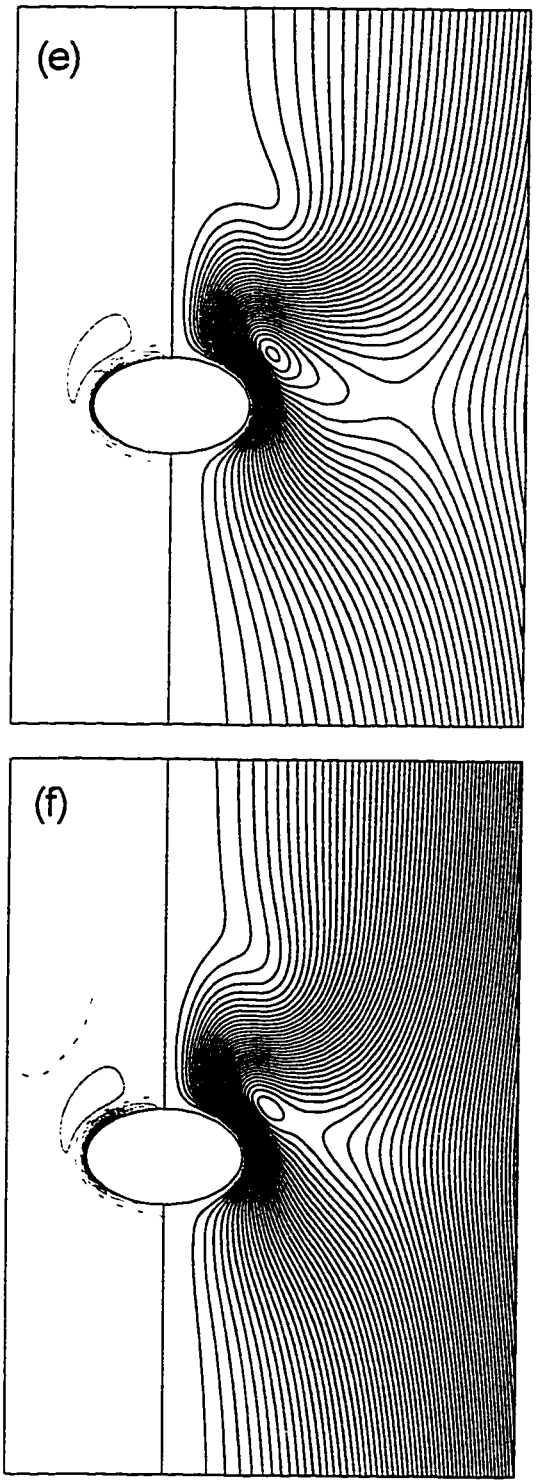

Figure 6.29 (e, f)

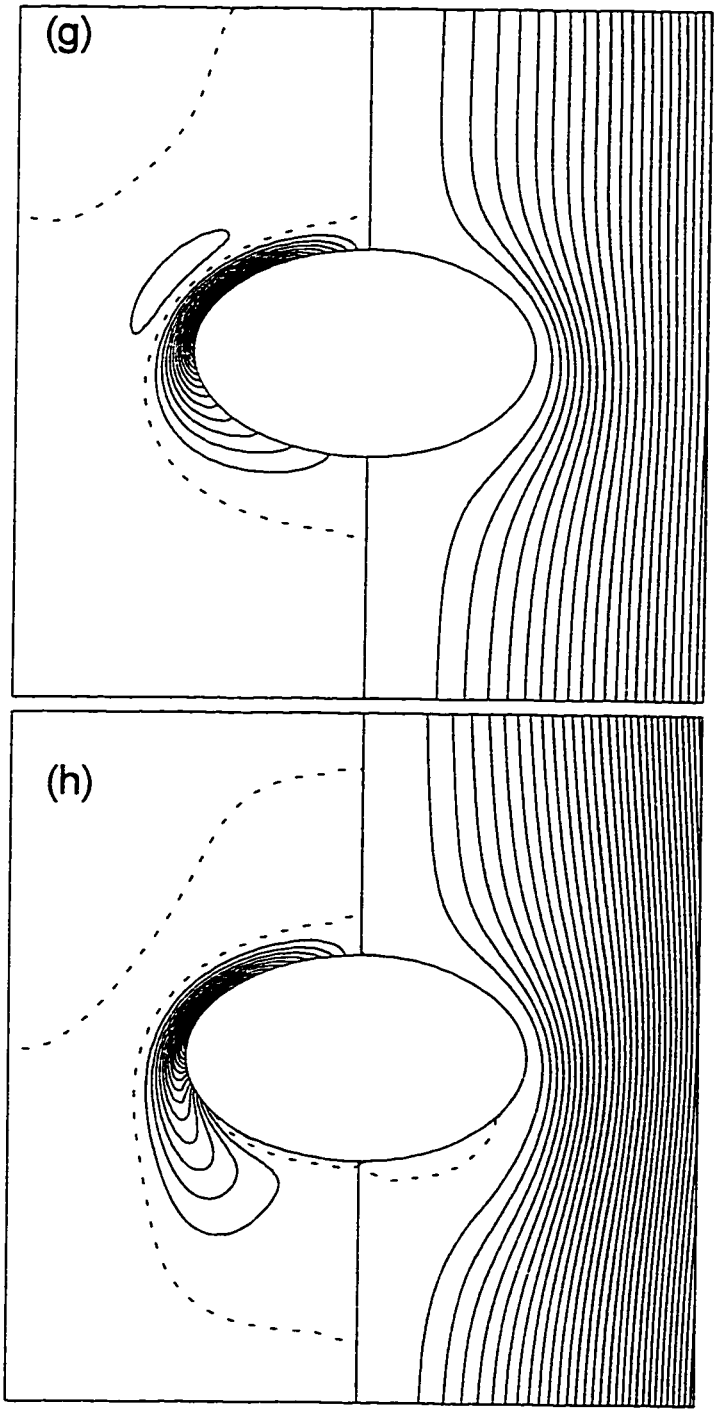

Figure 6.29 Streamlines and vorticity development with time for the case Re = 100, S = $\pi/4$. $\Delta\psi$ for a,b,g,h =0.1. Others = 0.01. $\Delta\zeta$=1.0 (a) t = 18, (b) t = 19, (c) t = 19.98, (d) t = 20, (e) t = 20.02, (f) t = 20.04, (g) t = 21, (h) t = 22. Dotted lines indicate zero values.

spheroid. When the free-stream velocity is zero, the streamline pattern will be as shown in figure 6.29d where two vortices are counter rotating near the spheroid. The streamlines will then follow the new direction of motion and the counter rotating vortices die out as the flow accelerates in the other direction. The streamlines will then become similar to potential flow until a separation bubble is formed on the other end of the spheroid causing a mirror-image behavior in the following half of the oscillation. During this process, the detached vorticity region subsides and the inner one grows until the velocity peaks again causing another inner vorticity region to be created on the surface and the process is repeated.

When the free-stream velocity decelerates, the region of recirculation travels upstream until it encompasses the whole spheroid. Figure 6.30 compares the time development of the separation angle for different Reynolds numbers. It is evident from the figure that for higher Re, the separation occurs earlier and the bubble takes longer time to encompass the whole spheroid. Table 6.5 lists the phase angles at which separation is first observed (Φ_s). It is clear that increasing Re or decreasing S will result in a lower Φ_s. Figure 6.31 compares the separation angle for Re = 40 number at different Strouhal numbers. At small phase angles, the separation angle is higher for lower Strouhal numbers. As time progresses, higher Strouhal number-flows exhibit larger separation angles. The figure shows that close to $\Phi = 3\pi/4$, the separation angle for a fixed Reynolds number is not a function of the Strouhal number. This was also observed at other Reynolds numbers.

The length of the separation bubble measured from the spheroid surface at $\eta = 0$ for different cases are plotted in figures 6.32 and 6.33. It is clear from the curves that lower Strouhal numbers will result in longer separated regions. The behavior at the same Strouhal number but different Reynolds numbers is not uniform through the deceleration portion of motion. Figure 6.32 shows the length of the separated region for Re of 5, 10, 20, 40, and 100 when $S = \pi/4$. At early phase angles, higher Re will produce longer

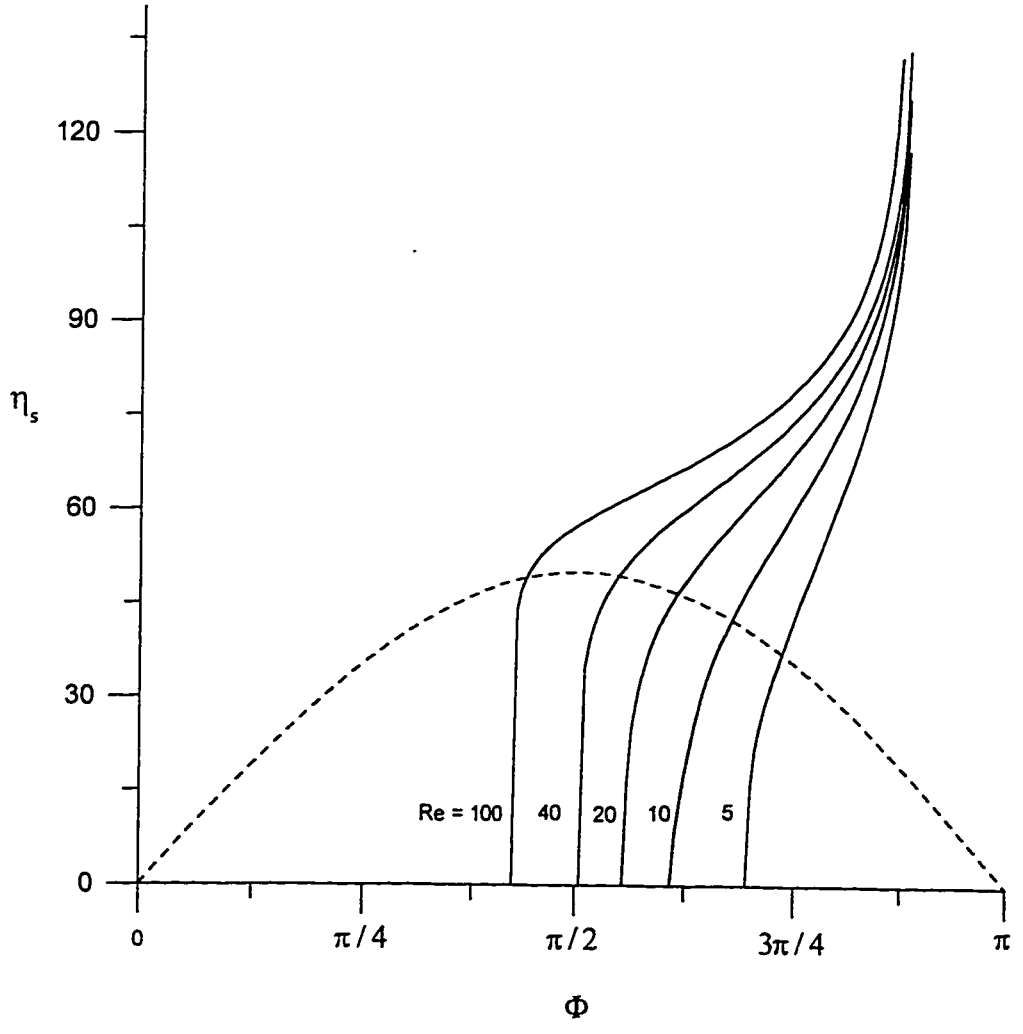

Figure 6.30 Time Development of the separation angle for the case $S = \pi/4$.

------- Free Stream Velocity (not to scale)

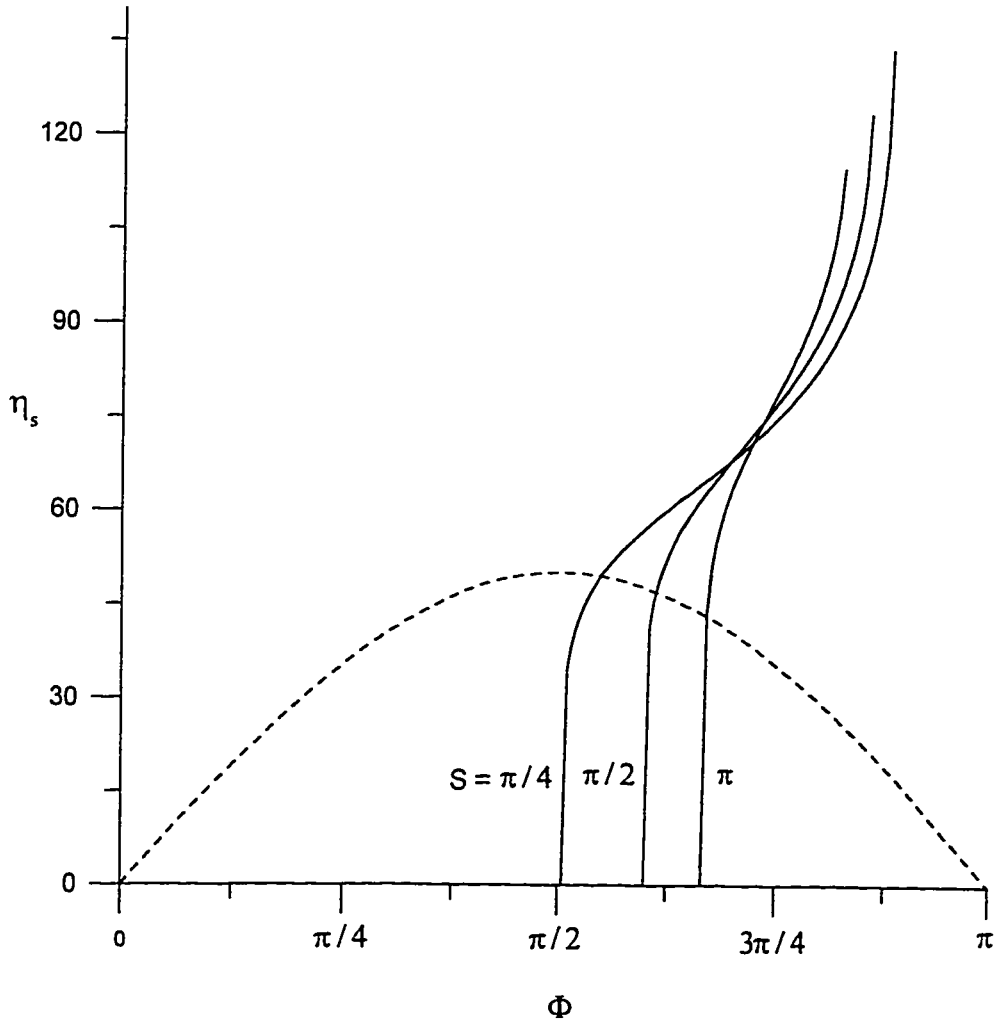

Figure 6.31 Time Development of the separation angle for the case Re = 40

------- Free Stream Velocity (not to scale)

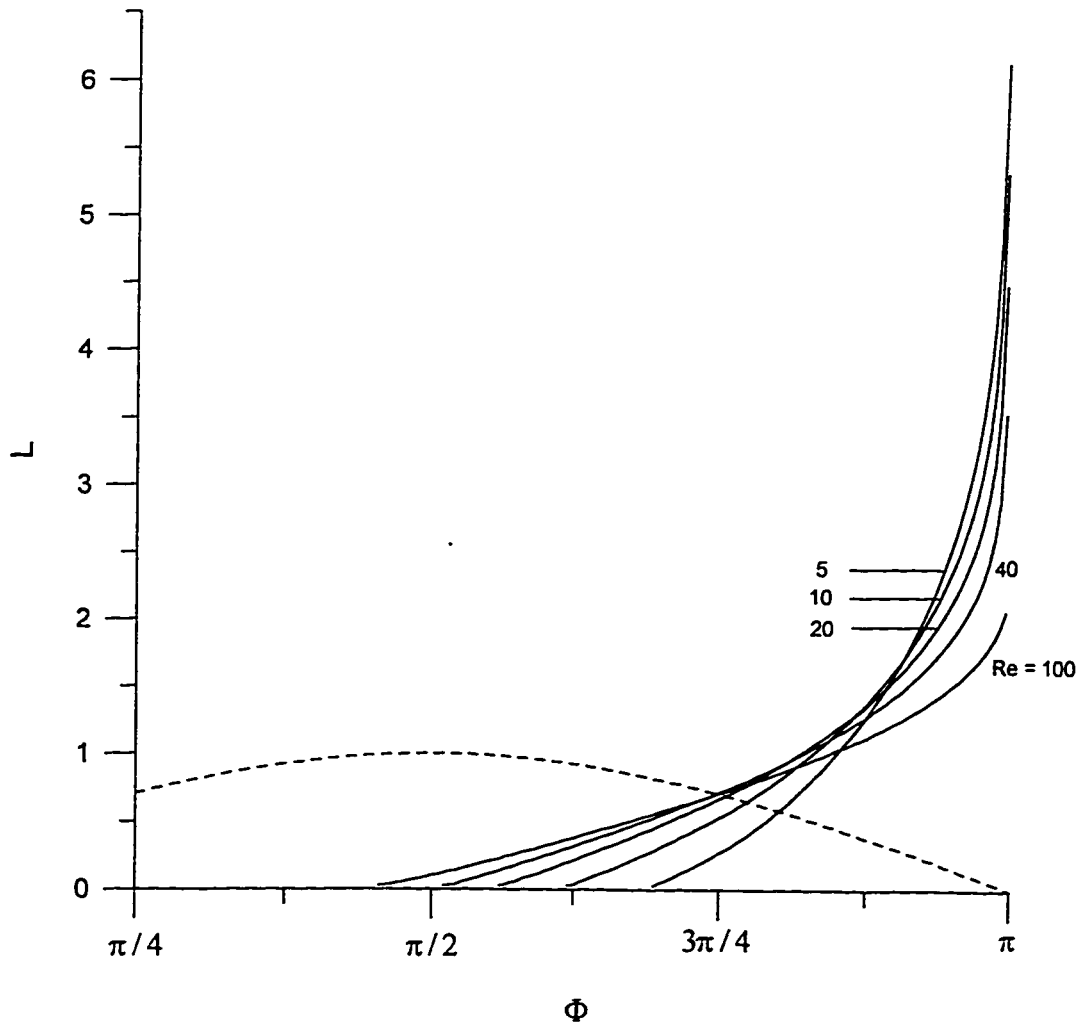

Figure 6.32 Time Development of the wake length for the case $S = \pi/4$.

------- Free Stream Velocity

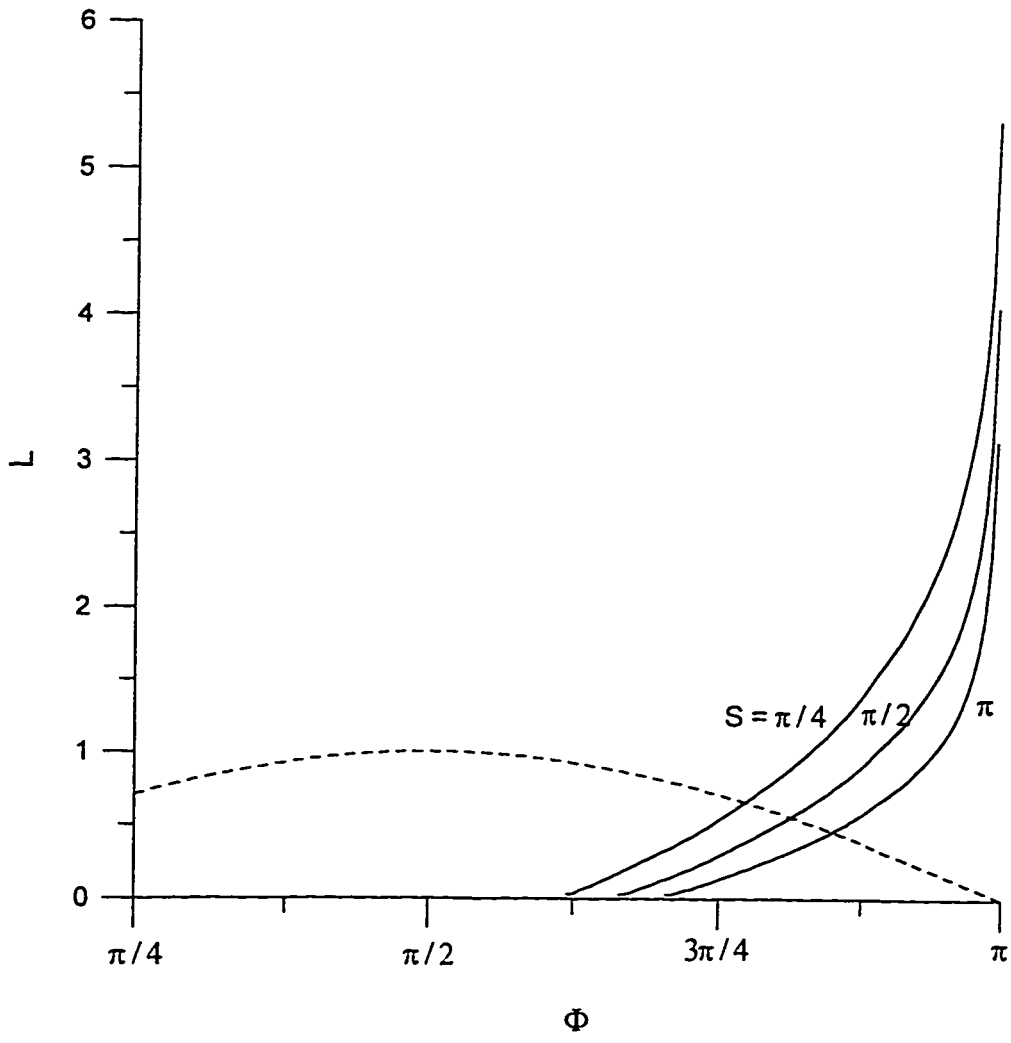

Figure 6.33 Time Development of the wake length for the case Re = 10.

------- Free Stream Velocity

recirculation regions. The trend is reversed at later times. The reversal of the trend takes place before the bubble surrounds the sphere. The same trend was observed for other Strouhal numbers.

The time-averaged stream function and vorticity over the fifth oscillation cycle are shown in figure 6.34 for the case Re = 5 and $S = \pi / 4$. The double boundary layer structure noted by the CM study is amply confirmed. The symmetry of the counter rotating eddies is slightly distorted. This is due to the fact that the solution was advanced only to the fifth cycle and the velocity field is not yet periodic.

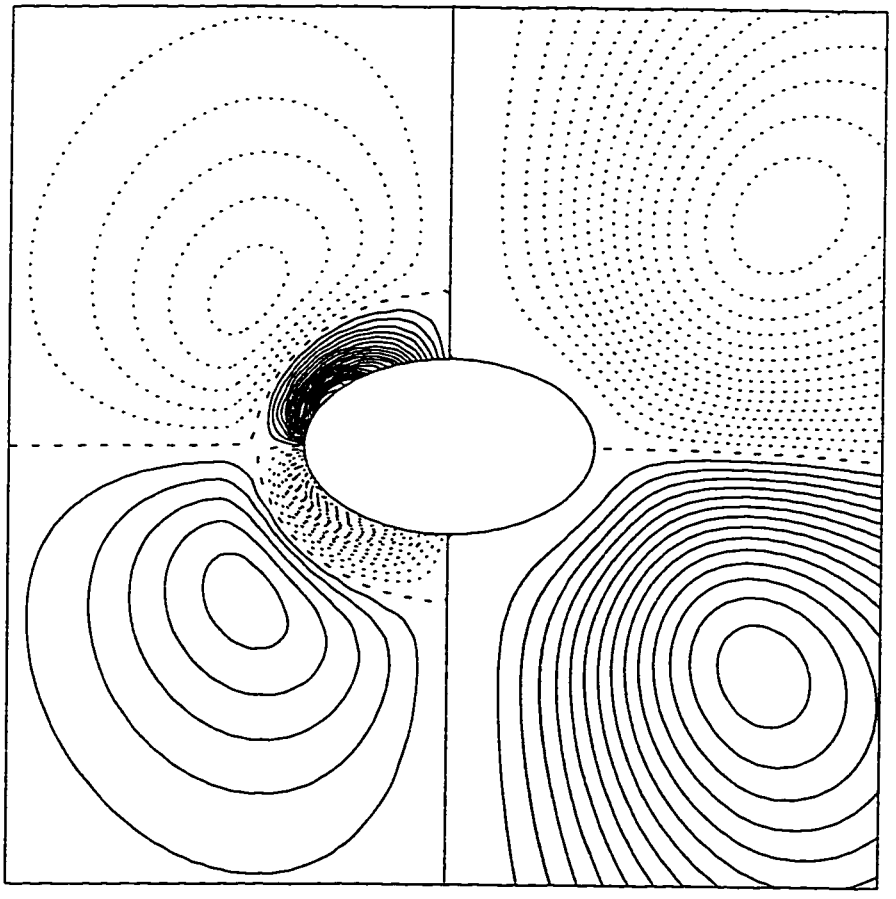

Figure 6.34 Time-averaged patterns over the fifth cycle of oscillation for the case $Re = 5$, $S = \pi/4$. ____ zero values, ... negative values, _____ positive values $\Delta\zeta = 0.02$, $\Delta\psi = 0.01$.

CHAPTER 7

VISCOUS FLOW OVER PROLATE SPHEROIDS

In this chapter, we extend the series truncation method of solution to the case of oscillating axisymmetric flow over a prolate spheroid having an axis ratio of 0.6 for Reynolds numbers up to 100. The Strouhal number is fixed at a value of $\pi/4$. Although the problem has already been studied by Kanwal (1955) and Lai and Mockros (1972), the solutions are, however, based on the linearized Stokes equations of motion instead of the full Navier-Stokes equations and the obtained results are limited to very low Reynolds numbers. Although the general solution of the Stokes stream function was obtained, Kanwal was unable to determine the constants of integration. Lai and Mockros were able to perform the necessary calculations to obtain a formula for the drag on a spheroid executing general axial translatory accelerations.

7.1 Governing Equations and Method of Solution

Using the prolate spheroidal coordinates system, the governing equations (3.16) and (3.17) can be written in the following dimensionless form:

$$(\sinh^2\xi+\sin^2\eta)\zeta+\frac{\partial}{\partial\xi}\left(\frac{1}{\sin\eta\,\sinh\xi}\frac{\partial\psi}{\partial\xi}\right)+\frac{\partial}{\partial\eta}\left(\frac{1}{\sin\eta\,\sinh\xi}\frac{\partial\psi}{\partial\eta}\right)=0 \tag{7.1}$$

$$(\sinh^2\xi+\sin^2\eta)\,\frac{\partial\zeta}{\partial t}+\frac{\partial\psi}{\partial\eta}\frac{\partial}{\partial\xi}\left(\frac{\zeta}{\sinh\xi\,\sin\eta}\right)-\frac{\partial\psi}{\partial\xi}\frac{\partial}{\partial\eta}\left(\frac{\zeta}{\sinh\xi\,\sin\eta}\right)= \frac{2}{\mathrm{Re}}\left\{\frac{\partial}{\partial\xi}\left[\frac{1}{\sinh\xi}\frac{\partial}{\partial\xi}(\sinh\xi\,\zeta)\right]+\frac{\partial}{\partial\eta}\left[\frac{1}{\sin\eta}\frac{\partial}{\partial\eta}(\sin\eta\,\zeta)\right]\right\} \tag{7.2}$$

The variables in the equations are normalized in the same way used for oblate spheroids. The oscillations are also sinusoidal. The no-slip and impermeability conditions on the

spheroid surface and the free stream condition far away lead to the following boundary conditions:

$$\psi = \frac{\partial \psi}{\partial \eta} = \frac{\partial \psi}{\partial \xi} = 0 \quad \text{at} \quad \xi = \xi_o \tag{7.3}$$

$$\frac{\partial \psi}{\partial \xi} = \frac{1}{2}\sinh 2\xi \, \sin^2 \eta \, \sin(St) \quad \text{, and} \quad \frac{\partial \psi}{\partial \eta} = \frac{1}{2}\sinh^2 \xi \, \sin 2\eta \, \sin(St) \quad \text{as } \xi \to \infty \tag{7.4}$$

Conditions (7.4) can be written as

$$\psi = \frac{1}{2}\sinh^2 \xi \, \sin^2 \eta \, \sin(St) \quad \text{as} \quad \xi \to \infty \tag{7.5}$$

The flow away from the prolate spheroid is irrotational leading to,

$$\zeta \to 0 \qquad \text{as} \quad \xi \to \infty \tag{7.6}$$

Upon using the series expansions presented in chapter 6, the following equations can be obtained similar to those of the oblate spheroid case:

$$\frac{\partial^2 f_n}{\partial \xi^2} - \coth\xi \frac{\partial f_n}{\partial \xi} - n(n+1) f_n = \sinh\xi \, n(n+1)\left[\cosh^2 \xi - \frac{2n^2+2n-3}{(2n-1)(2n+3)}\right] g_n - \sinh\xi \frac{n(n+1)(n+2)(n+3)}{(2n+3)(2n+5)} g_{n+2} + \sinh\xi \frac{n(n-1)(n-2)(n+1)}{(2n-1)(2n-3)} g_{n-2} \tag{7.7}$$

$$\left[\cosh^2 \xi - \frac{2n^2+2n-3}{(2n-1)(2n+3)}\right]\frac{\partial g_n}{\partial t} - \frac{(n+2)(n+3)}{(2n+3)(2n+5)}\frac{\partial g_{n+2}}{\partial t} - \frac{(n-1)(n-2)}{(2n-1)(2n-3)}\frac{\partial g_{n-2}}{\partial t} = \frac{2}{Re}\left[\frac{\partial^2 g_n}{\partial \xi^2} + \coth\xi \frac{\partial g_n}{\partial \xi} - \left\{\frac{1}{\sinh^2 \xi} + n(n+1)\right\} g_n\right] + S_n \tag{7.8}$$

The boundary conditions can now be written with respect to the coefficient functions (modes) of the series as

$$f_n(\xi_o, t) = \frac{\partial f_n}{\partial \xi}(\xi_o, t) = 0 \tag{7.9}$$

$$f_n(\xi, t) \to \sinh^2 \xi \; \sin(St)\delta_{n1} \quad \text{and} \quad g_n(\xi, t) \to 0 \quad \text{as} \quad \xi \to \infty \tag{7.10}$$

Equations (7.7) and (7.8) are very similar to those of the oblate spheroid case and can be solved by minor modifications to the method used there. Therefore, no details are given here for the method of solution. Instead, we concentrate on the results and interpretations as follows in the next section.

7.2 Results and Discussions

The problem of oscillating flow over a prolate spheroid of axis ratio 0.6 was solved for Reynolds numbers in the range $5 \le Re \le 100$ and for a Strouhal number S = $\pi/4$. With the projected area of the prolate spheroid being A ($=\pi c'^2 \sinh^2 \xi_o$), integrating the elementary friction and pressure forces over the entire surface gives the following formulas for C_{DF} and C_{DP}:

$$C_{DF} = \frac{16 \coth \xi_o}{3\,Re} g_1(\xi_o, t) \tag{7.11}$$

$$C_{DP} = -\frac{8}{3\,Re}\left[\coth \xi_o \; g_1(\xi_o, t) + \frac{\partial g_1}{\partial \xi}(\xi_o, t)\right] \tag{7.12}$$

In order to verify the mathematical model and the computational scheme, we use the analytical formula for C_D obtained by Lai and Mockros (1972) as a base for comparisons. The formula was based on the solution of the linearized Stokes equations for the case of a prolate spheroid oscillating in an infinite still fluid. The formula is valid at low frequencies and the solution is restricted to the low Re cases. The formula can be expressed as :

$$C_D^* = \frac{4}{3} F_1(\lambda_o) S \cos(St) + \frac{16}{Re} F_2(\lambda_o) \sin(st) - \frac{64}{3} F_3(\lambda_o) \sqrt{\frac{S}{2\,Re}} \cos(St + \frac{3\pi}{4}) \tag{7.13}$$

where,

$$F_1(\lambda_o) = \frac{\lambda_o}{1 - (\lambda_o^2 - 1) Q_1}, \quad F_2(\lambda_o) = \frac{1}{\kappa(\lambda_o^2 - 1)}, \quad F_3(\lambda_o) = \frac{1}{\kappa^2 (\lambda_o^2 - 1)}, \quad Q_1 = \frac{\lambda_o}{2} \ln(\frac{\lambda_o + 1}{\lambda_o - 1}) - 1,$$

$\kappa = \frac{1}{2}(\lambda_o^2 + 1) \ln(\frac{\lambda_o + 1}{\lambda_o - 1}) - \lambda_o$, and $\lambda_o = \cosh \xi_o$. The first part of equation (7.13) is the

potential flow drag. The other two are the steady viscous and the history terms respectively. Figure 7.1 shows the time variation of the drag coefficient (C_D) obtained from the present study and a comparison with the drag coefficient (C_D^*) obtained from the above equation for the case of Re = 20. The figure shows an excellent agreement. The relative deviation of C_D^* from C_D is presented in terms of the parameter ε defined as:

$$\varepsilon = \frac{C_D - C_D^*}{\max\left[C_D^*\right]} \tag{7.14}$$

The time variation of ε over one complete cycle is shown in figure 7.2 for the cases Re = 1, 5, 10, 20, 40, and 100. The figure shows a very small deviation (less than 1%) for the case Re = 1, however, the deviation increases as Re increases until reaching about 6% in the case of Re = 100. This behavior is expected since Lai and Mockros solution is based on the linearized Stokes equations which is only valid for low Re values. Figure 7.3 shows the time variation of C_D at different Reynolds numbers. The figure shows that the phase shift between C_D and the free stream velocity U depends on Re. As Re increases the phase lead increases. This phase shift was attributed by Chang and Maxey to the adverse pressure gradient created during the deceleration period of motion. The same trend can be deduced from equation (7.13). Figures 7.4 and 7.5 show the corresponding C_{DF} and C_{DP} respectively. Although C_{DF} is comparable to C_{DP} in the low Re range, the later becomes dominant as Re increases. This is quite expected since the pressure distribution follows closely the potential flow solution except for the separated flow region. On the other hand, the frictional drag coefficient decreases as Re increases similar to the normal trend for the case of a sphere.

The dimensionless pressure $p^*(\eta,t)$ can be easily obtained as:

$$p^*(\eta,t) = \frac{4}{Re}\sum_{n=1}^{N}\left[P_n(\cos\eta) - (-1)^n\right]\left[\frac{\partial g_n}{\partial \xi}(\xi_o,t) + \coth\xi_o\ g_n(\xi_o,t)\right] \tag{7.15}$$

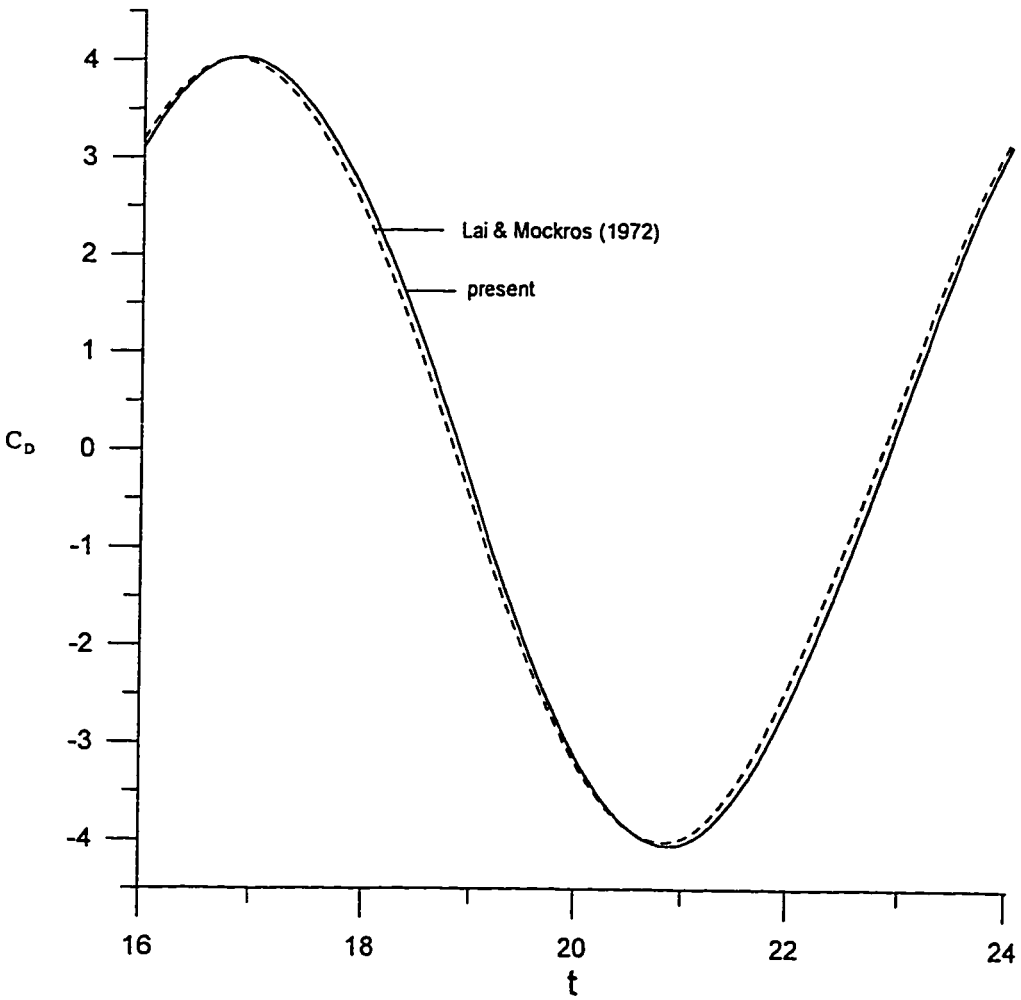

Figure 7.1 Comparison of the drag coefficient with the analytical drag of Lai and Mockros (1972).

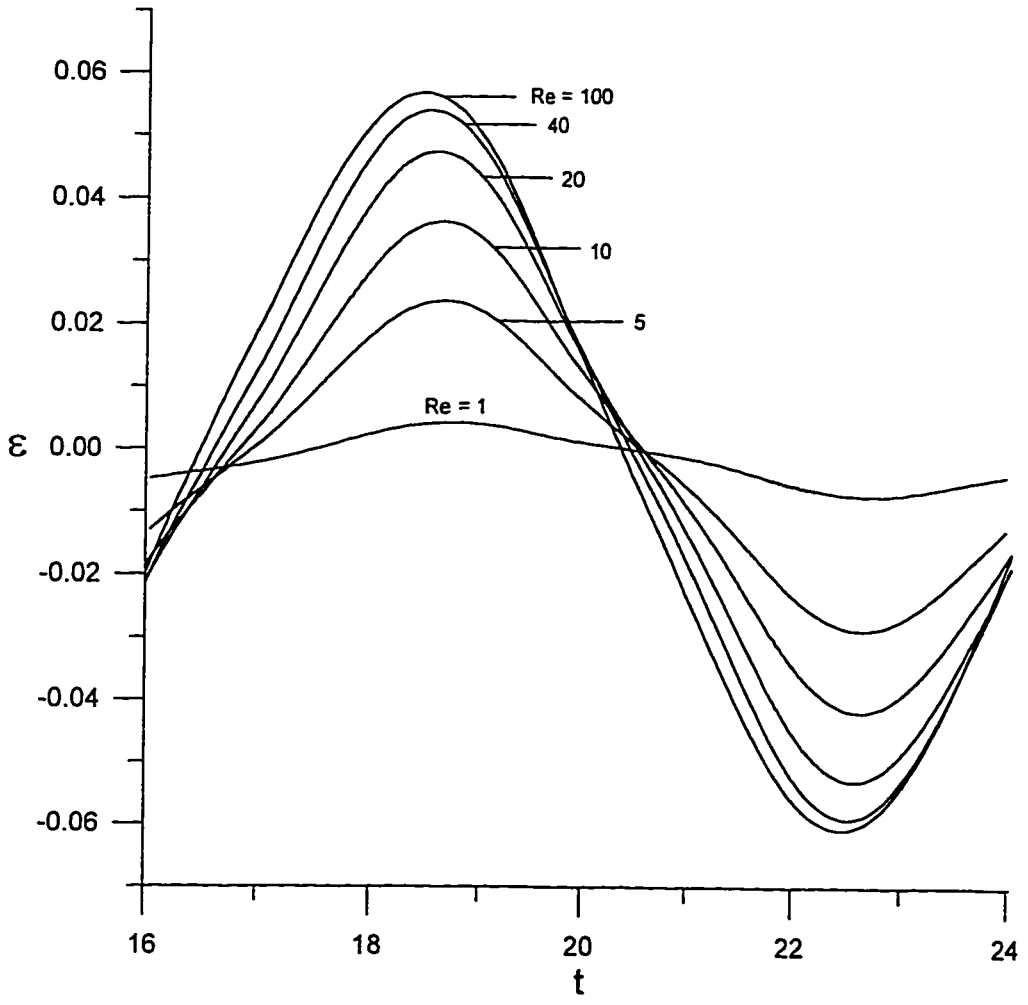

Figure 7.2 The difference between the drag of the present study and that of Lai and Mockros (1972) at different Reynolds numbers.

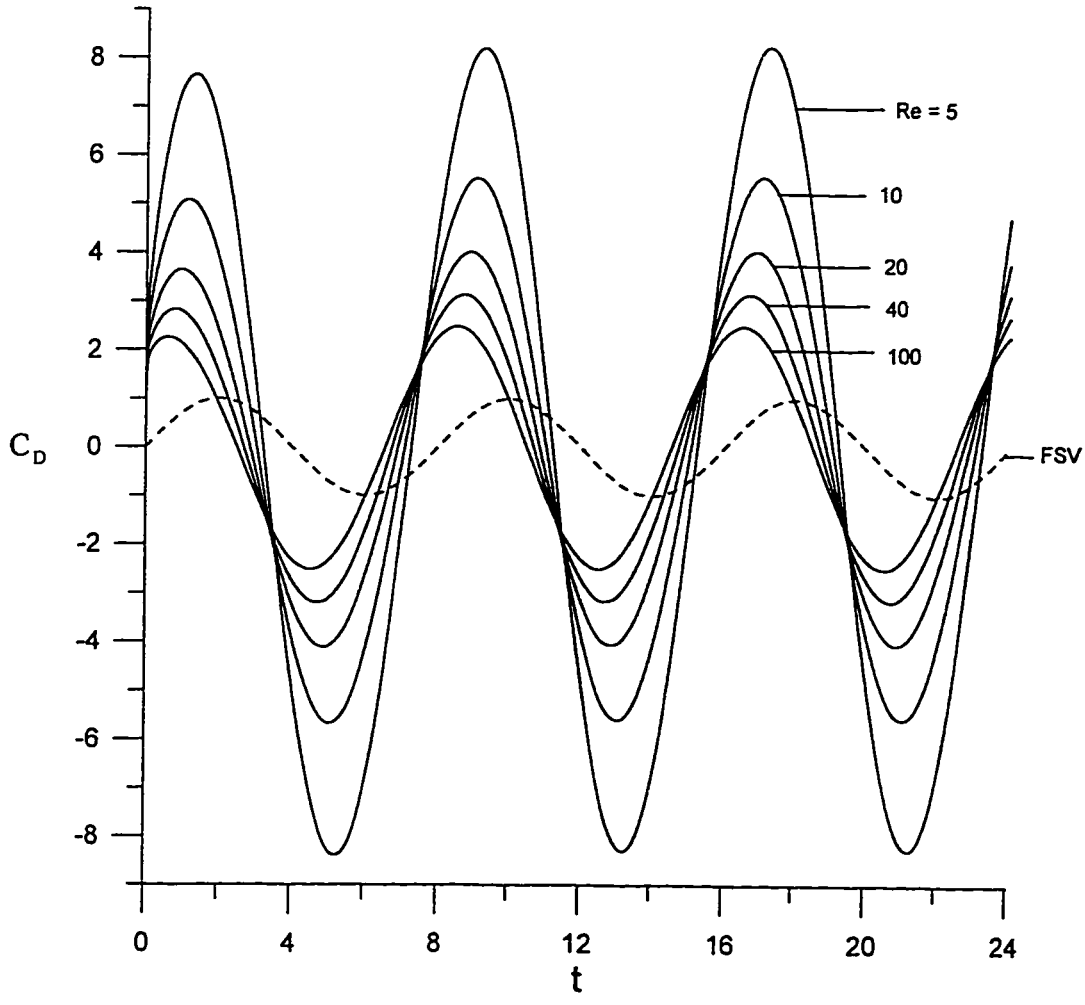

Figure 7.3 The time variation of the drag coefficient at different Reynolds numbers. (FSV = Free Stream Velocity)

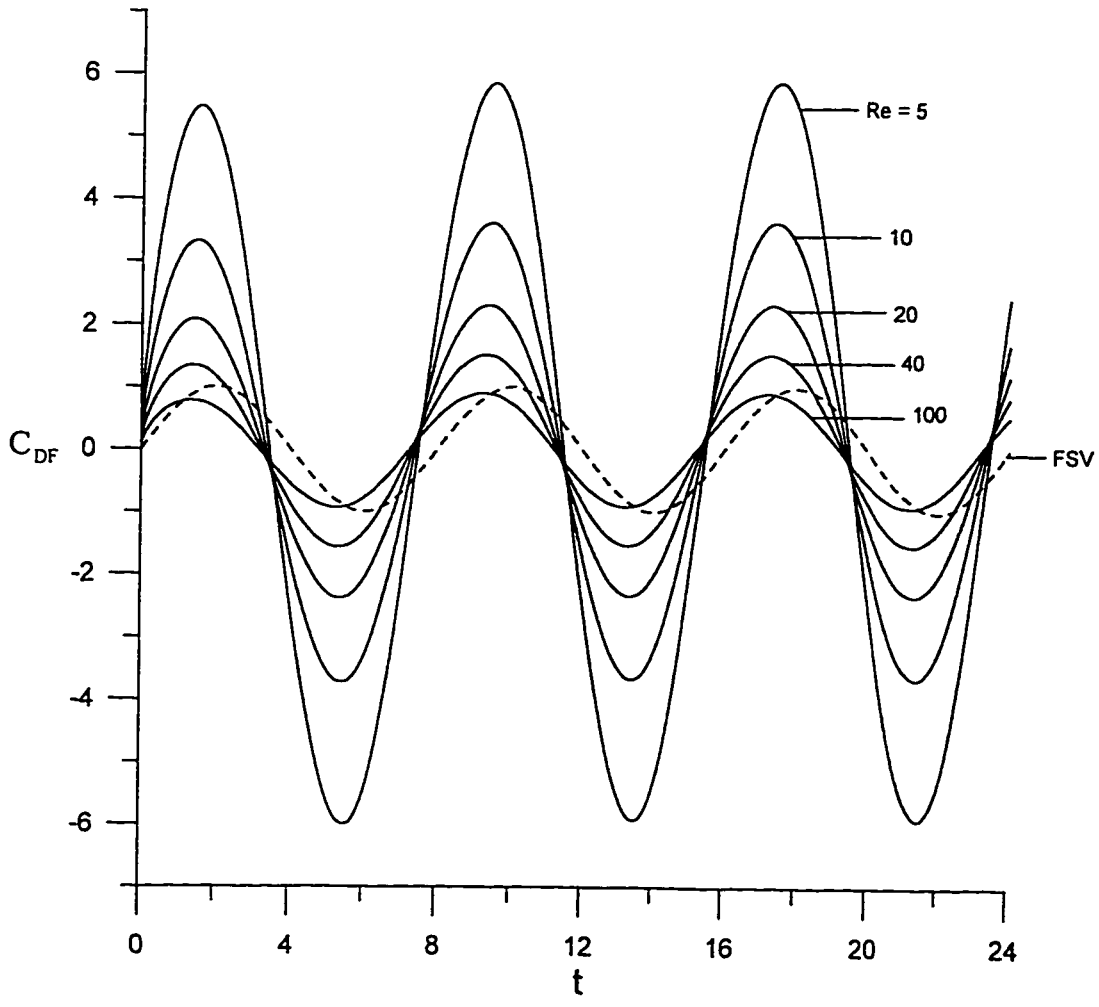

Figure 7.4 The time variation of the friction component of drag at different Reynolds numbers. (FSV=Free Stream Velocity)

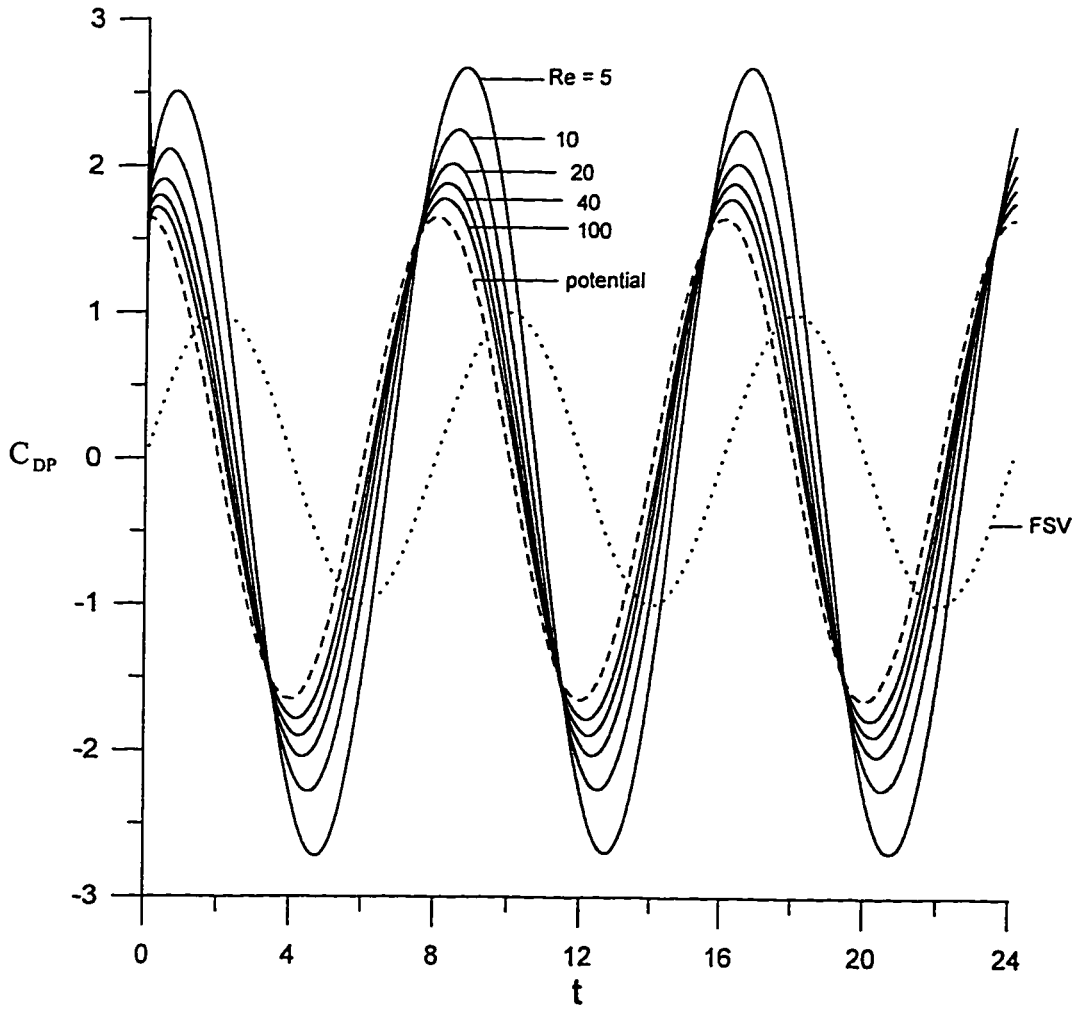

Figure 7.5 The time variation of the pressure component of drag at different Reynolds numbers. (FSV = Free Stream Velocity)

The dimensionless inviscid pressure distribution, $p_p^*(\eta,t)$, is given by equation (4.50). Figure 7.6 shows the time development of $p^*(\eta,t)$ over one half of an oscillation cycle for the case Re = 100. The corresponding surface vorticity distributions are shown in figure 7.7. The pressure distribution is found to be in good agreement with the potential flow pressure distribution at $t = 19.5$. In fact, the curves of $p^*(\eta,t)$ for all Re were very close to each other and to $p_p^*(\eta,t)$ at this time. At other times, however, $p^*(\eta,t)$ for higher Re is closer to $p_p^*(\eta,t)$. Figure 7.8 shows $p^*(\eta,t)$ and $p_p^*(\eta,t)$ at $t = 20$ which corresponds to a zero free stream velocity.

The time development of the streamline and vorticity patterns for the case Re = 100 over one half of a complete oscillation are shown in figure 7.9. The half cycle chosen is from t = 18 (maximum U) to t = 22 (minimum U). At peak velocity, no separation is observed (figure 7.9a). As time progresses, the free stream starts to decelerate and a small recirculation region starts to develop near the rear stagnation region (figure 7.9b). This recirculating region grows until the bubble encompasses the whole prolate spheroid (figure 7.9c). As the flow reverses direction, two counter rotating vortices can be observed (figure 7.9d). The two vortices will subside as the streamlines stretch in the other direction due to the acceleration of the flow in the opposite direction. The left portion of the figures show the corresponding vorticity pattern. It is observed that the negative vorticity which dominates at peak velocity detaches and decays during this half cycle. Another region of positive vorticity is simultaneously created. The behavior is repeated in the following half cycle.

It is interesting to measure the angle of separation as well as the length of the recirculation region from the rear stagnation point ($\eta = 0$). Figures 7.10 and 7.11 show the separation angle and the wake length at different Reynolds numbers. The time at which separation is first observed is quite dependent on Re. The time at which the bubble

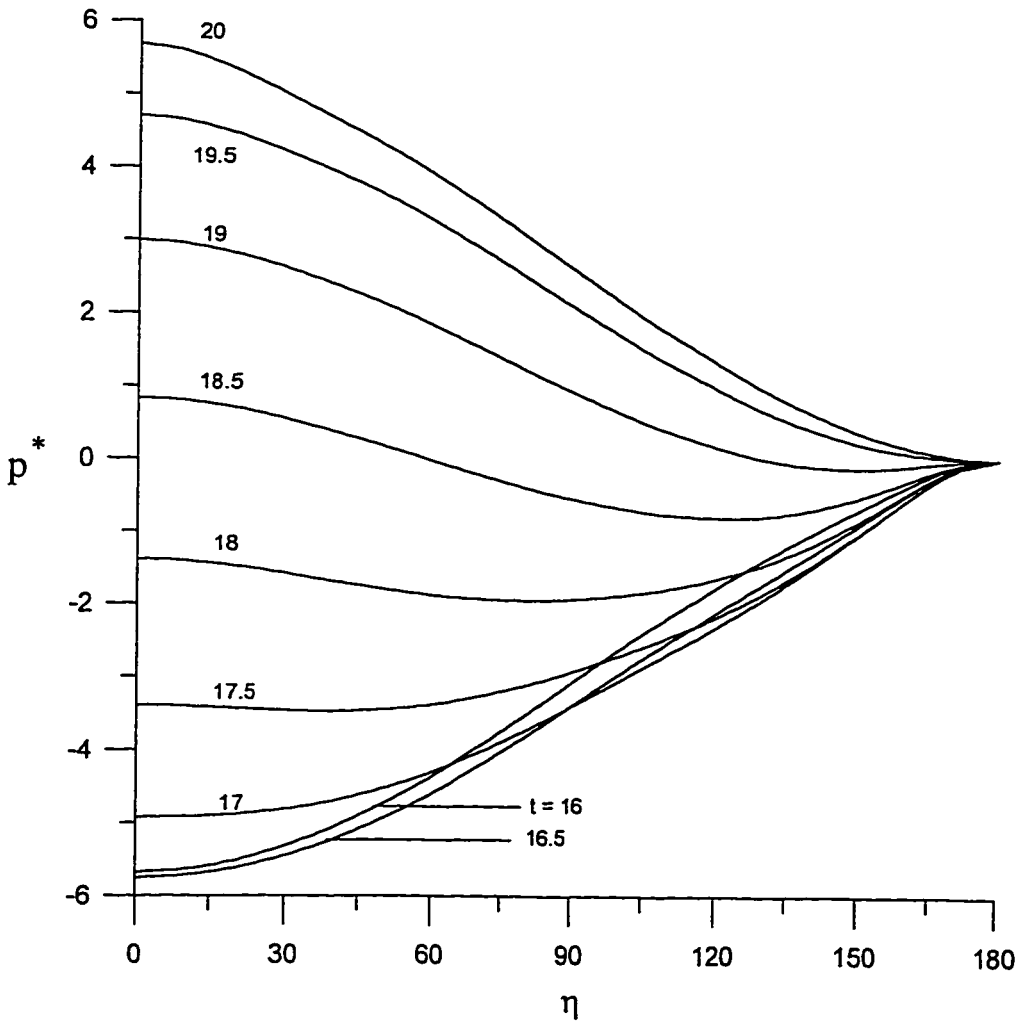

Figure 7.6 The time variation of pressure during one half of a complete oscillation for the case Re = 100.

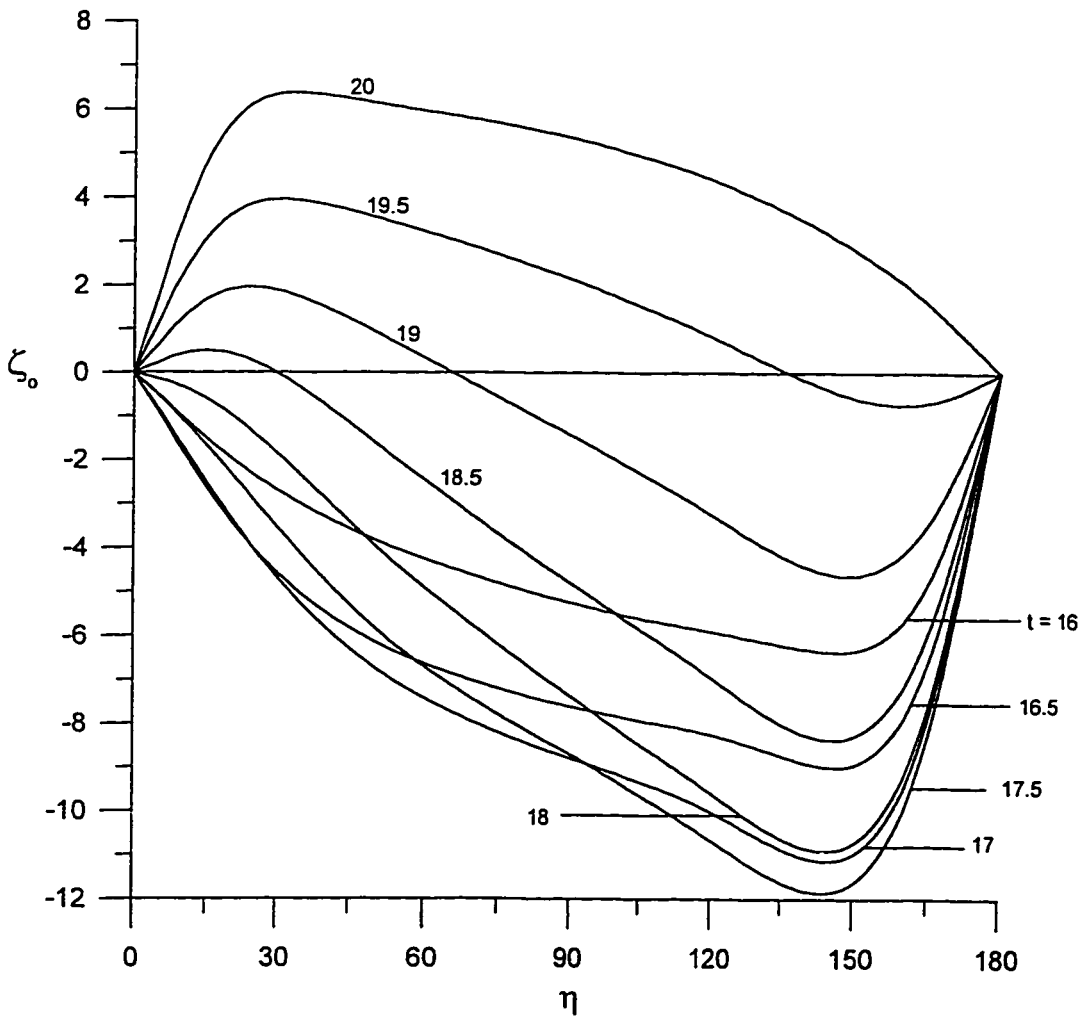

Figure 7.7 The time variation of the surface vorticity during one half of a complete oscillation for the case Re = 100.

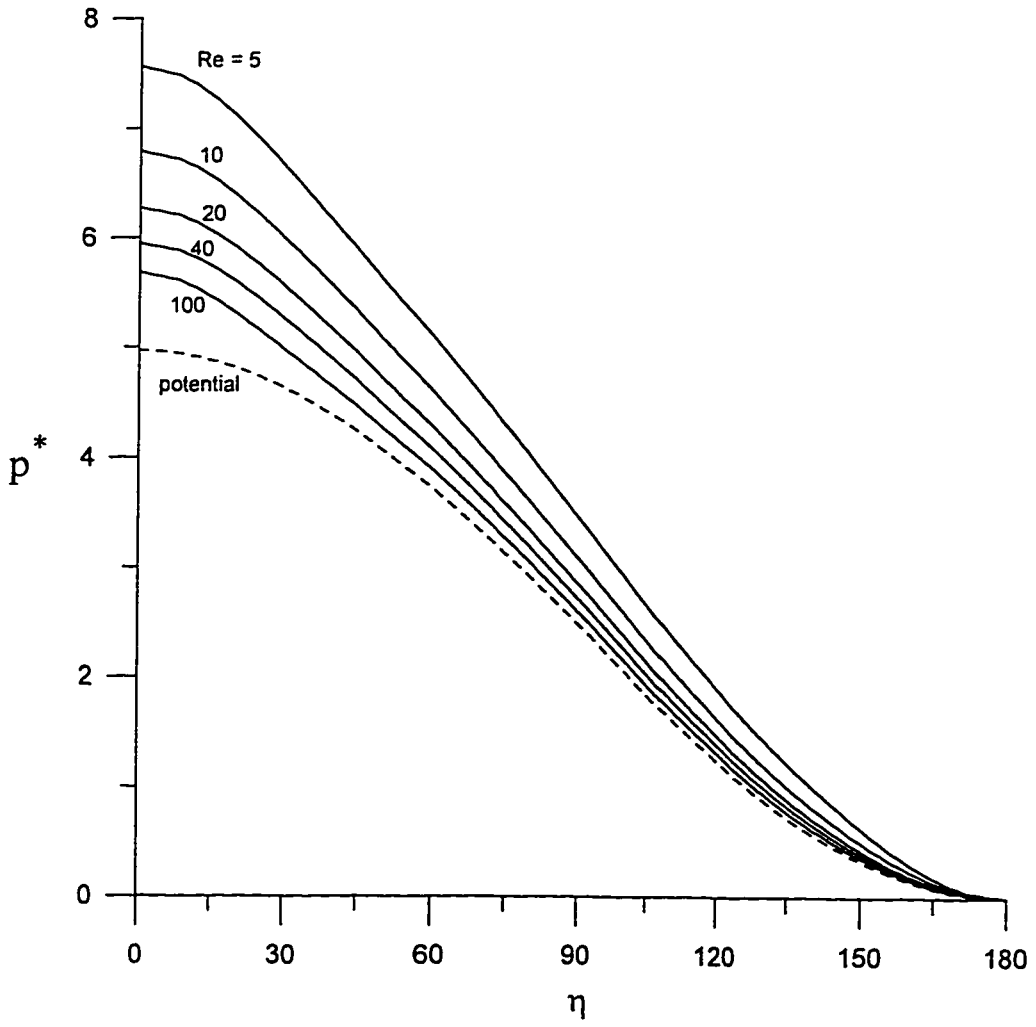

Figure 7.8 Comparison of the pressure distribution at t = 20 for different Reynolds numbers

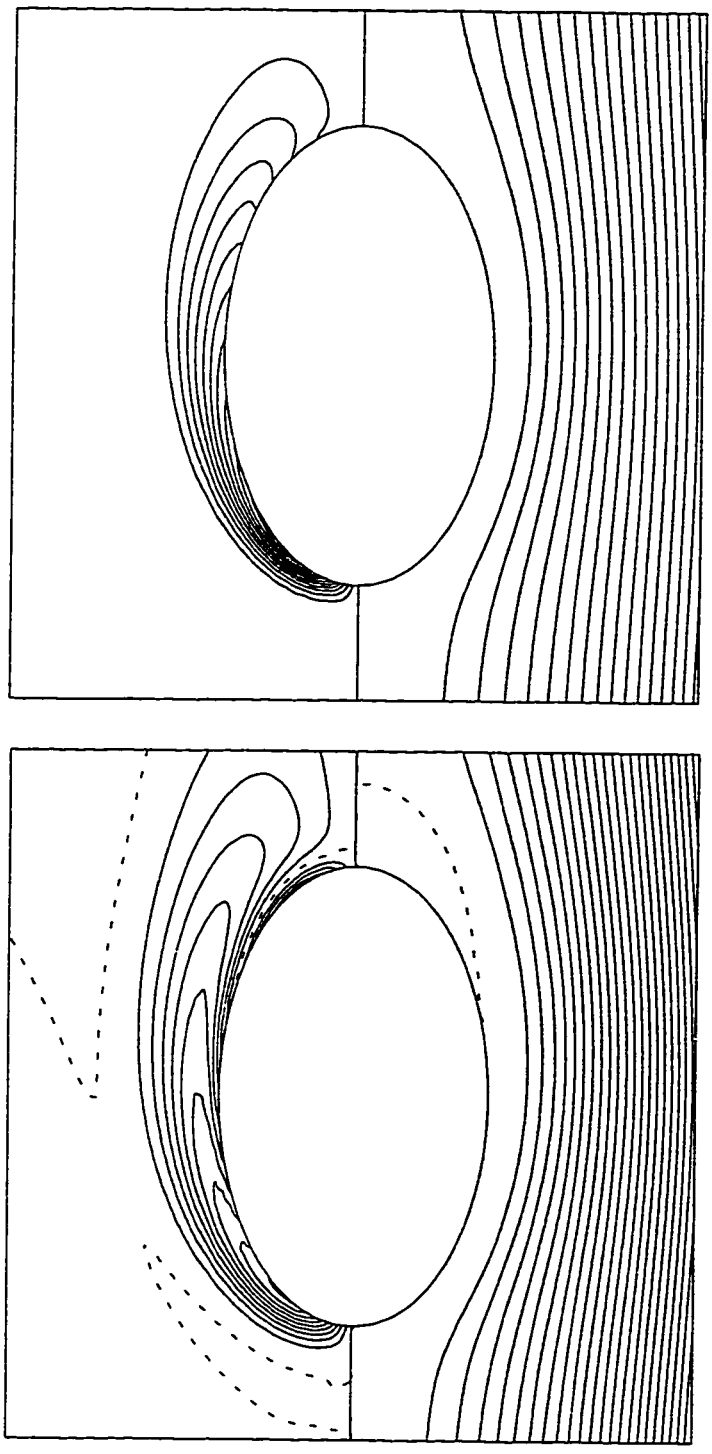

Figure 7.9(a-b) (t=18,19)

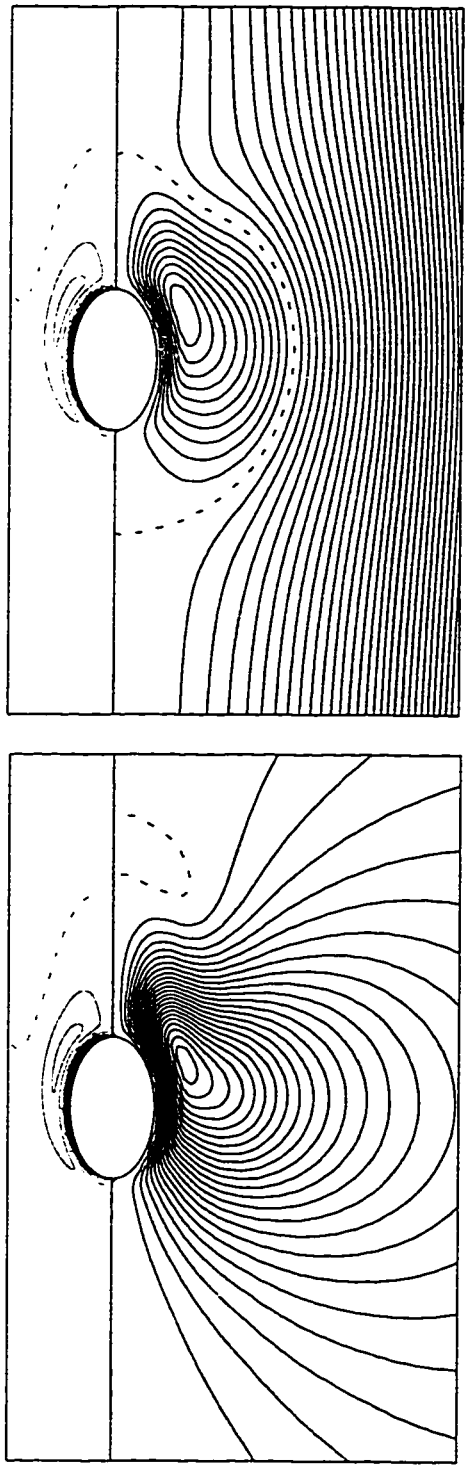

Figure 7.9 (c-d) (t=19.98,20)

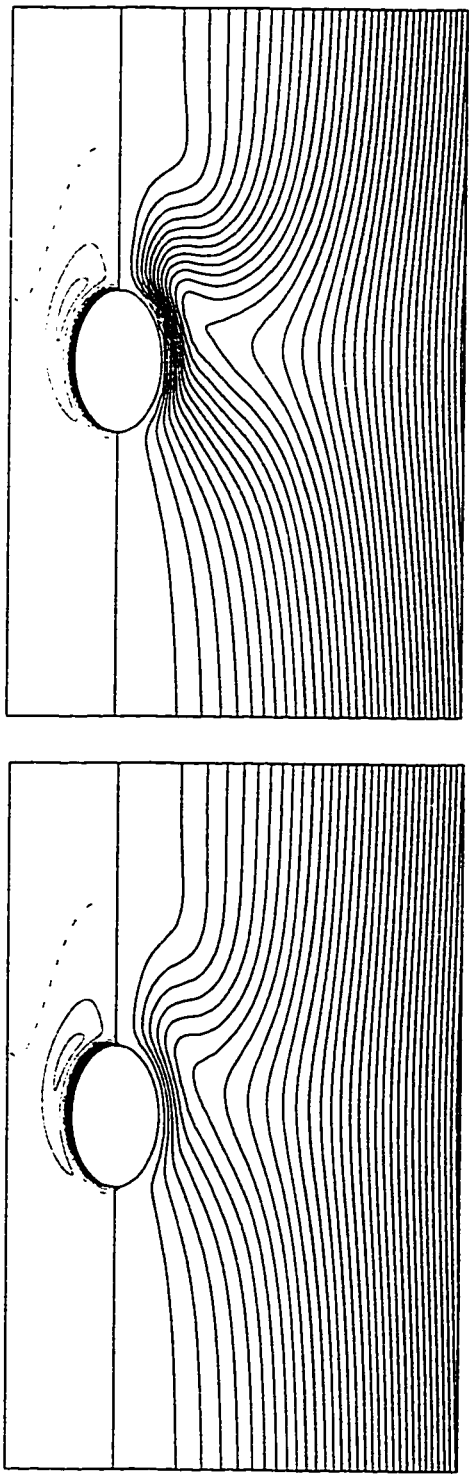

Figure 7.9(e-f) (t=20.02,20.04)

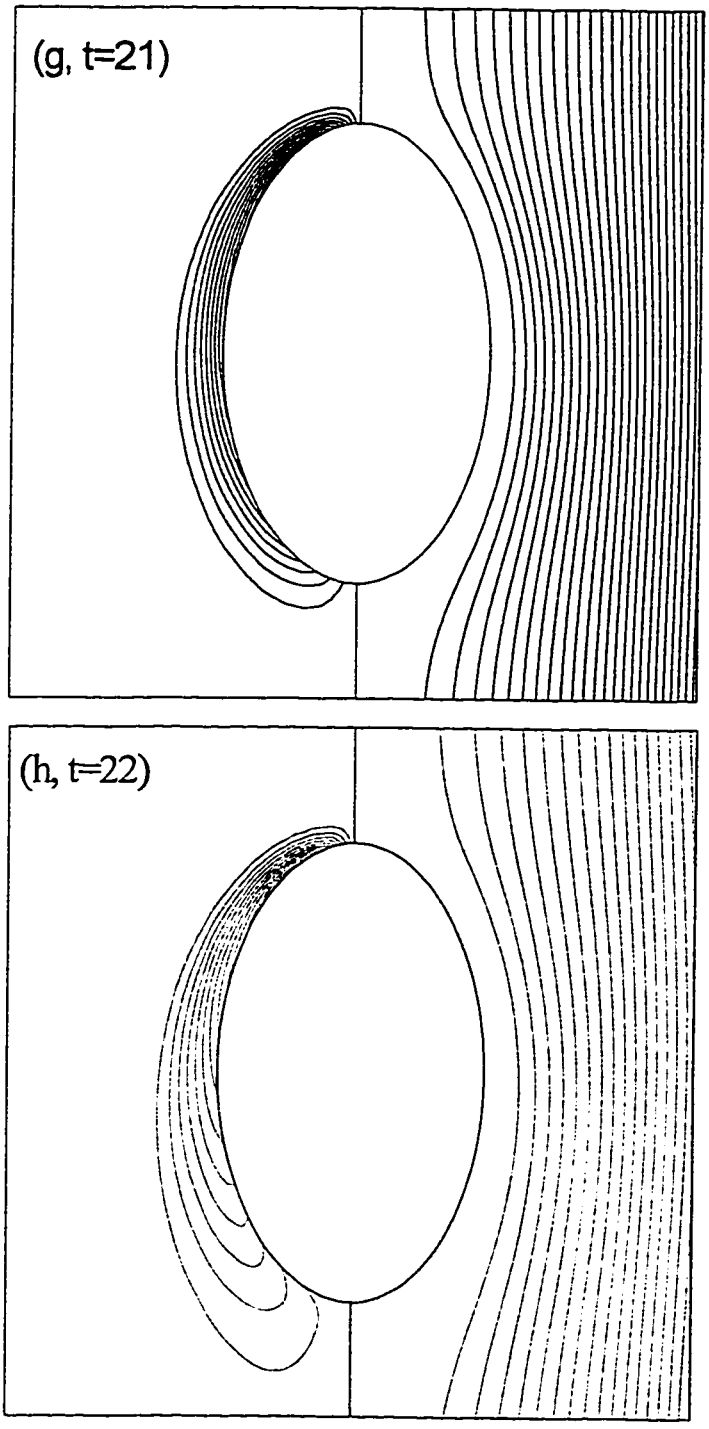

Figure 7.9 (g-h)

Figure 7.9 Instantaneous streamline (right) and vorticity (left) distributions for the case Re = 100.

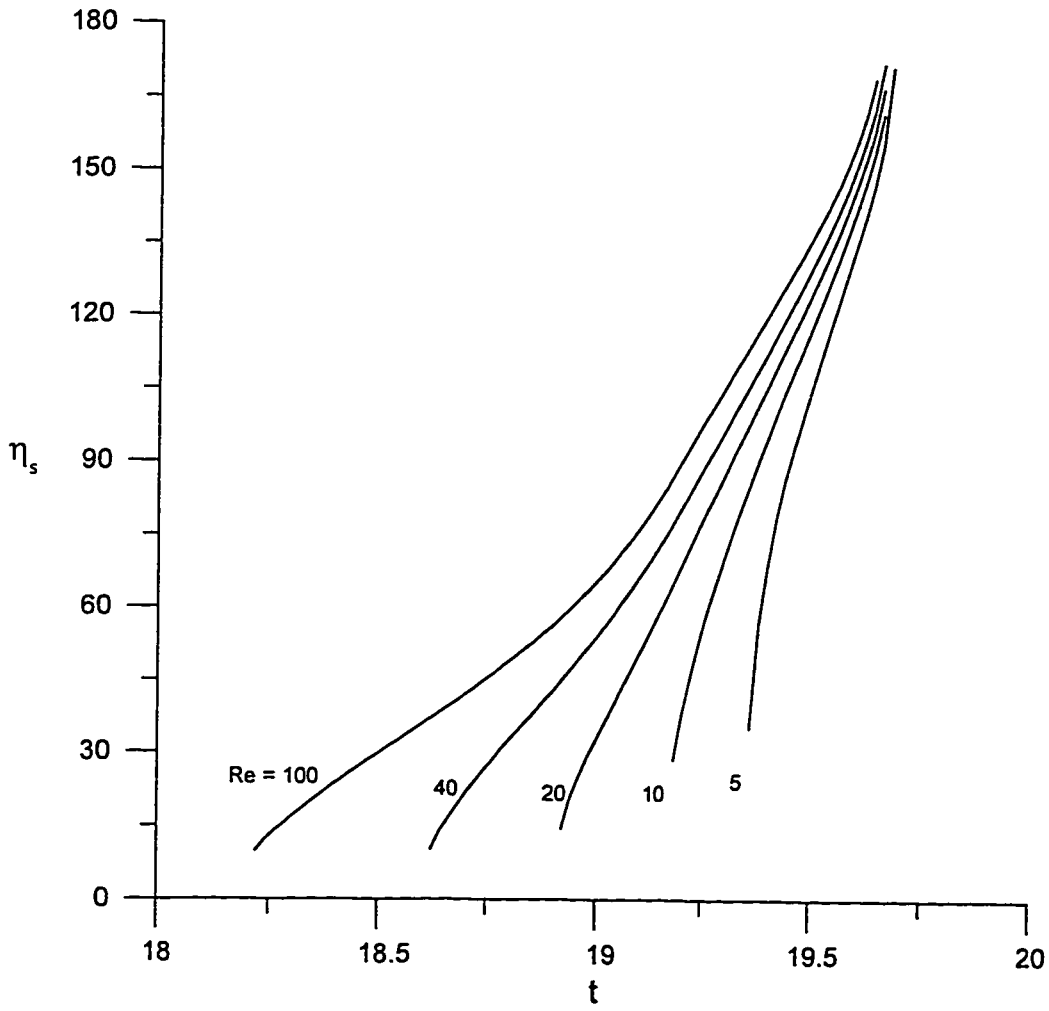

Figure 7.10 Time development of the separation angle

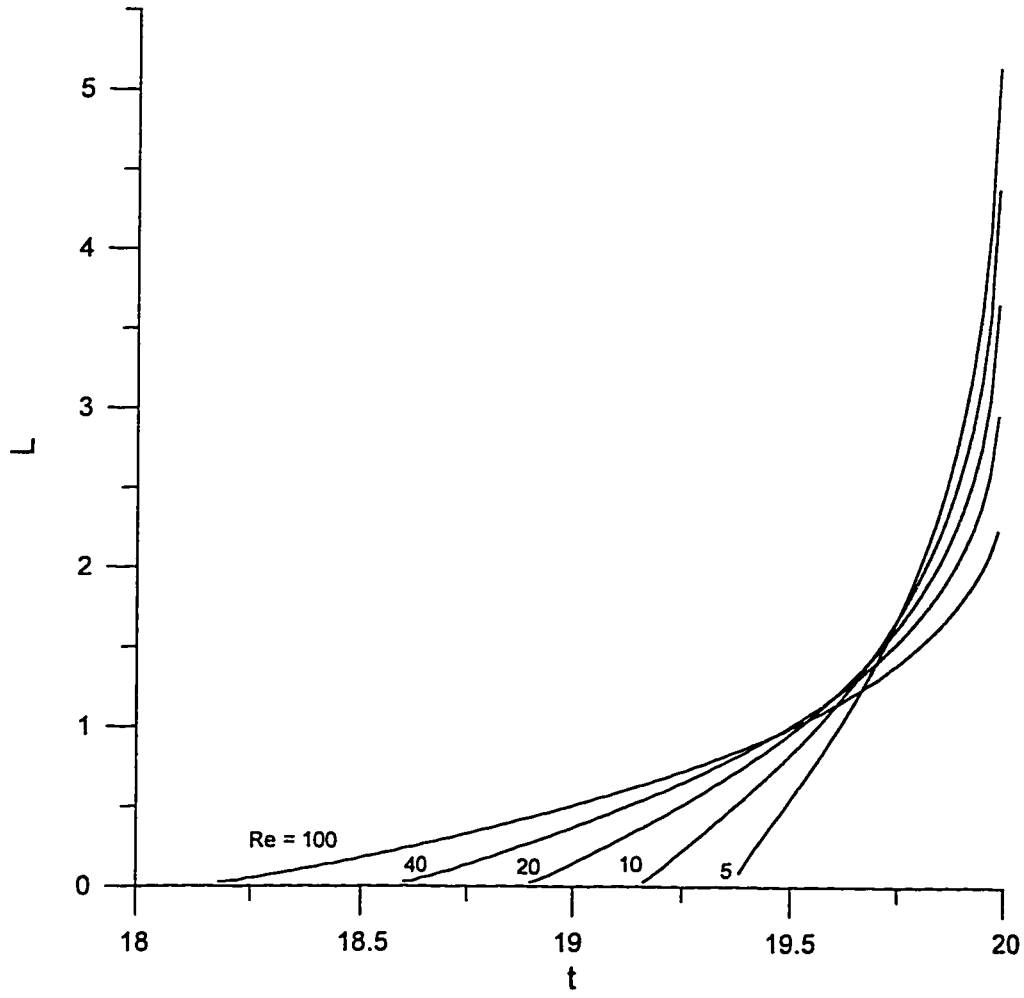

Figure 7.11 Time development of the wake length

surrounds the spheroid is less dependent on Re. Although separation takes place earlier at higher Re, the speed at which the separation point travels towards the front stagnation point ($\eta = \pi$) is lower than at smaller Re.

In the study of Chang and Maxey, it was observed that at certain conditions a double boundary-layer structure was observed upon averaging the stream function and vorticity over one full oscillation. Figure 7.12 shows the same behavior for the case Re = 5. In fact, the double boundary layer structure was observed for the whole range of parameters considered in this study.

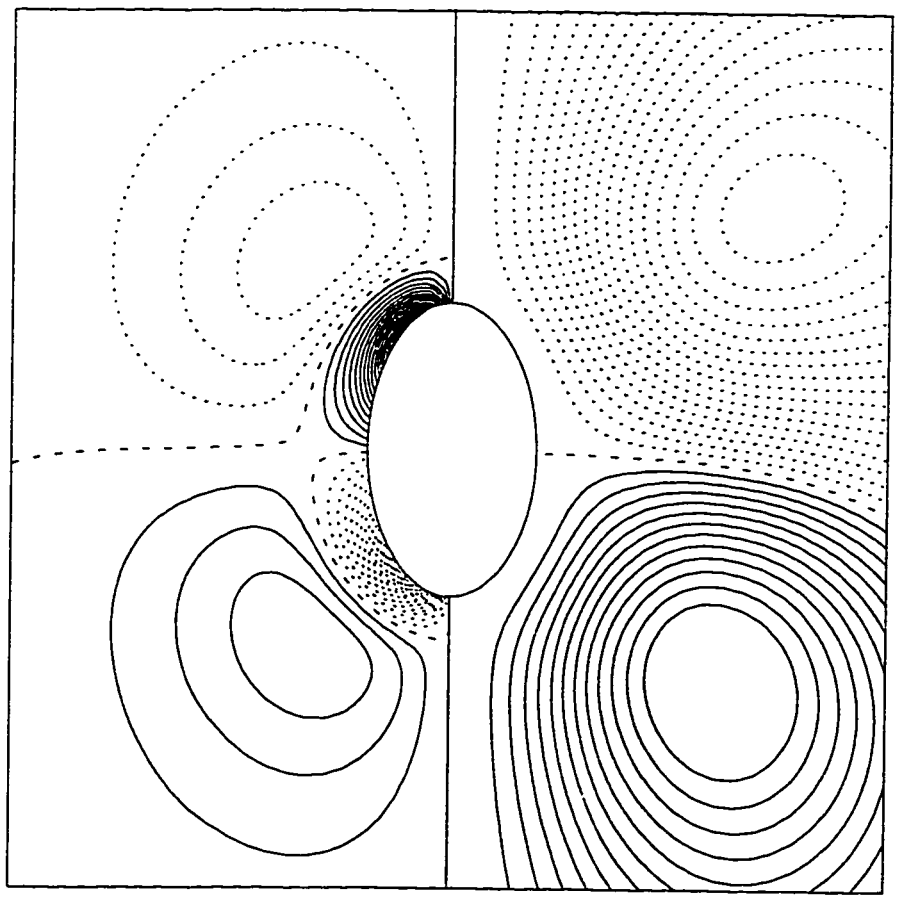

Figure 7.12 Time-averaged streamline (right) and vorticity (left) patterns over one full cycle for the case Re = 5.
_ _ _ zero, ... negative, ____ positive values.
$\Delta\psi$ =0.005, $\Delta\zeta$ = 0.02

CHAPTER 8

CONCLUSIONS AND RECOMMENDATIONS

8.1 CONCLUSIONS

In this study, the problem of incompressible axisymmetric flow over spheroidal bodies was considered. The analysis covered steady and unsteady flows of inviscid and viscous fluids. The spheroidal bodies may take the shape of spheres, oblate or prolate spheroids. To describe the geometries of these bodies, the spherical, oblate spheroidal, and prolate spheroidal coordinates were used. While the main interest is to determine the characteristics of the viscous flow, it is also important to determine the potential flow solution for such motion. In this regard, Euler's equations which govern the inviscid oscillating flows over oblate and prolate spheroids were analytically solved. Analytical expressions were obtained for the potential and stream functions as well as surface pressure distributions and the hydrodynamic force coefficients. The solutions of the two limiting cases of oscillating flows over disks and spheres were obtained as special cases from the presented analytical solutions. The analytical expressions describing the velocity field are essential in understanding the viscous flow problem and may provide the far-field boundary conditions outside the viscous flow region.

Viscous flows over spheres, oblate spheroids, and prolate spheroids were treated by semi-analytical techniques. The method of solution of the full Navier-Stokes equations adopted is the series truncation where the stream function and vorticity are approximated using Legendre functions. The resulting differential equations are then solved numerically. The cases considered were the oscillating flows over spheres, oblate spheroids, and prolate spheroids, fluctuating flow about a non-zero mean over spheres, steady viscous flow over oblate spheroids, and the impulsively started flow over oblate

spheroids. Several conclusions can be drawn from the presented analysis. They are summarized in the following points:

1. The drag coefficient was found to exhibit a phase lead over the free-stream velocity. This lead which increases as Reynolds and Strouhal numbers increase, is attributed to flow separation. This is quite significant because instead of retarding the flow, the presence of the object in the flow would help it to reverse direction.

2. It was found that the pressure distribution approaches that of the potential flow as Reynolds and Strouhal numbers increase.

3. Separation is not expected at low Reynolds numbers for uniform velocity profiles. For example, separation for the flow over a sphere occurs for $Re > 20$. In oscillating flow, however, separation can take place well below this value due to the adverse pressure gradients which are created during the decelerating part of motion.

4. Separation occurs earlier for higher Reynolds numbers but the bubble takes longer time to encompass the body. Separation also occurs earlier for lower Strouhal-number flows. At small phase angles, the separation angle is higher for lower Strouhal-number flows. As time progresses, higher Strouhal-number flows exhibit larger separation angles.

5. The wake length increases with decreasing Strouhal number. At early phase angles, the wake is longer for higher Reynolds numbers. The trend is, however, reversed at later times.

6. The double boundary layer structure was observed for the whole range of parameters considered in this study.

7. Comparisons with the analytical solutions of Lai and Mockros (1972) showed excellent agreements at low Reynolds and Strouhal numbers. These formulas which provide the solutions of the problem of oscillating flows over oblate and prolate spheroids are based on Stokes equations in which the non-linear inertia terms are neglected.

8. In the case of fluctuating flow over a sphere, it was shown that vortex shedding is motivated by increasing Reynolds and Strouhal numbers. The impulsively started flow over a sphere was indirectly obtained by setting the amplitude of oscillations to zero.

9. The steady drag formulas by Payne and Bell (1960) and Breach (1961) were found to underestimate the actual force on the spheroid with Breach formula being closer to the present study results. A range of validity for the two formulas was set by accepting a 5% deviation from the present study. It was found that Payne and Bell relations are valid for $Re < 0.3$ while Breach formula is valid for higher Reynolds numbers provided that a proper restriction on the axis ratio is imposed.

10. As Reynolds number increases for steady flow over oblate spheroids, the magnitude of the pressure distribution decreases and the magnitude of the surface vorticity increases. Increasing axis ratio results in decreasing the magnitudes of the pressure and surface vorticity.

8.2 RECOMMENDATIONS

Although this study has covered a wide range of flows over spheroidal bodies, further work can be conducted to cover the following problems:

1. The present models for oblate and prolate spheroids take excessive time for high Reynolds-number flows. Another approach to accelerate convergence is needed.

2. It is of interest to solve the problem at high Reynolds numbers ($Re = 10^3, 10^4$)

3. Generalizing the method to deal with three-dimensional oscillating flows is needed.

4. Wider range of axis ratios, especially the limiting case of a flat disk, need to be considered.

5. The problems of the steady and the impulsively started flows over prolate spheroids have not been considered and may be considered as an extension of the present study.

APPENDIX

SOME USEFUL INTEGRALS

The series truncation method used in this study requires the knowledge of some integrals related to Legendre functions. The following are some of these important integrals.

$$\int_{-1}^{1} P_n^{(k)}(z)\, P_m^{(k)}(z)\, dz = \frac{2\,(n+k)!}{(2n+1)\,(n-k)!}\delta_{nm} \tag{A1}$$

$$\int_{-1}^{1} \frac{dP_m(z)}{dz} \int_{z}^{1} P_n(t)\, dt\, dz = \frac{2}{(2n+1)}\delta_{nm} \tag{A2}$$

$$\int_{z}^{1} P_n(t)\, dt = \frac{P_{n-1}(z) - P_{n+1}(z)}{n\,(n+1)} = -\frac{\sqrt{1-z^2}\; P_n^{(1)}(z)}{n\,(n+1)} \tag{A3}$$

$$\int_{-1}^{1} \left[P_n^{(3)}(z) + \frac{4\,z}{\sqrt{1-z^2}} P_n^{(2)}(z) - 2\, P_n^{(1)}(z) \right] P_m^{(1)}(z)\, dz = -\frac{2\,n^2\,(n+1)^2}{(2n+1)}\delta_{nm} \tag{A4}$$

$$\int_{-1}^{1} z^2\, P_n^{(1)}(z)\, P_m^{(1)}(z)\, dz = \begin{cases} \dfrac{2\,m\,(m+1)\,(m+2)\,(m+3)}{(2m+1)\,(2m+3)\,(2m+5)} & \text{if} \quad n = m+2 \\ \dfrac{2\,m\,(m+1)\,(2m^2+2m-3)}{(2m-1)\,(2m+1)\,(2m+3)} & \text{if} \quad n = m \\ \dfrac{2\,m\,(m-2)\,(m-1)\,(m+1)}{(2m-3)\,(2m-1)\,(2m+1)} & \text{if} \quad n = m-2 \\ 0 & \text{otherwise} \end{cases} \tag{A5}$$

$$\int_{-1}^{1} P_n^{(1)}(z)\, P_i(z)\, P_j^{(1)}(z)\, dz = -\sqrt{4\,n\,(n+1)\,j\,(j+1)} \begin{pmatrix} n & i & j \\ -1 & 0 & 1 \end{pmatrix} \begin{pmatrix} n & i & j \\ 0 & 0 & 0 \end{pmatrix} \tag{A6}$$

$$\int_{-1}^{1} P_n^{(1)}(z)\, P_i^{(1)}(z)\, P_j^{(2)}(z)\, dz = \sqrt{4\,n\,(n+1)\,i\,(i+1)\,j\,(j+2)\,(j^2-1)} \begin{pmatrix} n & i & j \\ -1 & -1 & 2 \end{pmatrix} \begin{pmatrix} n & i & j \\ 0 & 0 & 0 \end{pmatrix} \tag{A7}$$

BIBLIOGRAPHY

Arfken, G., Mathematical Methods for Physicists. Academic Press, London, 1970.

Barshinger, R.N. and J.F. Geer, Stokes flow past a thin body of revolution: Axially incident uniform flow, SIAM J. APPL. MATH., Vol. 44, no. 1, 1984.

Bassett, A.B., A Treatise in Hydrodynamics, vol. II. Deighton, Bell, and Co., 1888.

Bentwich, M. and T. Miloh, The unsteady matched Stokes-Oseen solution for the flow past a sphere. J. Fluid Mech., 88, part 1, pp. 17-32, 1978.

Breach, D.R., Slow flow past ellipsoids of revolution, J. Fluid Mech. 10, 306, 1962.

Briley W. R., Numerical study of laminar separation bubbles using the Navier-Stokes equations. J. Fluid Mech., 47, pp. 713-736, 1970.

Chang, E.J. and M.R. Maxey, Unsteady flow about a sphere at low to moderate Reynolds number. Part 1. Oscillatory motion. J. Fluid Mech. 277, 347-379, 1994.

Chester, W. and D.R. Breach, On the flow past a sphere at low Reynolds number. J. Fluid Mech., 37, part 4, pp. 751-760, 1969.

Costis, C.E. and D.P. Telionis, Vortical wakes over a prolate spheroid. AIAA Journal, vol. 26, no. 10, 1988.

Dennis S.C.R. and J.D.A Walker, Aero. Res. Counc. no. 26, 1964.

Dennis S.C.R. and J.D.A Walker, Calculation of the steady flow past a sphere at low and moderate Reynolds numbers. J. Fluid Mech., 48, part 4, pp. 771-789, 1971.

Dennis S.C.R. and J.D.A Walker, Numerical solution for time-dependent flow past an impulsively started sphere, The Physics of Fluids, vol. 15, no. 4, 1972.

Drummond, C.K. and F.A. Lyman, Mass transfer from a sphere in an oscillating flow with zero mean velocity. Computational Mechanics, 6, pp. 315-326, 1990.

Fornberg, B., Steady viscous flow past a sphere at high Reynolds numbers. J. Fluid Mech., 190, pp. 471-489, 1988.

Gee, K. and R.M. Cummings, Turbulence model effects on separated flow about a prolate spheroid. AIAA Journal, vol. 30, no. 3, 1992.

Hamielec, A. E., Hoffman, T. W. & Ross, L. L. A.I.Ch.E.J. 13, 212, 1967.

Higa,M. and T. Takahashi, Stationary flow induced by an unharmonically oscillating sphere. Journal of the Physical Society of Japan, vol. 56, no. 5, pp. 1703-1712, May 1987.

Jenson, V.G., Viscous flow round a sphere at low Reynolds numbers(<40). Proc. Roy. Soc. A. 249, 346, 1959.

Juncu, GH. and R. Mihail, Numerical solution of the steady incompressible Navier-Stokes equations for the flow past a sphere by a multigrid defect correction technique, International Journal For Numerical Methods In Fluids, vol. 11, pp. 379-395, 1990.

Kanwal, R.P., Rotary and longitudinal oscillations of axi-symmetric bodies in a viscous fluid. Quart. Journ. Mech. and Applied Math., Vol. VIII, Pt. 2, 1954.

Kawaguti, M. Rep. Inst. Sci. Tokyo, 4, 154, 1950.

Kholeif, A. and M.H. Kamel, The deceleration of a sphere in an infinite viscous fluid. Convers. Mgmt, vol. 34, no. 3, pp. 239-241, 1993.

Klamkin, M.S., Stokes flow: An elementary treatment. SIAM Review, vol. 31, no. 4, pp. 667-670, 1989.

Lai, R.Y.S. and L.F. Mockros, The Stokes-flow on prolate and oblate spheroids during axial translatory accelerations. J. Fluid Mech., 52, pp. 1-15, 1972.

Lawrence, C.J. and S. Weinbaum, The force on an axisymmetric body in linearized, time-dependent motion: a new memory term. J. Fluid Mech., 171, pp. 209-218, 1986.

Lawrence, C.J. and S. Weinbaum, The unsteady force on a body at low Reynolds number; the axisymmetric motion of a spheroid. J. Fluid Mech., 189, pp. 463-489, 1988.

LeClair, B. P., Hamielec, A.E. & Pruppacher, H. R. J. Atmos. Sci. 27, 308, 1970.

Lee, D.K., M.J. Downie, and P. Bettess, An axisymmetric model of a separated flow about a sphere using discrete vortices, International Journal For Numerical Methods In Fluids, vol. 12, pp. 809-823, 1991.

Lister, M. Ph.D. Thesis, London, 1953.

Maxey, M.R. and J.J. Riley, Equation of motion for a small rigid sphere in a nonuniform flow. Phys. Fluids, 26(4), 1983.

Mei, R., Flow due to an oscillating sphere and an expression for Unsteady drag on the sphere at finite Reynolds number. J. Fluid Mech. 270, 133-174, 1994.

Mei, R. and R. Adrian, Flow past a sphere with an oscillation in the free-stream velocity and unsteady drag at finite Reynolds number. J. Fluid Mech. 237, 323-341, 1992.

Mei, R., C.J. Lawrence, and R. Adrian, Unsteady drag on a sphere at finite Reynolds number with small fluctuations in the free-stream velocity. J. Fluid Mech. 233, 613-631, 1991.

Natarajan, R. and A. Acrivos, The instability of the steady flow past spheres and disks. J. Fluid Mech. 254, pp. 323-344, 1993.

Odar, F. and S. Hamilton, Forces on a sphere accelerating in a viscous fluid. J. Fluid Mech., 18, 302, 1964.

Odar, F., Verification of the proposed equation for calculation of the forces accelerating in a viscous fluid. J. Fluid Mech., 25, part 3, pp. 591-592, 1966.

Oliver, D.L.R. and J.N. Chung, Flow about a fluid sphere at low to moderate Reynolds numbers. J. Fluid Mech. 177, pp. 1-18, 1987.

Oseen, C.W., Uber die Stokes'sche Formel umd uber eine verwandte Aufgabe in der Hydodynamik. Ark.f. Math.Astron. och Fys. 6, 29, 1910.

Patel, V.C., Flow around the impulsively started elliptic cylinder at various angles of attack. Computers and Fluids, vol. 9, no. 4, pp. 435-462, 1981.

Patel, V.C. and J.H. Baek, Boundary layer and separation on a spheroid at incidence. AIAA Journal, vol. 23, no. 1, 1985.

Payne, L.E., and W.H. Pell, The Stokes flow problem for a class of axially symmetric bodies. J. Fluid Mech. 7, 1960.

Raghavarao, C.V. and K. Pramadavalli, Numerical studies of slow viscous rotating flow past a sphere. I, International Journal For Numerical Methods In Fluids, vol. 7, pp. 307-317, 1987.

Raghavarao, C.V. and K. Pramadavalli, Numerical studies of slow viscous rotating flow past a sphere. III, International Journal For Numerical Methods In Fluids, vol. 9, pp.

1321-1329, 1989.

Raghavarao, C.V. and T.V.S. Sekhar, The flow past a spinning sphere in a slowly rotating fluid at small Reynolds numbers-A numerical study. Int. J. Engn Sci., vol. 31, no. 9, pp. 1219-1231, 1993.

Raman, V.M., Numerical Prediction of a laminar boundary layer flow on a rotating sphere. Computer Methods in Applied Mechanics and Engineering, 43, pp. 37-44, North-Holland, 1984.

Riley, N., On a sphere oscillating in a viscous fluid. Quart. Journ. Mech. and Applied Math., vol. XIX, Pt. 4, 1966.

Rimon, Y. & Cheng, S. I., Phys. Fluids, 12, 949, 1969.

Rubel, A., Axisymmetric shear flow over spheres and spheroids. AIAA Journal, vol. 24, no. 4, 1986.

Sano, T., Unsteady flow past a sphere at low Reynolds number, J. Fluid Mech., 112, pp. 433-441, 1981.

Shirayama, S., Flow past a sphere: Topological transitions of the vorticity field. AIAA Journal, 1992.

Spall, R.E. and M.R. Malik, Linear stability of three-dimensional boundary layers over axisymmetric bodies at incidence. AIAA Journal, vol. 30, no. 4, 1992.

Stokes, G.G., On the effect of the internal friction of fluids on pendulums. Trans. Camb. Phil. Soc. 9, 8, 1851.

Su, W., B. Tao, and L. Xu, Three-dimensional separated flow over a prolate spheroid. AIAA Journal, vol. 31, no. 11, 1993.

Williams, M.M.R., Thermophoretic forces acting on a spheroid. J. Phys. D.: Appl. Phys. 19, pp. 1631-1642, 1986.

Wu, T. and S. Shen, Emergence of three-dimensional separation over a suddenly started prolate spheroid at incidence. AIAA Journal, vol. 30, no. 11, 1992.

VITA

Rajai Samih AlAssar was born September 5, 1965. He received his primary, intermediate, and secondary education in Taif, Saudi Arabia. In 1983, he joined KFUPM where he received his B.Sc. and M.Sc. in civil engineering in 1988 and 1992, respectively. Since 1992 to date, he has been working as a lecturer in the civil engineering department at KFUPM and, at the same time, working towards his Ph.D.